ABSTRACT

Title of Dissertation: TRANSIENT MODELING OF TWO-STAGE AND VARIABLE REFRIGERANT FLOW VAPOR COMPRESSION SYSTEMS WITH FROSTING AND DEFROSTING

Hongtao Qiao
Doctor of Philosophy, 2014

Dissertation Directed By: Reinhard Radermacher, Professor
Department of Mechanical Engineering

This thesis presents the development of an advanced modeling framework for the transient simulation of vapor compression systems. This framework contains a wide range of components and its modular nature enables an arbitrary cycle configuration to be analyzed. One of the highlights of this framework is the first-principles heat exchanger models with many salient simulation capabilities. Specifically, a high-order discretized model employing finite volume analysis is developed based on a decoupled approach to modeling the heat transfer and pressure drop performance of the heat exchanger. The frosting and defrosting models developed in the thesis are integrated into this heat exchanger model, allowing more

accurate performance assessment of heat pumps. Meanwhile, an advanced low-order moving boundary heat exchanger model is developed with switched model representations to accommodate the changing numbers of fluid zones under large disturbances. Compared to the existing moving boundary models in the literature, this new model accounts for refrigerant pressure drop and possesses a more accurate evaluation for the air side heat transfer.

Based on this modeling framework, the transient characteristics of a flash tank vapor injection (FTVI) heat pump system undergoing cycling, frosting and reverse-cycle defrosting operations are thoroughly explored. The dynamic system response when subjected to a step change in the opening of the upper-stage electronic expansion valve is also investigated. Comparison between the predictions and experimental data shows that the simulation can adequately capture the transient heat transfer and fluid flow phenomena of the system and thus demonstrating the fidelity of the models. Furthermore, a pull-down simulation for a multi-split variable refrigerant flow (VRF) air-conditioning system with six indoor units has been carried out. Control strategy that aims to maintain the indoor air temperatures at set values is proposed. The simulation test for controllability shows that the proposed control strategy is feasible to achieve the temperature control of individual zones.

TRANSIENT MODELING OF TWO-STAGE AND VARIABLE REFRIGERANT FLOW VAPOR COMPRESSION SYSTEMS WITH FROSTING AND DEFROSTING

By

Hongtao Qiao

Dissertation submitted to the Faculty of the Graduate School of the
University of Maryland, College Park, in partial fulfillment
of the requirements for the degree of
Doctor of Philosophy
2014

Advisory Committee:
Professor Reinhard Radermacher, Chair
Professor Marino diMarzo
Associate Professor Bao Yang
Associate Professor Peter Sunderland
Assistant Professor Amir Riaz

Dedication

In dedication to my father

I miss you so much and I will always love you and remember you

Acknowledgments

It would not have been possible to write this doctoral thesis without the help and support of the kind people around me, to only some of whom it is possible to give particular mention here.

First of all, I would like to express my deepest gratitude to my advisor, Dr. Reinhard Radermacher, for his guidance, patience, and providing me with a very stimulating research atmosphere. It has been a great pleasure and privilege to learn from him. Many thanks to my advisory committee, Dr. Marino diMarzo, Dr. Bao Yang, Dr. Peter Sunderland, and Dr. Amir Riaz, for their service and contribution to making this thesis as strong as possible.

I am grateful to Dr. Vikrant Aute for his insightful comments both in my work and in this thesis, and for many inspiring discussions. I also wish to thank the former CEEE graduate students Xing Xu for providing me experimental data to perform model validation in this thesis and Laeun Kwon for sharing his expertise in VRF systems. Special thanks go to Dr. Hubertus Tummescheit at Modelon Inc. and Dr. Christian Hermes at the Federal University of Paraná for their valuable advice in two-phase flow modeling.

Over the past years, I have been very privileged to get to know and to collaborate with many other great people. Many thanks to Long Huang and Jiazhen Ling, who have been a great pleasure to work with. Special thanks to Song Wei Li for the Ping-Pong time every Sunday afternoon. I appreciate them all and other CEEE students from my heart for all the great fun while together.

Most importantly, I would like to thank my wonderful wife, Ruijin Zhu, for her love and sacrifice over the years. She was always there cheering me up and stood by me through the good times and bad. My parents and my sister have given me their unequivocal support throughout everything. Without the encouragement from them, this achievement would not have been possible.

Table of Contents

List of Tables

List of Figures

xiv

Nomenclature

a	curve fitting constant [-]
A	area [m^2]
ASHRAE	American Society of Heating, Refrigerating and Air Conditioning Engineers
b	curve fitting constant [-]
c	curve fitting constant [-]
c_p	specific heat capacity at constant pressure [$J\ kg^{-1}\ K^{-1}$]
c_{sv}	vaporization coefficient of surface water [m/s]
c_v	specific heat capacity at constant volume [$J\ kg^{-1}\ K^{-1}$]
C_v	flow coefficient [-]
C_w	heat capacity of the walls per unit length [$J\ m^{-1}\ K^{-1}$]
d	diameter [m]
D	water vapor diffusion coefficient [$m^2\ s^{-1}$]
e_{sh}	error between the measured superheat and the set point [K]
EB	energy balance [-]
f	friction factor [-] or frequency [Hz]
F	spring force [N]
FPI	number of fins per inch [-]
G	mass flux [$kg\ m^{-2}$]
h	specific enthalpy [$J\ kg^{-1}$]
$\bar{h}$	mass flow weighted enthalpy [$J\ kg^{-1}$]

$\bar{h}_{FT}$	mass-based refrigerant mean enthalpy in flash tank [J kg^{-1}]
$\bar{h}_{\rho}$	density weighted enthalpy [J kg^{-1}]
H	height [m]
$\dot{H}$	enthalpy flow rate [J s^{-1}]
$\dot{I}$	momentum flow [kg m s^{-2}]
k	thermal conductivity [W/m-K] or isothermal compressibility [Pa^{-1}]
K	PID gain [-], constant for tracking temperature [-]
K_c	abrupt contraction coefficient [-]
K_e	abrupt expansion coefficient [-]
L	Length [m]
Le	Lewis number [-]
$\dot{m}$	mass flow rate [kg s^{-1}]
$\dot{m}''$	mass flux [kg s^{-1} m^{-2}]
M	mass [kg]
n	polytropic index [-]
N	motor speed [min^{-1}] or number [-]
NPT	National Pipe Thread
p	pressure [N m^{-2}]
P	perimeter [m]
P_r	row pitch [m]
P_t	tube pitch [m]
q	heat transfer rate [W]

q'	heat transfer rate per unit length [W m^{-1}]
q''	heat flux [W m^{-2}]
Q	energy [J]
R	thermal resistance [K W^{-1}], water vapor constant = 461.5 J kg^{-1} K^{-1}
R_e	equivalent fin radius [m]
Re	Reynolds number [-]
s	specific entropy [J K^{-1}]
S	slip ratio [-]
t	time [s]
T	temperature [K]
u	velocity [m s^{-1}] or specific internal energy [J kg^{-1}]
U	internal energy [J]
v	specific volume [m^3 kg^{-1}]
V	volume [m^3]
$\dot{V}$	volumetric flow rate [m^3 s^{-1}]
$\dot{W}$	power [W]
x	flow quality [-]
$\hat{x}$	static quality [-]
y	spring deflection [m]
Δ	difference
Δy	segment length along the direction of air flow [m]
Δz	segment length along the direction of refrigerant flow [m]

Greek letters

α	heat transfer coefficient [W m^{-2} K^{-1}] or mass transfer coefficient [kg s^{-1} m^{-2}]
β	angle [degree] or isobaric coefficient of expansion [k^{-1}]
χ	fraction of compressor power dissipated to the ambient [-]
δ	thickness [m]
ε	emissivity [-], local porosity [-] or minimum threshold [-]
ϕ	pressure ratio [-]
γ	void fraction [-]
η	efficiency [-]
φ	valve opening fraction [-] or two-phase pressure drop multiplier [-]
κ	spring constant [N m^{-1}]
μ	dynamic viscosity [kg m^{-1} s^{-1}]
θ	angle [degree]
ρ	density [kg m^{-3}]
σ	Boltzmann constant [m^2 kg^2 s^{-2} K^{-1}] or the ratio of the minimum free flow are to the frontal-area [-]
τ	time constant [s], wall shear stress [N m^{-1}] or tortuosity factor [-]
ϖ	frequency ratio [nd] or compressor speed [min^{-1}]
ω	humidity ratio [kg H$_2$O / kg dry air]
ξ_{shf}	fraction of mechanical loss at the shaft [-]
ζ	built-in volume ratio of the first stage [-], the fraction of the heat exchanger [-] or absorption coefficient [-]

Subscripts

a	air
acc	accumulator
als	between ambient and compressor lower-shell
amb	ambient
aus	between ambient and compressor upper-shell
b	sensor bulb of TXV
bub	bubble point
c	correction or contraction
cir	circuit
comp	compression
cond	conduction
cs	cold stream
d	derivative or densification
Darcy	Darcy friction factor
dew	dew point
diaph	diaphragm of TXV
dis	discharge
disp	displacement
dry	dry
e	expansion
eff	effective
ent	entrance

eo	evaporator outlet
eq	equalization
exp	expansion device
ext	exit
f	saturated liquid or frost
face	frontal face
fan	fan
fg	liquid to gas
fin	fin
frict	frictional
fs	frost surface
FT	flash tank
g	saturated vapor
h	mass flow weighted
hcs	between hot stream and cold stream
hom	homogeneous
hs	hot stream
H_2O	water
i	integral or internal
ice	ice
if	ice to liquid
ig	ice to vapor
in	inlet

inj	injected flow
int	intermediate stage
L	length
lat	latent
liq	liquid
LMTD	Logarithm Mean Temperature Difference
lo	liquid outlet or liquid only
load	load
ls	compressor lower-shell
m	motor, mass transfer or mean value
M	momentum
max	maximum
mech	mechanical
melt	melt
min	minimum
mix	mixing
new	new
nom	nominal
o	external
offset	offset
open	open
ops	operating superheat
ori	orifice of TXV

os	opening superheat
out	outlet
p	proportional
parent	parent
pin	pin of TXV
pseudo	pseudo
r	refrigerant
rated	rated conditioning
rev	reversing valve
rise	rise
rls	between refrigerant and compressor lower-shell
rm	room or between refrigerant and compressor motor
row	tube row
rscr	between refrigerant and compressor scroll set
rshf	between refrigerant and compressor shaft
s	surface
sat	saturation
sc	subcooled
scr	scroll set
sen	sensible
set	set point
sh	superheat or superheated
shf	shaft

ss	static superheat
st	stored
suc	suction
t	tube or time
target	target
tot	total
tp	two-phase
upstream	upstream
us	compressor upper-shell
v	water vapor
vap	vapor
vo	vapor outlet
w	wall
water	condensate water
wet	wet
zone	zone
ρ	density relevant
δ	thickness relevant

1 Introduction

1.1 Background and Motivation

In modern day HVAC&R (Heating, Ventilation, Air-Conditioning and Refrigeration) industry, numerical simulations have been widely employed to assist in the design and optimization of advanced products in response to the increasing pressure of cost reduction and high energy efficiency standards. With the aid of simulation tools, design engineers can evaluate a not-yet-existing product on computers instead of building real systems and conducting expensive tests in the laboratory, thereby shortening the design cycle.

In general, vapor compression system simulations can fall into one of two categories: steady-state or transient. The evaluation of the steady-state, full-load performance of vapor compression systems is often used to determine the capacity requirement and the size of the unit. However, vapor compression systems rarely operate under steady-state conditions. Examples of the transient operations include: (1) start-up and shut-down surges; (2) part-load operation with capacity control measures; (3) frost accumulation on coil surfaces which gradually degrades system performance; and (4) defrosting processes needed to be initiated periodically in order to remove frost buildup and free coil surfaces before the equipment can return to normal operation, etc. Taking these circumstances into account, a transient simulation is expected to capture the overall system performance more accurately (Murphy and Goldschmidt, 1985 & 1986; Yasuda *et al*., 1990; Liu *et al*., 2003; Zhang and Zhang, 2011b). Moreover, in order to investigate the effects of integrated control on the operation of vapor compression systems, it is important to predict the transient

response and stability characteristics of the overall systems as well as its components (Yasuda *et al.*, 1983; He *et al.*, 1998; Shah *et al.*, 2004; Li *et al.*, 2010a).

A basic four component vapor compression system is shown in Figure 1.1.The hot vapor discharged by the compressor flows through the condenser where the lower temperature heat sink removes the heat from the refrigerant until it condenses into the subcooled liquid when exiting the condenser. Then the refrigerant liquid goes through the expansion valve where the pressure and temperature decrease abruptly. This process results in a vapor-liquid mixture flowing through the evaporator where the liquid evaporates. The resulting refrigerant vapor returns to the compressor inlet, and is then compressed and discharged at a higher temperature, thus completing a thermodynamic cycle.

With the emergence of advanced technologies in the HVAC&R industry, however, system configurations grow in complexity. For instance, two-stage compression system with vapor injection has been gaining in popularity recently, since it is superior to the traditional single-stage systems with no vapor injection due to higher energy efficiency and lower discharge temperature as well as the flexibility in adjusting the system capacity. Another example is that the multi-split variable refrigerant flow (VRF) system, consisting of an outdoor unit and multiple indoor units, is receiving plenty of attention because of the primary advantages of higher energy saving potential and better indoor thermal comfort. The introduction of new complex systems requires a transient simulation tool to be capable of handling cycle configurations beyond that of the basic four component system. Meanwhile, the simulation of such advanced cycles brings a great many challenges that often

intimidate researchers, such as more complicated system topologies, extravagant modeling details and computational complexities.

Although the extant work has made great progress in the area of transient simulations of vapor compression systems, there are still a plenty of challenges worth devoting effort to further delve thoroughly. The rest of this chapter will detail the techniques for transient modeling of vapor compression systems and will try to identify the research gaps in the existing studies.
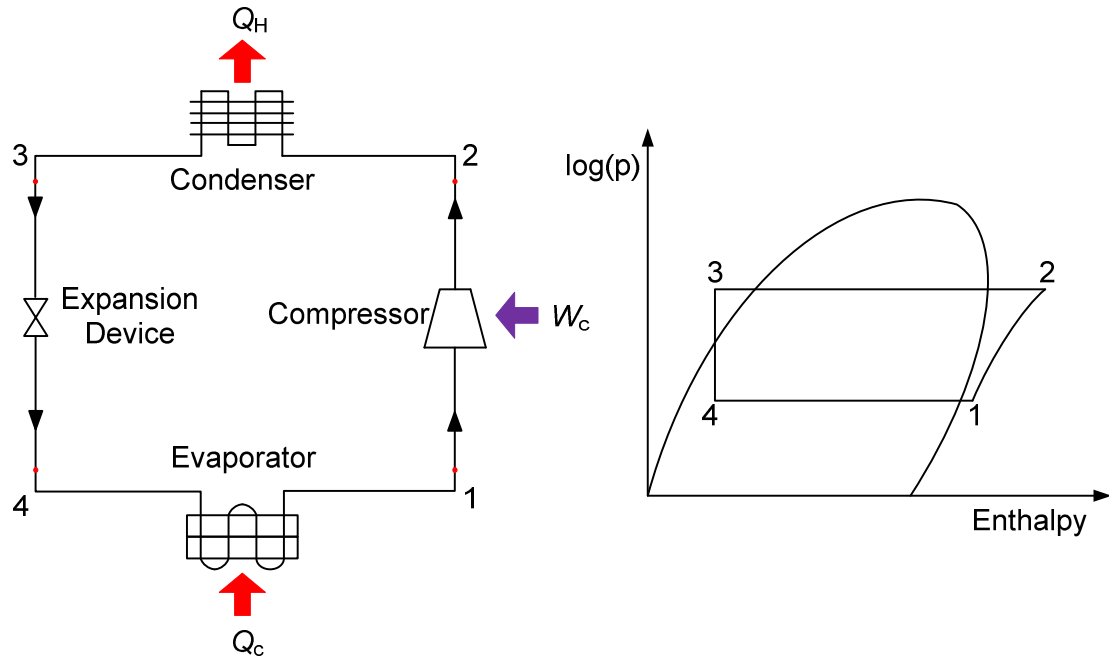
Figure 1.1 A four-component basic vapor compression system

1.2 Overview of Transient Modeling of Vapor Compression Systems

1.2.1 Compressor Models

Compressors are the heart of vapor compression systems and determine the system capacity along with the expansion devices. Therefore, performance prediction for the compressors is essential for system level simulations because firstly, the prediction discrepancy of refrigerant mass flow rate will be propagated to other

component models; secondly, the heat exchangers are typically oversized for the design condition. Therefore, the prediction of the system performance largely relies on the computation of the mass flow rate.

A number of compressor models have been developed so far. In general, these compressor models can fall into three categories (Zhao *et al*., 2009): 1) map-based models or black-box models; 2) efficiency-based models or gray-box models and 3) detailed models or white box models.

Map-based models (ANS/AHRI Standard 540, 2004; Shao *et al*., 2004) are based on extensive experimental data from compressor performance tests and are most likely to have an accurate performance prediction in terms of the mass flow rate, power consumption and discharge temperature. One of the most recognized models in this category is ARI 10 coefficient model, which correlates the performance indicators with saturated suction and discharge temperatures using ten coefficients (ANS/AHRI Standard 540, 2004). Since no complicated physical and geometric parameters are included in this model, it is very convenient to for system level simulations. However, such map-based models are refrigerant dependent if the saturated temperatures instead of pressures are used in the models. Also, they are only valid over specific ranges and do not maintain good accuracy for extrapolation. This necessitates developing map-based models which can maintain their accuracy over regions of extrapolative use.

Efficiency-based models (Jabardo *et al*., 2002) are based on the ideal compression process and make use of volumetric efficiency and isentropic efficiency via empirical or semi-empirical formulas to predict the compressor performance.

Since these models involve more physical fundamentals than the map-based models and thus can maintain good accuracy for the extrapolative calculations. Both map-based models and efficiency-based models usually use the suction state and discharge pressure as inputs to evaluate the compressor performance.

The third category, detailed compressor models (Chen *et al.*, 2002; Chen *et al.*, 2004; Rigola *et al.*, 2005; Mathison *et al.*, 2008), requires many geometric parameters of the compressor, and simulates almost every individual process including the compression process, heat transfer between refrigerant and metallic parts, internal refrigerant leakage, and overall energy balance of the compressor, etc. This type of models is useful for the compressor design and not suited for system level simulations due to computational complexity.

In the transient simulations of vapor compression systems, the compressor is often treated as a quasi-steady state component, meaning that the calculated mass flow rate, power consumption and discharge temperature update instantaneously based on the current suction condition and discharge pressure. This is a valid assumption since the dynamics associated with the variation in the compressor mass flow rate are much faster than those associated with the heat exchanger performance (Winkler, 2009).

Although they can be used in transient simulations, the steady-state compressor models cannot capture the transient characteristics, such as the variation in the compressor shell temperature and refrigerant storage inside the suction or discharge chamber. A detailed model that accounts for the variation within each cycle of the compression process would be too computationally expensive. This dilemma

necessitates another approach, which divides the compressor model into two parts, i.e., the steady-state part for the mass flow rate calculation without considering the refrigerant mass storage inside the compressor shell, and the transient part for the heat transfer calculation accounting for the thermal storage of the compressor shell (Ding, 2007).

1.2.2 Expansion Device Models

In vapor compression systems, capillary tubes, orifices and expansion valves are used as the throttling devices to regulate the refrigerant mass flow. The fluid through these expansion devices experiences a drastic change in thermophysical properties and the mechanism behind is very complex. Based on the modeling approach, expansion device component models mainly tend to fall into two groups: correlation-based models and physics-based models.

Correlation-based models (Stoecker, 1983; Kim *et al*., 1994; Kim and O'Neal, 1994; ASHRAE, 2002; Choi *et al*., 2003; Li *et al*., 2004; Park *et al*., 2007) tend to calculate the mass flow rate given the inlet condition and downstream pressure. These models use simple equations and have good accuracy over the range of regression. However, the downside of these models is the unpredictable accuracy over the regions of extrapolative use. When the fluid conditions are out of the regression range, the resulting predictions based on these models are usually skeptical. Furthermore, these models tend to be refrigerant-dependent, and they might work well for some refrigerants, but not for others (Zhang and Ding, 2001).

Compared to correlation-based models, physics-based models are more worthy to investigate from a research point of view. As a matter of fact, a number of studies have focused on the modeling of capillary tubes and short tube orifices (Kim and

O'Neal, 1995; Zhang and Ding, 2001; García-Valladares *et al.*, 2002; Bassiounay and O'Neal, 2004; Zhang and Yang, 2005; Yang and Zhang, 2005; Madsen *et al.*, 2005; Agrawal and Bhattacharyya, 2008). Physics-based models can be further classified into homogeneous flow models (Bansal and Rupasinghe, 1998) and separated flow models (Wong and Ooi, 1996; Ding, 2007), based on whether the assumption of homogeneous flow is adopted or not. Homogenous flow models assume that the slip ratio between liquid phase and vapor phase is unity, and the void fraction can be analytically evaluated. While separated two-phase flow is considered, the void fraction needs to be estimated using semi-empirical models.

In general, there are four regions along the capillary tube, including subcooled liquid region, metastable liquid region, metastable two-phase region and equilibrium two-phase region (García-Valladares *et al.*, 2002). The existence of metastable flow regions actually increases the mass flow because it results in the delay of flash point. As a consequence, the overall resistance of the capillary tube is reduced. In capillary tube models, however, the metastable flow is usually neglected due to its unpredictability. Studies show that the resulting deviation without considering metastable flow is acceptable, and the predictions can be readily corrected by other means (Ding and Zhang, 2001; Ding, 2006).

When modeling the refrigerant flowing through the capillary tube, it is generally assumed that no heat transfer occurs, and the stagnation enthalpy of the refrigerant is considered to be conserved throughout. However, in some applications this is not the case. For instance, in household refrigerators and automobile air-conditioners, capillary tube is often in thermal contact with the suction line to achieve

7

better system performance. To consider the heat transfer when refrigerant flows through the capillary tube, non-adiabatic capillary tube models are required.

Non-adiabatic capillary tube models (Chen and Gu, 2005; Agrawal and Bhattacharyya, 2007; Hermes *et al*., 2008) differ from the adiabatic models in two aspects. One is that for non-adiabatic models, the calculation needs to account for the heat transfer through the tube wall in order to evaluate the refrigerant outlet state for each calculation domain. This greatly increases model complexity. The other aspect is that in the adiabatic cases, the entropy increases during the throttling process and can be used as the criteria to judge whether the flow is choked or not. In the non-adiabatic case, however, the entropy might decrease due to heat rejection and therefore cannot be used to as the criteria to determine the choked flow. In this situation, that the local refrigerant velocity equals the local sonic velocity is used to judge the occurrence of choked flow (Chen and Gu, 2005).

1.2.3 Heat Exchanger Models

The thermal inertia of the components, and more importantly the dynamics of the refrigerant flow, dictate the transient characteristics of vapor compression systems operating under disturbances. It has been found that the migration of refrigerant during the off-cycle is mainly responsible for the cycling losses during the start-up operation (Murphy and Goldschmidt, 1986; Wang and Wu, 1990; Janssen *et al*., 1992; Rubas and Bullard, 1995). During normal operating conditions, most of refrigerant resides inside the heat exchangers, which are the major components that experience the exchange of mass, energy and momentum with other components, including the compressor and expansion device as well as other auxiliary components, and with the secondary fluids (Björk and Palm, 2006a and 2006b). Consequently, it is crucial to

obtain an accurate prediction for refrigerant charge inside the heat exchangers so as to more accurately capture two-phase fluid flow phenomena (Jakobsen *et al*., 1999; Kærn *et al*., 2011b). In addition, heat transfer is another factor that plays a significant role in dictating the thermal dynamics of the system. However, the calculation of heat transfer between the refrigerant and the secondary fluids through the heat exchanger materials relies heavily on the choice of empirical correlations and yields large uncertainties. In contrast with heat transfer, pressure loss has a less decisive impact upon system performance. In the early efforts, refrigerant pressure loss was often neglected, thereby eliminating the need of the momentum conservation equation in the simulations, to improve the computational efficiency. With the augmentation of computer power, more studies tend to take it into consideration. Likewise, it is very difficult to accurately predict refrigerant pressure loss due to the parasitic uncertainties associated with the empirical correlations.

As discussed above, the heat exchangers exert the most influence on the transient thermal performance of the system. Therefore, it is essential to deduce an adequate model representation describing the main heat transfer and fluid flow phenomena in the heat exchangers. The common modeling techniques of the heat exchangers can be classified into four categories: black box models, lumped parameter models, moving boundary models and distributed parameter models. Each one of these modeling techniques is reviewed hereinafter.

1.2.3.1 <u>Black-Box Models</u>

In contrast with physics-based modeling approaches (transparent models) that are described by the conservation laws, black-box models are created directly from experimental data and typically used to investigate control problems. With this

modeling technique, heat exchangers are represented by a set of transfer functions with several constants that have been identified by experiments (Aprea and Renno, 2001). This type of models has the advantages of simplicity and quantitative accuracy within the prescribed operating range represented by the data (Rasmussen, 2012). However, when the operating conditions deviate from the prescribed range, model predictions become unreliable. The challenges associated with generating black box models are related to the selection of model structure and the design of the transient experiments. According to Rasmussen (2012), caution must be taken to avoid over-fitting the data to the model, and lower order models with fair accuracy are always favorable. Meanwhile, the magnitude and frequency of input citation signals should be chosen properly. Since the data-driven modeling approach is not the focus of this thesis, the author will not dig further to elaborate it. Interested readers are encouraged to refer to the review paper by Rasmussen (2012) for more information.

1.2.3.2 Lumped Parameter Models

In the open literature, lumped parameter models are often referred to the models that simplify the description of the characteristics of an inherently spatially-distributed physical system with some mean properties assumed being homogeneous throughout by averaging out the spatial variations of its physical properties. In this section, lumped parameter models are the models that denote the entire heat exchanger with a single lumped control volume or several individual control volumes, each of which is representative of a particular fluid phase within the heat exchanger (i.e., superheated vapor, two-phase regime, subcooled liquid).

In the single-control volume models, the entire heat exchanger is analyzed based on the lumped parameters that represent the characteristics of the system.

Specifically, in these models, there is only one time-varying value for each system property, e.g., refrigerant pressure, enthalpy, temperature and density, etc. The heat transfer between the refrigerant and secondary fluids is evaluated based on an average heat transfer coefficient in the entire heat exchanger. These models are often used in the early research efforts because they offer the advantages of simplicity and computation efficiency.

However, since these models disregard the spatial variation in refrigerant properties and the distinct differences of the heat transfer mechanisms between single-phase and two-phase fluids, they without question result in the most inaccurate predictions among the four modeling approaches mentioned above. Therefore, multi-control volumes are necessary to distinguish the single-phase regimes from the two-phase regime and achieve more satisfactory predictions with higher precision.

Two-control volume models are often applied for the evaporator (evaporation and superheating regime), whereas three-control volume models are often applied for the condenser (desuperheating, condensation and subcooling regimes). The conservation laws of mass, energy and momentum are established for each regime. Heat transfer is also calculated separately for individual regimes based on the corresponding temperature difference and heat transfer coefficient between the refrigerant and secondary fluids. Unlike single-control volume models in which a uniform pressure is present throughout the entire heat exchanger, it is possible to evaluate the pressure loss between different regimes with the multi-control volume approach. However, it is worthwhile to point out that the number of control volumes in these models depends upon the number of available phases currently present within

the heat exchanger and might not be fixed. The creation or destruction of fluid phases will occur under large disturbances, especially during start-up and shut-down operations of vapor compression systems. This scenario can be well addressed by the moving boundary models equipped with the switching schemes. Moving boundary model is a variation of the lumped parameter approach, and it owns unique characteristics different from other lumped parameter models. Therefore, the author would like to single this modeling approach out and elucidate it separately in the subsequent section.

1.2.3.3 <u>Moving Boundary Models</u>

Although distributed parameter models render the most accurate predictions, they are not generally well suited for control design where low-order models are more favorable. A class of low-order models can be categorized as moving boundary models which are superior to distributed parameter models for control design. They are characterized by dividing the heat exchanger into control volumes each of which exactly compasses a particular fluid phase (superheated vapor, two-phase flow, subcooled liquid). The control volumes are separated by a moving interface where the refrigerant phase transition occurs between single-phase regimes and the two-phase regime. In contrast to the distributed parameter models, the number of control volumes in moving boundary models may vary depending on the number of available phases currently present within the heat exchanger. Therefore, a heat exchanger may own three control volumes at most and one control volume at least at a time. The objective of these models is to capture the thermodynamic behavior inside these control volumes and the time-varying positions of phase boundaries.
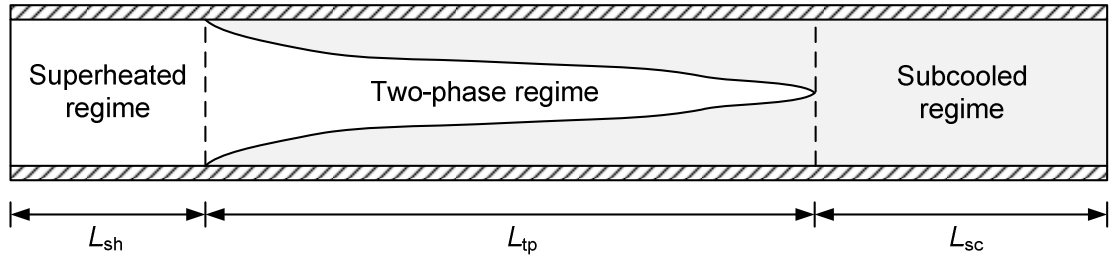
Figure 1.2 Moving boundary heat exchanger model

In moving boundary models, as shown in Figure 1.2, each control volume is still analyzed with the lumped parameter approach. To integrate the conservation equations over the control volume, it is necessary to make reasonable assumptions for the distribution of mass and energy inside the volume. A common practice is to assume a linear profile for the enthalpy along the length of each control volume so that the overall mass and energy storage inside control volume can be readily evaluated. Hence, the mean enthalpy for the single-phase control volume can be computed as the arithmetic average of the instantaneous enthalpy that enters and leaves the control volume. However, a more sophisticated approach is needed to handle the case in which the control volume is occupied by two-phase flows. The two-phase mean void fraction model, originated by Wedekind and Stoecker (1968) to study the transient response of the mixture-vapor transition point in horizontal evaporating flow, can be applied to calculate the overall mass and energy of two-phase flows. This concept, which has been demonstrated to successfully predict a variety of transient two-phase flow phenomena (Wedekind, *et al*. 1978; Beck and Wedekind, 1981), greatly facilitates the development of various moving boundary models by possibly simulating the two-phase region in lumped parameter fashion. However, a key simplification in these works is that the time-varying effect of the

mean two phase void fraction has been neglected because its change tends to be small during transients, and also because its time dependence is related to dynamic modes that are faster than the dominant system dynamics (Rasmussen, 2006). However, it turns out that this simplification may result in numerical discontinuities during the phase change (Zhang and Zhang, 2006). Therefore, some recent publications discard this simplification and include the time derivative of the mean void fraction in their model formulations (Zhang and Zhang, 2006; Eldredge *et al*., 2008; Li and Alleyne, 2010).

One of distinctions between different moving boundary models lies in how to assume the wall temperature at the boundaries between neighboring regions. Unlike the assumption of a continuous distribution for the enthalpy along the heat exchanger, the corresponding wall temperature associated with each region is spatially independent and uniform within that region. Therefore, the wall temperature is discontinuous at the phasic boundaries, which poses numerical challenges in the simulation. Common ways to calculate the wall temperature at the phase boundaries are summarized as follows: 1) the wall temperature at the boundary equals the wall temperature in the two-phase region (Rasmussen and Alleyne, 2004); 2) take the average temperature of the left and right walls (Jensen, 2003); 3) the wall temperature at the boundary is determined based on the boundary velocity (McKinley and Alleyne, 2008); and 4) a weighted mean temperature based on the length ratio of the neighboring regions (Zhang and Zhang, 2006). Of these four different formulations, the last two are more commonly used perhaps because they are more physically solid.

Another key to simplify moving boundary models is the assumption of the uniform pressure distribution throughout the heat exchanger given the fact that the pressure loss results in minor influence on the system performance compared to the heat transfer. Although it results in deviations from real systems, this simplification is universally accepted because the equation of momentum balance is not required in the analysis and thus modeling complexity being substantially reduced. A couple of exceptions are found in Tian and Li (2005), Tian *et al*. (2005) and Yebra *et al*. (2005). In Tian's work, static pressure loss is assumed to concentrate at the end of each region. However, this approach only works fine when there is no creation or destruction of fluid phases. Otherwise, a mathematical discontinuity in pressure will be experienced. While following the staggered grid scheme and finite volume method, Yebra *et al*. (2005) presented a three-zone moving boundary model including the momentum conservation. But their work can be further enhanced with four control volume analysis.

It is worthwhile to point out that there are a variety of model reduction techniques to further simply the moving boundary modeling paradigm. Common practices include neglecting the dynamics in the superheated region and lumping the wall and fluid temperature to set them equal to each other (Jensen, 2003). These model reduction techniques are often applied for different applications.

As mentioned earlier, the number of available fluid phases in the heat exchanger may vary under large disturbances and fluid phases can disappear or appear. Early moving boundary models often have a fixed number of zones and they are severely restricted from broader applications. However, the condenser may

experience transitions two times during the start-up operation, vapor → vapor & two-phase → vapor, two-phase & liquid. Therefore, moving boundary models accounting for the changing number of fluid phases are needed to ensure smooth transition between different model representations. Although the recent research efforts in moving boundary modeling framework have focused on tackling drastic transients experienced by the heat exchangers operating under start-up and shut-down conditions (Li and Alleyne, 2010), this type of models are inherently not as robust as distributed parameter models (Bendapudi *et al*., 2008) because of the potential numerical failures as a result of model transition, such as chattering and numerical singularities.

1.2.3.4 <u>Distributed Parameter Models</u>

Distributed parameter models (Figure 1.3) are often characterized by subdividing the entire heat exchanger into a fixed number of non-deforming control volumes, each of which represents a single refrigerant state and is analyzed using the lumped parameter approach by imposing the conservation laws. In contrast to the moving boundary method, these control volumes are stationary and do not vary in position or size irrespective of the transition of fluid phases. The number of control volumes is predetermined before the simulation and will not alter thereafter. The more refined grid discretization, the more accurate predictions will be attained. However, it is not difficult to understand that the accuracy and the simulation speed go hand in hand, i.e., higher precision means more computational cost. Therefore, an inevitable trade-off should be made between the prediction accuracy and the computation speed.

16
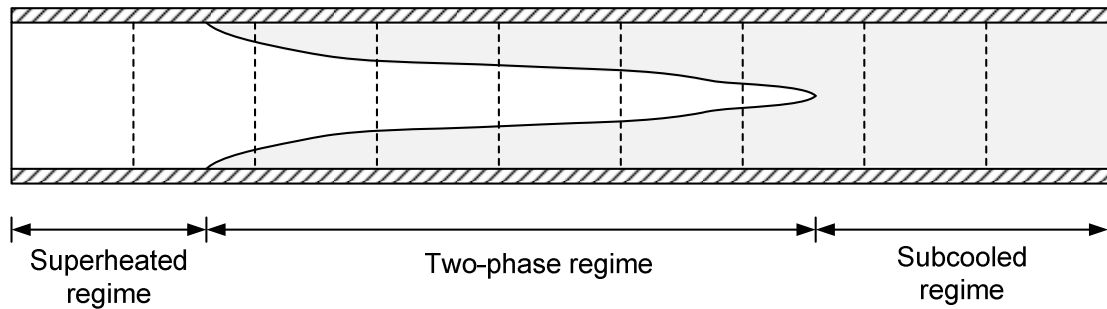
Figure 1.3 Distributed parameter heat exchanger model

In distributed parameter models, the original governing equations for one-dimensional fluid flow in a form of partial differential equations (PDEs) are spatially discretized and can be solved by various methods like finite difference, finite volume or finite element methods. The finite volume method is often chosen because it has good properties with regard to maintaining the conserved quantities.

The distributed parameter approach makes itself so attractive in the heat exchanger modeling because it can describe the transient behavior of a two-phase flow heat transfer system in great detail with local heat transfer coefficients. Meanwhile, this approach lends itself to great flexibility by accounting for complex coil circuitry instead of simplifying each refrigerant circuit as a straight tube, a common assumption adopted by the moving boundary approach, therefore providing better agreement with real systems.

The prediction for the transient behavior of the heat exchanger is heavily dependent on the prediction of refrigerant charge which is in turn dictated by the way of calculating the average properties of control volumes. If a control volume is in single-phase, properties can be easily evaluated by the refrigerant thermophysical property routines based on the known states, such as the pressure and enthalpy. However, if a control volume is in two-phase, the situation becomes a little touchy.

In general, there are three different ways to tackle this two-phase flow problem. The simplest way is called the homogeneous equilibrium model (HEM), which assumes the refrigerant liquid and vapor phases are in thermodynamic equilibrium and both of them have the same phasic velocity. Therefore, two phases can be treated as a single phase with average properties. The HEM model is the better choice for bubbly or mist flow, since the liquid-vapor interface is very small and the slip ratio is very close to unity. Another case in which the homogeneous model will yield good results is near the critical point ($\rho_l = \rho_v$), in which case $\gamma \approx x$. However, a large portion of the heat exchanger usually operates under the separated flow conditions where unequal density and viscosity of liquid and vapor will force the vapor to attain a relative velocity or slip with respect to the liquid. Under this circumstance, the HEM tends to significantly over predict the void fraction and results in a prediction of lower refrigerant mass and faster transients. The HEM model is often applied in many studies in order to allow a more tractable computation (MacArthur, 1984a and 1984b; Chen and Lin, 1991; Nyers and Stoyan, 1994; Jia *et al*., 1995; Aprea and Renno, 1999 and 2002; Jiang and Radermacher, 2003; Schalbart and Haberschill, 2013).

A common remedy to the HEM model is to allow only velocity to differ for the two phases such that the conversation equations can be written for the combined flow as in the case of the homogeneous flow where equal phasic velocities are assumed. Under this circumstance, the two-phase flow density is corrected by employing an appropriate void fraction model and thus a closer prediction for the refrigerant mass being obtained. In this way, the two-phase flow can be modeled with little modifications to the conservation equations. Furthermore, this approach simplifies the

transition between the single-phase flow and two-phase flow since the same set of conservation equations is used. This approach is often referred as the inhomogeneous mixture model (InHEM) without interfacial exchange (MacArthur and Grald, 1987 & 1989; Wang and Touber, 1991; Judge and Radermacher, 1997; Ploug-Sørensen *et al*., 1997; Jia *et al*., 1996 and 1999; Jakobsen *et al*. 1999; Rossi and Braun, 1999; Mithraratne *et al*., 2000; Koury *et al*., 2001; Jensen, 2003; Haberschill *et al*., 2003; García-Valladares, 2004; Bendapudi *et al*. 2005; Beghi and Cecchinato, 2009; Morales-Ruiz *et al*., 2009; Kapadia *et al*., 2009; Ndiaye and Bernier, 2010; Xuan *et al*., 2010; Kærn *et al*., 2011b; Colorado *et al*., 2011; Choi *et al*., 2011b).

A more detailed approach to deal with the slip effects between the two phases is called two-fluid model (TFM) which takes into account the fact that the liquid and vapor phases are not in thermodynamic equilibrium and have different velocities (Liao and Wang, 1990). In its most sophisticated version, each phase is analyzed by separate equations of continuity, energy and momentum incorporating with the interfacial exchange terms. However, these six equations can be simplified and reduced with simplifying assumptions. For instance, if thermal equilibrium exists in two phases at saturation temperature, there is no need to use separate energy equations; if a drift flux model (Wallis, 1969) is used to specify the relation between liquid and vapor velocities, only a mixture momentum equation is needed. Therefore, the InHEM model is the simplest version of the TFM (Levy, 1999).

The first two approaches are often more favored in the transient modeling of vapor compression systems, while the last one is rarely used because it is computationally complicated although it best represents the prevailing physics.

Unlike the moving boundary models where a uniform pressure is assumed throughout the heat exchanger, the momentum equation can be included into the computation in the discretized heat exchanger modeling paradigm such that refrigerant pressure loss can be evaluated. However, different distributed parameter models adopt differing approaches regarding how to incorporate the momentum equation into the simulation, which renders one of the major distinctions between different models.

In some publications, the original transient form of the momentum equation is employed in the model so that the mass flow rates are also the state variables and need to be integrated along with other state variables, e.g., pressures and enthalpies (Nyers and Stoyan, 1994; Jia *et al*., 1995; Jia *et al*., 1996 and 1999; Judge and Radermacher, 1997; Aprea and Renno, 1999 and 2002; Koury *et al*., 2001; García-Valladares *et al*., 2004; Beghi and Cecchinato, 2009; Kapadia *et al*., 2009; Zhang *et al*., 2009a; Ndiaye and Bernier, 2010; Colorado *et al*., 2011; Schalbart and Haberschill, 2013). In contrast, similar to the moving boundary approach, many publications neglect the spatial variation in the pressure and try to avoid the resulting complexity brought by the equation of momentum balance (Note: the outlet mass flow rate must be given as the boundary condition instead of the outlet pressure in this approach) (Wang and Touber, 1991; Rossi and Braun, 1999; Jiang and Radermacher, 2003; Haberschill *et al*., 2003; Bendapudi *et al*., 2005; Choi *et al*., 2011b). In this case, the refrigerant mass flow rates are the algebraic variables and need to be computed through the coupling between the equations of continuity and energy. Clearly, the approaches described above are the two extreme cases of

handling the equation of momentum. The former approach results in the most complicated model representation by introducing more state variables but attains the most accurate prediction, whereas the latter reduces the number of partial differential equations from $3N$ to $2N$ (N is the number of control volumes) and yields a prediction with larger deviations. In addition to these two extreme approaches, some publications try to seek other practical alternatives for model reduction to handle the equation of momentum in order to achieve a balance between the computational efficiency and the preservation of the major fluid flow characteristics. One of the alternatives is to neglect the inertia term in the equation of momentum due to its very small time-scale dynamics, thus the static form of the momentum balance is utilized to calculate the mass flow rates purely based on the pressure difference (Zhang and Zhang, 2011a and 2011b). Zhang *et al*. (2009b) directly compared these three different ways of handling the equation of momentum in the transient simulation of vapor compression systems. It was concluded that the static-state form yields the same prediction as the transient form while exhibiting a faster computation speed. Meanwhile, it was suggested that neglecting pressure drop is a reasonable approximation for model based control design since it results in a simpler model representation without significant loss of accuracy. An even simpler alternative is to further omit the acceleration term, which is of minor importance and generally does not impose an appreciable effect on the prediction (Brasz and Koenig, 1983). Another possible alternative is to assume that the time derivatives of pressures are spatially invariant given the fact that the acoustic waves propagate with a speed of sound in the direction of fluid flow (Lemke, 2005; Richter, 2008; Li *et al*., 2012b). In this way, the

21

number of pressure states is reduced to a single numerical state per pressure level. As a consequence, the computational cost decreases substantially. However, the pressure distribution in the heat exchanger model still depends on the selected pressure drop model and thus on the mass flow rate (Richter, 2008). All of these three alternatives for model reduction still need to apply the local momentum balance for each cell, while Jensen (2003) proposed a novel approach that only applies an average global momentum balance for the entire pipe instead of for each cell by assuming a linear pressure distribution from the inlet to outlet of the heat exchanger. This new approach results in much fewer state variables and thus a faster simulation speed being guaranteed.

1.3 Literature Review

Transient modeling of vapor compression systems dates back to 1970s. During the period, numerous interesting and note-worthy papers have been published. In general, research into the transient modeling of vapor compression systems can be classified into two categories: 1) small changes occurring on the refrigerant side, such as the instability phenomena of two-phase flows or the "hunting" behavior of the thermostatic expansion valve, and 2) large transients on the refrigerant side during start-up, shut-down or defrosting operation.

Dhar (1978) was one of the pioneers to present the transient simulation of an entire vapor compression refrigeration system. Lumped parameter heat exchanger models were implemented, in which vapor and liquid phases were separated and coupled by the mass and energy exchange at the interface through evaporation or condensation. The heat transfer phenomena occurring inside the compressor shell and

the associated effects thanks to the presence of lubricating oil were modeled. As described previously, lumped parameter models have the primary advantage of simplicity and high computational efficiency, they were utilized by many subsequent studies to conduct real-time simulations for various applications, e.g., liquid chillers (Browne and Bansal, 2002), refrigeration systems (Ding *et al*., 2004a; Lu *et al*., 2004) and heat pumps (Chi and Didion, 1982; Vargas and Parise, 1995; Fu *et al*., 2003).

Brasz and Koenig (1983) were among the first to suggest the distributed parameter model to study the heat transfer phenomena in heat exchangers. It was found that the model could be reduced substantially by neglecting inertial and acceleration terms in the momentum equation since they were of minor importance for a heat transfer analysis.

Murphy and Goldschmidt (1984, 1985 and 1986) scrutinized the cyclic characteristics of an air-conditioner and attributed the cycling losses to refrigerant migration during shut-down.

Aiming at investigating the effects of integrated control on the operation of heat pump systems, MacArthur (1984a; 1984b) derived a sophisticated model based on first-principles. The heat exchangers were modeled in distributed parameter fashion, while other components were simulated with the lumped parameter approach without accounting for refrigerant pressure drop. Later on, MacArthur and his collaborator (MacArthur and Grald, 1987 & 1989) enhanced the model by incorporating the void fraction model to more accurately predict refrigerant mass distribution. Following the modeling techniques in MacArther and Grald (1989), Haberschill *et al*. (2003) presented a simulation study on the dynamic response of refrigeration systems with

the zeotropic mixture R-407C subjected to variation in EEV (electronic expansion valve) opening and compressor speed.

Sami *et al*. (1987) developed a computer program called DAHP (Dynamic Analysis of Heat Pump) to simulate the dynamic response of heat pumps by employing the modeling techniques similar to the work by Dhar (1979). Later, Sami and Duong (1991) presented an enhanced version of the program, within which fully distributed parameter heat exchanger models were formulated by the finite difference method. A series of studies were commenced based on the new program to investigate the dynamic performance of heat pumps using different working fluids (Sami and Comeau, 1992; Sami and Zhou, 1995; Sami and Dahmani, 1996).

Janssen *et al*. (1988) investigated the transient behavior of a small refrigeration system during start-up and shut-down using a hybrid heat exchanger model in which the moving boundary approach was used to model the two-phase region while the single-phase region was modeled in distributed-parameter fashion. In a subsequent contribution, the same modeling approach was adopted to analyze the cycling losses in domestic refrigerators (Janssen *et al*., 1992).

Liao and Wang (1990) carried out a theoretical investigation on the transient response of two-phase condensing flow in a tube-in-tube heat exchanger. The spatially discretized TFM model was utilized to describe the behavior of the condensing flow. Similar studies were later carried out by other authors using the InHEM two-phase model (García-Valladares, 2004, García-Valladares *et al*., 2004; Colorado *et al*. 2011).

Chen and Lin (1991) conducted a study to optimize the capillary tube within a small-scaled refrigeration system based on the dynamic simulation. The HEM modeling approach was applied to the heat exchangers without accounting for pressure drop. The choke flow condition within the capillary tube was handled with caution.

Ploug-Sørensen *et al.* (1997) built a detailed household refrigerator model within the framework of *Sinda/Fluint*. In this simulation, system dynamics during on-off periods were fully inspected and compared against experimental data. A similar investigation was conducted by Hermes and Melo (2008) by adopting different models for the non-adiabatic capillary tube (Hermes *et al.*, 2008) and the compressor.

Jakobsen *et al.* (1999) experimentally and numerically showed that the homogeneous two-phase flow assumption produced too fast response whereas the slip-flow model agreed well with experimental data. The findings were also corroborated by Kærn *et al.* (2011b).

Koury *et al.* (2001) presented a discretized two-phase mixture model for the heat exchangers to simulate the transient behavior of a refrigeration system during the start-up period and subjected to the step changes in compressor speed and valve opening. Koury *et al.* (2013) extended the analysis to study the dynamic characteristics of an air-to-water heat pump in a more recent publication.

Bendapudi *et al.* (2005) developed a first-principles dynamic model for a centrifugal chiller. The shell-and-tube heat exchangers were modeled based on the finite volume formulation with neglecting refrigerant pressure drop, initially developed by Rossi and Braun (1999). Furthermore, the author conducted a

comprehensive comparison between the moving boundary and finite volume formulations (Bendapudi, 2004; Bendapudi *et al*., 2008).

Wang *et al*. (2007) presented a discretized TFM that separately analyzed the vapor and liquid phases in the two-phase region of the heat exchangers with neglecting refrigerant pressure drop. No evidence was shown that the proposed model was superior to the InHEM mixture model given the unconvincing validation against experimental measurements, let alone much more massive computation required.

Llopis *et al*. (2008) presented a lumped three-zone model for a shell-and-tube condenser, in which the refrigerant flowed through the shell assuming the two-phase region being completely occupied by the saturated vapor.

Kapadia *et al*. (2009) numerically compared the start-up characteristics and cycling losses of split air-conditioners that use R22 and R410A as refrigerants. The heat exchangers were simplified as a straight tube with the cross flow configuration. The discretized InHEM model was applied to perform the analysis.

Zhang *et al*. (2009a) conducted a systematic investigation on the effect of the momentum balance on the open loop stability of heat exchangers. Various scenarios were analyzed and it was concluded that the system was stable only if the flow velocity was sufficiently large.

Choi *et al*. (2011b) performed a numerical simulation to analyze the dynamic characteristics of a multi-indoor unit heat pump system. A two-step solution method was proposed to solve distributed heat exchanger models by uncoupling the convection term and the source term in the governing equations.

Uhlmann and Bertsch (2012) applied moving boundary heat exchanger models

to investigate the start-up and shut-down behavior of a residential heat pump. The authors pointed out that a tremendous amount of effort had been spent on developing robust switching schemes for handling transitions between different model representations.

Ndiaye and Bernier (2012a & 2012b) introduced a first-principle model to study the cycling behavior of a water-to-air heat pump. A fully distributed approach was used, and each component was modeled individually and then linked into a system model. The equation of momentum was eliminated during the simulation for the off-period.

Schalbart and Haberschill (2013) inspected the transients of a centrifugal chiller during quick start-up using the discretized heat exchanger model with the density and the internal energy being selected as the state variables.

Many publications had focused on the dynamic behavior of tube-fin heat exchangers and the fully discretized modeling approach was widely exploited since it accounted for complex coil circuitry (Wang and Touber, 1991; Nyers and Stoyan, 1994; Jia *et al*., 1995; Judge and Radermacher, 1997; Jia *et al*., 1996 and 1999; Aprea and Renno, 1999 and 2002; Rossi and Braun, 1999; Jiang and Radermacher, 2003; Zhou and Braun, 2007a and 2007b; Beghi and Cecchinato, 2009; Ndiaye and Bernier, 2010). There was no significant difference in how to treat the air side and pipe walls among these studies, whereas the major distinctions lied in 1) whether the HEM or InHEM approach was employed to describe the behavior of two-phase flows and 2) how to handle the equation of momentum, as summarized previously.

The stability of thermostatic-expansion-valve-controlled refrigeration systems was thoroughly investigated and two different modeling approaches were often adopted, i.e., lumped evaporator models with the evaporative region described by the mean void fraction along with the common assumption of incompressible superheated vapor (Broersen and van der Jagt, 1980; Yasuda *et al*., 1983; Ibrahim, 2001; Tian and Li, 2005; Tian *et al*., 2005; Lei and Zaheeruddin, 2005), and fully discretized evaporator models (Gruhle and Isermann, 1985; Mithraratne *et al*., 2000; Mithraratne and Wijeysundera, 2001 and 2002).

By extending the concept of phase transition, originated by Wedekind and Stoecker (1968), Grald and MacArthur (1992) came up with a moving-boundary model to describe the two-phase flow transients in the evaporator. The time-invariant mean void fraction was employed to evaluate the mass and energy balance in the two-phase region (Wedekind *et al*., 1978; Beck and Wedekind, 1981). By neglecting the time-varying effects of refrigerant properties, the expression of the phase boundary was simplified. However, the response of tube wall was still modeled based on the spatial dependent approach, which was too complex to be applied for controls design.

He *et al*. (1994) improved Grald and MacArthur's model by dividing the tube walls into a multi-node lumped-parameter form with boundaries synchronizing with the moving boundaries and including the time-varying effect of refrigeration properties. By casting the resulting equations into a linearized state-space form, the model could be used to predict the transients under minor variations around a steady-state operating point and to investigate the multivariable feedback control of HVAC

systems (He, 1996; He *et al*., 1997 and 1998; Gordon *et al.*, 1999; Shah *et al*. 2004; Diaz, 2007; Kumar *et al*., 2008).

Gordon *et al.* (1999), Shah *et al*. (2004) and Shao *et al*. (2012) presented the dynamic modeling of a multiple-zone vapor compression system consisting of multiple parallel evaporators with each having an upstream expansion device. The moving boundary approach was used to model the conservation of mass and energy for each heat exchanger in the system. In order to avoid a high index DAE (differential algebraic equations) problem, Gordon *et al.* (1999) and Shah *et al*. (2004) utilized a steady state momentum equation to determine the mass flow distribution among parallel evaporators based on the pressure drop from the center of the two phase region to the entrance of the downstream component.

Quite a few papers presented very similar moving boundary frameworks (Willatzen *et al*., 1998; Jensen and Tummescheit, 2002; Leducq *et al*., 2003; Rasmussen and Alleyne; 2004; Schurt *et al*., 2009; Liang *et al*., 2010b). In these publications, the time-varying effect of the mean void faction was excluded and the enthalpy leaving the heat exchanger was included in the state vector.

Pettit *et al*. (1998) introduced pseudo-state variables and auxiliary equations based on the modeling framework of Willatzen *et al*. (1998) to ensure smooth state variables under large disturbances resulting in creation or destruction of fluid phases. The switching approach was based on the initialization of newly created dynamic states.

By examining Willatzen *et al*. (1998) model, Zhang and Zhang (2006) pointed out that the assumption of the time-invariant mean void fraction in the formulation

yielded possible numerical discontinuities during model transitions. It was shown that the inclusion of the time-dependent void fraction in the two-phase region could improve model robustness and ensured smooth prediction under large disturbances compared to the model presented by Pettit *et al.* (1998).

McKinley and Alleyne (2008) proposed a two-node moving boundary condenser model with a novel switching approach. The mean two-phase void fraction was included in the state vector to serve the switching purpose without introducing appreciable mass and energy imbalances during the transition. Eldredge *et al.* (2008) introduced an alternative model in which the calculation of void fraction was extended to the single phase to handle small deviations from the saturated states for refrigerant outlet conditions. This approach was believed to only work for the heat exchangers with accumulator or receiver.

Li and Alleyne (2010) extended the work by McKinley and Alleyne (2008) to address other possible transitions that condenser and evaporator might experience during the start-up and shut-down operations. By utilizing the extended modeling framework, Li and collaborators performed a series of studies on the dynamic modeling and control of vapor compression systems.

Li *et al.* (2010a) studied a hysteretic on-off control scheme with optimization algorithms for temperature regulation in a refrigerated transport system.

Li *et al.* (2011a & 2011b) simulated the dynamic characteristics of refrigerant migration during compressor start-up and shut-down operations of an automotive air conditioning system.

Li *et al*. (2012a) presented a dynamic simulation for refrigerated transport systems which need to operate under an alternative sequence of heating and cooling modes in order to achieve a tight temperature control. The previous evaporator model (Li and Alleyne, 2010) was extended to accommodate a new two-zone model representation (superheated and two-phase) in the heating mode.

In order to create an intrinsically mass conservative moving boundary evaporator model, Cecchinato and Mancini (2012) suggested that the average density of the two-phase region and that of the superheated region can be selected as the state variables instead of the outlet enthalpy and the two-phase zone length. In this case, the two-phase zone length could not be determined straightforwardly and algebraic manipulation was required, which was not favorable from a mathematical point of view. Furthermore, the approach was believed to impose difficulties in developing the condenser model where the superheated zone length was required to be determined as well.

Modelica is a publicly available, object-oriented, equation-based language for modeling large, complex physical systems. Models in Modelica are described by differential, algebraic and discrete equations (Modelica Association, 2014). Unlike the traditional modeling procedures, one of the primary advantages of using Modelica or other commercial tools like Simulink® (Mathworks, 2014b) and Simscape™ (Mathworks, 2014a) is that modelers can focus more on the underlying physics instead of devoting much effort on how to solve the resulting mathemacal equaitons of the model, which are handled by the PDE or ODE (Ordinary Differential Equation) solvers embeded in these tools.

Several Modelica-based simulation packages have been introduced recently, e.g., the Thermo-Fluid Library (Eborn, 2001; Tummescheit, 2002), the AirConditioning Library (Modelon, 2014), the Modelica_Fluid Library (Casella *et al*., 2006), the HITLib (Videla and Lie, 2006), the TIL (Richter, 2008), the FluidFlow (Ljubijankic *et al*., 2009). Meanwhile, a great many studies were conducted on the transient modeling of thermo-fluid systems in Modelica environment (Bauer, 1999; Jensen and Tummescheit, 2002; Casella and Schiavo, 2003; Elmqvist *et al*., 2003; Pfafferott and Schmitz, 2004; Tummescheit *et al*., 2005; Wei *et al*. 2008; Li *et al*., 2010b; Li *et al*., 2012c; Bonilla *et al*., 2011 and 2012; Chamoun *et al*. 2012; Mortada *et al*., 2012). Here, the author would like to highlight some representative studies.

Bauer (1999) described a robust model accounting for the non-homogeneous effect of two-phase flows with dynamic or static slip correlation in his Master thesis. The model was developed in the context of establishing a Modelica base library for thermo-hydraulic applications. The model depicted the transient behavior of a fluid flowing through a pipe during phase change caused by heat transfer or pressure changes. Physical approaches were taken to model friction and momentum exchange between the phases in the case of the dynamic slip flow.

Tummescheit (2002) designed a Modelica library for thermo-fluid systems, which served as the basic framework of the AirConditioning Library (Modelon, 2014), a commercial library mainly utilized for the modeling, simulation and analysis of the dynamics of automobile air-conditioning systems. In this library, a generalized thermo-fluid system could be represented as an alternating sequence of control volume models and flow models, which was favorable from a computational point of

view because this logic topology could be readily solved by the staggered grid discretization, a scheme for spatial discretization commonly used in computational fluid dynamics (Patanka, 1980).

Richter (2008) developed a new Modelica library called TIL, a library for the simulation of refrigeration, air-conditioning and heat pump systems. The major difference between this new library and other Modelica libraries was the number of pressure states. In this library, the time derivative of pressure was spatially invariant along the heat exchanger. Given the fact that the acoustic waves propagate with a speed of sound in the direction of fluid flow, this was a fairly reasonable approximation reducing the number of pressure states to a single numerical state per pressure level. As a consequence, the computational cost could be reduced substantially.

In order to gain a deeper understanding of flow maldistribution in fin-an-tube evaporators, Kærn (2011) conducted a numerical study on a residential air-conditioning system. A fully distributed one-dimensional InHEM mixture model was employed for the evaporator in order to account for different tube circuitries and predict the refrigerant flow maldistribution dictated by the pressure drop. In contrast, the moving boundary approach was utilized for the condenser based on the work by Zhang and Zhang (2006). Verification against CoilDesigner (Jiang *et al*., 2006) showed a favorable consistency (Kærn *et al*., 2011a).

More recently, Modelica language has been very successfully applied to conduct the system-level simulations of vapor compression systems. Pfafferott and Schmitz (2004) studied the start-up transients of a CO_2 refrigeration system. Both

refrigerant and air side were discretized along the corresponding flow direction to attain a more accurate prediction for heat transfer (Pfafferott and Schmitz, 2002).

Zhang *et al*. (2009c, 2009d) adopted moving boundary modeling paradigm to investigate the coupling characteristics between the main and sub EEV of an air-cooled chiller employing an economized screw compressor. Zhang and Zhang (2011b) presented a validated dynamic model of a multi indoor unit air conditioning system with a rapid cycling scroll compressor. Discretized heat exchanger models with quasi-steady state momentum conservation were used in the analysis. The same approach was adopted to study the on-line control for the high-side pressure of carbon dioxide transcritical refrigeration systems (Zhang and Zhang; 2011a).

Li *et al*. (2012c) proposed a preprocessing scheme to handle the initialization problem encountered in the transient simulation of centrifugal chillers, by establishing a smooth transition for the compressor mass flow rate from its pseudo-physical analogy to the analytical solution.

Mortada *et al*. (2012) presented a tube-by-tube approach to model the tube-fin heat exchangers using Modelica in the study of the dynamic behavior of an air-to-air heat pump system.

Chamoun *et al*. (2012) exploited the finite volume method to model the plate heat exchangers using Modelica in the study of the dynamic behavior of an industry heat pump using water as refrigerant.

1.4 Summary of Background

A thorough review of the literature in Section 1.3 indicates that transient modeling of vapor compression systems has primarily focused on the conventional

single-stage vapor compression systems while little attention has been focused on more advanced system configurations, e.g., flash tank vapor injection (FTVI) heat pump systems and multi-split variable refrigerant flow (VRF) systems. As a matter of fact, advanced systems have proven to be more energy efficient in comparison to the conventional systems and are nowadays widely used in the HVAC&R industry. Meanwhile, the simulation of such advanced cycles brings a great many challenges that often intimidate researchers, such as more complicated system topologies, extravagant modeling details and computational complexities.

Another observation from the literature review is that most of the transient simulations of vapor compression systems confine themselves to study system transients under cycling operation, and very few publications have investigated the transient behavior of heat pump systems under frosting and defrosting conditions except experimental investigations. Most frost/defrost related modeling studies only concentrate on the phenomena occurring on the heat exchanger level. However, under frosting conditions, the entire system will experience significant variation on both air side and refrigerant side, and suffer considerable performance degradation. Meanwhile, during the defrosting process, the system performance is further penalized by consuming additional energy and the refrigerant side undergoes drastic changes as a consequence of operating mode switch. Although the concept of the reverse-cycle defrosting is very simple, the resulting dynamics of the systems are quite involved. In this case, it is impossible to single out the outdoor coil alone to study the defrosting phenomena. Thus, the overall system needs to be examined to have a more comprehensive investigation. However, modeling the system transients

under frosting and defrosting conditions is challenging due to the underlying complexities in the understanding of the phenomenon as well as the mathematical and computational details.

Heat exchangers are a major component in vapor compression systems and the moving boundary method is a popular approach for control-oriented modeling of heat exchangers. The literature review shows that nearly all moving boundary heat exchanger models rely on the common hypothesis that refrigerant pressure drop is negligible. However, it is important to include the momentum balance in some occasions, such as electronics cooling where micro channels are commonly used and significant pressure drop is observed in micro-scale heat exchangers (Kandlikar *et al*., 2006), and large-scale heat exchangers in solar thermal plants (the tube length can be as long as several hundred meters) where pressure drop must be considered. Another major challenge of moving boundary modeling framework is to provide robust and consistent switching schemes to accommodate the changing number of fluid phases under large disturbances, given the fact that the current switching methods in the literature clearly have flaws and may cause serious numerical problems when modeling cycling transients of vapor compression systems.

In summary, these observations identify the gap that this thesis intends to fill in the extant research. A systematic study will be conducted to tackle underlying challenges encountered during resolving the identified problems and details will be presented.

1.5 Research Objectives

The proposed work concerns itself with transient modeling of vapor compression systems focusing on two aspects in particular. The first part focuses on developing a comprehensive Modelica-based modeling framework for transient simulation of vapor compression systems in general, which includes first-principles based heat exchanger models and a variety of supporting component models. The second part concentrates on using the developed framework to explore the transient behavior of advanced vapor compression systems, specifically, flash tank vapor injection heat pump system and multi-split variable refrigerant flow system. The latter involves the experimental validation and control strategy study.

As identified in the literature review, the current research gaps hinder the practitioners in the HVAC&R industry to gain a deeper understanding of the transient operating characteristics of vapor compression systems. This thesis will try to make further progress in transient modeling of vapor compression systems by fulfilling the following objectives.

1. Develop a comprehensive transient modeling framework with a wide range of component models supporting arbitrary vapor compression system configurations

2. Develop fully-fledged first-principles heat exchanger models with the following capabilities

   - Account for non-homogeneous effects in two-phase flows

   - Account for 1) complex tube circuitry; 2) air flow maldistribution; 3) dry and dehumidifying conditions; 4) the change in air flow rate due to on/off operation of the fan

- A detailed frosting model to account for the non-uniform frost growth on the heat exchangers and the resulting air flow redistribution

- A hot gas defrosting model

- An advanced switched moving boundary modeling paradigm

3. Advanced system modeling

- To explore the dynamic behavior of a flash tank vapor injection heat pump system undergoing cycling, frosting and reverse-cycle defrosting operations

- A pull-down simulation for a multi-split VRF system

4. Control study

- A feasible control strategy to achieve individual zone control for multi-split VRF system

5. Comprehensive experimental validation

- To verify the fidelity of the models in the modeling framework

1.6 Thesis Organization

The remainder of the thesis is organized as follows. Chapter 2 describes a discretized heat exchanger model based on the finite volume approach. Chapter 3 presents the modeling and experimental validation of the transient behavior of a flash tank vapor injection heat pump under cycling conditions. Chapter 4 details the modeling of non-uniform frost growth on tube fin heat exchangers. The dynamics of the same FTVI heat pump system under frosting conditions are also presented. A hot gas defrost model and the transient characteristics of the same FTVI system undergoing the reverse-cycle defrosting are given in Chapter 5. An advanced switched moving boundary heat exchanger is presented in Chapter 6. Chapter 7

presents the transient modeling of a multi-split VRF air-conditioning system. Summary and conclusions of this thesis are given in Chapter 8. Contributions and suggestions for future work are given in Chapter 9.

2 Discretized Heat Exchanger Model

2.1 Motivation

Tube-fin heat exchangers are extensively used for air cooling and heating. They are often integrated into vapor compression systems with refrigerant flowing inside tubes and used as the condenser or evaporator in which refrigerant undergoes phase change under nearly constant temperature. The air flow driven by a fan passes across the tube bundles, either heating up or cooling down the refrigerant inside the tubes by forced convection. In general, the heat transfer coefficient on the air side is much lower than that on the refrigerant side, leading to a high resistance for heat transfer. A common way to minimize the adverse effect of this low heat transfer coefficient is to use the extended fin surfaces to increase the heat transfer area.

These heat exchangers often have complex and asymmetric tube circuiting configurations for a few reasons: 1) optimize refrigerant flow distribution; 2) minimize refrigerant pressure drop; 3) minimize the detrimental effects of fin conduction between adjacent tubes; 4) minimize the adverse impact of non-uniform air flow distribution on the heat exchanger performance. In general, the heat exchangers often work under a variety of operating conditions, including dry, dehumidifying, frosting and defrosting. Meanwhile, the operation of heat exchangers is subjected to the variation in air flow and refrigerant flow associated with compressor and fan On/Off.

All these intertwined complications necessitate a dynamic model that is able to adequately capture the resulting heat transfer and fluid flow phenomena. Obviously, a fully discretized model is preferable in this case. In comparison to the lumped

parameter models and moving boundary models, discretized models possess a great many advantages. One of advantages is that flow maldistribution and asymmetric tube circuitries can be straightforwardly handled, which is impossible if using the other two approaches. Discretization on the air side is extremely important to correctly model the phenomena of dehumidification and frost growth, which are highly dependent upon on the spatial variation in the surface temperatures of tube and fins. Another advantage of using discretized models is the possibility of applying local void fraction correlations taking the spatial variation into account to more accurately determine the refrigerant mass distribution, whereas the mean void fraction must be supplied in lumped models or moving boundary models.

Based on the above reasoning, the discretized approach is utilized to model tube-fin heat exchangers, as shown in Figure 2.1. The model should be able to account for various operating conditions, including frosting and defrosting. In order to present a more concise and coherent description, frosting and defrosting modeling is given in Chapter 4 and 5, while this chapter will mainly focus on presenting the details of modeling the transient heat transfer and fluid flow behavior on the refrigerant side, and air side performance under dry and wet conditions.
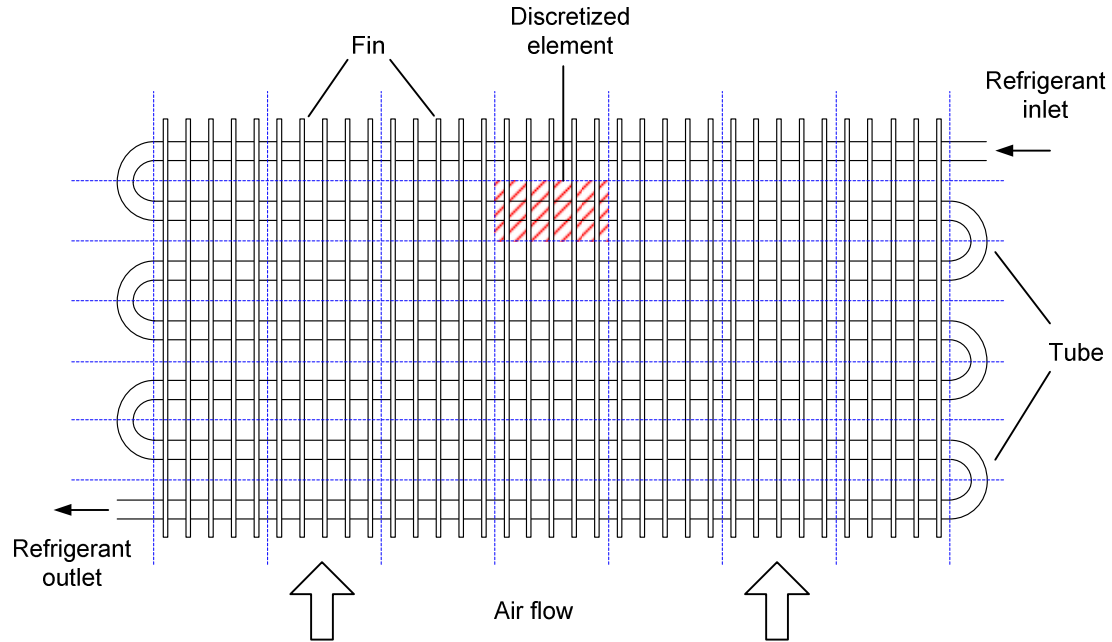
Figure 2.1 Discretized heat exchanger model

2.2 Refrigerant Flow Modeling

2.2.1 Formulations

The refrigerant flow is simplified as one-dimensional flow with fluid properties varying only in the direction of flow. In other words, fluid properties are uniform or averaged at every cross section along the axis of the channel. In addition, the following assumptions are made in the derivation of the governing set of equations for one-dimension in-tube flow.

o Newtonian fluid;

o changes in kinetic energy and potential energy are negligible;

o negligible viscous dissipation. In a viscous fluid flow, the viscosity of the fluid will take energy from the motion of the fluid (kinetic energy) and transform it into internal energy of the fluid and thus heating up the fluid. This irreversible process is referred to as viscous dissipation. In general, viscous dissipation is orders of

magnitude smaller than the dominant energy exchange between the refrigerant flow and the tube walls;

o   axial conduction is not taken into account. Péclet number, defined as the ratio of the rate of advection of a flow to its rate of thermal diffusion, is the measure of the quantity of the axial heat conduction effects in the fluid flow. Under normal operating conditions, this number is very high and the axial conduction is insignificant compared to the advection effects;

o   the refrigerant liquid and vapor phases are in thermodynamic equilibrium.

Thus, the governing equations of mass, energy and momentum can be written as follows (Levy, 1999)

$$\frac{\partial}{\partial t}(\bar{\rho}A) + \frac{\partial}{\partial z}(GA) = 0 \tag{2-1}$$

$$\frac{\partial}{\partial t}(\bar{\rho}\bar{h}_{\rho}A) + \frac{\partial}{\partial z}(G\bar{h}A) = Pq_w'' + \frac{\partial}{\partial t}(pA) \tag{2-2}$$

$$\frac{\partial}{\partial t}(GA) + \frac{\partial}{\partial z}\left(\frac{G^2 A}{\bar{\rho}_M}\right) = -A\frac{\partial p}{\partial z} - \bar{\tau}_w P - \bar{\rho}gA\sin\theta \tag{2-3}$$

where

$$\bar{\rho} = \frac{1}{A}\int_A \rho \, dA = \text{average density at position } z$$

$$G = \frac{1}{A}\int_A \rho u \, dA = \text{average mass flow per unit area at } z$$

$$\bar{h}_{\rho} = \frac{1}{\bar{\rho}}\left(\frac{1}{A}\int_A \rho h \, dA\right) = \text{average density-weighted enthalpy at } z$$

$$\bar{h} = \frac{1}{G}\left(\frac{1}{A}\int_A \rho u h \, dA\right) = \text{average flow-weighted enthalpy at } z$$

$$\frac{1}{\overline{\rho}_M} = \frac{1}{G^2}\left(\frac{1}{A}\int_A \rho u^2 \, dA\right) = \text{average momentum density at } z$$

$$\overline{\tau}_w = \frac{1}{P}\int_P \tau_w \, dl = \text{average wall shear stress at } z$$

$q'' = \text{average surface heat flux}$

For the single-phase flow, the refrigerant density can be assumed uniform at the cross section area, and one can easily derive the following relations

$$\overline{\rho} = \overline{\rho}_M = \rho \tag{2-4}$$

$$\overline{h}_\rho = \overline{h} = h \tag{2-5}$$

For the two-phase flow, average densities and enthalpies are defined as

$$\overline{\rho} = \rho_g\gamma + \rho_f(1-\gamma) \tag{2-6}$$

$$\frac{1}{\overline{\rho}_M} = \frac{1}{\rho_g}\frac{x^2}{\gamma} + \frac{1}{\rho_f}\frac{(1-x^2)}{1-\gamma} \tag{2-7}$$

$$\overline{h}_\rho = \frac{1}{\overline{\rho}}\left[\rho_g h_g \gamma + \rho_f h_f(1-\gamma)\right] \tag{2-8}$$

$$\overline{h} = \frac{1}{G}\left[\rho_g u_g h_g \gamma + \rho_f u_f h_f(1-\gamma)\right] = h_g x + h_f(1-x) \tag{2-9}$$

where the void fraction and flow quality are defined as

$$\gamma = \frac{A_g}{A_g + A_f} = \frac{A_g}{A} \tag{2-10}$$

$$x = \frac{\text{mass flow of gas}}{\text{total mass flow}} = \frac{\rho_g u_g \gamma}{\rho_g u_g \gamma + \rho_f u_f(1-\gamma)} = \frac{\rho_g u_g \gamma}{G} \tag{2-11}$$

It is understandable to confuse the flow quality x with the static quality $\hat{x}$, which is defined as the ratio of mass of vapor to that of mixture.

$$\hat{x} = \frac{M_g}{M_g + M_f} = \frac{\rho_g \gamma}{\rho_g \gamma + \rho_f (1 - \gamma)} \tag{2-12}$$

The density-weighted enthalpy can be related to the static quality

$$\overline{h}_\rho = \hat{x} h_g + (1 - \hat{x}) h_f \tag{2-13}$$

The void fraction can be directly related to the static quality

$$\gamma = \frac{\hat{x}}{\hat{x} + (1 - \hat{x}) \dfrac{\rho_g}{\rho_f}} \tag{2-14}$$

According to Rice (1987), void fraction correlations can be classified into four categories: homogeneous, slip-ratio-correlated, X_{tt}-correlated (Lorckhart-Martinelli correlating parameter X_{tt}) and mass-flux-dependent. From a simulation point of view, the first two categories provide the most suitable correlations to calculate the void fraction since they are more straightforward and do not add significant numerical complication compared to the last two categories.

Therefore, the void fraction can be represented by the slip-ratio S, the ratio of the gas velocity to the liquid velocity $\dfrac{u_g}{u_f}$

$$\gamma = \frac{x}{x + (1 - x) \left(\dfrac{\rho_g}{\rho_f} \right) S} \tag{2-15}$$

In general, $S \geq 1$, and the equal sign holds for the assumption of homogeneous flow, i.e., the velocity difference between two phases is zero.

It is not difficult obtain the following expression relating the flow quality to the slip ratio

$$x = \frac{\rho_g u_g \gamma}{\rho_g u_g \gamma + \rho_f u_f (1-\gamma)} = \frac{\rho_g \gamma}{\rho_g \gamma + \rho_f (1-\gamma)\frac{1}{S}} \tag{2-16}$$

As can be seen, the flow quality and static quality are equal to each other when the slip ratio is unity.

Pressure p and the density-weighted enthalpy $\bar{h}_\rho$ are selected as the state variables in this case, because they are the thermodynamic properties and can be readily computed by the refrigerant property routines. Certainly, there is a freedom of choosing other state variables due to the redundant thermodynamic properties that can be used to determine a specific state. Alternatively, one can choose the combination of density $\bar{\rho}$ and enthalpy $\bar{h}_\rho$, or internal energy $\bar{U}$ and mass M. Different selection of state variables results in different model representations. However, the pitfall that should be circumvented is that the selection of state variables might have a decisive effect on the simulation speed. For instance, the pressure is very sensitive to change in density, which is on the order of the square of the speed of sound. It might cause a stiff problem that requires very small time steps to maintain convergence if the density is selected as the independent state variable. On the other hand, it is wise to select the enthalpy as the independent state variable because the enthalpy can be readily used to distinguish whether the refrigerant is in single-phase or two-phase region and hence appropriate correlations for heat transfer and pressure drop can be applied accordingly.

By applying the chain rule, the derivative of the density with respect to time can be calculated

$$\frac{\partial \bar{\rho}}{\partial t} = \frac{\partial \bar{\rho}}{\partial p}\bigg|_{\bar{h}_\rho} \frac{dp}{dt} + \frac{\partial \bar{\rho}}{\partial \bar{h}_\rho}\bigg|_p \frac{d\bar{h}_\rho}{dt} \qquad (2\text{-}17)$$

Please be noted that p, $\bar{h}_\rho$ and $\bar{\rho}$ themselves are all thermodynamic properties since

they are all mass based. Thus, $\bar{\rho}$ can be readily computed from the Equation of State

$$\bar{\rho} = \rho\left(p, \bar{h}_\rho\right) \qquad (2\text{-}18)$$

Meanwhile, the partial derivatives of the density can be analytically calculated based

on the thermodynamic relations. Please refer to Appendix I for more details.

2.2.2 Discretization

The partial differential equations (2-1) to (2-3) can be solved by various

methods, like finite difference, finite volume and finite element. Finite volume

method is chosen here because it has proven highly successful in approximating the

solution of a wide range of conservation-law systems and owns the merit of

maintaining quantity conservation.

In order to apply the finite volume method to solve the governing equations, the

domain of the refrigerant flow needs to be spatially discretized into N control

volumes.
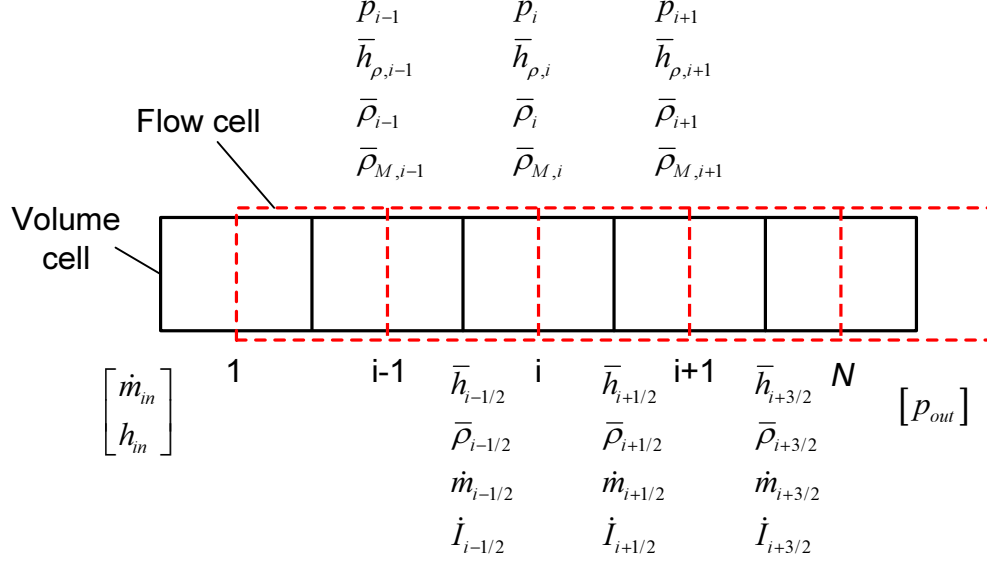
Figure 2.2 Discretization on the refrigerant side

Integrating the equation of mass and energy over the ith control volume yields by recognizing $\dot{m} = GA$

$$A\Delta z \frac{d\bar{\rho}_i}{dt} = \dot{m}_{i-1/2} - \dot{m}_{i+1/2} \tag{2-19}$$

$$A\Delta z \left[\bar{\rho}_i \frac{d\bar{h}_{\rho,i}}{dt} + \bar{h}_{\rho,i} \frac{d\bar{\rho}_i}{dt} - \frac{dp_i}{dt} \right] = \dot{m}_{i-1/2}\bar{h}_{i-1/2} - \dot{m}_{i+1/2}\bar{h}_{i+1/2} + P\Delta z q_i'' \tag{2-20}$$

$$\Delta z \frac{d\dot{m}_{i+1/2}}{dt} = \left(\dot{I}_i - \dot{I}_{i+1} \right) - A\left(p_{i+1} - p_i \right) - \bar{\tau}_{w,i+1/2} P\Delta z - \bar{\rho}_{i+1/2} gA\Delta z \sin\theta \tag{2-21}$$

where

$$\dot{I} = \frac{\dot{m}^2}{\bar{\rho}_M A} \tag{2-22}$$

and $i = 1, 2, ..., N$

It should be pointed out that the staggered grid scheme is utilized to derive the above equations. This scheme is commonly used in computational fluid dynamics to decouple the equation of mass and energy with the equation of momentum.

48

Specifically, there are two types of cells here, volume cells (solid blocks enclosed in black solid lines) and flow cells (dash blocks enclosed in red dash lines) centered at the interface of the volume cell, as shown in Figure 2.2. The mass and energy balance is calculated within the volume cell while the momentum balance is calculated between the volume cells, i.e., within the flow cell.

It is necessary to introduce additional equations relating the quantities in volume and flow cells.

$$\varphi_{i+1/2} = \varphi_i \delta + (1-\delta)\varphi_{i+1} \tag{2-23}$$

For convection dominated flows the upwind difference scheme is recommended to approximate thermodynamic quantities onto the staggered cells, because the central difference scheme may lead to non-physical solutions (Patankar, 1980).

$$\delta = \begin{cases} 1 \text{ when } \dot{m}_{i+1/2} \geq 0 \\ 0 \text{ when } \dot{m}_{i+1/2} < 0 \end{cases} \tag{2-24}$$

Therefore, one can easily obtain the flow-weighted enthalpy at the interface of the volume cells (i.e., the center of the flow cells)

$$\overline{h}_{i+1/2} = \begin{cases} \overline{h}_i & \text{when } \dot{m}_{i+1/2} \geq 0 \\ \overline{h}_{i+1} & \text{when } \dot{m}_{i+1/2} < 0 \end{cases} \tag{2-25}$$

The momentum at the interface of flow cells is often calculated using second-order center difference in order to avoid the discontinuity caused by the reverse flow, i.e., $\delta = 1/2$ in this case. Specifically,

$$\dot{I}_i - \dot{I}_{i+1} = \frac{1}{2}\left(\dot{I}_{i-1/2} + \dot{I}_{i+1/2}\right) - \frac{1}{2}\left(\dot{I}_{i+1/2} + \dot{I}_{i+3/2}\right) = \frac{1}{2}\left(\dot{I}_{i-1/2} - \dot{I}_{i+3/2}\right) \tag{2-26}$$

where

$$\dot{I}_{i-1/2} = \frac{\dot{m}_{i-1/2}^2}{\bar{\rho}_{M,i-1/2}A} = \frac{\dot{m}_{i-1/2}^2}{\frac{1}{2}(\bar{\rho}_{M,i-1} + \bar{\rho}_{M,i})A} \tag{2-27}$$

$$\dot{I}_{i+3/2} = \frac{\dot{m}_{i+3/2}^2}{\bar{\rho}_{M,i+3/2}A} = \frac{\dot{m}_{i+3/2}^2}{\frac{1}{2}(\bar{\rho}_{M,i+1} + \bar{\rho}_{M,i+2})A} \tag{2-28}$$

Likewise, the mass-weighted density at the interface of volume cells is equal to

$$\bar{\rho}_{i+1/2} = \frac{1}{2}(\bar{\rho}_i + \bar{\rho}_{i+1}) \tag{2-29}$$

Boundary models are applied for the first and last flow cell.

$$\dot{I}_1 - \dot{I}_2 \approx \frac{(|\dot{m}_{in}| + |\dot{m}_{3/2}|)^2}{4\bar{\rho}_{M,1}A} - \frac{1}{2}(\dot{I}_{3/2} + \dot{I}_{5/2}) \tag{2-30}$$

$$\dot{I}_N - \dot{I}_{N+1} \approx \frac{[|\dot{m}_{N-1/2}| + |\dot{m}_{out}|]^2}{4\bar{\rho}_{M,N}A} - \frac{\dot{m}_{out}^2}{\bar{\rho}_{M,N}A} \tag{2-31}$$

2.2.3 Model Reduction

Section 2.2.2 illustrates the discretization of the original equations that govern one-dimensional in-tube flow. It can be noted that the inclusion of the momentum equation adds significant complexity to the computation. As suggested by Brasz and Koenig (1983), dynamic pressure waves are of minor importance for a heat transfer analysis and they can be neglected while still preserving the physical integrity. Hence, the model can be reduced substantially by eliminating the terms on the left-hand side of Eq. (2-3). Furthermore, by neglecting the gravity effect, the last term on the right side can be dropped out as well. As a consequence, the equation of momentum becomes

$$A\frac{\partial p}{\partial z} + \bar{\tau}_w P = 0 \tag{2-32}$$

The discretization of the above equation yields

$$p_i - p_{i+1} = \Delta p_{frict,i} = \frac{\bar{\tau}_{w,i+1/2} P}{A} \Delta z \tag{2-33}$$

It can be noticed that by adopting the above simplification, the number of partial differential equations is reduced from $3N$ to $2N$. Comparing to the original model which has $3N$ state variables $\left(\dot{m}_{3/2}, p_1, \bar{h}_{\rho,1}, ..., \dot{m}_{N+1/2}, p_N, \bar{h}_{\rho,N} \right)$, the reduced model only has $2N$ state variables $\left(p_1, \bar{h}_{\rho,1}, ..., p_N, \bar{h}_{\rho,N} \right)$. The mass flow rates, dictated by the pressure difference, are the algebraic variables and computed by the reduced momentum equations.

2.2.4 Constituent Equations

It is necessary to provide additional information to close the model derived previously. The heat flux between the refrigerant and the tube walls is calculated by

$$q_r'' = \alpha_r \left(T_w - T_r \right) \tag{2-34}$$

where α_r is the heat transfer coefficient on the refrigerant side, which is determined by choosing appropriate heat transfer correlations based on whether the refrigerant is in single-phase or two-phase regime.

While the frictional pressure drop is often evaluated as

$$\Delta p_{frict} = f_{Darcy} \frac{\Delta z}{2d} \frac{G^2}{\rho} \tag{2-35}$$

Where f_{Darcy} is the Darcy friction factor and can be computed by the correlations.

More often than not, the heat transfer coefficient and pressure loss are a function of mass flow rate and other thermodynamic properties. To simplify the computation, it is assumed that that α and Δp_{frict} are only dependent upon the inlet

state. Therefore, the upwind scheme can be used here to determine the thermodynamic properties at the interface of the cell. While the inlet mass flow rate can be also picked to calculate Reynolds number as required. Of course, it is more accurate to use the average of the inlet and outlet state in the evaluation to determine α and Δp_{frict}. One can easily apply the 2nd order center difference to calculate the corresponding properties. Please refer to part that depicts the discretization of the original momentum equation.

So far we have not presented how to calculate the flow-weighted enthalpy $\bar{h}$ for two-phase flows yet. Based on the approximation of homogeneous flow, one can easily deduce that the density-weighted enthalpy is equivalent to the flow-weighted enthalpy since there is no phasic velocity difference, i.e., $\bar{h} = \bar{h}_\rho$. However, for the non-homogeneous flow, it is not the case anymore. The derivation of calculating $\bar{h}$ will be described below.

The analysis first selects the pressure p and the density-weighted enthalpy $\bar{h}_\rho$ as the state variables (the partial derivatives of the density are still required, see Eq.(2-17)). Since $\bar{h}_\rho$ is the state variable, it is known at each time step. If an expression can be established that relates $\bar{h}_\rho$ and $\bar{h}$, the computation will become much more tractable.

This introduces the enthalpy correction Δh_c

$$
\begin{aligned}
\Delta h_c &= \bar{h} - \bar{h}_\rho \\
&= x h_g + (1-x) h_f - \hat{x} h_g - (1-\hat{x}) h_f \\
&= (x - \hat{x})(h_g - h_f)
\end{aligned}
\tag{2-36}
$$

It should be noted here that x and $\hat{x}$ are zero for the subcooled liquid, and unity for the superheated vapor, respectively. Hence, Δh_c becomes zero for single-phase flows.

All the variables in Equation (2-36) are the thermodynamic properties, and can be readily calculated except for the flow quality x. Specifically, h_{g} and h_{f} can be evaluated based on the pressure, whereas the static quality $\hat{x}$ can be obtained via Equation (2-13) since $\overline{h}_\rho$ is known at every time step.

Butterworth (1975) has shown that the slip-ratio-based void fraction equations can be fit to a standard expression form of

$$x = \frac{\gamma^{1/q}}{\gamma^{1/q} + \left[\dfrac{1}{c}\left(\dfrac{\rho_f}{\rho_g}\right)^r\left(\dfrac{\mu_g}{\mu_f}\right)^s\right]^{1/q}(1-\gamma)^{1/q}} \tag{2-37}$$

The constants and exponents for different void fraction models are given in Table 2.1.

Table 2.1 Constants and exponents for various void fraction models

Models	c	q	r	s
Homogeneous	1	1	1	0
Zivi (1964)	1	1	0.67	0
Turner (1966)	1	0.72	0.40	0.08
Smith (1969)	0.79	0.78	0.58	0
Lockhart-Martinelli (1949)	0.28	0.64	0.36	0.07
Thome (1964)	1	1	0.89	0.18
Baroczy (1965)	1	0.74	0.65	0.13

The procedure of calculating the flow-weighted enthalpy $\overline{h}$ is given in Figure 2.3. By using the enthalpy correction method described above, the same set of governing equations (2-1), (2-2) & (2-32) can be applied to both single-phase and

two-phase flows without requiring any modifications. Meanwhile, Equation (2-36) ensures that the correction only applies for the two-phase flow and gives a seamless transition between the single-phase and two-phase flows. Furthermore, by selecting p and $\bar{h}_\rho$ as the state variables, all the thermophysical properties, including the partial derivatives of the density, can be calculated in a consistent manner irrespective of the type of void fraction model used. Table 2.2 compares the existing discretized heat exchanger models with the new model.
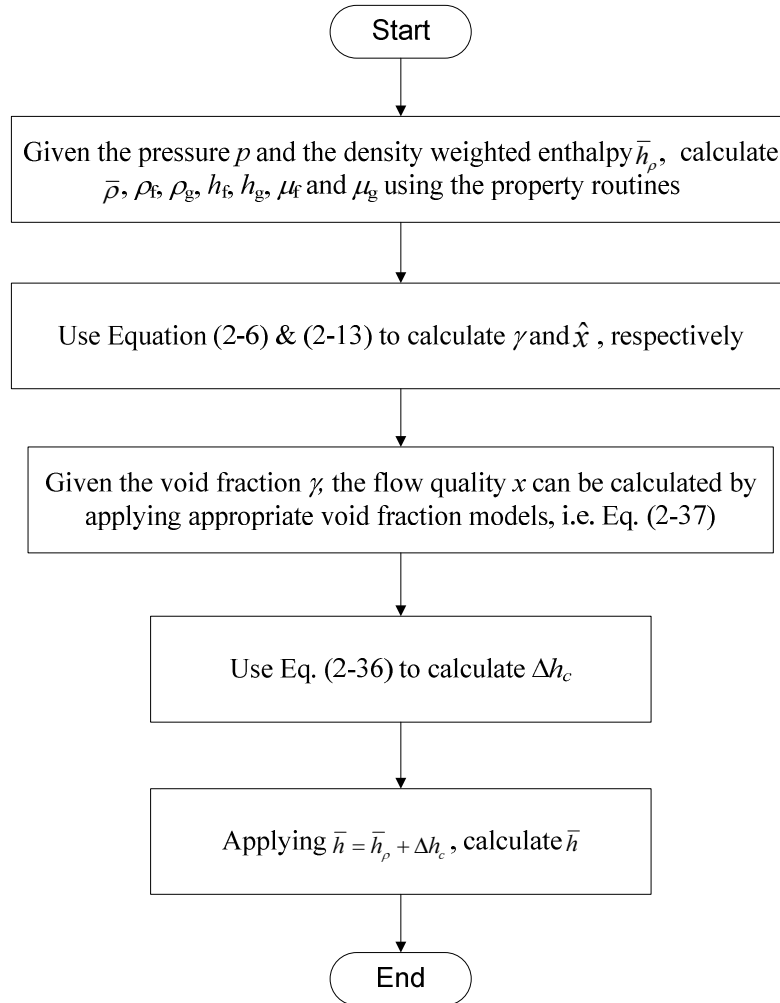
Figure 2.3 Flowchart for calculating the flow-weighted enthalpy

Table 2.2 Comparison between the existing discretized heat exchanger models and the new model

Citation	Two-phase Model	Momentum Balance	Remarks
Nyers & Stoyan (1994)	HEM	Dynamic	Invalid assumption: Less refrigerant mass & faster transients
Jia et al. (1995)		Dynamic	
Aprea & Renno (1999 & 2002)		Dynamic	
Jiang & Radermacher (2003)		No pressure drop	
Winkler (2009)		Dynamic	
Schalbart & Haberschill (2013)		Dynamic	
Tummescheit (2002)		Static	
Richter (2008)		Static w/o acceleration DP	
MacArthur & Grald (1989)	HEM + density correction	No pressure drop	Fundamentally erroneous: Do not differentiate the flow-weighted enthalpy from the density-weighted enthalpy
Judge & Radermacher (1997)		Dynamic	
Ploug-Sørensen et al. (1997)		Dynamic	
Rossi & Braun (1999)		No pressure drop	
Mithraratne et al. (2000)		No pressure drop	
Koury et al. (2001)		Dynamic	
Haberschill et al. (2003)		No pressure drop	
Bendapudi et al. (2005)		No pressure drop	
Zhang et al. (2009)		Static	
Ndiaye & Bernier (2010)		Dynamic	
Xuan (2010)		Static	
Choi et al. (2011)		No pressure drop	
Zhang & Zhang (2011)		Static	
Wang and Touber (1991)	SFM	No pressure drop	Complex transition between the single-phase and two-phase flows
Jia et al. (1996 & 1999)		Dynamic	
Beghi & Cecchinato (2009)		Dynamic	
Kapadia et al. (2009)		Dynamic	
Bauer (1999)		Dynamic	Complex computation for slip ratio & too specific
Kærn et al. (2011)		Dynamic	No details about implementation
New model	**SFM**	**Static w/o acceleration DP**	**Physically sound & simple**

SFM: Separated Flow Model w/o interfacial exchange

2.2.5 Numerical Treatments

It is a well-known fact that the heat transfer coefficient estimated by the correlations is not continuous at the phase transition point. The discontinuities in the heat transfer coefficients can lead to fatal numerical failures during the simulation. One of these numerical problems is called chattering, which is characterized with high-frequency oscillation in the numeric integration process reducing the simulation performance. Jensen (2003) presented an excellent example describing the chattering phenomenon caused by discontinuities in heat transfer coefficient and the author would like to use the example here.

Let's consider that the refrigerant state is very close to the saturated vapor, but still in the two-phase regime, e.g., $x = 0.99$. Also we assume that the heat transfer coefficient α is 2000 W/ (m^2-K) for the two-phase regime and 800 W/ (m^2-K) for the vapor phase. Since the heat transfer coefficient in the two-phase regime is much higher, the augmented heat flow will heat up the refrigerant to the superheated vapor. However, once the refrigerant becomes vapor, the heat flow instantaneously decreases significantly due to a much lower heat transfer coefficient. As a result, the refrigerant will return back to the two-phase regime because of an insufficient heat flow supply and the entire process will start over again. This type of limit cycles is known as *chattering* and may occur when discontinuities exist in the solution. Once chattering occurs, the simulation nearly stalls and does not make a progress even after a long period of time.

One of the remedies to avoid chattering is to smooth the discontinuities in the model. The phase boundaries require special attention. Bonilla *et al*. (2012) studied

56

the chattering problem that arises in a dynamic two-phase flow model due to discontinuous density changes with discontinuous partial derivatives. In this section, we will mainly focus on dealing with discontinuities in heat transfer coefficients. The following procedure is proposed to determine the heat transfer coefficient over the entire regime

$$\alpha_r = \begin{cases} \alpha_{vap} & \text{when } x \geq 1 \\ \text{spliceFunction}\left(\alpha_{vap}, \alpha_{tp}, x - \left(1 - \dfrac{\Delta x_{vap}}{2}\right), \dfrac{\Delta x_{vap}}{2}\right) & \text{when } 1 - \Delta x_{vap} < x < 1 \\ \alpha_{tp} & \text{when } \Delta x_{liq} \leq x \leq 1 - \Delta x_{vap} \\ \text{spliceFunction}\left(\alpha_{tp}, \alpha_{liq}, x - \dfrac{\Delta x_{liq}}{2}, \dfrac{\Delta x_{liq}}{2}\right) & \text{when } 0 < x < \Delta x_{liq} \\ \alpha_{liq} & \text{when } x \leq 0 \end{cases}$$

$$(2\text{-}38)$$

where small values are chosen for Δx_{vap} and Δx_{liq}, e.g., 0.05.

spliceFunction in the Modelica library is used to interpolate the heat transfer coefficient around the region close to the bubble point and dew point. spliceFunction is defined as

$$\text{spliceFunction}\left[f(x), g(x), p(x), \delta\right] = y \cdot f(x) + (1 - y) \cdot g(x) \qquad (2\text{-}39)$$

where

$$y = \begin{cases} 1 & \text{if } p(x) >= \delta \\ \dfrac{1}{2}\left[\tanh\left(\tan\left(\left(\dfrac{p(x)}{\delta} - \dfrac{1}{2}\right)\pi\right)\right) + 1\right] & \text{if } -\delta < p(x) < \delta \\ 0 & \text{if } p(x) <= -\delta \end{cases} \qquad (2\text{-}40)$$

2.3 Tube Walls and Fins

Tube walls and associated fins are modeled using a lumped capacitance method. In general, there is a temperature distribution on the fins. By applying the fin efficiency, however, one can lump the tube walls and fins together using one temperature. Without considering the axial conduction along the tubes, the energy equation of the tube walls and associated fins is

$$\left(M_t c_{p,t} + M_{fin} c_{p,fin} \right) \frac{dT_w}{dt} = q_r + q_a \tag{2-41}$$

where

$$q_r = \alpha_r A \left(T_r - T_w \right) \tag{2-42}$$

$$q_a = \dot{m}_a \left[c_{p,a} \left(T_{a,in} - T_{a,out} \right) + \left(\omega_{a,in} - \omega_{a,out} \right) \Delta h_{fg} \right] \tag{2-43}$$

where $c_{p,a}$ is the specific heat of moist air per unit mass of dry air determined as $1.005 + 1.86\omega$ kJ/kg-K, and Δh_{fg} is the vaporization heat of water determined as $2501 + 1.86 \left(T - 273.15 \right)$ kJ/kg.

2.4 Air Side

The air side is analyzed based on the following assumptions (Figure 2.4)

1) one-dimensional quasi-steady airflows;

2) negligible heat conduction in air flow direction;

3) the temperature profile within fins follows the steady-state profile, allowing the use of heat transfer and combined heat and mass transfer fin efficiencies;

4) simultaneous heat and mass transfer follows the Lewis analogy;

5) equal temperature of tube wall and fins at one section.

58
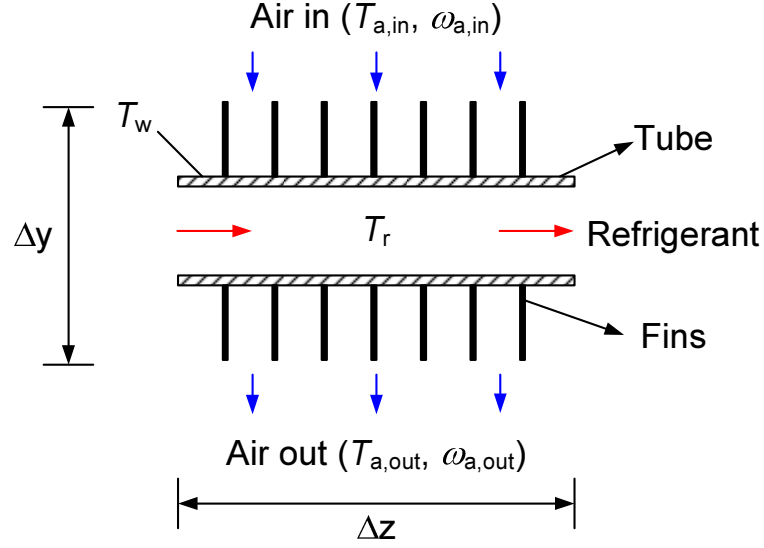
Figure 2.4 Schematic of a discretized segment

2.4.1 Fan On

The governing equations for the air side are

$$\dot{m}_a c_{p,a} \frac{dT_a}{dy} \Delta y = \alpha_a \left(A_{o,t} + \eta_{fin} A_{o,fin} \right) \left(T_w - T_a \right) \tag{2-44}$$

$$\dot{m}_a \frac{d\omega_a}{dy} \Delta y = \alpha_m \left(A_{o,t} + \eta_{fin} A_{o,fin} \right) \min \left(0, \omega_{w,s} - \omega_a \right) \tag{2-45}$$

where $\omega_{w,s}$ is the humidity ratio of saturated air, evaluated at the surface temperature T_w. α_m is the mass transfer coefficient and is determined by applying the Lewis analogy

$$\alpha_m = \frac{\alpha_a}{c_{p,a} Le^{2/3}} \tag{2-46}$$

where $Le^{2/3} = 0.9$ (Kuehn *et al.*, 1998).

Solving Equation (2-44) and (2-45) yields the air outlet state by knowing the air temperature and humidity ratio ($T_{a,in}$ and $\omega_{a,in}$) at the inlet

$$T_{a,out} = T_{a,in} + \left(T_w - T_{a,in}\right)\left\{1 - \exp\left[-\frac{\alpha_a\left(A_{o,t} + \eta_{fin}A_{o,fin}\right)}{\dot{m}_a c_{p,a}}\right]\right\} \tag{2-47}$$

$$\omega_{a,out} = \omega_{a,in} + \left\{1 - \exp\left[-\frac{\alpha_a\left(A_{o,t} + \eta_f A_{o,fin}\right)}{\dot{m}_a c_{p,a} Le^{2/3}}\right]\right\} \min\left(0, \omega_{a,s} - \omega_{a,in}\right) \tag{2-48}$$

The fin efficiency is calculated using the equation proposed by Hong and Webb (1996)

$$\eta_{fin} = \frac{\tanh\left(mr\phi\right)}{mr\phi}\cos\left(0.1mr\phi\right) \tag{2-49}$$

$$m = \sqrt{\frac{2\alpha_a}{k_{fin}\delta_{fin}}} \tag{2-50}$$

$$\phi = \left(\frac{R_e}{r} - 1\right)\left(1 + 0.35\ln\left(\frac{R_e}{r}\right)\right) \tag{2-51}$$

where R_e is defined as the radius of an equivalent circular fin that has the same fin efficiency as that of the plate fin (Schmidt, 1949)

$$\frac{R_e}{r} = 1.28\frac{P_t}{d_o + 2\delta_{fin}}\left(\frac{P_r}{P_t} - 0.2\right)^{1/2} \tag{2-52}$$

$$r = \frac{d_{o,t}}{2} + \delta_{fin} \tag{2-53}$$

where P_t is the tube pitch (vertical spacing), P_r is the row pitch (horizontal spacing), and $d_{o,t}$ is the outside tube diameter.

While the fin efficiency at wet condition ($\omega_{a,s} - \omega_{a,i} < 0$) is determined by replacing α_a with the effective heat transfer coefficient α_{eff} defined as (Elmahdy and Biggs, 1983)

$$\alpha_{eff} = \alpha_a \left(1 + \frac{\Delta h_{fg}}{c_{p,a}} \frac{d\omega_{a,s}}{dT} \bigg|_{T_w} \right) \tag{2-54}$$

where $\dfrac{d\omega_{a,s}}{dT}$ is the derivative of saturated humidity ratio with respect to the temperature and Δh_{fg} is the vaporization heat of water, both of which are evaluated at the wall surface temperature T_w.

2.4.2 Fan Off

When the fan is off, the heat exchange between the ambient air and the heat exchanger is dominated by natural convection. In this case, the heat transfer is calculated by neglecting dehumidification and assuming the air temperature is uniform for the entire heat exchanger.

Radiation heat transfer needs to be taken into account for the outer most tubes, i.e. the tubes in the first and last tube bank, which are directly exposed to the ambient. For each segment of these tubes, one can have

$$q_a = \alpha_a \left(A_{o,t} + \eta_{fin} A_{o,fin} \right) \left(T_a - T_w \right) + \varepsilon \sigma A_{face} \left(T_a^4 - T_w^4 \right) \tag{2-55}$$

where A_{face} and ε are the frontal area and the emissivity of fin material (0.04 for aluminum foil), respectively.

2.5 Summary

A new discretized heat exchanger model has been developed based on a decoupled approach to modeling the heat transfer and pressure drop performance of the heat exchanger. The model is capable of accounting for the complex tube circuitry and handling dry and dehumidifying conditions. To reduce the computational complexity, the equation for the momentum balance has been simplified by

neglecting the inertia term and the acceleration term. However, this simplification can still preserve the prevailing physics of fluid flow characteristics.

The separated flow model without interfacial exchange is utilized for analysis of two-phase flows. The method of "enthalpy correction" has been developed to account for the slip effect in two-phase flows so that a more accurate prediction for the transient characteristics of two-phase flows can be achieved.

3 Transient Modeling of a Flash Tank Vapor Injection Heat Pump System

3.1 Introduction

The flash tank vapor injection (FTVI) system has been gaining in popularity since it was first introduced to the market in late 1970s (Umezu and Suma, 1984). Its applications have increased considerably in order to satisfy various needs, such as heating, cooling and refrigeration (Baek *et al*., 2008; Cho *et al*., 2009; Scarcella and Chen, 2010). Compared to the conventional systems without vapor injection, FTVI systems are operated under lower discharge temperatures and have higher performance in energy efficiency. Moreover, these systems are able to adjust the capacity by altering the vapor injection ratio (Winandy and Lebrun, 2002). Experimental studies (Table 3.1) were carried out to evaluate the performance of FTVI systems using various working fluids under different operating conditions. The studies unanimously found that the system capacity and COP improved when vapor injection was applied. In low ambient temperature heating applications, heating capacity and COP could increase by 45% and 24%, respectively, compared to non-injection systems (Baek *et al*., 2008). In high ambient temperature cooling applications, cooling capacity and COP improved by 14.2% and 16.5%, respectively (Cho *et al*., 2009).

Despite all the advantages, FTVI systems are more difficult to control compared to the conventional systems. Instead, a proper liquid level in the flash tank needs to be maintained during the operation (Xu *et al*., 2011a). Moreover, the same authors (Xu *et al*., 2011b) experimentally demonstrated that the superheat of the

injected vapor could be used as the control signal to the upper-stage expansion valve. In order to maintain sufficient superheat of the injected vapor, an electric heater with constant power input was applied on the injection line.

Table 3.1 FTVI experimental studies

| Citation | Refrigerant | Application | Operating Conditions | | | |
| | | | Indoor | | Outdoor | |
			DB (°C)	WB (°C)	DB (°C)	WB (°C)
Baek *et al.* (2008)	CO_2	heating	20	15	7	6
Cho *et al.* (2009)	CO_2	cooling	27	19.5	35	24
Wang *et al.* (2009)	R410A	cooling	27.8 35 46.1		26.7	19.4
		heating	16.7 8.3 -8.3 -17.8	14.7 6.1 -9.4	21.1	<=15.6
Xu *et al.* (2013d)	R410A & R32	cooling	27.8 35 46.1		26.7	19.4
		heating	8.3 -8.3 -17.8	6.1 -9.4	21.1	
			Condensing Temperature (°C)		Evaporating Temperature (°C)	
Ma & Zhao (2008)	R22	heating	42 & 45		-25 to -7	
Xu *et al.* (2013b)	R32	cooling	40 & 45		5	
		heating	40 & 45		-10, -5 & 0	

The purpose of the present paper differs from the study by Xu *et al.* (2011b) by focusing on the numerical modeling, to investigate the controllability of FTVI systems, and to gain the knowledge about the liquid level fluctuation during cycling operation, which might help in optimizing the size of the flash tank.

Comprehensive review of the literature (Bendapudi and Braun, 2002; Rasmussen, 2012) in this field indicates that a majority of the previous studies focused on conventional, single-stage vapor compression systems, and no studies have focused on FTVI systems. Therefore, this study attempts to broaden this aspect of research and explore the dynamic behavior of such systems.

3.2 System Description

The studied system and its log(p)-h diagram are shown in Figure 3.1. The high pressure and high temperature vapor (2) discharged by the compressor enters the condenser. The refrigerant passing through the condenser rejects heat to the high temperature reservoir and changes to a subcooled liquid (3). Then, the refrigerant flows through the upper-stage expansion valve and undergoes a drastic drop in pressure. This process results in a vapor-liquid mixture that enters the flash tank (4) where the vapor and liquid separate. The saturated vapor (6) is injected to the compressor. The saturated liquid (5) flows through the lower-stage expansion valve and undergoes another throttling process. The low pressure, low temperature, and low quality refrigerant (7) enters the evaporator, where it gains heat from the low temperature reservoir and reaches a superheated vapor state (1) at the evaporator exit. The compressor receives the refrigerant at state (1) and compresses it to an intermediate pressure (8) during the first compression stage, after which the refrigerant mixes with the injected vapor. Finally, the mixed refrigerant (9) is further compressed to a high pressure during the second compression stage. The compression process is associated with an increase in refrigerant temperature.

a) Schematic   b) Process in log(p) - h diagram
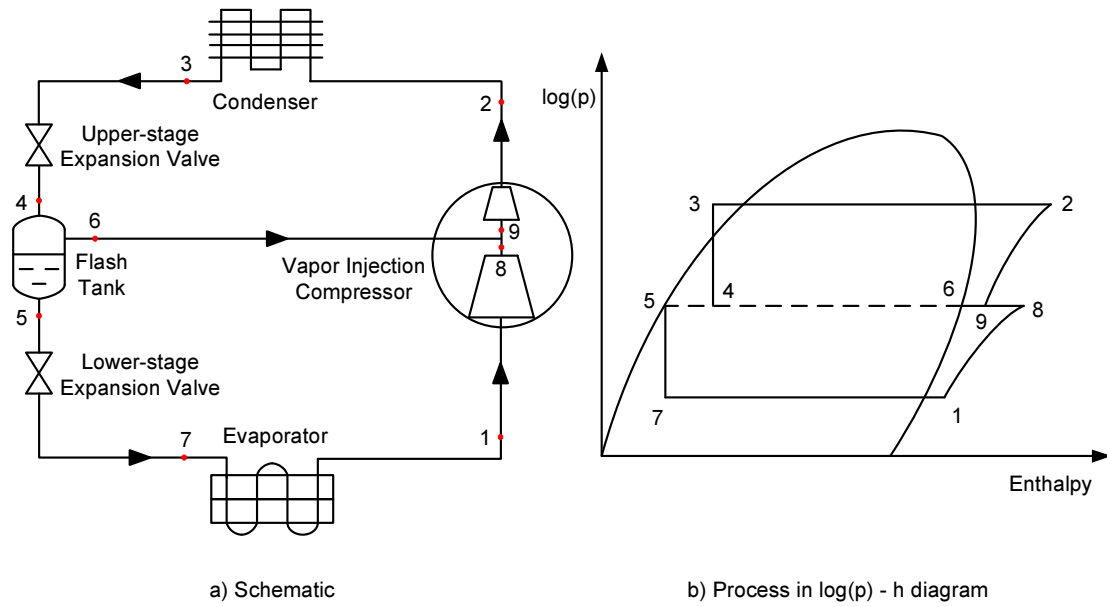
Figure 3.1 FTVI system

3.3 Model Development

3.3.1 Compressor Model

A vapor injection scroll compressor was used in this experiment. Figure 3.2 displays various elements of a vapor injection scroll compressor and the refrigerant flow path. Vapor injection can be turned on or off by opening or closing the solenoid valve prior to the economizer port on the injection line. In the present study, the solenoid valve is kept open to enable vapor injection. Refrigerant leaving the evaporator enters the suction chamber. This refrigerant absorbs heat from the metallic elements, and cools the motor before being drawn into the compression chamber. At the transition point of the compression process, the refrigerant compressed to the intermediate pressure mixes with the injected vapor from the economizer port and completes the remaining compression process before being discharged into the discharge chamber.

66
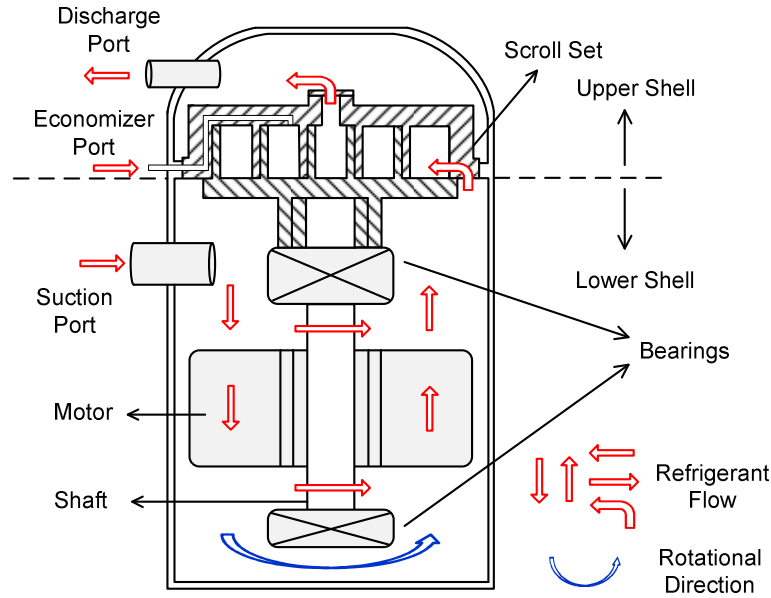
Figure 3.2 Schematic of a vapor injection scroll compressor

The compressor is divided into separate lumps with internal heat transfer (Figure 3.3) and analyzed with the following assumptions:

(1) there is no pressure drop inside the suction chamber;

(2) the oil effects are negligible;

(3) any refrigerant entering the suction chamber mixes homogeneously with the refrigerant inside the suction chamber before being drawn into the scrolls;

(4) heat conduction and radiation between metallic elements are neglected;

(5) the compression process is presumably completed in one large pocket;

(6) the low and high stage compression processes are assumed to have the same polytropic index.

The boundary conditions of the compressor model are defined as the mass flow rate and enthalpy entering the suction port, the mass flow rate and enthalpy entering the economizer port, and the discharge pressure. As a result, a small control volume

at the economizer port and a discharge pressure loss are included in the model. The reason of such boundary conditions will be explained in Section 3.4.

Figure 3.3 Model representation of an economized scroll compressor: 1 – Suction chamber control volume; 2 – Economizer port control volume; 3 – Compression process; 4 – Discharge chamber control volume; 5 – Shaft and bearings; 6 – Scroll set; 7 – Motor; 8 – Low-side shell; 9 – High-side shell; 10 – Discharge port pressure loss

3.3.1.1 Compressor On

The mass and energy conservation of the refrigerant within the suction chamber (CV 1) can be described as

$$V_1 \frac{d\rho_1}{dt} = \dot{m}_{suc} - \dot{m}_1 \tag{3-1}$$

$$V_1 \left(\rho_1 \frac{dh_1}{dt} - \frac{dp_1}{dt} \right) = \dot{m}_{suc} \left(h_{suc} - h_1 \right) + q_{ls} + q_m + q_{shf} + q_{scr} \tag{3-2}$$

Similarly, the mass and energy conservation equations for the refrigerant in the discharge chamber can be formulated.

The heat transfer between the refrigerant and pertinent elements is determined as follows:

$$
\begin{cases}
q_{ls} = \dfrac{T_{ls} - T_1}{R_{rls}} \\[2ex]
q_m = \dfrac{T_m - T_1}{R_{rm}} \\[2ex]
q_{shf} = \dfrac{T_{shf} - T_1}{R_{rshf}} \\[2ex]
q_{scr} = \dfrac{T_{scr} - T_1}{R_{rscr}}
\end{cases}
\tag{3-3}
$$

The refrigerant in the suction chamber is not necessarily superheated, and the compressor might experience liquid flooding at the very beginning of the start-up operation. Therefore, adopting constant thermal resistances might not be appropriate in the simulation. In order to estimate the thermal resistances accurately, the heat transfer area of each metallic element is measured, and the corresponding heat transfer coefficients are calculated using empirical correlations according to the refrigerant state in the suction chamber. Specifically, the Dittus-Boelter (1985) correlation and the Gungor-Winterton (1987) correlation are used for single-phase and two-phase heat transfer coefficient calculations, respectively. During the "off-period", the Churchill-Chu (1975) correlation and the Cooper (1984) correlation are used to calculate the natural convection and boiling heat transfer coefficients, respectively.

The motor efficiency and mechanical efficiency are defined as

$$
\eta_m = \frac{\dot{W}_{shf}}{\dot{W}_{tot}}
\tag{3-4}
$$

$$
\eta_{mech} = \frac{\dot{W}_{comp}}{\dot{W}_{shf}}
\tag{3-5}
$$

The thermal storage for various metallic elements of the compressor can be formulated as

$$M_{ls} c_{p,ls} \frac{dT_{ls}}{dt} = \frac{T_{amb} - T_{ls}}{R_{als}} - q_{ls} \tag{3-6}$$

$$M_{us} c_{p,us} \frac{dT_{us}}{dt} = \frac{T_{amb} - T_{us}}{R_{aus}} - q_{us} \tag{3-7}$$

$$M_m c_{p,m} \frac{dT_m}{dt} = (1 - \eta_m) \dot{W}_{tot} - q_m \tag{3-8}$$

$$M_{shf} c_{p,shf} \frac{dT_{shf}}{dt} = \xi_{shf} (1 - \eta_{mech}) \dot{W}_{shf} - q_{shf} \tag{3-9}$$

$$M_{scr} c_{p,scr} \frac{dT_{scr}}{dt} = (1 - \xi_{shf})(1 - \eta_{mech}) \dot{W}_{shf} - q_{scr} \tag{3-10}$$

The refrigerant mass flow rate drawn by the scroll set from CV 1 is calculated as

$$\dot{m}_1 = \left[a_1 - a_2 \left(\frac{p_4}{p_1} \right)^{\frac{1}{n}} \right] \rho_1 V_{disp} \frac{N}{60} \tag{3-11}$$

where the polytropic index n is estimated to be 1.35 based on the compressor performance test.

The injection flow is calculated by conceiving the injection port as a fixed orifice through which the reverse flow can possibly occur

$$\dot{m}_2 = \text{sign}(p_2 - p_{int}) \cdot a_3 \sqrt{\rho_{in} |p_2 - p_{int}|} \tag{3-12}$$

where p_{int} is the internal intermediate pressure after the first stage compression (state point 8 in Figure 3.1) and can be determined by assuming a polytropic compression process

$$\frac{p_{int}}{p_1} = \zeta^n \tag{3-13}$$

70

where the built-in volume ratio of the first stage ζ is 1.21 in the present study.

The flow direction through the economizer port is dependent on the difference between the pressure at the economizer port control volume and the internal intermediate pressure. If the pressure difference is positive, the compressor will absorb the vapor from the flash tank. If the pressure difference is negative, the compressed vapor after the first stage compression will be discharged to the flash tank, as observed at the very beginning of the start-up operation.

As a consequence, the conservation of mass and energy for the control volume at the economizer port (CV 2) should be considered separately for these two scenarios assuming negligible heat transfer.

$$V_2 \frac{d\rho_2}{dt} = \dot{m}_{inj} - \dot{m}_2 \tag{3-14}$$

$$V_2 \left(\rho_2 \frac{dh_2}{dt} - \frac{dp_2}{dt} \right) = \begin{cases} \dot{m}_{inj} \left(h_{inj} - h_2 \right) & \text{when } p_2 - p_{int} \geq 0 \\ -\dot{m}_2 \left(h_{int} - h_2 \right) & \text{when } p_2 - p_{int} < 0 \end{cases} \tag{3-15}$$

where $\dot{m}_{inj}$ and $\dot{m}_2$ are positive for the normal flow and negative for the reverse flow. The refrigerant temperature after the first stage compression can be calculated as

$$T_{int} = T_1 \left(\frac{p_{int}}{p_1} \right)^{\frac{n}{n-1}} \tag{3-16}$$

Refrigerant enthalpy after mixing (point 9, Figure 3.1) the suction flow and injection flow can be determined through the energy conservation

$$h_{mix} = \begin{cases} \dfrac{\dot{m}_1 h_{int} + \dot{m}_2 h_2}{\dot{m}_1 + \dot{m}_2} & \text{when } p_2 - p_{int} > 0 \\ h_{int} & \text{when } p_2 - p_{int} \leq 0 \end{cases} \tag{3-17}$$

The polytropic compression work is evaluated as

$$\dot{W}_{comp} = \frac{n}{n-1} \left\{ p_1 \dot{V}_1 \left[\left(\frac{p_{\text{int}}}{p_1} \right)^{\frac{n}{n-1}} - 1 \right] + p_{\text{int}} \dot{V}_{mix} \left[\left(\frac{p_4}{p_{\text{int}}} \right)^{\frac{n}{n-1}} - 1 \right] \right\} \tag{3-18}$$

where $\dot{V}_1$ and $\dot{V}_{mix}$ are the volumetric flow rates evaluated based on ρ_1 and ρ_{mix}, respectively.

The refrigerant temperature after the entire compression process is

$$T_3 = T_{mix} \left(\frac{p_4}{p_{\text{int}}} \right)^{\frac{n-1}{n}} \tag{3-19}$$

The discharge mass flow rate is determined through the following expression

$$\dot{m}_4 = \frac{\sqrt{\rho_4 (p_4 - p_{dis})}}{f_{dis}} \tag{3-20}$$

Finally, the total power input required by the compressor is determined via the following correlation deduced from the compressor performance map

$$\dot{W}_{tot} = b_1 p_1 \dot{V}_1 \left[\left(\frac{p_{\text{int}}}{p_1} \right)^{b_2} - 1 \right] + b_3 p_{\text{int}} \dot{V}_{mix} \left[\left(\frac{p_4}{p_{\text{int}}} \right)^{b_4} - 1 \right] + b_5 \tag{3-21}$$

3.3.1.2 Compressor Off

During the "off-period", the compressor stops pumping the refrigerant to the discharge side, which is disconnected from the suction side to prevent backflow by the internal check valve. However, the flash tank is still connected to the low-pressure suction side by the economizer port. As a result, refrigerant from the injection line will travel through the economizer port to the suction chamber (Figure 3.3b). In this case, the mass flow rate through the economizer port is

$$\dot{m}_2 = a_3 \sqrt{\rho_2 (p_2 - p_1)} \tag{3-22}$$

The suction chamber is modeled as an accumulator with internal heat transfer and the governing equations are

$$V_1 \frac{d\rho_1}{dt} = \dot{m}_{suc} + \dot{m}_2 \qquad (3\text{-}23)$$

$$V_1 \left(\rho_1 \frac{dh_1}{dt} - \frac{dp_1}{dt} \right) = \dot{m}_2 \left(h_2 - h_1 \right) + \dot{m}_{suc} \left(h_{suc} - h_1 \right) + q_{ls} + q_m + q_{shf} + q_{scr} \qquad (3\text{-}24)$$

where $\dot{m}_{suc}$ is negative, denoting that the refrigerant is flowing out of the control volume. h_{suc} is the enthalpy of the refrigerant leaving the suction chamber, which is determined by the state of the refrigerant inside the suction chamber. For modeling details, readers should refer to Section 3.3.4 for the flash tank modeling, since the only difference is that the accumulator only has the vapor outlet. Other parts of the compressor can be analyzed by applying the same equations for the "on-period" by recognizing that the power consumption is zero for the "off-period".

The selection of state variables has a decisive effect on the simulation speed. In this study, unless specified otherwise, the pressure p and the enthalpy h have been selected as the state variables because they usually serve as the independent properties of property routines. Moreover, the enthalpy can also act as the independent state variable to distinguish whether the refrigerant is single-phase or two-phase, and therefore appropriate correlations for heat transfer and pressure drop can be applied accordingly. As a result, the derivative of the density with respect to the time in the continuity equation can be expanded as follows

$$\frac{d\rho}{dt} = \left. \frac{\partial \rho}{\partial p} \right|_h \frac{dp}{dt} + \left. \frac{\partial \rho}{\partial h} \right|_p \frac{dh}{dt} \qquad (3\text{-}25)$$

The partial derivatives of the density can be calculated either analytically based on the thermodynamic relations or numerically. Please refer to Appendix for more details.

3.3.2 Expansion Device Models

In the system, an electronic expansion valve (EEV) is used in the upper-stage and a thermostatic expansion valve (TXV) is used in the lower-stage. The following assumptions are made:

(1) the valve is adiabatic;

(2) the expansion process is isenthalpic;

(3) TXV bulb content is at the uniform temperature;

(4) the friction and inertia of the mechanical parts are negligible.

3.3.2.1 Electronic Expansion Valve

In general, injection flow is either a saturated vapor or in two-phase. An electric heater with 60W power input was attached to the surface of the injection line in order to maintain injection superheat. A pressure sensor and an in-stream thermocouple were installed in the injection line to measure the pressure and temperature of the injected vapor, respectively. As such, the superheat of the injected vapor can be determined. The injection superheat signal is received by the EEV controller, which adjusts the opening of the valve.
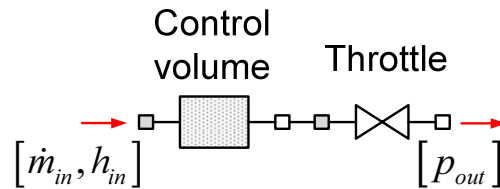
Figure 3.4 Modeling representation of an expansion device

Similar to the compressor model, a small adiabatic control volume is added to the expansion device model to accommodate the boundary conditions which consist of the inlet mass flow rate and enthalpy as well as outlet pressure (Figure 3.4). The governing equations for the mass and thermal storage of the control volume can be easily derived by following the derivation in Section 3.3.1.1 and thus not repeated here for brevity.

The mass flow rate through the throttle is determined by the flow coefficient, the flow area, the inlet density, and the pressure difference across the valve

$$\dot{m}_{exp} = C_v A \sqrt{\rho_{in} \Delta p} \tag{3-26}$$

where $\dot{m}_{exp}$ is the mass flow rate through the throttle, C_v is the flow coefficient, ρ_{in} is the refrigerant density in the control volume.

Generally speaking, it is not easy to derive the mathematical expression that relates the flow area to the valve opening for EEV. However, the combined valve of $C_v A$ can be readily obtained by regression based on experimental data

$$C_v A = c_0 + c_1 \varphi + c_2 \varphi^2 + c_3 \varphi^3 \tag{3-27}$$

where φ is the percentage of valve opening determined by the PID controller based on error between the measured superheat and the set point, $e_{sh}(t)$

$$\varphi(t) = K_p e_{sh}(t) + K_i \int_0^t e_{sh}(\tau) d\tau + K_d \frac{d}{dt} e_{sh}(t) \tag{3-28}$$

Since the pressure and temperature of the injection flow are both measured on the vapor line, the superheat can be sensed instantaneously. Hence, there is no need to add a time delay for the superheat signal to the PID controller.

3.3.2.2 Thermostatic Expansion Valve

The TXV comprises of two portions: the throttling portion and the sensor bulb portion. The throttling portion regulates the refrigerant mass flow through the valve, and the sensor bulb portion monitors the refrigerant temperature leaving the evaporator. The sensor bulb also converts the change in temperature into the change in pressure on the diaphragm, causing the needle to move upwards or downwards (Figure 3.5).

Since the superheat is sensed by the bulb attached on the suction line, there is an inevitable delay between the sensed superheat and the actual instantaneous superheat due to the thermal inertia of the bulb and the heat transfer resistance between the substance in the bulb and the refrigerant flowing in the suction line. The sensor bulb is modeled as a lumped section and the relationship between the bulb temperature and the refrigerant temperature at the evaporator outlet is given by

$$\tau_b \frac{dT_b}{dt} = T_{r,eo} - T_b \tag{3-29}$$

where T_b is the bulb temperature, τ_b is the time constant, and $T_{r,eo}$ is the refrigerant temperature at the evaporator outlet.

The spring deflection needs to be known in order to find the effective flow area. The force exerted by the spring can be found from a force balance on the diaphragm shown in Figure 3.6a. We assume that the spring force is a linear function of the spring deflection, yielding

$$Ky + F_{offset} = \left(p_b - p_{eq} \right) A_{diaph} \tag{3-30}$$

where K is the spring constant and y is the spring deflection and should be always equal or greater than zero. p_b is the vapor pressure of the thermostatic element in the

bulb, acting on the top of diaphragm to open the valve. p_{eq} is the equalization pressure or the evaporating pressure which acts in a closing direction below the diaphragm. $F_{offset} + Ky$ is the spring force also applied underneath the diaphragm in a closing direction, where F_{offset} is contributed by the initial spring deflection preset by the static superheat whereas Ky is contributed by the extra deflection of the spring caused by the additional superheat beyond the initial static superheat.

Once the spring deflection is known, the effective flow area can be calculated based on the internal geometry of the valve. In order to clarify the analysis, important geometry parameters of the valve are defined, as illustrated in Figure 3.6b and Figure 3.6c.

The effective flow area is defined as the minimum free flow area that the refrigerant passes through the valve. It can be observed that the effective flow area is determined by the length of line $\overline{ac}$. It is not difficult to obtain the following expressions given the fact that line $\overline{ac}$ is perpendicular to line $\overline{bc}$

$$
\begin{aligned}
\overline{ab} &= y \\
\overline{oa} &= \frac{d_{ori}}{2\sin\beta} \\
\overline{ac} &= y\cos\beta \\
\overline{oc} &= \frac{d_{ori}}{2\sin\beta} - y\cos\beta
\end{aligned}
\tag{3-31}
$$

Clearly, the effective flow area is the surface area of the truncated cone as shown in Figure 3.6d, and can be calculated as a function of spring deflection

$$
A = \min\left[\pi\left(d_{ori} - \frac{y}{2}\sin 2\beta\right)y\cos\beta, \frac{\pi}{4}\left(d_{ori}^2 - d_{pin}^2\right)\right]
\tag{3-32}
$$

Equation (3-26) is used to determine the mass flow rate through the throttle. When the valve is fully open, the maximum flow rate corresponding to the actual conditions is reached. Manufacturers predict that the maximum flow rate can be between 110% and 140% of the rated flow rate (ASHRAE, 1998). The flow coefficient can be determined either using the condition with the maximum flow rate in the characteristic curve (Figure 3.7) when the valve is fully open or by assuming that the valve is fully open when the maximum mass flow rate is 20% greater than the value of nominal operating conditions (Fu *et al.*, 2003), i.e.

$$C_v = \frac{1}{A_{max}} \left(\frac{1.2\dot{m}}{\sqrt{\rho \Delta p}} \right)_{rated}$$

(3-33)
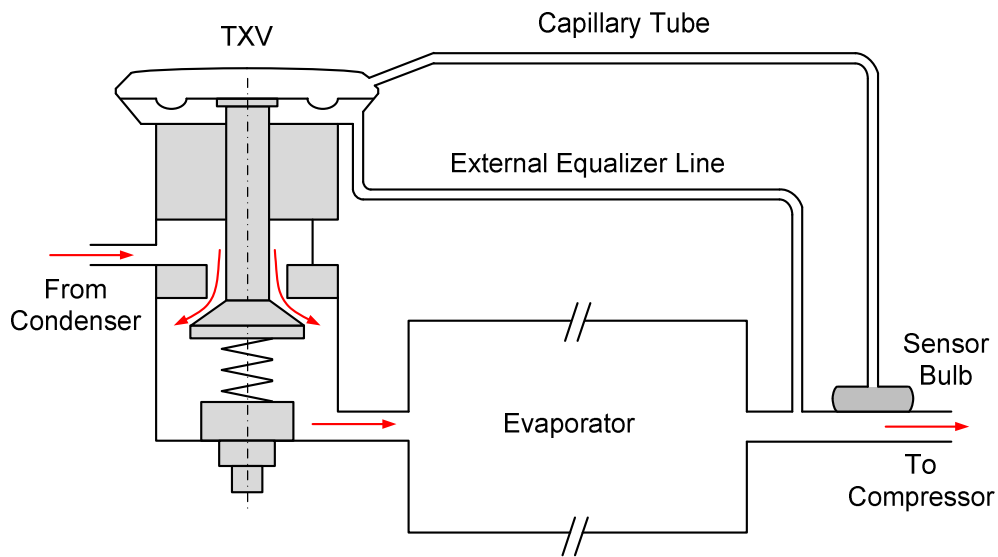
Figure 3.5 Schematic of a TXV with an external equalizer
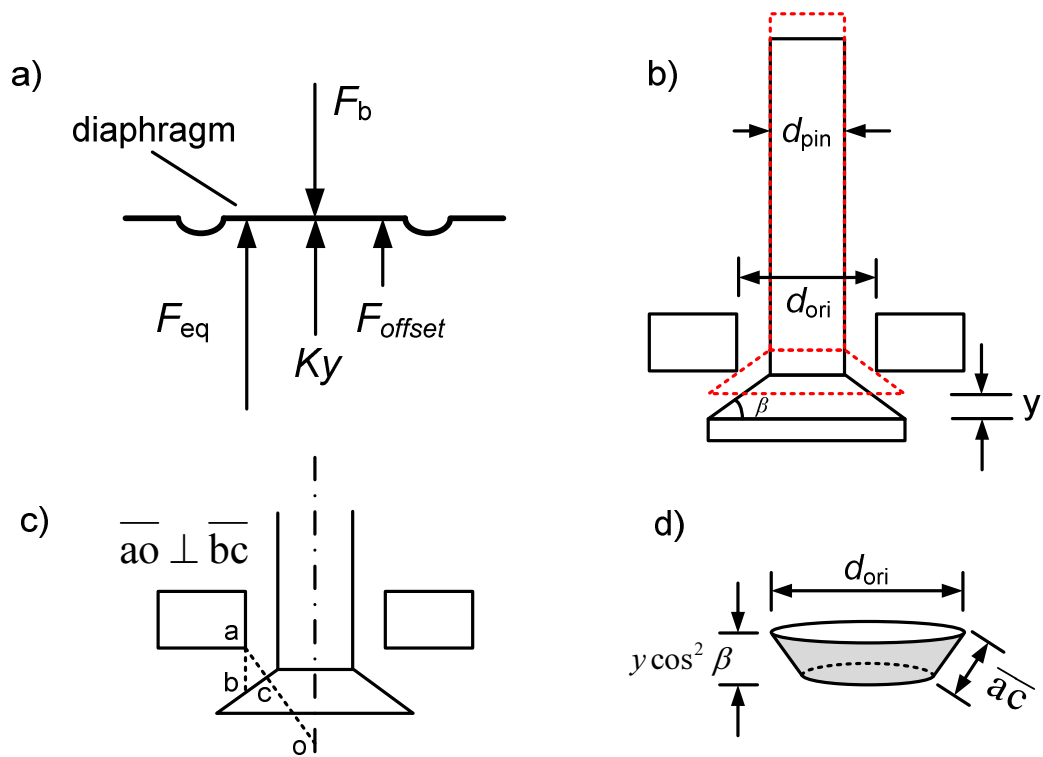
Figure 3.6 a) Force balance on the diaphragm; b) Valve geometry; c) Various lengths; d) Effective flow area
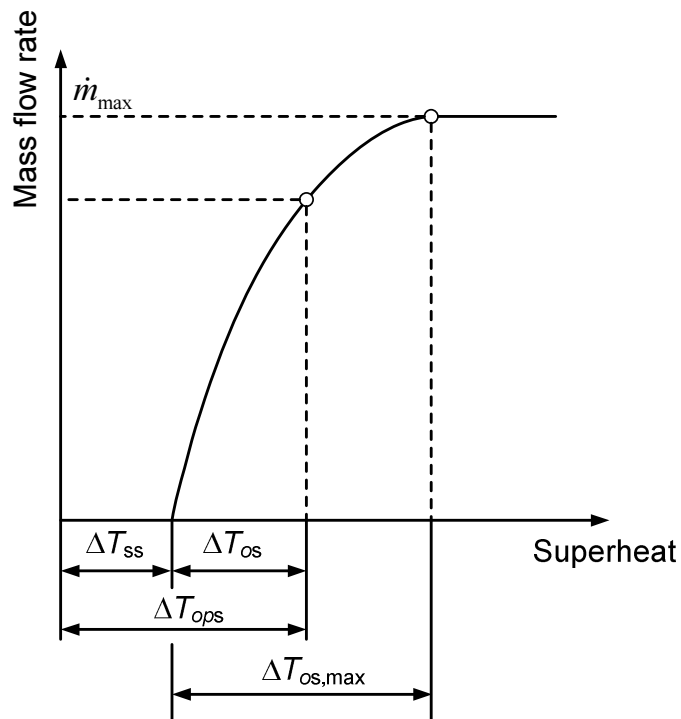
Figure 3.7 Characteristic curve of thermostatic expansion valve

3.3.3 Heat Exchanger Model

Heat exchangers are modeled using a finite volume approach and accounting for the complex tube circuitry. The separated flow model without interfacial exchange is utilized for two-phase flows in order to incorporate an appropriate void fraction model so that a more accurate prediction for refrigerant mass distribution can be achieved. Please refer to Chapter 2 for more details.

3.3.4 Flash Tank Model

The liquid-vapor refrigerant mixture enters the flash tank, separates, and exits as single-phase (Figure 3.8). The flash tank is modeled as a lumped control volume with one inlet and two outlets by adopting the following simplifications:

(1) ideal phase separation;

(2) vapor and liquid in the flash tank are in thermodynamic equilibrium;

(3) pressure drop inside the flash tank is negligible;

(4) adiabatic flash tank.

The governing equations for the flash tank can be described as follows

$$V_{FT} \frac{d\bar{\rho}_{FT}}{dt} = \dot{m}_{in} - \dot{m}_{lo} - \dot{m}_{vo} \tag{3-34}$$

$$V_{FT} \left(\bar{\rho}_{FT} \frac{d\bar{h}_{FT}}{dt} - \frac{dp_{FT}}{dt} \right) = \dot{m}_{in} \left(h_{in} - \bar{h}_{FT} \right) - \dot{m}_{lo} \left(h_{lo} - \bar{h}_{FT} \right) - \dot{m}_{vo} \left(h_{vo} - \bar{h}_{FT} \right) \tag{3-35}$$

The leaving enthalpies of the vapor and liquid streams are dependent on the state of the refrigerant in the flash tank. There are two cases that need to be taken into account: 1) the refrigerant state is two-phase ($h_f < \bar{h}_{FT} < h_g$) and 2) the refrigerant state is single-phase ($\bar{h}_{FT} <= h_f$ or $\bar{h}_{FT} >= h_g$).

Case 1: Leaving enthalpies of two outlet streams are determined as

$$
h_{lo} = \begin{cases} h_f & \text{if } H_{liq} > H_{lo} + d_{liq} \\ h_g - \left(\dfrac{H_{liq} - H_{lo}}{d_{liq}} \right) \left(h_g - h_f \right) & \text{if } H_{lo} + d_{liq} \geq H_{liq} \geq H_{lo} \\ h_g & \text{if } H_{liq} < H_{lo} \end{cases}
$$

$$
h_{vo} = \begin{cases} h_f & \text{if } H_{liq} > H_{vo} + d_{vap} \\ h_g - \left(\dfrac{H_{liq} - H_{vo}}{d_{vap}} \right) \left(h_g - h_f \right) & \text{if } H_{vo} + d_{vap} \geq H_{liq} \geq H_{vo} \\ h_g & \text{if } H_{liq} < H_{vo} \end{cases}
$$

(3-36)

where the liquid height is determined as

$$
H_{liq} = \frac{\overline{\rho}_{FT} - \rho_g}{\rho_f - \rho_g} H_{FT} \tag{3-37}
$$

Case 2: Leaving enthalpies of the two outlet streams should be equal to the mean enthalpy of the refrigerant in the flash tank

$$
\begin{cases} h_{lo} = \overline{h}_{FT} \\ h_{vo} = \overline{h}_{FT} \end{cases} \tag{3-38}
$$

The mass flow rate of the two steams can be calculated by

$$
\begin{cases} \dot{m}_{lo} = \dfrac{\sqrt{\rho_f \left(p_{FT} - p_{lo} \right)}}{f_{liq}} \\ \dot{m}_{vo} = \dfrac{\sqrt{\rho_g \left(p_{FT} - p_{vo} \right)}}{f_{vap}} \end{cases} \tag{3-39}
$$
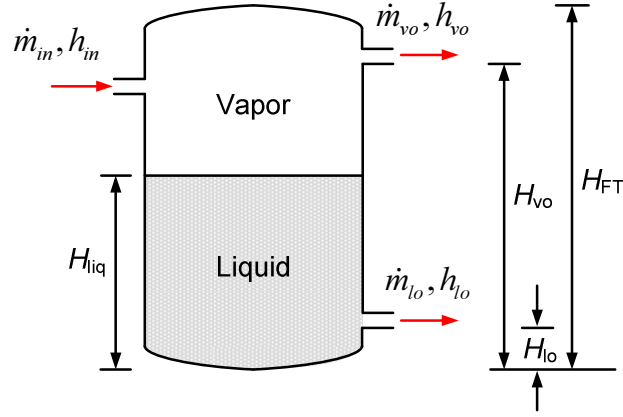
Figure 3.8 Schematic of the flash tank

3.3.5 Reversing Valve Model

The reversing valve is used to switch between cooling and heating in a heat pump system by changing the refrigerant flow direction. In this study, the reversing valve is represented by two control volumes and two pairs of throttles (Figure 3.9). Only one pair of throttles is kept at a full operational position at a time, denoting the on-state, whereas the other pair is operating in a minimum opening position, denoting the off-state. Heat exchange between the hot stream and cold stream is accounted for. The leakage through the pair of closed throttles is also considered.

The conservation of mass and energy for the high-side and low-side control volumes can be analyzed without difficulty by following the analysis for the compressor, and will not be presented here.

The on/off state of the throttles is not changed instantaneously during the transition between cooling and heating mode, the opening of the throttle is assumed to follow the expression below

$$\frac{d\varphi}{dt} = \frac{1}{\tau}\left(\varphi_{\text{target}} - \varphi\right) \tag{3-40}$$

where φ_{target} is the target opening, 100% for the on-state and 0.01% for the off-state.

The mass flow rate through the throttles can be calculated by taking the form of Equation (3-20) with the appropriate density and pressure difference, and finally it needs to be multiplied by the current opening, i.e.

$$\dot{m} = \varphi \frac{\sqrt{\rho_{in} \Delta p}}{f} \tag{3-41}$$

The heat transfer between the hot stream and cold stream is evaluated based on the thermal resistance, i.e.,

$$q_{rev} = \frac{T_{hs} - T_{cs}}{R_{hcs}} \tag{3-42}$$

where R_{hcs} is estimated to be 1.0 K/W based on the measured refrigerant temperature difference across the suction side of the valve under the steady-state operation.

With the proposed reversing valve model, the same integral system model can be utilized to simulate both cooling and heating mode, therefore two separate models are no longer required. This is particularly convenient to model system transients during the reverse cycle defrosting. The proposed model structure allows all the component models to be linked systematically so that two control volumes are not directly coupled without an intermediate throttle during the transition stages between cooling and heating mode.

There are also two three-way valves before the flash tank in the experimental setup to change the refrigerant flow direction, ensuring that the inlet and outlet are not switched in the reversed mode. The reversing valve model, without applying heat exchange, is used to simulate this dual three-way valve configuration in the study.

On

1

From compressor
discharge

To outdoor coil

q_{rev} Off Off

On

2

From
indoor coil

To compressor
suction

a) cooling mode

Off

1

From compressor
discharge

From outdoor coil

q_{rev} On On

Off

2

To indoor
coil

To compressor
suction

b) heating mode

→ hot stream

→ cold stream → heat transfer

⋯→ leakage
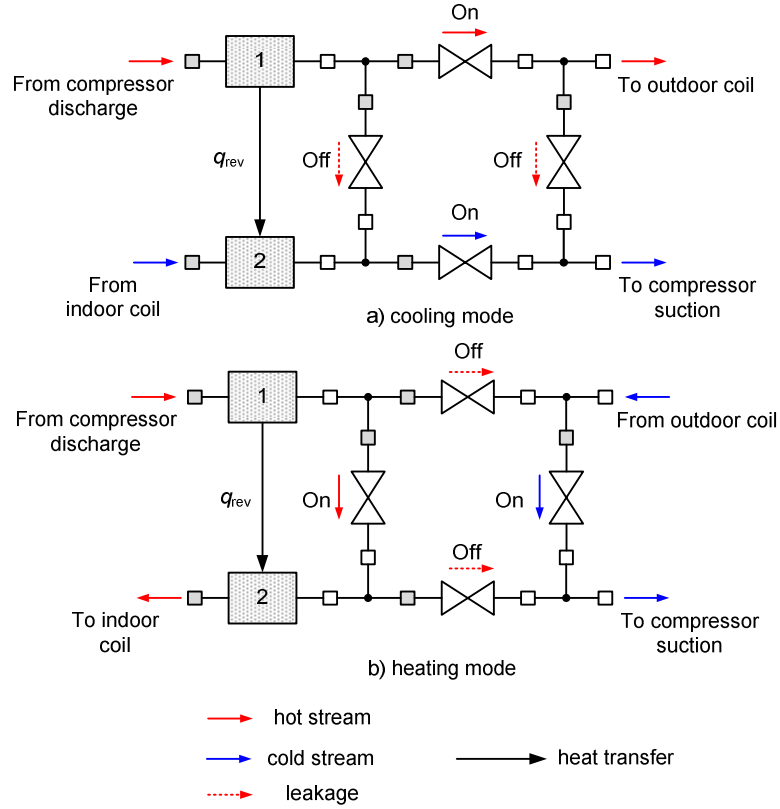
Figure 3.9 Model representation of a reversing valve

3.3.6 Check Valve Model

The check valve is a valve that normally allows fluid to flow through it in only one direction. It is extensively used in heat pump systems to adjust the refrigerant flow direction when switching between heating and cooling mode.

The on/off state of the check valve can be determined by

$$\frac{d\varphi}{dt} = \begin{cases} \dfrac{\varphi_{max} - \varphi}{\tau} & \text{if } \Delta p > \Delta p_{open} \\ \dfrac{\varphi_{min} - \varphi}{\tau} & \text{otherwise} \end{cases} \qquad (3\text{-}43)$$

where φ_{max} is the maximum opening of the valve, i.e., 100%. φ_{min} is the minimum opening of the valve, i.e., 0.01%. The mass flow rate through the valve can be calculated by Eq. (3-41).

3.3.7 Pipe Model

A large portion of refrigerant resides in the connecting pipes, contributing significantly to the transient characteristics of the system. The governing equations for the pipe model are essentially the same as those for the heat exchanger model, except that the air side heat transfer is natural convection. Readers are referred to Chapter 2 for the heat exchanger modeling.

3.3.8 Fan Model

Air pressure rise through the fan can be calculated through a polynomial fan curve, i.e.

$$\Delta p_{rise} = c_0 + c_1 \dot{V} + c_2 \dot{V}^2 + c_3 \dot{V}^3 \tag{3-44}$$

where $c_0 \sim c_3$ are the coefficients reduced by the fan test data.

The fan curve is essential to evaluate the variation in the air flow rate through the outdoor coil during the frosting period, as will be shown in Chapter 4.

3.4 System Model and Implementation

3.4.1 System Model

The system model is formed by combining all the component models (Figure 3.11). The basic elements used to model the refrigerant flow are the control volume and the throttle. Each component model is comprised of an alternative sequence of control volumes and throttles, and always begins with a control volume and ends with a throttle (Tummescheit, 2002). Mass and energy conservation is evaluated within the control volume, whereas the momentum conservation is solved using the throttle.

The inputs to the control volume are defined as the mass flow rate and the enthalpy flow rate entering and exiting the control volume, and the outputs are the

time-varying pressure and enthalpy of the control volume. The enthalpy flow rate is defined as the product of the mass flow rate and the upstream connected flow-weighted enthalpy, e.g.,

$$\dot{H} = \dot{m} h_{upstream} \tag{3-45}$$

The inputs to the throttle are the pressure and enthalpy of the adjacent control volumes connected to the throttle, and the outputs are the mass flow rate and enthalpy flow rate across the throttle.
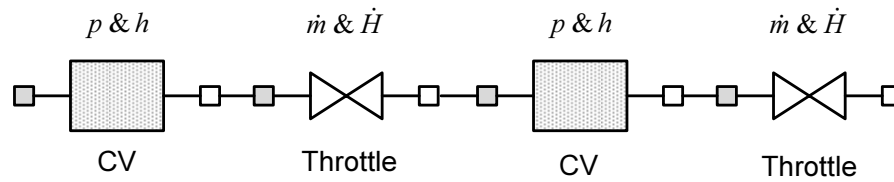
Figure 3.10 Basic modeling elements

Thus, the outputs of the throttle are the inputs to the adjacent control volumes, whereas the outputs of the control volume serve as the inputs to the adjacent throttles. Therefore, each component model has the same boundary conditions, i.e., the upstream connected mass flow rate and enthalpy flow rate, and the downstream connected pressure and enthalpy (note: the downstream connected enthalpy is only used when reverse flows occur). The modular nature of the component models allows flexibility in the system configuration. As a result, the component models can be seamlessly linked together in an arbitrary manner, regardless of whether they are the flow equipment, like the compressors and valves, or the heat transfer equipment, like the heat exchangers.

Three-way valve configuration
Liquid line
Indoor coil
Discharge line
EEV
Injection line
Reversing valve
Flash tank
Compressor
TXV
Outdoor coil
Suction line
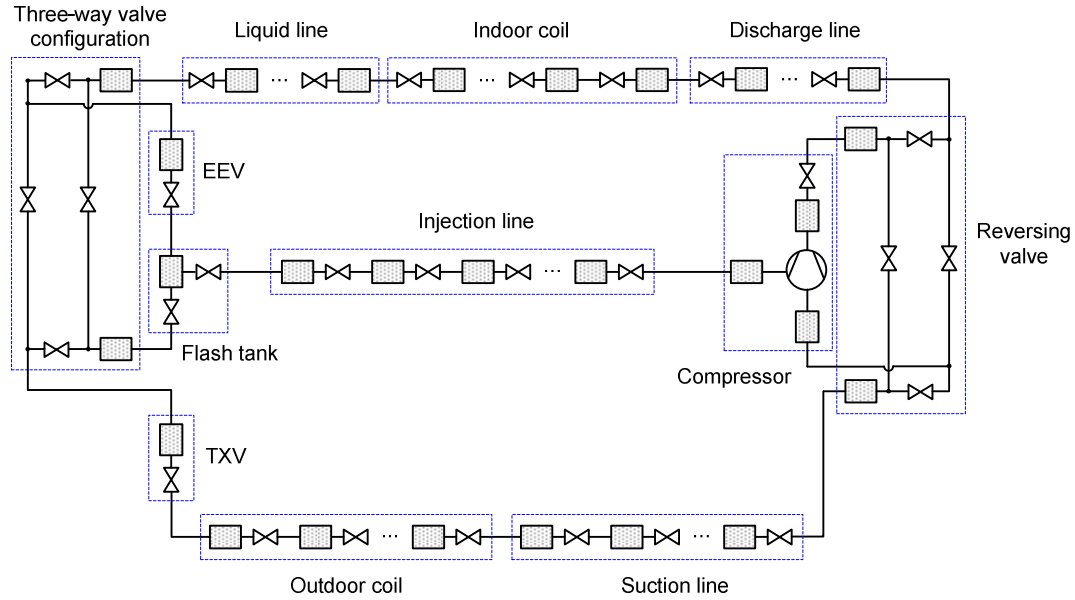
Figure 3.11 Model representation of the refrigerant side of FTVI system

Table 3.2 Correlation summary

Air side	
Heat transfer	
Forced convection - dry condition	Wang *et al*. (1999)
Forced convection - wet condition	Wang *et al*. (2000)
Natural convection	Churchill-Chu (1975)
Pressure drop	
Forced convection - dry condition	Wang *et al*. (1999)
Forced convection - wet condition	Wang *et al*. (2000)
Single-phase	
Heat transfer	Gnielinski (1976)
Pressure drop	Blasius (Incropera & DeWitt, 1996)
Two-phase (condensation)	
Heat transfer	Shah (1979)
Pressure drop	Lockhart-Martinelli (1949)
Two-phase (evaporation)	
Heat transfer	Kandlikar (1990)
Pressure drop	Grönnerud (1979)
Void fraction	Smith (1969)

3.4.2 Implementation

The proposed transinet models are implemented using the Modelica modeling language and the Dymola 7.4 (AB Dassault Systemes, 2014) simulation environment.

All the refrigerant properties are evaluated using in-house curve-fitted property routines, developed based on the REFPROP 9.0 database (Lemmon *et al*., 2010). Empirical correlations are used to calculate the heat transfer coefficients and the pressure drops on both refrigerant side and air side in the models for heat exchangers and pipes (Table 3.2).

3.5 Experimental Facility

3.5.1 Experimental Facility Layout

Figure 3.12 shows the schematic of the test facility of a FTVI cycle, utilizing R-410A as the working fluid. The indoor unit (Figure 3.13) is located within a closed psychrometric loop, and the air is driven by the blower of the air-handling unit. The air flows through the nozzle, which measures the air volume flow rate, and then enters the indoor unit. At the inlet and outlet of the indoor unit, two thermocouple grids, with nine thermocouples each, were installed to measure the inlet and outlet air temperature. Relative humidity sensors were installed to measure the relative humidity of the inlet and outlet air. The outdoor unit (Figure 3.14) was located inside an environmental chamber, where temperature and humidity could be controlled according to ASHRAE Standard 116 (2010). Thermocouples and dew point sensors were installed to measure the outdoor unit inlet and outlet air temperatures and dew points, respectively. Pressure transducers and in-stream thermocouples were installed in the vapor compression system to measure the refrigerant-side pressures and temperatures. Mass flow meters were installed to measure the refrigerant mass flow rates of the injected vapor and liquid through the condenser. Two mass flow meters were installed in the liquid line, and only one mass flow meter was in use during

either cooling or heating mode operations because the mass flow meters were only calibrated with one flow direction. Finally, a watt meter was installed to measure the outdoor unit power consumption.

The heat pump system could be operated in both cooling and heating mode. In the cooling mode, refrigerant was discharged from the compressor and entered the outdoor unit for condensing. After being throttled through the upper-stage expansion valve (2), the refrigerant entered the flash tank; the vapor refrigerant was injected into the compressor whereas the liquid refrigerant entered the lower-stage expansion valve (4), and circulated through the indoor unit. After evaporating from the indoor unit, the refrigerant then entered the suction port of the compressor to complete the closed-loop cycle. In the heating mode, the electrical coil of the four way valve was energized, and therefore, the valve reversed the refrigerant flow direction. The refrigerant exiting the compressor circulated through the indoor unit for condensing, then expanded through the upper-stage expansion valve (2), and entered the flash tank. The vapor refrigerant was injected into the compressor; meanwhile the liquid refrigerant circulated through the lower-stage expansion valve (3), evaporated in the outdoor coil, and then entered the compressor to complete the cycle.

3.5.2 Major Component Description

The compressor used in the experimental study was a vapor-injected scroll compressor. It had a constant speed of 3500 RPM with a displacement of 29.5 cm^3. The system could be operated either with or without vapor injection by controlling an injection control valve (1) located in the vapor injection line. The vapor injection control valve was installed close to the compressor in order to minimize the re-expansion of compressed vapor trapped between the control valve and injection port

of the compressor. The specifications of the outdoor and indoor heat exchangers are shown in Table 3.3. The schematic of the circuitries of both coils are shown in Figure 3.15. The upper-stage expansion valve utilized in the system was an EEV controlled by an electric stepper motor with 500 steps from closed to fully open, and the lower-stage expansion valve was a thermostatic expansion valve with a nominal cooling capacity of 14-21 kW. Figure 3.16 shows the flash tank used in the experimental study. It is a cylindrical vessel equipped with a flash visualization window.

Table 3.4 shows the specifications of the flash tank. To better measure the liquid level inside of the flash tank, a capacitance liquid level sensor was utilized. The liquid level sensor was inserted into the flash tank, connected by an NPT fitting at the top of the tank, which is shown in Figure 3.17. The liquid level sensor measured the liquid level inside of the flash tank by determining the capacitance difference between the submerged section in the liquid and the section exposed to the vapor. The purpose of measuring the liquid level is to better analyze liquid level variations at different operating conditions. The flash tank was insulated during the test, with only the visualization section exposed to the ambient environment.

All measuring instruments were calibrated before the experimental tests. Table 3.5 summarizes the instrumentation and propagated uncertainties in the experimental study. Both air-side and refrigerant-side capacities were determined and recorded during the tests. Energy balance between air side and refrigerant side is calculated by

$$EB = \frac{q_r - q_a}{q_r} \tag{3-46}$$

Figure 3.18 summarizes the air-side and refrigerant-side steady-state energy balances. All energy balances were within ±6% according to ASHRAE Standard 37 (2009).

3.5.3 Experimental Facility Operating Conditions

ASHRAE 116 (2010) prescribes the test condition for transient heating test, and this test condition (Table 3.6) was used for experimental validation.
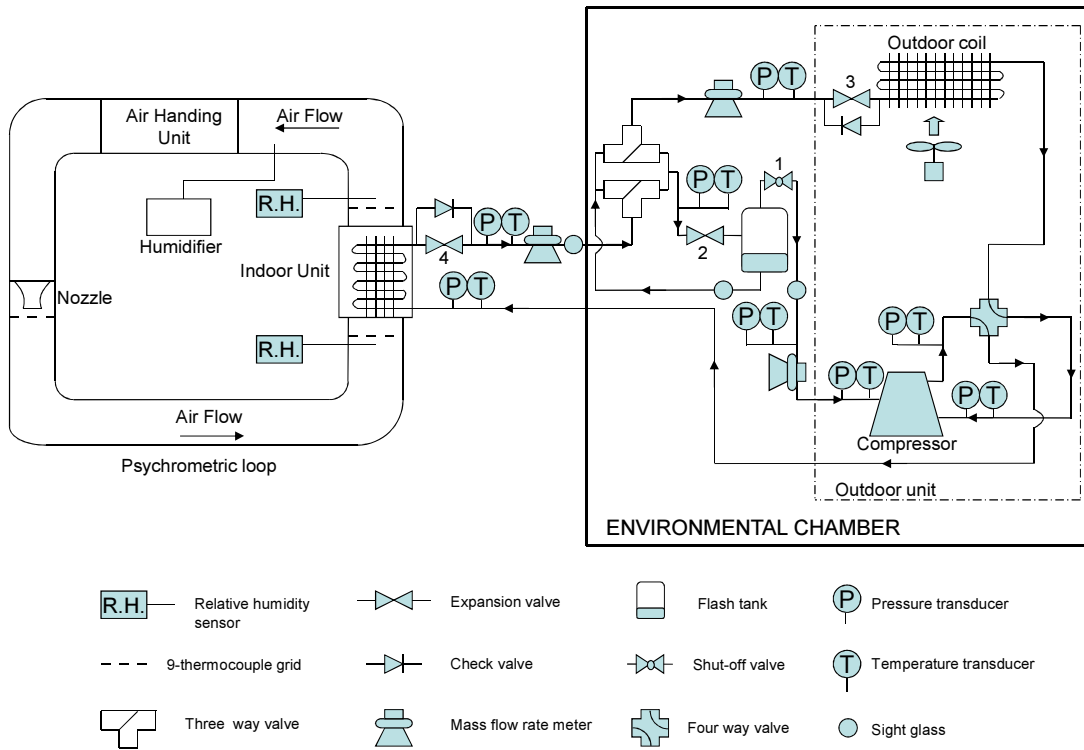
Figure 3.12 Schematic of the flash tank vapor injection heat pump system (heating mode operation)

Figure 3.13 Indoor unit of FTVI heat pump system

Figure 3.14 Outdoor unit of FTVI heat pump system

Table 3.3 Specifications of the outdoor and indoor heat exchangers

Parameter	Unit	Outdoor Coil	Indoor Coil
Tube length	mm	2,565	483
Tube outer diameter	mm	7.9	9.5
Tube wall thickness	mm	0.8	0.8
Tubes per row	-	32	26
Number of rows	-	2	3
Coils in parallel	-	1	2
Tube horizontal spacing	mm	15.7	25.4
Tube vertical spacing	mm	24.1	25.4
Fins per inch	-	22	12
Fin thickness	mm	0.1	0.1
Fin type	-	Louver fin	Louver fin

(a) Indoor coil   (b) Outdoor coil
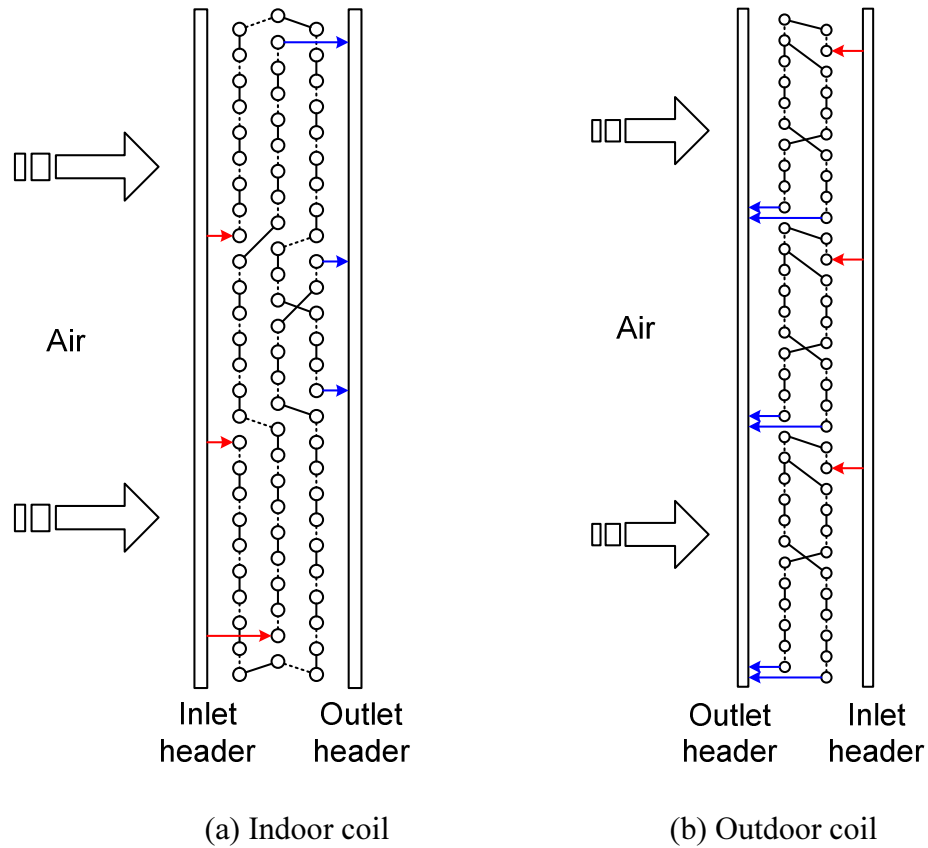
Figure 3.15 Schematic of the heat exchangers in the heating mode
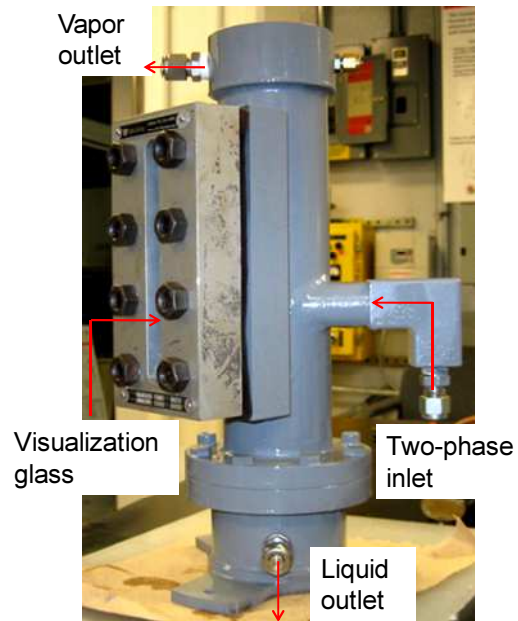
Figure 3.16 Flash tank used in the experimental study
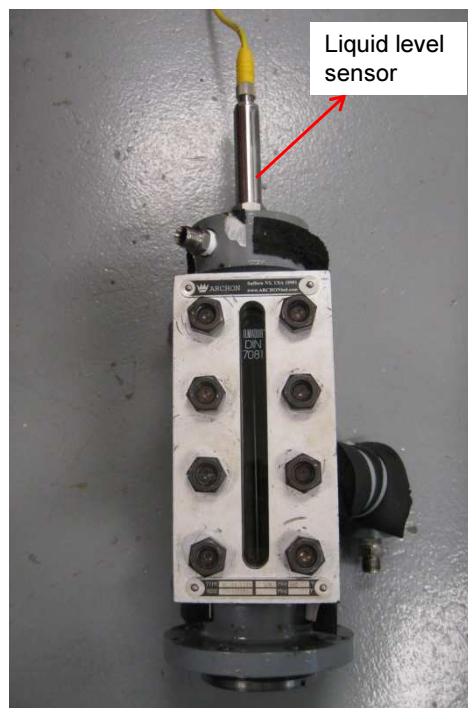
Figure 3.17 Flash tank with the liquid level sensor installed

Table 3.4 Specifications of the flash tank

Parameter	Unit	Dimension
Flash tank height	m	0.32
Diameter	m	0.07
Flash tank volume	m^3	0.001
Sight glass height	m	0.15

Table 3.5 Instrumentation and propagated uncertainties of the experiments

Manufacturer	Instrument and Calculated Parameter	Uncertainty
Omega Engineering, Inc.	T type thermocouple (range: -200 - 350ºC)	±0.5ºC
Setra Systems, Inc.	Pressure transducer (range: 0 - 3,447 kPa)	±3.79 kPa
WIKA, Inc.	Pressure transducer (range: 0 - 6,895 kPa)	±8.62 kPa
Vaisala	Relative humidity sensor (range: 0% - 100%)	±1.0%
General Eastern	Dew point sensor (range: -80 - 95ºC)	±0.2ºC
Micro Motion, Inc.	Mass flow meter (range: 0 - 100 g s^{-1})	±0.2% of flow rate
Ohio Semitronics, Inc.	Watt meter (range: 0 - 5 kW)	±0.5% of full scale
N/A	Refrigerant-side capacity	±0.6% of calculated value
N/A	Refrigerant-side COP	±1.1% of calculated value
N/A	Air-side capacity	±6.5% of calculated value
N/A	Air-side COP	±6.6% of calculated value
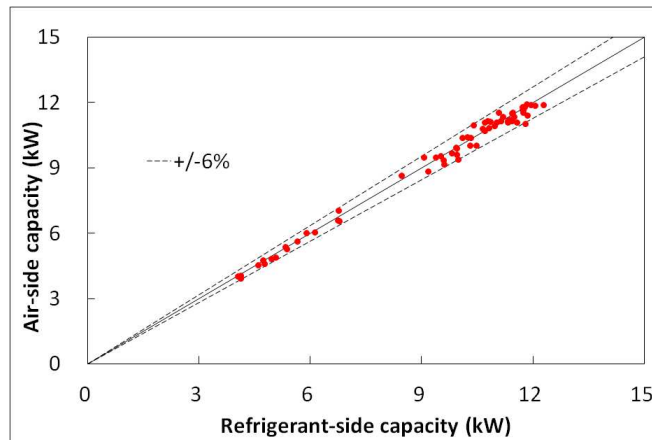
Figure 3.18 Steady-state energy balances of the experiments

Table 3.6 Test conditions

ASHRAE Condition	Indoor Dry Bulb [°C]	Indoor Wet Bulb [°C]	Outdoor Dry Bulb [°C]	Outdoor Wet Bulb [°C]
High Temp 2	21.1	≤15.6	8.3	6.1

3.6 Simulation Results and Experimental Validation

3.6.1 Experimental Results Description

The vapor injection system was activated, and the upper-stage EEV maintained an opening fraction of 18%. As the system reached steady-state operation (after 2200 seconds), the EEV opening fraction was increased from 18% to 20%, 25% and 28%, respectively, with a corresponding time interval of 600 seconds, 900 seconds, and 1100 seconds, respectively. Then, the EEV opening fraction decreased to 18%. At 6000 seconds, the system was powered off. All the relevant system parameters were recorded through a data acquisition system in order to validate the simulation results.

3.6.2 Model Inputs and Initial Conditions

In the present study, only the heating mode was considered, and a frost-free operating condition was chosen. The cooling mode could be simulated using the same model without requiring modifications. The model inputs for the simulation are summarized in Table 3.7.

The initial conditions (Table 3.8) represent the state of the studied FTVI system after it has been shut down for 24 minutes, when it had been previously running for about one hour. Based on the pressure and temperature measurements in the experiment, we can determine the state of refrigerant in each component before the system is turned on again, i.e., vapor, liquid, or two-phase. The refrigerant is in single-phase in most components, except the flash tank and the outdoor coil. The

refrigerant mass in these components and flash tank (the height of the refrigerant liquid can be measured) can be readily determined. However, the refrigerant mass in the outdoor coil cannot be determined by directly subtracting the refrigerant mass in all the other components from the real system charge (please refer to Section 3.7 for further explanation). Instead, it needs to be adjusted in order to match the calculated steady-state pressures to the measured pressures.

Table 3.7 Model inputs

Parameter	Units	Value
Compressor		
Motor speed	RPM	3500
Built-in volume ratio of 1st stage	-	1.21
Polytropic index	-	1.35
Motor efficiency	-	0.90
Mechanical efficiency	-	0.95
Fraction of shaft friction loss	-	0.85
Discharge pressure loss coefficient	-	1.0e4
Indoor coil		
Air mass flow	kg s^{-1}	0.70
Inlet air temperature	°C	21.1
Relative humidity	-	48%
Outdoor coil		
Air mass flow	kg s^{-1}	1.18
Inlet air temperature	°C	8.3
Relative humidity	-	75%
TXV		
Flow coefficient	-	0.50
Bulb time constant	s	150
Reversing valve		
Thermal resistance	K W^{-1}	1.0
Pressure loss coefficient	-	8.0e3
Flash tank		
Vapor stream pressure loss coefficient	-	5.9e4
Liquid stream pressure loss coefficient	-	3.6e4
Heater power	W	60

Table 3.8 Initial conditions of the model

Parameter	Units	Value
System pressure	kPa	1137.0
Compressor		
Upper shell temperature	°C	25.0
Lower shell temperature	°C	25.0
Motor temperature	°C	25.0
Shaft temperature	°C	25.0
Scroll temperature	°C	25.0
Suction chamber density	kg m^{-3}	41.9
Discharge chamber density	kg m^{-3}	40.8
Indoor coil		
Refrigerant density	kg m^{-3}	41.2
Tube wall temperature	°C	21.0
Outdoor coil		
Refrigerant density	kg m^{-3}	677.0
Tube wall temperature	°C	10.0
Flash tank		
Refrigerant density	kg m^{-3}	783.5
TXV		
Sensor bulb temperature	°C	8.3
Suction line		
Refrigerant density	kg m^{-3}	42.9
Tube wall temperature	°C	18.0
Discharge line		
Indoor portion		
Refrigerant density	kg m^{-3}	41.2
Tube wall temperature	°C	21.0
Outdoor portion		
Refrigerant density	kg m^{-3}	43.1
Tube wall temperature	°C	8.3
Liquid line		
Indoor portion		
Refrigerant density	kg m^{-3}	43.6
Tube wall temperature	°C	21.0 – 10.0
Outdoor portion		
Refrigerant density	kg m^{-3}	65.6 – 1124.9
Tube wall temperature	°C	10.0
Injection line		
Refrigerant density	kg m^{-3}	44.0
Tube wall temperature	°C	8.3

3.6.3 Start-up Transients

It is difficult to obtain the actual compressor speed from the experimental measurement, so the following ramp expression is used to regulate the compressor speed for the start-up simulation

$$\frac{d\varpi}{dt} = \frac{\varpi_{nom} - \varpi}{\tau}$$

(3-47)

where ϖ_{nom} is the nominal compressor speed, ϖ is the current compressor speed, and τ is the time constant. Here $\tau = 3$ seconds.

In order to avoid any undesirable complications caused by the controller, the start-up simulation was conducted by fixing EEV opening at 18%, determined by the results from the previous experiments with the controller enabled. Before the compressor is activated, the entire system is in pressure equilibrium. The simulation lasts for 1000 seconds and the pertinent outputs are shown in Figure 3.19.

Suction, discharge, and intermediate pressure transients are shown in Figure 3.19a. The system takes about 10 minutes to attain the steady-state operation. Within the first two minutes, the discharge pressure increases rapidly, then gradually slows down the ascending trend and finally levels off. The surge in the discharge pressure is mainly attributed to the imbalance between the mass flow entering and leaving the condenser, and to the delayed condensation of the refrigerant. Immediately following the compressor start-up, the refrigerant is pumped into the condenser from the low side. However, the mass flow through the upper-stage EEV is not enough to offset the refrigerant flow entering the condenser because it needs time to establish a significant pressure difference across the EEV. Additionally, it takes some time for the condenser to produce enough liquid to supply the EEV with single-phase liquid

99

instead of the two-phase mixture or superheated vapor. As a result, the refrigerant accumulates inside the condenser and causes a rapid increase in pressure. Eventually, the accumulation of refrigerant in the condenser reaches its steady-state amount and a stable pressure level can be achieved.

The suction pressure declines in the first three minutes and increases slowly thereafter. The decrease in the suction pressure is caused by the depletion of refrigerant from the evaporator since the TXV is closed at the very beginning due to the two-phase refrigerant flow exiting the evaporator. At the same time, the two-phase refrigerant inside the evaporator absorbs heat from the air and is vaporized. Until the actual superheat at the evaporator outlet is greater than the static superheat of the TXV, the valve cannot be opened to feed the evaporator with the refrigerant from the flash tank. The suction flow rate decreases thanks to a reduction in the suction density and an increase in the compressor pressure ratio. After the feeding flow from the TXV surpasses the suction flow, the suction pressure starts reaching its steady-state value.

The trend in variation in the intermediate pressure is almost synchronized with that in the suction pressure. However, it increases along with the discharge pressure at the very beginning as a consequence of the backflow from the compressor to the flash tank through the economizer port. Due to the insufficient supply of refrigerant from the EEV within the first three minutes, the intermediate pressure continues to decrease until a dip is experienced. The subsequent recovery can be attributed to the surplus flow from the EEV when a larger pressure difference across the valve is established.

The pressure transients can be further clarified by examining the variations in mass flow rates (Figure 3.19b). The injection flow and the EEV flow are negative right after compressor start-up, representing reverse flow.

Compared to the discharge pressure, the transients of the intermediate and suction pressures are less varied because their steady-state values are much closer to the initial system pressure. The steady-state values of the suction, intermediate and discharge pressures are 732kPa, 1220kPa and 2770kPa, respectively.

Figure 3.19c shows the temperature transients after the compressor start-up. The discharge temperature rises quickly in the first three minutes and then plateaus until it reaches 90°C after 10 minutes. The suction temperature drops quickly for the first minute and subsequently recovers to its steady-state value, i.e., 8 °C. The temperature decrease is associated with the reduced suction pressure and can be attributed to the two-phase refrigerant initially flowing into the suction chamber of the compressor. The subsequent temperature rise is attributed to the heat gain from the air. The injection temperature follows a similar trend to the suction temperature, and eventually maintains a temperature of 19°C. Given the fact that the heat transfer from the electrical heater (constant power input of 60W) to the vapor line of the flash tank, and then to the refrigerant flow inside the pipe, is difficult to determine, the deviation between the predicted and measured injection temperatures for the 100 to 200 seconds interval is acceptable.

Figure 3.19d indicates that there is no suction superheat during the first 40 seconds. It also validates that the two-phase refrigerant gets transferred to the suction chamber of the compressor, and the remaining liquid in the evaporator coil requires

101

some time to completely vaporize. The superheat quickly increases to a value of 14K after around 150 seconds, and then it gradually drops and stabilizes at around 10K. The overshoot of the superheat can be attributed to the thermal inertia of the sensor bulb of the TXV. The discrepancy of the steady-state superheat between the predicted and measured value is about 0.7K. Although the simulation is unable to predict the overshoot of the injection superheat at around 150 seconds, the steady-state superheat of 4K coincides with the measurement. The cause for the discrepancy is the inaccurate estimation of heat transfer from the electrical heater, as previously mentioned. The condenser does not exhibit subcooling during the first 30 seconds due to the delayed condensation, but finally the subcooling stabilizes at around 9K.

Figure 3.19e illustrates the variation in air side heat load of both heat exchangers and compressor power consumption. The air side heat load of the condenser rises rapidly within the first two minutes, and then gradually approaches the steady-state value of around 10kW after 10 minutes. However, a small hump around 100 seconds is observed in both simulation and experiment. Careful inspection of the results indicates that at the beginning of start-up a large portion of the condenser coil is in the desuperheating region and the coil is heated up within a short period of time. Consequently, the average temperature difference between the coil surfaces and the air stream is relatively large, leading to an anticipated maximum heat rejection from the condenser to the air stream. Once the desuperheating portion diminishes, the average temperature difference declines, so does the heat rejection. After the hump, the heat rejection continues to increase because the condenser coil needs to condense more refrigerant. Similar phenomena were reported in both

Murphy & Goldschmidt (1984) and MacArthur (1984). The hump for the evaporator heat absorption is due to the maximum average temperature difference between the coil surfaces and the air stream when the suction pressure hits the lowest value.

Figure 3.19f depicts the refrigerant charge distribution after start-up. Before start-up, a large amount of refrigerant resides in the evaporator, whereas very little refrigerant, mainly superheated vapor, is stored in the condenser. After the compressor starts up, the refrigerant is pumped into the condenser, which eventually holds more than 50% of the total charge, while the evaporator holds less than 10%. Meanwhile, only 3% of the total charge is left in the flash tank during on-cycles, which is consistent with the liquid level in the flash tank. The refrigerant liquid in the flash tank drains quickly after start-up, and maintains a very low level thereafter, which was confirmed during the experiment as well. Bubbles were also observed through the sight glass on the liquid line of the flash tank during the steady-state operation. This is a result of the upper-stage EEV not being optimized during the test, indicating that the liquid level is not high enough to effectively separate the vapor from the liquid-vapor mixture, and therefore the potential to optimize the intermediate pressure and improve system performance still exists. The simulation shows that a substantial amount of refrigerant is stored in the pipes, more than 30% in this case. Given the overall internal volume of the piping that connects the various components located in two separate chambers, the number is not that surprising. This also reaffirms the significance of including the connecting pipes in the simulation.
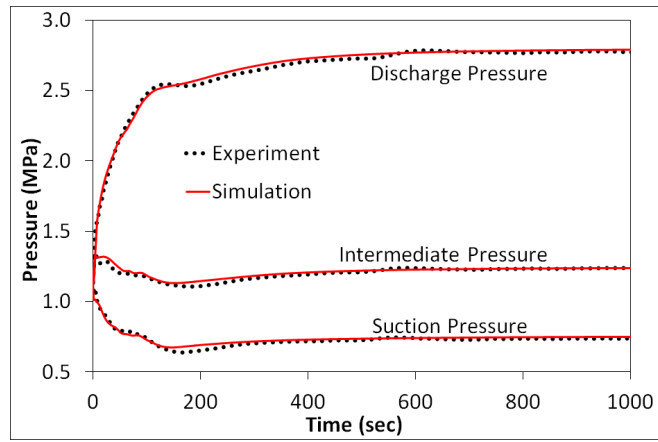
(a)
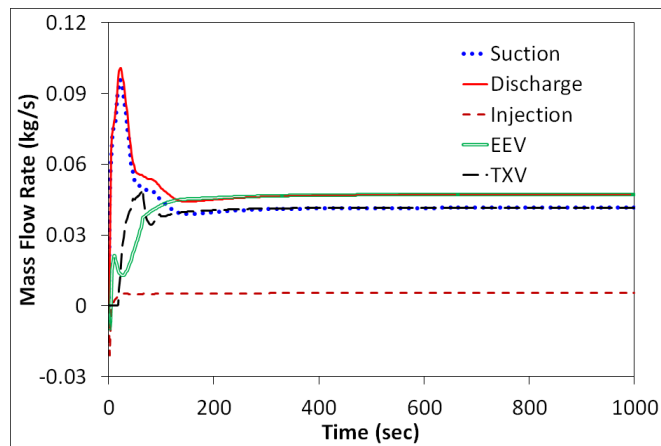
(b)
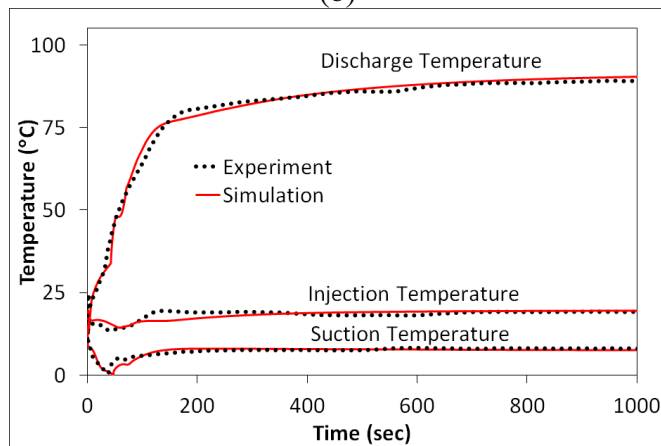
(c)
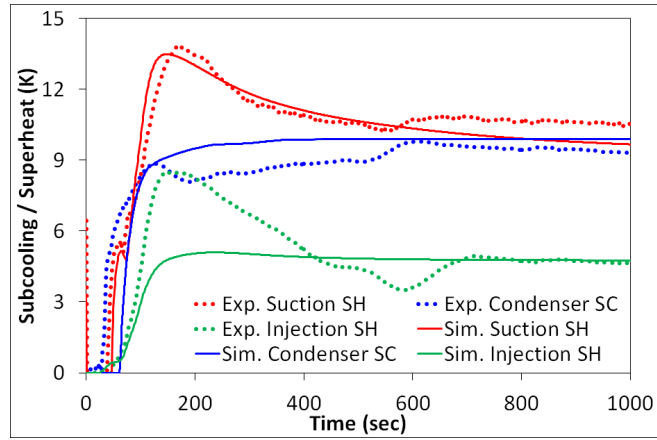
(d)
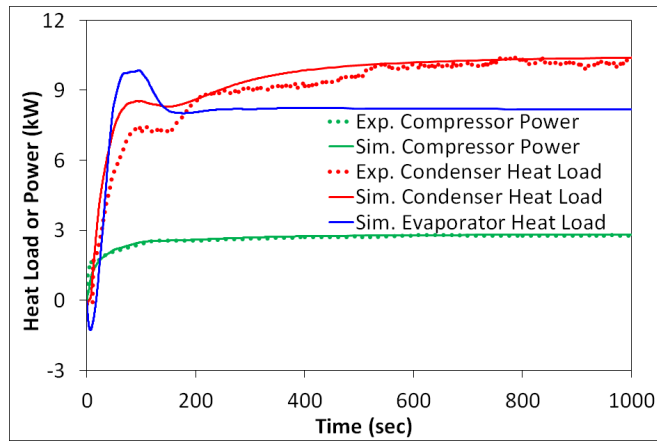
(e)
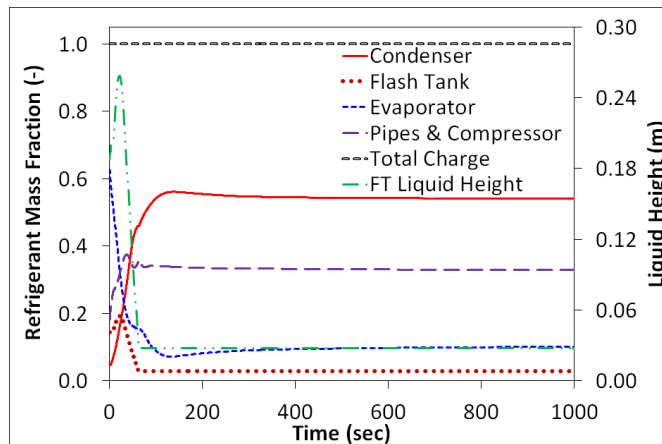
(f)

Figure 3.19 Start-up transients: (a) - Pressure response; (b) - Simulated refrigerant mass flow response; (c) - Temperature response; (d) - Superheat and

subcooling response; (e) – Air side heat load and compressor power response; (f) - Simulated refrigerant mass distribution and flash tank liquid height

3.6.4 Shut-down Transients

The system shuts down after running for 100 minutes. Figure 3.20a shows the response of pressures after the compressor shut-down. It takes approximately 10 minutes for the entire system to reach the pressure equilibrium. The discharge pressure drops immediately following the compressor shut-down due to the absence of refrigerant flow into the condenser, whereas the refrigerant in the condenser continues flowing out into the flash tank through the upper-stage EEV.

The refrigerant in the flash tank would migrate to the low side via two flow paths. The first path begins at the vapor line of the flash tank, through the economizer port of the compressor, and arrives at the suction chamber of the compressor and the evaporator (Please note that the solenoid valve on the vapor line of the flash tank is kept open). The second path is from the liquid line of the flash tank, through the TXV, to the evaporator. The low-side pressure increases as a result of refrigerant migration from the flash tank. The refrigerant migration primarily occurs through the first flow path because the TXV is closed shortly after the compressor shuts down. The intermediate pressure decreases within the first minute because of the shortage of the refrigerant supply from EEV. Since the pace of refrigerant migration from the flash tank to the low-side slows with the diminishing pressure difference, the intermediate pressure gradually increases. After 10 minutes, all the pressures converge to 1270kPa. During the operation, the evaporator operates below ambient temperature. After the unit is turned off, the evaporator coil temperature rises above the ambient temperature due to the energy stored in the refrigerant that migrates to the

evaporator. As a result, the equalized pressures continue to decrease because of the continuous heat dissipation from the refrigerant in the evaporator to the ambient. If the simulation runs long enough, eventually the final system pressure should plateau at the saturation pressure corresponding to the ambient temperature of the evaporator.

Figure 3.20b shows the response of the various mass flow rates after shut-down. Observations show that the refrigerant flow through the compressor suction becomes negative after the compressor shuts down, denoting refrigerant migration from the suction chamber of the compressor to the evaporator. Since the two-phase flow might be experienced during the period, the measured refrigerant flow exhibits fluctuations. Overall, the simulation results agree with the measurements fairly well, given all the challenges of simulating off-cycles.

Figure 3.20c shows the refrigerant charge distribution after compressor shut-down. The trends show that approximately 60% of the total charge migrates to the coldest location, i.e., the evaporator. The flash tank is almost filled with refrigerant liquid during off-cycles, accounting for more than 20% of the total charge, which conforms to our observation during the experiment. The shut-down simulation results can be used to determine the mass distribution for start-up simulation.

3.6.5 Step Change in Upper-stage EEV Opening

An FTVI system is inherently more difficult to control compared to the conventional systems since a proper liquid level needs to be maintained in the flash tank during the operation (Xu *et al*., 2011a). The efficiency of phase separation will deteriorate if too much or too little liquid exists in the flash tank. During the experiments, it was found that the opening of upper-stage EEV has a significant impact on system performance and the liquid level in the flash tank. In an attempt to

develop a control algorithm for the degree of injection superheat, several simulations are conducted to inspect the system response subjected to step changes in the EEV opening.

Starting from the steady-state operation, the EEV opening was changed from 18% to 20%, then to 25%, and finally to 28% (Figure 3.21a). Figure 3.21b shows the dynamic pressure response as a result of the variations in EEV opening. When EEV opening increases to 28%, the discharge pressure decreases by 350 kPa, whereas the intermediate pressure increases by 150 kPa. An increase in EEV opening results in more refrigerant flowing through the valve, and the pressure ratio must decline in order for the compressor to deliver higher refrigerant flow. However, the suction pressure is nearly stable when EEV opening is adjusted. This indicates that a moderate EEV adjustment has very little effect on the suction pressure.

The dynamic behavior of refrigerant mass flows is shown in Figure 3.21c. Clearly, the refrigerant flow leaving the condenser shows a more aggressive variation compared to both injection and suction flow, increasing from 0.048 kg/s to 0.055 kg/s. The fluctuations in the measured mass flow leaving the condenser indicate possible bubble entrainment of the flow through the mass flow meter when EEV opening increases to 28%, since no substantial subcooling is observed in this case.

Figure 3.21d shows the temperature transients. The discharge temperature decreases considerably, from 90 °C to 75 °C due to the decline in the compressor pressure ratio, whereas suction and injection temperatures display minor variations. The discrepancy between the measured and predicted discharge temperatures shows that there is room for improving the compressor model, but the overall prediction is

acceptable. Surprisingly, the predicted injection temperature reveals a trend opposite to that of the measurements when increasing EEV opening from 20% to 25%. This is attributed to the simplified modeling assumption of perfect phase separation in the flash tank model. However, this assumption may not be valid if a distinct and stable phase interface does not exist, especially when the incoming high-speed refrigerant flows into the flash tank and violently impinges the liquid inside it. In this case, there might be liquid droplets entrained in the injection flow that lower the injection temperature.

Figure 3.21e displays the dynamic behavior of injection superheat and suction superheat, as well as condenser subcooling. The slow decrease in condenser subcooling is attributed to the increased refrigerant flow and the reduced temperature potential between the air and the refrigerant. The measurement shows that there is still 1 K subcooling when EEV opening is at 28%, but it is considered as a measurement error since the simulation shows that the refrigerant already leaves as two-phase. As a result of EEV opening enlargement, the injection superheat and suction superheat decline from 4 K to 1.5 K and from 10 K to around 6.5 K, respectively. Although the exact oscillations that the measured injection superheat and suction superheat exhibit could not be predicted, the simulation results show similar trends.

Figure 3.21f illustrates the dynamic response of heat load and compressor power. The air side heat load of both heat exchangers increases due to the augmented refrigerant mass flow rate. The compressor power declines due to the reduced compressor pressure ratio.

Figure 3.21g reveals the impact of EEV opening on the refrigerant charge distribution and the liquid level in the flash tank. It appears that a significant amount of refrigerant migrates to the flash tank, accounting for 12% of the total charge, compared to only 3% before EEV opening adjustment. When increasing EEV opening, the condenser subcooling decreases along with the refrigerant mass stored in the condenser. As a consequence, the surplus refrigerant mass will be distributed between the flash tank and the evaporator. This phenomenon was verified by observing the increase in the liquid level of the flash tank during the experiment.

(a)

(b)

110
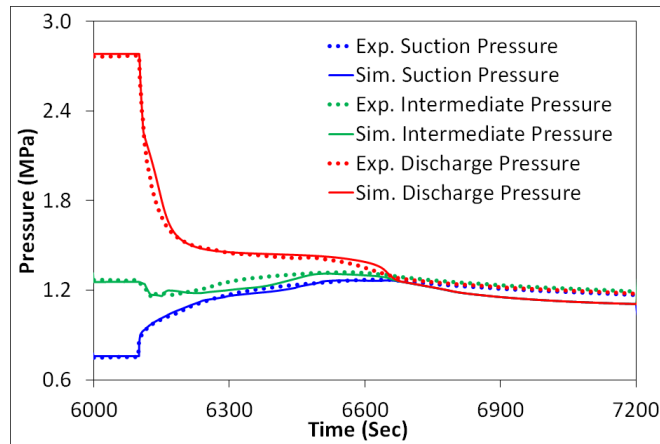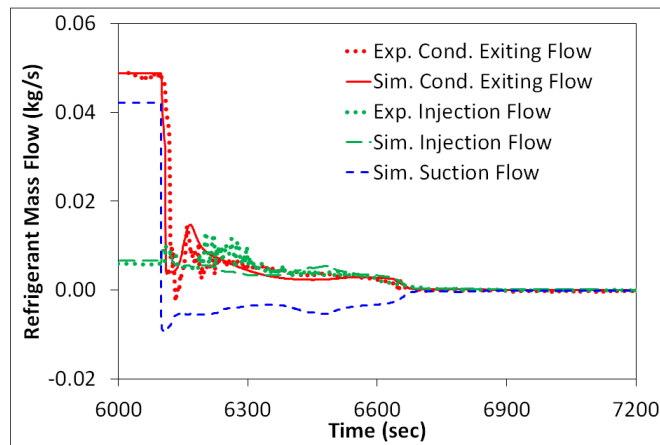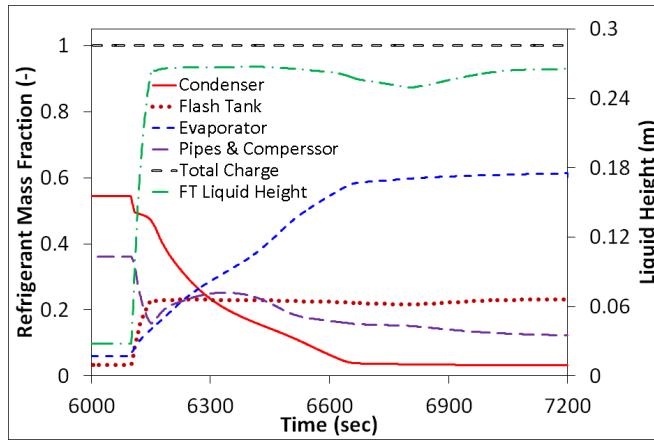
(c)

Figure 3.20 Shut-down transients: (a) - Pressure response; (b) - Refrigerant mass flows; (c) - Simulated refrigerant mass distribution and flash tank liquid height

(a)

(b)

111

(c)

(d)

(e)

112
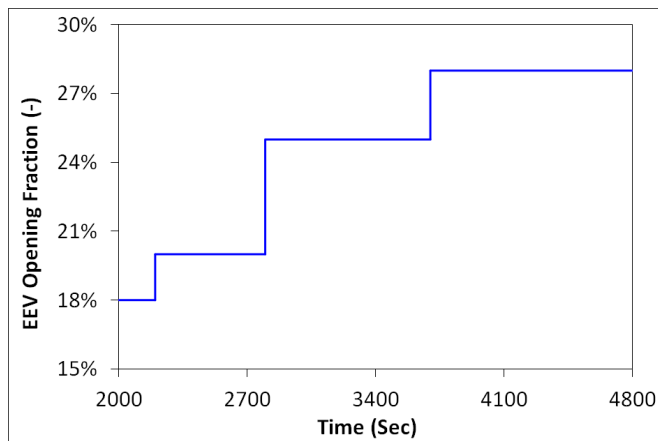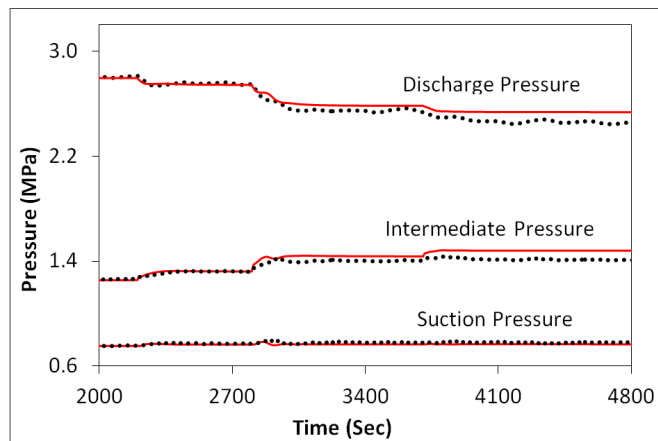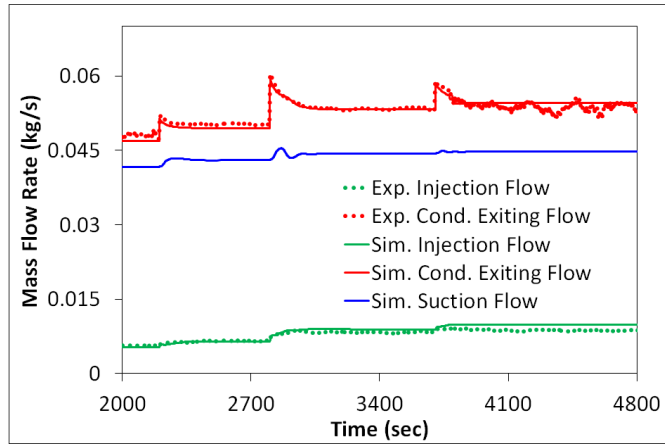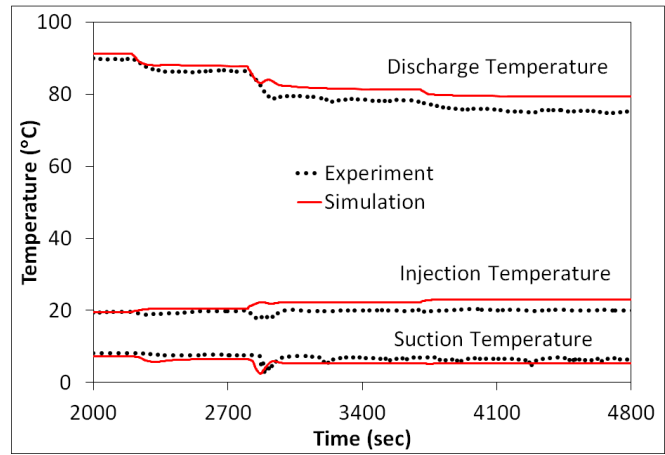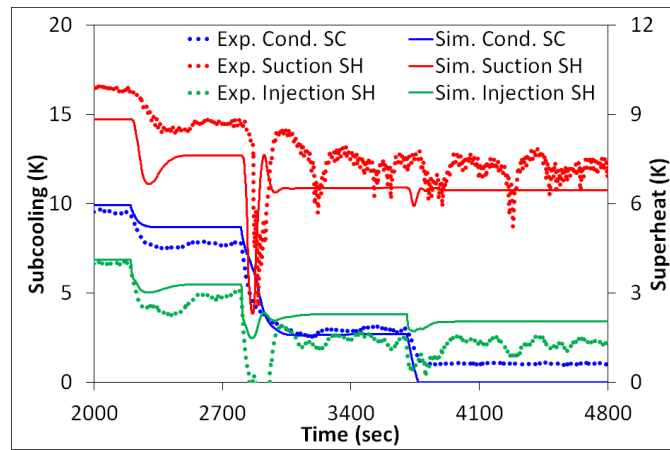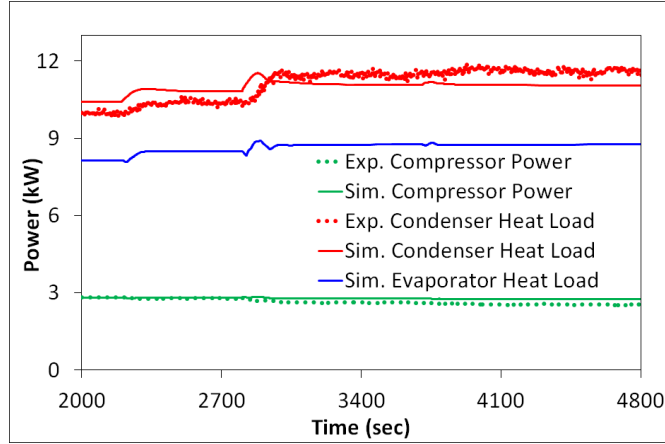
(f)
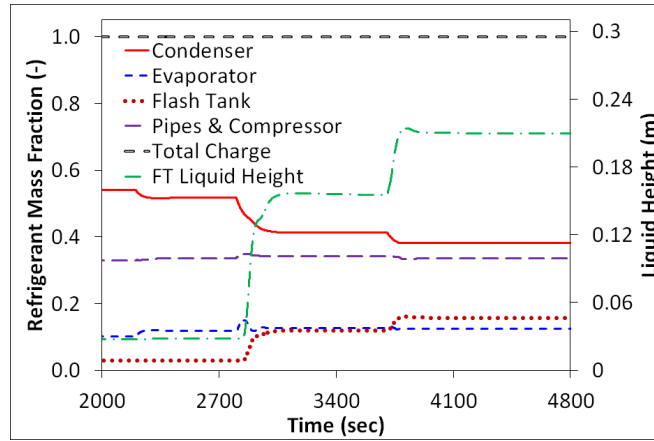
(g)

Figure 3.21 Step change transients: (a) - Step changes in upper-stage EEV opening; (b) - Pressure response; (c) - Mass flow response; (d) - Temperature response; (e) - Superheat and subcooling response; (f) – Air side heat load and compressor power response; (g) - Simulated refrigerant mass distribution and flash tank liquid level

3.7 Discussions

Overall, the comparison between the simulation results and the measurements correspond well and demonstrate that the proposed transient model is capable of describing the heat transfer and flow phenomena of FTVI systems. However, many challenges were encountered in this study. The authors also believe that these challenges are experienced by other researchers as well when conducting similar

113

studies. This paper does not intend to provide solutions to these challenges, but instead aims at stimulating discussions for future research.

(1) Charge estimation: Charge estimation is always a challenge when it comes to the simulation of vapor compression systems. Unlike the steady-state simulation, dynamic simulation is always performed by fixing system charge, and is often utilized to inspect system behavior under off-design conditions. Typically, the charge used in the simulation is smaller than the actual charge of the system. Therefore, it is essential to choose an appropriate void fraction model that accurately computes the refrigerant mass in the simulation. This is important because the dynamics of the refrigerant flow are heavily dependent upon the estimation for the mass. In this study, the real system charge is about 7 kg, and 80% is needed in the simulation. However, some studies reported that only about a half of the true charge was used in their simulations (Bendapudi *et al*., 2008).

(2) Dilemma of void fraction calculation: This challenge is often encountered when simulating start-up and shut-down transients of vapor compression systems. In general, the refrigerant is static or nearly static in the system before the compressor starts up. In this case, the void fraction should be calculated at zero flow speed. Once the compressor starts up, the refrigerant gains momentum and begins to flow quickly. At this point, the void fraction should be calculated using a suitable empirical model. However, no method thus far has been proposed to bridge the gap in the calculation of void fraction when the flow speed changes from zero to the range where the empirical model is applicable. This issue may become more significant when simulating the shut-down transients since the

duration for low speed refrigerant flow is substantially prolonged compared to the start-up case. To tackle this problem, a smooth and differentiable transition is required to determine the void fraction when flow speed approaches zero. In the presented study, the following approach is proposed: When the flow speed is zero, the void fraction ($\gamma = \gamma_{hom}$) is computed using the homogeneous model. When the flow reaches the speed at the nominal condition, the void fraction ($\gamma = \gamma_{nom}$) is computed using a suitable model. When the flow speed is in between, a differentiable function dependent upon the flow velocity is used to interpolate smoothly between γ_{hom} and γ_{nom}. The mathematical formulation is expressed as

$$\gamma = y \cdot \gamma_{nom} + (1 - y) \cdot \gamma_{hom} \tag{3-48}$$

where

$$y = \begin{cases} 1 & \text{if } \dfrac{u}{u_{nom}} >= 1 - 10^{-10} \\ \dfrac{1}{2}\left[\tanh\left(\tan\left(\left(\dfrac{u}{u_{nom}} - \dfrac{1}{2} \right)\pi \right) \right) + 1 \right] & \text{if } 10^{-10} < \dfrac{u}{u_{nom}} < 1 - 10^{-10} \\ 0 & \text{if } \dfrac{u}{u_{nom}} <= 10^{-10} \end{cases} \tag{3-49}$$

(3) Simulation speed for off cycles: Depending on the level of modeling complexity, on-cycles can be simulated in real time. However, for off-cycles, the simulation becomes much slower, especially when refrigerant mass flow rate approaches zero. Under this circumstance, relatively large time steps might allow for quicker computation if the modelers can use an adaptive but stable time-step approach. However, this is challenging when using commercially available simulation platforms since the built-in solvers determine the time-steps based on the local

truncation error. A solution to this problem is to not simulate the full-scale heat exchangers when simulating off-cycles. The heat exchangers can be simplified as ones with multiple symmetrical tube circuitries with only one of them being analyzed during the simulation.

(4) Determination of initial refrigerant distribution for start-up simulation: We found that the initial refrigerant distribution has a pronounced impact on start-up transients. In this study, temperature sensors were installed on the coil surfaces and on the pipes to measure tube wall temperatures. Based on tube wall temperatures and refrigerant pressures inside the tube, modelers can have a better idea of how the refrigerant is distributed in the system before start-up, i.e., whether the refrigerant is superheated, two-phase, or subcooled in each component. However, only with the pressure/temperature measurements, the refrigerant mass in the component still cannot be identified if the refrigerant is in two-phase. Therefore, it necessitates the simulation for off-cycles in order to provide appropriate initial conditions for subsequent on-cycles.

3.8 Summary

A first-principles transient model has been developed for FTVI system which employs a vapor injection scroll compressor. The highlights of the modeling approach are summarized as follows:

(1) The vapor injection scroll compressor is modeled using a lumped parameter approach. The internal heat transfer between the refrigerant and metallic parts has been taken into account. The backflow phenomenon through the economizer port

116

is handled carefully. The prevailing physics of the refrigerant during compressor "on" and "off" period are represented in the model.

(2) The heat exchangers are modeled using the segment-by-segment approach. The conditions for the fan "on" and "off" modes have been considered. A separated flow model without interfacial exchange is employed for two-phase flows to more accurately predict the refrigerant mass distribution. The method of "enthalpy correction" is proposed to account for the slip effect in two-phase flows.

(3) The flash tank is modeled as a lumped control volume with one inlet and two outlets. Ideal phase separation is assumed. All the possible scenarios of refrigerant state inside the tank have been considered (excluding the supercritical condition).

(4) The throttling portion of the electronic expansion valve and the thermostatic expansion valve is modeled using an empirical correlation, whereas the sensor bulb portion of the latter is modeled based on the energy balance.

(5) The reversing valve model is developed such that the same system model can be utilized to simulate both cooling and heating. This is particularly convenient when simulating system transients during reverse-cycle defrosting.

(6) The modular nature of the component models allows flexibility in the system configuration.

Cycling transients of a flash tank vapor injection heat pump system are investigated. The comparisons between the simulation and experimental data show that the proposed model can capture the major heat transfer and flow characteristics transients of the system under cyclic conditions. The dynamic system response when subjected to step changes in the opening of the upper-stage EEV was also studied.

The results demonstrate that EEV opening has a crucial impact on the system performance and the liquid level in the flash tank. It necessitates the development of a creative control strategy to control the degree of injection superheat. It was also found that a moderate adjustment of the upper-stage EEV has little impact on the suction pressure. This is conducive to the selection of the expansion device because of the weak coupling that is exerted by the upper-stage EEV upon the lower-stage TXV.

4 Modeling of Non-Uniform Frost Growth on Tube-Fin Heat Exchangers

4.1 Introduction

Air source heat pumps are used to transfer heat from outside to inside a building during winter operation. The outdoor coil works as an evaporator and frost might deposit on coil surfaces if the ambient temperature is lower than the freezing point. Frost accumulation on coil surfaces can considerably degrade the performance of heat pumps by reducing the capacity of the system in the following manners: 1) Frost layer results in an additional thermal resistance. With clean coil surfaces, heat flow is transferred from the fin-side fluid through fins, and the tube wall, and into the tube-side fluid. However, when coil surfaces are covered by frost, heat flow must penetrate the frost layer first before being carried away by the tube-side fluid at the end. For a given heat transfer temperature difference, heat flow reduces as a result of the augmented thermal resistance; 2) Air flow rate decreases thanks to the frost accumulation (Yasuda *et al*., 1990; Ye and Lee, 2013; Hwang and Cho, 2014). When the frost deposits on coil surfaces, the air flow passage shrinks resulting in higher air side pressure drop. It is well known that a fan running at a fixed speed provides smaller volumetric flow rates with greater pressure drops (if we are to the right of the peak in the fan curve). Without any intervention, frost will keep growing on coil surfaces until the coil becomes nearly or completely blocked. If the air pressure drop increases excessively, the fan might reach to the stall region and the system might not be able to operate steadily. 3) Frost accumulation will impose detrimental influences on the refrigerant side as well. Decrease in air flow rate of the evaporator will result

in a reduction of suction pressure, thereby decreasing the suction density and refrigerant mass flow rate. Meanwhile, the expansion device needs to adjust its opening to control the superheat leaving the evaporator. Too long a heating cycle without defrosting might lead to operating instability if a TXV is used in the system (Gong *et al*., 2008). 4) Heating mode needs to be interrupted periodically to initiate the defrosting cycle in order to remove frost buildup and free coil surfaces before the unit can return to deliver heating service again. Inevitably, the defrosting process incurs a further penalty in energy consumption and hence overall system performance degrades.

In summary, frost accumulation brings major problems to air source heat pump systems. In order to design a system to minimize the impacts of the frost buildup on the performance of the unit, a variety of studies have been conducted to gain the knowledge about frost properties, frost growth and its heat transfer characteristics. Experimental studies are often commenced to characterize frost properties, such as the thermal conductivity and density of the frost, because these properties are required for analyzing the heat transfer characteristics of the frost and its growth process (O'Neal and Tree, 1992; Iragorry *et al*., 2004). Brian *et al*. (1970) developed an empirical correlation for the thermal conductivity of frost based on frost density and temperature. Hayashi *et al*. (1977) correlated frost density with frost surface temperature and presented a method to theoretically evaluate the effective thermal conductivity of the frost layer based on the structure model. Tokura *et al*. (1983) and Mao *et al*. (1992 & 1999) applied dimensional analysis to correlate frost density, thermal conductivity and frost growth rate based on experimental data. Getu and

Bansal (2011) presented empirical frost property correlations for a flat-finned-tube heat exchanger based on a variety of parameters including on air inlet temperature and humidity ratio, frost-coil interface temperature, refrigerant inlet temperature, and Reynolds and Fourier numbers.

Frost formation is a rather complex phenomenon involving simultaneous heat and mass transfer, and it is difficult to analytically predict the frosting process. In order to make the numerical modeling more tractable, a common assumption is adopted in the literature, i.e., the water vapor transported onto the frost surface from the air stream consists of two parts. A part of this water vapor directly diffuses into the frost layer to solidify the frost, while the remainder deposits on the frost surface to increase the frost thickness (Sami and Duong; 1989). In general, fully transient models of frost accumulation are more attractive from an accuracy perspective since they can account for the early stage of frost formation and the spatial variation in temperature and density within the frost layer (Tao *et al.*, 1993; Le Gall *et al.*, 1997; Ismail and Salinas, 1999; Chen *et al.*, 2003; Prölss and Schmitz, 2006; Lenic *et al.*, 2009a and 2009b). However, quasi-steady state models are more favorable and more widely used because 1) fully transient models are too computationally expensive, and 2) the early stage of frost formation is thought to be of secondary interest while the period of frost growth is of primary interest.

In the quasi-steady modeling of frost accumulation, water vapor diffusion into the frost layer is handled by different approaches. One simplification is to assume that frost distribution is homogeneous, i.e., a flat density profile in the perpendicular direction. On the basis of this simplification, it can be deduced that the water vapor

ablimation rate is invariant within the frost layer (Fukata and Inoue, 1999; Martínez-Frías and Aceves, 1999; Şahin, 2000; Seker *et al*., 2004; Yao *et al*., 2004; Lee and Ro, 2005; Tahavvor *et al*., 2010; Kandula, 2011). An alternative is to assume that water vapor ablimation rate is proportional to water vapor density (Lee *et al*., 1997; Lee *et al*., 2003; Tso *et al*., 2006a and 2006b; Yang *et al*., 2006a and 2006b; Kim *et al*., 2009; Hermes, 2012). By utilizing either simplification, the temperature distribution within the frost layer can be determined analytically. All of the models cited above assume the water vapor is saturated at the interface between the air stream and frost layer. However, Na and Webb (2003 & 20004a) found that the water vapor at the frost surface was supersaturated instead, corroborated by a recent study by Cheikh and Jacobi (2014). Based on this finding, a new theoretical model that models frost deposition and growth was proposed (Na and Webb, 2004b).

It is worthwhile to mention that the frosting models are strongly dependent upon the initial condition of the frost layer including the frost thickness and density. Sensitivity analysis can be conducted beforehand to determine the value of initial frost layer thickness such that it does not impose a substantial impact on the simulation. In general, a very small value around zero can be used without causing serious problems in predicting the frost growth rate. However, it is not easy to determine the frost density for such a thin frost layer. Jones and Parker (1975) suggested the initial frost density can be selected within the range of 8-48 kg m^{-3}. In practice, the initial frost density can be adjusted to achieve good agreement with experimental data. In order to avoid this arbitrariness, some models tend to incorporate the empirical correlations that estimate the frost density based on the frost

surface temperature (Sherif *et al.*, 1993; Cheng and Cheng, 2001; Yun *et al.*, 2002; Hermes *et al.*, 2009; Wang *et al.*, 2012). In this way, the only independent state variable is the frost thickness. However, the disadvantage of this approach is that the accuracy of such empirical correlations for the frost density is strongly restricted by the experimental conditions and might not be guaranteed over the ranges of extrapolative use.

It is well recognized that the frost does not uniformly deposit on the surfaces of fan-supplied coils. More specifically, the frost deposits mainly on the front face of the coil with much less accumulation on the back portion of the coil because the coil surface temperature varies from the inlet to the outlet of the heat exchanger circuits. Furthermore, possible air flow maldistribution during the operation further aggravates this non-uniformity. Meanwhile, non-uniform frost growth on coil surfaces will in turn affect the air flow distribution through the coil. Air flow maldistribution has been shown to be one of the dominant factors that degrade the heat exchanger performance (Guo *et al.*, 2008). Based on these facts, it is wise to incorporate the effect of air flow redistribution when modeling frost growth on the heat exchangers. However, most of studies on frost growth on heat exchangers neglect this effect (Sanders, 1974; Kondepudi and O'Neal, 1993; Chen *et al.*, 2003; Seker *et al.*, 2004; Yao *et al.*, 2004; Tso, *et al.*, 2006a and 2006b; Yang *et al.*, 2006c; Aljuwayhel, 2006; Kim *et al.*, 2009; Silva *et al.*, 2011; Cui *et al.*, 2011) except a recent study by Padhmanabhan *et al.* (2011) in which it was found that neglecting the air flow redistribution imposed large deviations in the simulation. By thoroughly reviewing Padhmanabhan's work, it is found that there is still room for improvement. First of all, the heat exchanger model

was validated against experimental data obtained from an air-to-brine coil and there was no phase change on the brine side. This simplified the study profoundly because it was anticipated that phase transition of the refrigerant would exacerbate the non-uniformity of frost growth on the coil. Moreover, since it was a single-phase coil, there was no flow maldistribution on the tube side. Secondly, the air-to-brine coil had a very simple geometry (one row coil with 12 one-pass horizontal tubes). In practice, the heat exchangers are often multi-row coils with complicated asymmetric circuitries, and the air flow propagation has significant influences on the frost distribution. Thirdly, as mentioned earlier, air flow maldistribution due to frost can lead to TXV hunting. Therefore, the steady-state formulations of the refrigerant flow are not adequate, and transient formulations are necessary if the heat exchanger model is integrated into a system-level simulation to explore the transient characteristics of the entire system under frosting/defrosting conditions. Lastly, the significance of Padhmanabhan's framework is to identify the effect of non-uniform frost growth on the air flow redistribution. Consequently, a large system of complex non-linear air pressure equalization equations needs to be solved at each time step. This induces a great amount of computation burden to the solution process and hence slows down the simulation significantly. In Padhmanabhan's case, 48 air pressure drop equations in total needed to be solved simultaneous at each time step (4 segments for each of total 12 tubes). In practice, however, the heat exchangers are often much larger in size than this coil and more equations are required to be solved accordingly. As a result, an efficient numerical scheme capable of handling air flow redistribution due to non-uniform frost growth is in need.

As can been seen from the discussions, despite plenty of studies in the field, there is still a need for an advanced model that predicts non-uniform frost growth on the heat exchanger and accounts for the resulting air flow maldistribution. Since the transient formulations of refrigerant flow have been presented in Chapter 2, this chapter intends to focus the detailed modeling of the frosting process. A novel scheme is proposed to analytically solve the air flow redistribution by linearizing the system of non-linear air pressure drop equalization equations. The proposed scheme has proven to expedite the simulation considerably.

4.2 Model Development

In this section, a first-principles model to predict frost growth and densification on cold surfaces is presented. This frosting sub-model will be then integrated with a detailed distributed parameter model to predict the heat exchanger performance under frosting conditions.

Prerequisites have to be satisfied in order for the frost to form when moist air comes into contact with cold surfaces: 1) the surface temperatures must be below the dew point; 2) the surface temperatures must be beneath the freezing point of the ice. Heat transfer at the frost surface consists of simultaneous sensible and latent heat transfer (Figure 4.1).
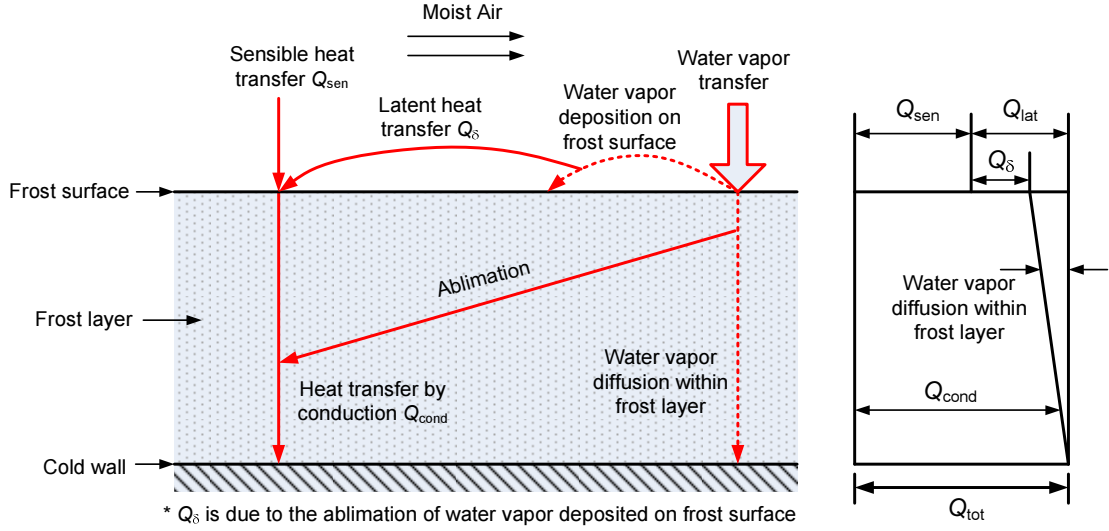
Figure 4.1 Heat and mass transfer on frost surface and inside frost layer

Sensible heat is transferred from the air to the frost surface, driven by the temperature difference between them. While the latent heat transfer comes from the phase change of water vapor transport to the frost surface from the air stream and is dictated by the water vapor concentration gradient. Part of this water vapor diffuses into the existing porous frost layer and contributes to an increase in the frost density without an appreciable increase the frost thickness, whereas the remainder deposits on the upper frost surface and contributes to an increase in the frost thickness without an appreciable increase in the frost density. Hence, the mass balance of the water vapor transferred from the air stream can be expressed as follows

$$\dot{m}_v'' = \frac{d}{dt} \int_{x=0}^{x=\delta_f} \rho_f dx \tag{4-1}$$

where ρ_f is the local density of the frost layer, δ_f is the thickness of the frost layer, $\dot{m}_v''$ is the mass flux of water vapor transferred to the frost layer from the air stream. The average density of the frost layer can be defined as

$$\bar{\rho}_f = \frac{1}{\delta_f} \int_{x=0}^{x=\delta_f} \rho_f dx \qquad (4\text{-}2)$$

Thus, Eq. (4-1) can be written as

$$\dot{m}_v'' = \frac{d}{dt}\left(\bar{\rho}_f \delta_f\right) = \bar{\rho}_f \frac{d\delta_f}{dt} + \delta_f \frac{d\bar{\rho}_f}{dt} \qquad (4\text{-}3)$$

The frost densification rate and frost growth rage are given below, respectively

$$\dot{m}_\rho'' = \delta_f \frac{d\bar{\rho}_f}{dt} \qquad (4\text{-}4)$$

$$\dot{m}_\delta'' = \bar{\rho}_f \frac{d\delta_f}{dt} \qquad (4\text{-}5)$$

The essence of modeling the frosting process is to determine the percentage of the quantity of $\dot{m}_\rho''$ versus that of $\dot{m}_\delta''$. In order to simplify the analysis, the following assumptions are adopted in the study.

1. the frosting process is assumed to be quasi-steady state;

2. one-dimensional heat and mass transport process;

3. the frost layer is characterized by average properties;

4. frost thermal conductivity is only dependent upon the average frost density;

5. convection and radiation heat transfer within the frost layer is negligible;

6. the amount of water vapor absorbed within the frost layer is proportional to the local water vapor density in the frost layer;

7. the air pressure is uniform in the air stream and throughout the frost layer;

8. perfect gas law is applied for the water vapor and local thermodynamic conditions prevail throughout the frost layer;

9. Lewis analogy is applicable.

4.2.1 At the Air-Frost Interface

The sensible and latent heat transfer occurs simultaneously on the frost surface. The sensible heat flux from the air stream to the frost surface is calculated as

$$q''_{sen} = \frac{\dot{m}_a c_{p,a} \left(T_{a,in} - T_{fs} \right) \left\{ 1 - \exp\left[-\frac{\alpha_a \left(A_{o,t} + \eta_{fin} A_{o,fin} \right)}{\dot{m}_a c_{p,a}} \right] \right\}}{A_{o,t} + A_{o,fin}} \qquad (4\text{-}6)$$

where T_{fs} is frost surface temperature, $A_{o,t}$ is the external area of tube surfaces, $A_{o,fin}$ is the external area of fin surfaces, α_a is the heat transfer coefficient, and η_{fin} is the fin efficiency.

The mass flux of water vapor transported from the air stream to the frost surface is determined via

$$\dot{m}''_v = \frac{\dot{m}_a \left(\omega_{a,in} - \omega_{a,fs} \right) \left\{ 1 - \exp\left[-\frac{\alpha_m \left(A_{o,t} + \eta_{fin} A_{o,fin} \right)}{\dot{m}_a} \right] \right\}}{A_{o,t} + A_{o,fin}} \qquad (4\text{-}7)$$

where $\omega_{a,fs}$ is the saturated humidity ratio of the moist air at the frost surface. The mass transfer coefficient α_m is related to the heat transfer coefficient by the Lewis analogy

$$\alpha_m = \frac{\alpha_a}{Le^{2/3} c_{p,a}} \qquad (4\text{-}8)$$

As depicted in Figure 4.1, not the total amount of water vapor will solidify on the frost surface; only the part contributing to an increase in the frost thickness will do so. Therefore, the latent heat flux released due to the solidification of this part of water vapor is

$$q''_\delta = \dot{m}''_\delta \Delta h_{ig} \qquad (4\text{-}9)$$

where Δh_{ig} is the heat of sublimation and is 283.76 kJ/kg.

By applying the energy conservation to the air-frost interface, it can be deduced that this amount of latent heat flux q''_δ, together with the sensible heat flux from the air stream q''_{sen}, must be carried into the frost layer by the heat conduction, i.e.

$$k_f \left.\frac{\partial T_f}{\partial x}\right|_{x=\delta_f} = q''_{sen} + q''_\delta \tag{4-10}$$

It is noted that $\left.\dfrac{\partial T_f}{\partial x}\right|_{x=\delta_f}$ is the temperature gradient at the frost surface and k_f is the thermal conductivity of the frost layer and will be introduced later.

The molecular diffusion of water vapor into the frost layer is due to the Brownian motion and is governed in accordance with Fick's law. At the frost surface, the diffusion flux of water vapor, which will penetrate into the porous frost layer, is determined by

$$\dot{m}''_\rho = -D_{eff} \left.\frac{\partial \rho_v}{\partial x}\right|_{x=\delta_f} \tag{4-11}$$

where D_{eff} is the effective diffusion coefficient.

4.2.2 Within the Frost Layer

As it diffuses through the porous frost layer, water vapor is absorbed by the interface between the gas and ice and solidifies into ice which fills the pore region within the frost layer. As a consequence, the volume of the pore region shrinks and the frost is densified. At the same time, heat is released out as a result of the solidification process. The phenomena occurring within the frost layer can be

analyzed by imposing the conservation law upon the differential control volume in the frost layer (Figure 4.2).
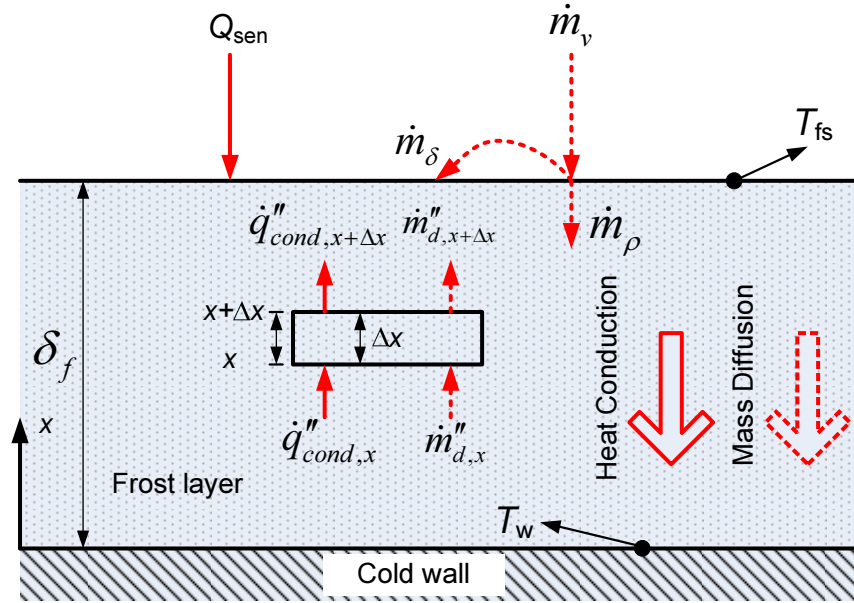
Figure 4.2 Energy and mass transport of a control volume

4.2.2.1 Mass Balance

First, let's look at the mass conservation of the differential control volume (Figure 4.3). It can be inferred that the net diffusion flux of water vapor completely contributes to the increase in the frost density. Mathematically, it can be expressed as

$$\dot{m}''_{d,x} - \dot{m}''_{d,x+\Delta x} = -\frac{\partial \dot{m}''_{d,x}}{\partial x}\Delta x = \frac{\partial}{\partial t}\left(\rho_f \Delta x\right)$$

$$\Rightarrow \frac{\partial \rho_f}{\partial t} = -\frac{\partial \dot{m}''_{d,x}}{\partial x}$$

$$\Rightarrow \frac{\partial \rho_f}{\partial t} = \frac{\partial}{\partial x}\left(D_{eff}\frac{\partial \rho_v}{\partial x}\right)$$

$$\Rightarrow \frac{\partial \rho_f}{\partial t} \approx D_{eff}\frac{\partial^2 \rho_v}{\partial x^2}$$

(4-12)

$$\dot{m}''_{d,x+\Delta x} = \dot{m}''_{d,x} + \frac{\partial \dot{m}''_{d,x}}{\partial x}\Delta x$$

$$\dot{m}''_{d,x} = -D_{eff}\frac{\partial \rho_v}{\partial x}$$
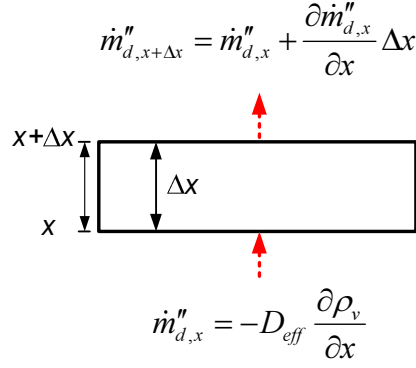
Figure 4.3 Mass conservation of a control volume

4.2.2.2 Energy Balance

Imposing the energy balance upon the differential control volume yields (Figure 4.4)

$$\Delta x\left[-\frac{\partial q''_{cond,x}}{\partial x} - \frac{\partial}{\partial x}\left(\dot{m}''_d h_v\right)\right] = \frac{\partial}{\partial t}\left(\rho_f h_f \Delta x\right)$$
$$\Rightarrow -\frac{\partial q''_{cond,x}}{\partial x} - \frac{\partial}{\partial x}\left(\dot{m}''_d h_v\right) = \rho_f\frac{\partial h_f}{\partial t} + h_f\frac{\partial \rho_f}{\partial t} \qquad (4\text{-}13)$$
$$\Rightarrow -\frac{\partial q''_{cond,x}}{\partial x} - \dot{m}''_d\frac{\partial h_v}{\partial x} - h_v\frac{\partial \dot{m}''_d}{\partial x} = \rho_f\frac{\partial h_f}{\partial t} + h_f\frac{\partial \rho_f}{\partial t}$$

Substituting Eq. (4-12) into Eq. (4-13) and rearranging becomes

$$\frac{\partial}{\partial x}\left(k_f\frac{\partial T_f}{\partial x}\right) - \dot{m}''_d\frac{\partial h_v}{\partial x} - \left(h_v - h_f\right)\frac{\partial \dot{m}''_d}{\partial x} = \rho_f\frac{\partial h_f}{\partial t} \qquad (4\text{-}14)$$

Recognize that the variation in water vapor enthalpy is negligible, i.e. $\frac{\partial h_v}{\partial x} \approx 0$, so the second term on the left hand of Eq. (4-14) can be dropped out. Meanwhile, the heat of sublimation $h_v - h_f$ is relatively constant in the range of temperature of interest in this study and is replaced by Δh_{ig}. Finally, by inserting the definition of frost enthalpy, i.e. $h_f = c_{p,f}T_f$, the energy conservation equation can be simplified as

131

$$\frac{\partial}{\partial x}\left(k_f \frac{\partial T_f}{\partial x}\right) + \Delta h_{ig} \frac{\partial \rho_f}{\partial t} = \rho_f \frac{\partial}{\partial t}\left(c_{p,f} T_f\right) \tag{4-15}$$

where $c_{p,f}$ and T_f are the local specific heat and local temperature of the frost, respectively. The specific heat is obtained from the porosity of the frost layer
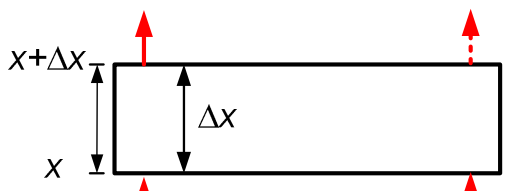
$$c_{p,f} = \frac{1}{\rho_f}\left[(1-\varepsilon)\rho_{ice}c_{p,ice} + \varepsilon\rho_a c_{p,a}\right] \tag{4-16}$$

where ρ_{ice} is the density of the ice, ρ_a is the density of the moist air. While ε is the local porosity of the frost layer and is defined based on volume averaging

$$\varepsilon = \frac{\rho_{ice} - \rho_f}{\rho_{ice} - \rho_a} \approx 1 - \frac{\rho_f}{\rho_{ice}} \tag{4-17}$$

The term on the right-hand side of Eq. (4-15) represents the thermal storage of the frost and will be neglected in the present analysis for the sake of simplicity, i.e.

$$\frac{\partial}{\partial x}\left(k_f \frac{\partial T_f}{\partial x}\right) = -\Delta h_{ig} \frac{\partial \rho_f}{\partial t}$$

$$\Rightarrow k_f \frac{\partial^2 T_f}{\partial x^2} \approx -\Delta h_{ig} \frac{\partial \rho_f}{\partial t} \tag{4-18}$$

$$q''_{cond,x+\Delta x} = \qquad\qquad \left(\dot{m}''_d h_v\right)_{x+\Delta x} =$$

$$q''_{cond,x} + \frac{\partial q''_{cond,x}}{\partial x}\Delta x \qquad \left(\dot{m}''_d h_v\right)_x + \frac{\partial\left(\dot{m}''_d h_v\right)}{\partial x}\Delta x$$

$$x+\Delta x \qquad \Delta x$$

$$x$$

$$q''_{cond,x} = -k_f \frac{\partial T_f}{\partial x} \qquad \left(\dot{m}''_d h_v\right)_x = -D_{eff}\frac{\partial \rho_v}{\partial x}h_v$$

Figure 4.4 Energy balance of a control volume

4.2.3 Distribution of Water Vapor Density within the Frost Layer

By applying the assumption that the amount of water vapor absorbed by frost layer is proportional to the local density of water vapor within the frost layer (Lee *et al.*, 1997), one can have

$$D_{eff} \frac{\partial^2 \rho_v}{\partial x^2} = \zeta \rho_v \qquad (4\text{-}19)$$

where ζ is the absorption coefficient determined based on the boundary conditions. Obviously, Eq. (4-19) is subjected to the following boundary conditions

$$
\begin{aligned}
&(1) \text{ at } x = \delta_f, \; \rho_v = \rho_{v,sat}\left(T_{fs}\right) \\
&(2) \text{ at } x = 0, \; \rho_v = \rho_{v,sat}\left(T_w\right) \\
&(3) \text{ at } x = 0, \; \frac{\partial \rho_v}{\partial x} = 0
\end{aligned}
\qquad (4\text{-}20)
$$

where T_w is the temperature of the cold surface. The first two boundary conditions are determined by the local thermodynamic equilibrium whereas the last one represents that the cold surface is impermeable by water vapor. By applying the ideal gas law, one can obtain the distribution of water vapor density within the frost layer and the absorption coefficient as follows

$$
\begin{aligned}
\rho_v\left(x\right) &= \rho_{v,sat}\left(T_w\right)\cosh\left(\varphi x\right) \\
&= \frac{p_{v,sat}\left(T_w\right)}{R_v T_w}\cosh\left(\varphi x\right)
\end{aligned}
\qquad (4\text{-}21)
$$

$$
\begin{aligned}
\zeta &= D_{eff}\left\{ \frac{1}{\delta_f}\cosh^{-1}\left[\frac{\rho_{v,sat}\left(T_{fs}\right)}{\rho_{v,sat}\left(T_w\right)} \right] \right\}^2 \\
&= D_{eff}\left\{ \frac{1}{\delta_f}\cosh^{-1}\left[\frac{T_w}{T_{fs}}\frac{p_{v,sat}\left(T_{fs}\right)}{p_{v,sat}\left(T_w\right)} \right] \right\}^2
\end{aligned}
\qquad (4\text{-}22)
$$

where $\varphi = \sqrt{\dfrac{\zeta}{D_{eff}}}$. $p_{v,sat}$ is the saturation pressure of water vapor evaluated at the

corresponding temperature.

4.2.4 Temperature Distribution within the Frost Layer

Substituting Eq. (4-12) into Eq. (4-18) yields

$$k_f \frac{\partial^2 T_f}{\partial x^2} = -\zeta D_{eff} \frac{\partial^2 \rho_v}{\partial x^2} \tag{4-23}$$

Eq. (4-19) allows Eq. (4-23) to be rewritten as

$$\frac{\partial^2 T_f}{\partial x^2} = -\frac{\zeta \Delta h_{ig}}{k_f} \rho_v(x) \tag{4-24}$$

Eq. (4-24) is subjected to the boundary conditions given as following

$$
\begin{aligned}
&(1)\,\text{at } x = 0,\, T_f = T_w \\
&(2)\,\text{at } x = \delta_f,\, k_f \frac{\partial T_f}{\partial x} = q''_{sen} + \dot{m}''_\delta \Delta h_{ig}
\end{aligned}
\tag{4-25}
$$

Solving Eq.(4-24) yields the temperature distribution within the frost layer

$$T_f(x) = -\frac{D_{eff} \Delta h_{ig} p_{v,sat}(T_w)}{R_v T_w k_f}\left[1 - \cosh(\varphi x)\right] + \frac{q''_{tot}}{k_f} x + T_w \tag{4-26}$$

where q''_{tot} is the total heat flux that occurs during the frosting process and is

calculated as

$$q''_{tot} = q''_{sen} + m''_v \Delta h_{ig} \tag{4-27}$$

The frost surface temperature can be calculated as

$$T_{fs} = -\frac{D_{eff} \Delta h_{ig} p_{v,sat}(T_w)}{R_v T_w k_f}\left[1 - \cosh(\varphi \delta_f)\right] + \frac{q''_{tot}}{k_f} \delta_f + T_w \tag{4-28}$$

It must be noted that Eq. (4-28) is an implicit equation without an analytical solution and needs to be solved numerically using a non-linear equation solver, e.g., Newton method. Once the frost surface temperature is determined, the distribution of water vapor density within the frost layer is readily known.

4.2.5 Densification and Growth of Frost Layer

From Eq. (4-21) it is easy to obtain the total amount of water vapor absorbed by the frost layer

$$
\dot{m}_\rho'' = D_{eff} \left. \frac{\partial \rho_v}{\partial x} \right|_{x=\delta_f} = D_{eff} \int_{x=0}^{x=\delta_f} \frac{\partial^2 \rho_v}{\partial x^2} dx = \int_{x=0}^{x=\delta_f} \zeta \rho_v(x) dx
$$
$$
= \frac{\zeta\, p_{v,sat}(T_w)}{R_v T_w \varphi} \sinh(\varphi \delta_f)
$$
(4-29)

Following the 1st order forward difference integration, the average density for the next time step is obtained from

$$
\overline{\rho}_{f,t+\Delta t} = \overline{\rho}_{f,t} + \frac{\dot{m}_\rho''}{\delta_f} \Delta t
$$
(4-30)

Substituting $\dot{m}_\rho''$ into Eq. (4-3) can readily calculate the frost thickness for the next time step

$$
\delta_{f,t+\Delta t} = \delta_{f,t} + \frac{\dot{m}_v'' - \dot{m}_\rho''}{\overline{\rho}_{f,t}} \Delta t
$$
(4-31)

The following initial conditions for the frost layer is chosen

$$
\overline{\rho}_{f,t=0} = 30 \text{ kg} / \text{m}^3
$$
$$
\delta_{f,t=0} = 10^{-6} \text{m}
$$
(4-32)

4.2.6 Constitutive Equations

4.2.6.1 Effective Diffusion Coefficient

The diffusion path follows the pore volume in the porous frost layer. As a result, the actual length of the diffusion path is longer than that of the path in free space for the same displacement because the pore region is generally tortuous in the porous media (Na, 2003). Hence, both porosity and tortuosity of the frost layer need to be accounted for when determining the effective diffusion coefficient, i.e.

$$D_{eff} = D_s \frac{\bar{\varepsilon}}{\bar{\tau}} \tag{4-33}$$

where $\bar{\varepsilon}$ and $\bar{\tau}$ are the average porosity and average tortuosity factor, respectively. D_s is the diffusion coefficient.

Porosity is defined as the ratio of the pore volume to the total volume and can be calculated as

$$\bar{\varepsilon} = 1 - \frac{\bar{\rho}_f}{\rho_{ice}} \tag{4-34}$$

The tortuosity as a function of the porosity can be given by the empirical relationship (Sanders, 1974)

$$\bar{\tau} = \frac{\bar{\varepsilon}}{1 - (1 - \bar{\varepsilon})^{0.5}} \tag{4-35}$$

Please be noted that the tortuosity is always greater than unity because of the tortuous nature of the actual diffusion path.

An empirical equation for the molecular diffusivity, mainly used for water vapor diffusion in the frosting process (Eckert and Drake, 1987), is adopted in the study

$$D_s = 2.302 \left(\frac{p_o}{p} \right) \left(\frac{T}{T_o} \right)^{1.81} \times 10^{-5} \tag{4-36}$$

where $p_o = 0.98 \times 10^5$ Pa and $T_o = 256$ K.

4.2.6.2 Thermal Conductivity of the Frost Layer

The thermal conductivity of the frost layer only varies with the average density

of the frost layer and is determined as (Lee *et al.*, 1997)

$$k_f = 0.132 + 3.13 \times 10^{-4} \bar{\rho}_f + 1.6 \times 10^{-6} \bar{\rho}_f^2 \left(50 < \bar{\rho}_f < 400 \text{ kg/m}^3 \right) \tag{4-37}$$

4.2.6.3 Air Pressure Drop

The pressure drop across the heat exchanger is made up of three parts: entrance

pressure drop (4-38), exit pressure rise (4-39) and frictional pressure drop (4-40)

(Kays and London, 1984)

$$\Delta p_{ent} = \frac{G_{max}^2}{2\rho_{a,in}} \left[K_c + 1 - \sigma^2 \right] \tag{4-38}$$

$$\Delta p_{ext} = \frac{G_{max}^2}{2\rho_{a,out}} \left[1 - \sigma^2 - K_e \right] \tag{4-39}$$

$$\Delta p_{frict} = f \frac{A_o}{A_{min}} \frac{G_{max}^2}{2\rho_{a,m}} \tag{4-40}$$

where G_{max} is the air mass flux evaluated inside the heat exchanger core, and σ is the

ratio of the minimum free flow area to the frontal-area. K_c and K_e are the abrupt

contraction and expansion coefficient, respectively. $\rho_{a,m}$ is the arithmetic mean of air

inlet and outlet densities.

4.2.6.4 Fin Efficiency

The fin efficiency is evaluated as a circular fin having the same fin efficiency

(Hong and Webb, 1996)

$$\eta_{fin} = \frac{\tanh(mr\phi)}{mr\phi}\cos(0.1mr\phi) \qquad (4\text{-}41)$$

$$m = \sqrt{\frac{2\alpha_{eff}}{k_{fin}\delta_{fin}\left(1+\dfrac{\delta_f}{k_f}\alpha_{eff}\right)}} \qquad (4\text{-}42)$$

$$\phi = \left(\frac{R_e}{r}-1\right)\left(1+0.35\ln\left(\frac{R_e}{r}\right)\right) \qquad (4\text{-}43)$$

where R_e is the equivalent fin radius defined as

$$\frac{R_e}{r} = 1.28\frac{P_t}{d_{eff}}\left(\frac{P_r}{P_t}-0.2\right)^{1/2} \qquad (4\text{-}44)$$

$$d_{eff} = d_{o,t} + 2\delta_f \qquad (4\text{-}45)$$

$$r = \frac{d_{eff}}{2} \qquad (4\text{-}46)$$

$$\alpha_{eff} = h_a\left(1+\frac{\left.\dfrac{d\omega_{a,sat}}{dT}\right|_{fs}}{c_{p,a}}\Delta h_{ig}\right) \qquad (4\text{-}47)$$

where $Le^{3/2} = 0.905$ (Lee $et\ al.$, 2003).

4.3 Dynamic Air Flow Redistribution

Since the frost sub-model is solved by the quasi-steady-state approach, the air flow redistribution of the heat exchanger can be handled in a similar fashion, i.e., steady-state conditions will be assumed for sufficiently small time intervals, but the overall analysis will remain transient in nature.

As stated at the beginning, to determine the time evolution of air flow distribution, a number of non-linear air pressure drop equalization equations need to

be solved at each time step. Considering that the correlations of calculating air pressure drop are very complicated in general, the computation overhead associated with determining the air flow redistribution is substantial and thus resulting in a significant decrease in simulation speed. However, this process can be greatly simplified by taking advantage of the approximation that the state of the fan-coil system at the next time step can be regarded as a perturbed state near the equilibrium state at the current time step. In this way, the corrections to the air mass flow rate for each time step can be readily determined without solving the set of pressure equalization equations simultaneously.

The analysis is started by assuming that one has already obtained the air flow rate across the ith segment of jth horizontal row at the current time step t, i.e., $\dot{m}_{i,j}$ (please refer to Figure 4.5 for how i and j are defined), and the total air volumetric flow rate delivered by the fan at the same time is $\dot{V}_{fan,t}$. The fan-coil system is assumed to operate steadily with this air flow distribution within the time interval between t and $t + \Delta t$ since Δt is sufficiently small. The air flow distribution remains unchanged until the arrival of the next time step, $t + \Delta t$.

(a)

(b)
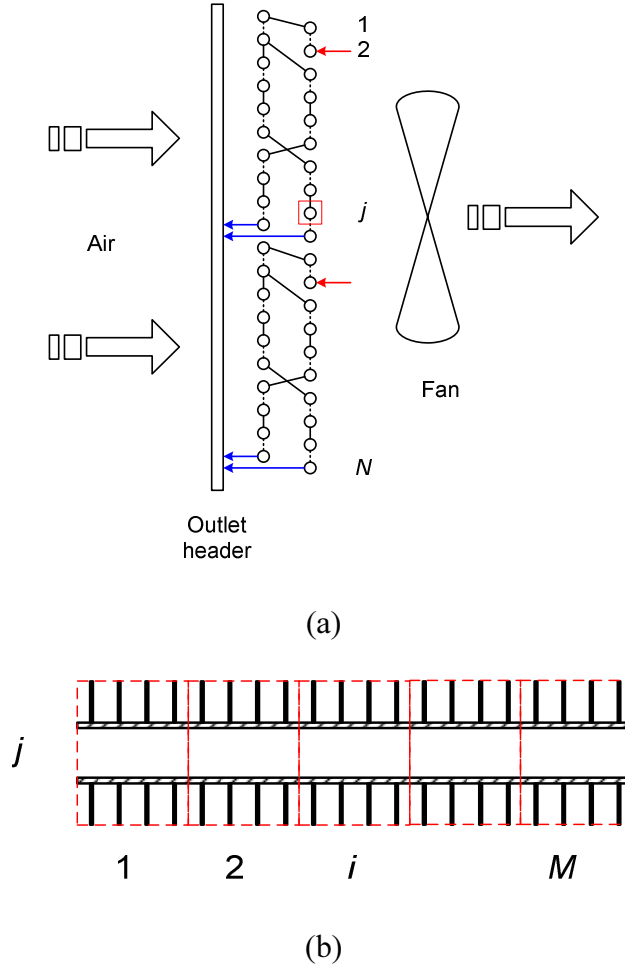
Figure 4.5 (a) Pressure equalization at the outlet the coil; (b) Descretization of the jth tube

At the next time step $t + \Delta t$, both frost density and thickness increases due to frost growth, and the air flow distribution changes accordingly. Assume that the air flow rate across the ith segment of the jth horizontal row becomes $\dot{m}_{i,j} + \Delta\dot{m}_{i,j}$ at $t + \Delta t$, and the total air volumetric flow rate that the fan delivers becomes $\dot{V}_{fan} + \Delta\dot{V}_{fan}$ at the same time. Obviously, the following expression holds

$$\Delta\dot{V}_{fan} = \frac{\sum_{i=1}^{M}\sum_{j=1}^{N}\Delta\dot{m}_{i,j}}{\rho_{fan,in}} \tag{4-48}$$

where $\rho_{\text{fan,in}}$ is the air density at the inlet to the fan at $t + \Delta t$. In a blow-thru configuration, the fan blows air through the coil located downstream of the fan. In this case, $\rho_{\text{fan,in}}$ is a constant and should be evaluated using the ambient condition. In a draw-thru configuration, the fan draws air through the coil located upstream. The air flow is assumed to be well mixed after leaving the coil. In this case, $\rho_{\text{fan,in}}$ varies with time and is evaluated using the air state leaving the coil after the mixing.

Since Δt is quite small, the state of the fan-coil system at $t + \Delta t$ can be regarded as a perturbed state near the equilibrium state at time t. Hence, by utilizing the first order approximation, one can linearize the expression of air pressure drop as follows (note: the pressure drop terms are evaluated with the frost thickness at $t + \Delta t$, i.e., $\delta_f + \Delta\delta_f$)

$$\Delta p_{i,j}\left(\dot{m}_{i,j} + \Delta\dot{m}_{i,j}\right) \approx \Delta p_{i,j}\left(\dot{m}_{i,j}\right) + \left.\frac{\partial\left(\Delta p_{i,j}\right)}{\partial\dot{m}_{i,j}}\right|_{\dot{m}_{i,j}} \Delta\dot{m}_{i,j} \tag{4-49}$$

$$\Delta p_{fan}\left(\dot{V}_{fan} + \Delta\dot{V}_{fan}\right) \approx \Delta p_{fan}\left(\dot{V}_{fan}\right) + \left.\frac{\partial\left(\Delta p_{fan}\right)}{\partial\dot{V}_{fan}}\right|_{\dot{V}_{fan}} \Delta\dot{V}_{fan} \tag{4-50}$$

where

$i = 1, 2, \ldots, M$ (each tube is subdivided into M segments)

$j = 1, 2, \ldots, N$ (the coil has N horizontal rows)

$\dot{m}_{i,j}$ is the air flow rate across the ith segment of the jth horizontal row at t

$\dot{m}_{i,j} + \Delta\dot{m}_{i,j}$ is the air flow rate across the ith segment of the jth horizontal row at $t + \Delta t$

$\dot{V}_{fan}$ is the total air volumetric flow rate delivered by the fan at t

$\dot{V}_{fan} + \Delta\dot{V}_{fan}$ is the total air volumetric flow rate delivered by the fan at $t + \Delta t$

141

$\Delta p_{i,j} \left(\dot{m}_{i,j} + \Delta \dot{m}_{i,j} \right)$ is air pressure drop through the ith segment of the jth horizontal

row at $t+\Delta t$, evaluated at $\dot{m}_{i,j} + \Delta \dot{m}_{i,j}$

$\Delta p_{fan} \left(\dot{V}_{fan} + \Delta \dot{V}_{fan} \right)$ is the air pressure rise through the fan at $t + \Delta t$

$\Delta p_{fan} \left(\dot{V}_{fan} \right)$ is the air pressure drop through the fan at t

$\Delta p_{i,j} \left(\dot{m}_{i,j} \right)$ is the air pressure drop through the ith segment of the jth horizontal row,

evaluated at $\dot{m}_{i,j}$

$\left. \dfrac{\partial \left(\Delta p_{i,j} \right)}{\partial \dot{m}_{i,j}} \right|_{\dot{m}_{i,j}}$ is the partial derivative of air pressure drop with respect to mass flow rate

for the ith segment of the jth horizontal row, evaluated at $\dot{m}_{i,j}$

$\left. \dfrac{\partial \left(\Delta p_{fan} \right)}{\partial \dot{V}_{fan}} \right|_{\dot{V}_{fan}}$ is the partial derivative of air pressure rise with respect to the volumetric

flow rate for the fan, evaluated at $\dot{V}_{fan}$

At time $t + \Delta t$, the fan-coil system operates at another equilibrium state and is subjected to the following constraints

$$\Delta p_{i,j} = \Delta p_{fan} \qquad (4\text{-}51)$$

where $i = 1, 2, \ldots, M$ and $j = 1, 2, \ldots, N$.

Hence one can obtain

$$\Delta p_{i,j}\left(\dot{m}_{i,j}\right) + \frac{\partial\left(\Delta p_{i,j}\right)}{\partial \dot{m}_{i,j}} \Delta \dot{m}_{i,j} = \Delta p_{fan}\left(\dot{V}_{fam}\right) + \left.\frac{\partial\left(\Delta p_{fan}\right)}{\partial \dot{V}_{fan}}\right|_{\dot{V}_{fan}} \Delta \dot{V}_{fan}$$

$$\Rightarrow \Delta \dot{m}_{i,j} = \frac{\Delta p_{fan}\left(\dot{V}_{fan}\right) - \Delta p_j\left(\dot{m}_{i,j}\right) + \left.\dfrac{\partial\left(\Delta p_{fan}\right)}{\partial \dot{V}_{fan}}\right|_{\dot{V}_{fan}} \Delta \dot{V}_{fan}}{\left.\dfrac{\partial\left(\Delta p_{i,j}\right)}{\partial \dot{m}_{i,j}}\right|_{\dot{m}_{i,j}}}$$

(4-52)

Since $\displaystyle\sum_{i=1}^{M}\sum_{j=1}^{N} \Delta \dot{m}_{i,j} = \rho_{fan,in}\Delta \dot{V}_{fan}$, one can have

$$\sum_{i=1}^{M}\sum_{j=1}^{N}\left[\frac{\Delta p_{fan}\left(\dot{V}_{fan}\right) - \Delta p_{i,j}\left(\dot{m}_{i,j}\right)}{\left.\dfrac{\partial\left(\Delta p_{i,j}\right)}{\partial \dot{m}_{i,j}}\right|_{\dot{m}_{i,j}}} + \frac{\left.\dfrac{\partial\left(\Delta p_{fan}\right)}{\partial \dot{V}_{fan}}\right|_{\dot{V}_{fan}} \Delta \dot{V}_{fan}}{\left.\dfrac{\partial\left(\Delta p_{i,j}\right)}{\partial \dot{m}_{i,j}}\right|_{\dot{m}_{i,j}}}\right] = \rho_{fan,in}\Delta \dot{V}_{fan}$$

(4-53)

Rearranging Eq. (4-53) yields

$$\Delta \dot{V}_{fan}\left\{ \left.\frac{\partial\left(\Delta p_{fan}\right)}{\partial \dot{V}_{fan}}\right|_{\dot{V}_{fan}} \left[\sum_{i=1}^{M}\sum_{j=1}^{N} \frac{1}{\left.\dfrac{\partial\left(\Delta p_{i,j}\right)}{\partial \dot{m}_{i,j}}\right|_{\dot{m}_{i,j}}}\right] - \rho_{fan,in}\right\}$$

$$= \sum_{i=1}^{M}\sum_{j=1}^{N} \frac{\Delta p_{i,j}\left(\dot{m}_{i,j}\right)}{\left.\dfrac{\partial\left(\Delta p_{i,j}\right)}{\partial \dot{m}_{i,j}}\right|_{\dot{m}_{i,j}}} - \Delta p_{fan}\left(\dot{V}_{fan}\right)\sum_{i=1}^{M}\sum_{j=1}^{N} \frac{1}{\left.\dfrac{\partial\left(\Delta p_{i,j}\right)}{\partial \dot{m}_{i,j}}\right|_{\dot{m}_{i,j}}}$$

(4-54)

Let $A = \displaystyle\sum_{i=1}^{M}\sum_{j=1}^{N} \frac{1}{\left.\dfrac{\partial\left(\Delta p_{i,j}\right)}{\partial \dot{m}_{i,j}}\right|_{\dot{m}_{i,j}}}$, $B = \displaystyle\sum_{i=1}^{M}\sum_{j=1}^{N} \frac{\Delta p_{i,j}\left(\dot{m}_{i,j}\right)}{\left.\dfrac{\partial\left(\Delta p_{i,j}\right)}{\partial \dot{m}_{i,j}}\right|_{\dot{m}_{i,j}}}$

$$\Delta \dot{V}_{fan} = \frac{\Delta \bar{p} - \Delta p_{fan}\left(\dot{V}_{fan}\right)}{\left.\dfrac{\partial\left(\Delta p_{fan}\right)}{\partial \dot{V}_{fan}}\right|_{\dot{V}_{fan}} - \dfrac{\rho_{fan,in}}{A}} \tag{4-55}$$

where $\Delta \bar{p} = \dfrac{B}{A}$, representing the mean air pressure drop across the coil.

All the terms in Eq. (4-55) can be computed explicitly. Once the correlation of calculating air pressure drop has been selected, the pressure drop terms in Eq. (4-55) are computed without difficulty.

In general, the partial derivatives of air pressure drop with respect to the air mass flow can be evaluated analytically if the correlation is chosen. Based on Eq.(4-38), (4-39) & (4-40), one can have

$$\frac{\partial\left(\Delta p_{ent}\right)}{\partial \dot{m}} = \frac{2}{\dot{m}}\Delta p_{ent} \tag{4-56}$$

$$\frac{\partial\left(\Delta p_{ext}\right)}{\partial \dot{m}} = \frac{2}{\dot{m}}\Delta p_{ext} \tag{4-57}$$

$$\frac{\partial\left(\Delta p_{frict}\right)}{\partial \dot{m}} = \frac{\Delta p_{frict}}{\dot{m}}\left[2 + \frac{\mathrm{Re}}{f}\frac{\partial f}{\partial \mathrm{Re}}\right] \tag{4-58}$$

where f is the friction factor which is a function of Reynolds number.

Therefore, Eq.(4-55) provides a means for readily determining the time evolution of air volumetric flow rate of the fan. Ideally, $\rho_{fan,in}$ should be evaluated using the air state at $t + \Delta t$. Recognizing the fact that Δt is so small and the change in the moist air density within Δt is negligible, $\rho_{fan,in}$ at time t can be used here for the sake of simplification without considerable loss of accuracy. Finally, the change in

mass flow rate of each segment at the time step $t + \Delta t$ can be calculated by substituting Eq. (4-55) into Eq. (4-52).

Figure 4.6 compares the new approach of calculating the air flow redistribution with Padhmanabhan's approach. It can be noted that the new approach can directly solve the air flow distribution at each time step without iteration. Elimination of iteration significantly speeds up the simulation (more than 20 times faster), especially for large coils.
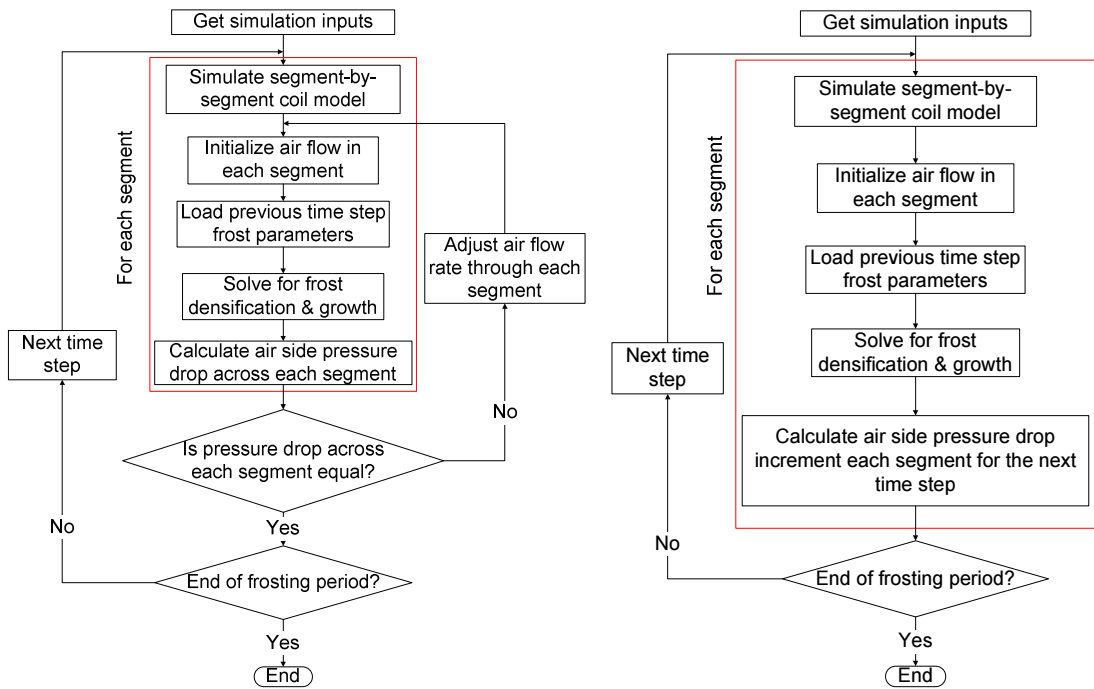
Figure 4.6 Comparison between the new approach (right) and Padhmanabhan's approach (left)

4.4 Model Validation

Utilizing the developed model along with other component models presented in Chapter 3, the transient behavior of the FTVI heat pump system described in Chapter 3 under the frosting condition is explored. The operating condition was that the

indoor temperature was at 21°C (48% RH) and the outdoor temperature was at 1.7°C (82% RH).

The frosting period lasts 5000 sec and can be divided into four stages: frost initiation stage, frost growth stage, pre-cyclic hunting stage and cyclic hunting stage. Unlike the case discussed in Section 3.6.3, the opening of the upper-stage EEV is adjusted by the controller in this study.

4.4.1 Frost Initiation Stage

The frost initiation stage ranges from the beginning of the start-up to around 700 sec. During this stage, the system parameters, such as pressures, temperatures, heat loads and refrigerant mass flow rates vary rapidly because of the refrigerant redistribution and other phenomena associated with the start-up operation. Before the system starts up, system pressures are in equilibrium at 1032 kPa. At the end of the stage, the entire system operates under a quasi-steady state condition. The suction, discharge and intermediate pressures reach to 600 kPa, 2520 kPa and 1033 kPa, respectively (Figure 4.7). The suction and discharge temperatures stabilize at 2.5 °C and 84 °C, respectively. The degree of the suction superheat maintains 10 K (Figure 4.8). The frost starts to grow on the outdoor coil surfaces shortly after the system starts up. The rate of the frost accumulation nearly remains constant during the entire frosting period and approximately 0.5 kg frost has built up on the outdoor coil surfaces by the end of this stage (Figure 4.10).

The deviations between the simulation results and experimental data can be attributed to the hysteresis effect of the upper-stage EEV, which is characterized by a phenomenon that shows different flow rates even at the same valve opening

depending on the moving direction of a valve stem. Because the upper-stage EEV opening varies drastically during this stage (Figure 4.11), it is extremely difficult to reduce the coefficients in Eq. (3-27) to obtain an accurate prediction for the mass flow rate through the valve. As a result, less favorable agreement has been obtained between the simulations and experimental data.

4.4.2 Frost Growth Stage

The frost growth stage ranges from 700 sec to 2600 sec. During this period, the frost grows steadily and the total mass of the frost deposition has increased to 1.95 kg, and the outdoor coil air flow rate has decreased by 40% (Figure 4.10). The frost build-up results in an augmented thermal resistance and reduced air flow rate. However, the system performance does not degrade noticeably during this stage (Figure 4.12). This is probably because the system is greatly oversized under this operating condition, even a considerable reduction of the air flow rate across the outdoor coil does not degrade the system performance. As a consequence, the suction and intermediate pressures do not exhibit appreciable changes, but the discharge pressure is more sensitive to the variation in the air flow rate of the outdoor coil and starts to decrease at 1600 sec. By the end of this stage, the discharge pressure has decreased by 200 kPa. The fact that the suction superheat and the upper-stage EEV opening remain nearly constant during this stage also indicates that the system operates under quasi-steady state conditions.

As indicated in Figure 4.13, frost does not necessarily grow uniformly on each tube. Please note that the tubes are numbered from top to bottom, left to right. Therefore, the tubes in the first row are numbered from 1 to 32, and are numbered from 33 to 64 in the second row. The frost tends to accumulate in the first row

because the concentration gradient of water vapor that drives a mass transfer process causing water vapor to be transported from the main moist air stream to the tube surfaces is much higher in the first row than in the second row. Figure 4.14 shows the tube locations where the frost accumulates the most and the least. A majority of the tubes on which the frost grows the least are close to the outlet of the circuit, where the refrigerant is superheated and the tube surface temperatures are relatively higher. One might wonder why Tube No. 39 has less frost accumulation than Tube No. 40 given the fact that the former is further away from the outlet of the circuit. This can be explained as follows: First of all, the frost tends to accumulate on Tube No. 7 than No. 8 because the surface temperature of Tube No. 7 is lower than that of Tube No. 8 since the latter is closer to the outlet of the circuit. Therefore, the concentration of water vapor for the air entering tube No. 39 is lower than that entering Tube No. 40. Secondly, although Tube No. 40 is closer to the outlet of the circuit, the difference in the tube surface temperatures between Tube No. 39 and 40 is insignificant. As a consequence, the concentration gradient of water vapor for Tube No. 39 is still lower than that for Tube No. 40, resulting in less frost accumulation on the former.

The air flow maldistribution over the outdoor coil due to non-uniform frost growth is illustrated in Figure 4.15. The initial air flow distribution for the clean coil, i.e., without frost accumulation, is determined by the measurements before the experiment. The outdoor coil is a U-shape coil and the fan is placed on top of it, so the tubes close to the fan receive more air flow than the tubes far away from the fan. With the frost accumulating on the coil surfaces, the air flow distribution will vary with time and the original distribution cannot be maintained. With the approach

presented in Section 4.3, the air flow maldistribution can be easily solved. It can be seen that Tube No. 10 and No. 42 receives the most air flow rate because they have the thinnest frost blockage.

Dynamic air flow maldistribution will in return influence the refrigerant flow distribution. Figure 4.16 shows the variation in the refrigerant outlet quality of each circuit. The refrigerant outlet quality of Circuit #5 and #6 is greater than that of the other circuits because of two reasons: (1) each of these two circuits has two more tubes and these additional tubes can compensate the shortage of air flow to some extent. As a result, the compound value of UA is comparable with that of other circuits; (2) additional tubes indicate that the refrigerant needs to travel longer distance, resulting in a larger pressure drop. However, refrigerant pressures leaving each circuit must be balanced at the outlet header. In order to have an equalized pressure at the outlet header, refrigerant flow in these two circuits has to reduce. It is not surprising that the refrigerant outlet quality of Circuit #1 and #2 is higher than that of Circuit #3 and #4 since Circuit #1 and #2 receive more air flow. The reason why the refrigerant outlet quality of Circuit #2 is slightly higher than that of Circuit #1 can be attributed to different air flow configurations of Circuit #1 and #2 although they have the same number of tubes. Circuit #1 has a much prolonged two-phase region than Circuit #2 because the temperatures of the air flow exchanging heat with Tube No. 35 to 38 in Circuit #1 are much lower than those of the air flow exchanging heat with Tube No. 3 to No. 6 in Circuit #2. Hence, there is not much remaining heat transfer area for the superheated region in Circuit #1. As a result, the refrigerant outlet quality of Circuit #1 is lower.

Figure 4.17 shows the transients of the refrigerant mass flow rates. It can be seen that the refrigerant mass flow rates remain nearly constant during this stage, which further corroborates the fact that the system operates under quasi-steady state conditions. The variation in air temperatures of both heat exchangers is given in Figure 4.18. The condenser air outlet temperature nearly stabilizes at 31.5 °C. However, the evaporator air outlet temperature decreases during this stage because the air flow rate reduces due to the frost blockage. Figure 4.19 illustrates the variation in the refrigerant temperatures of the condenser and evaporator. The refrigerant temperatures do not exhibit noticeable changes during this stage.
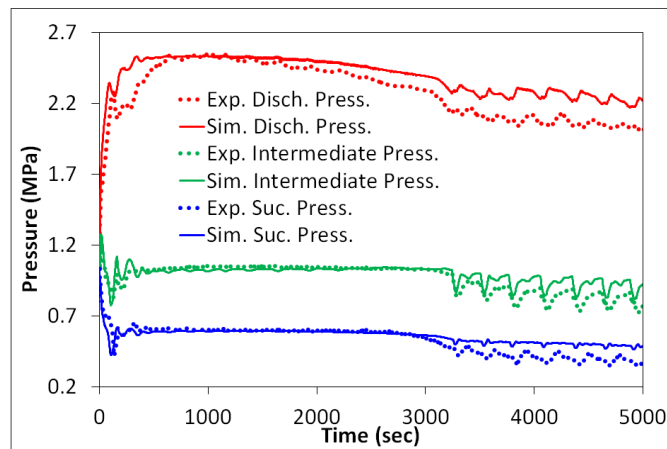
Figure 4.7 Pressure transients
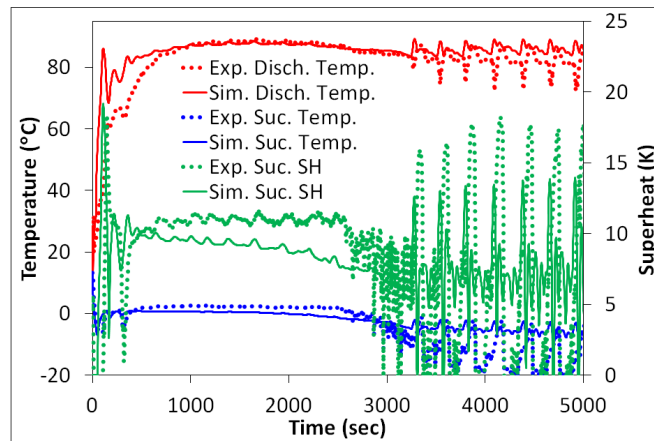
Figure 4.8 Transients of temperatures and suction superheat

150
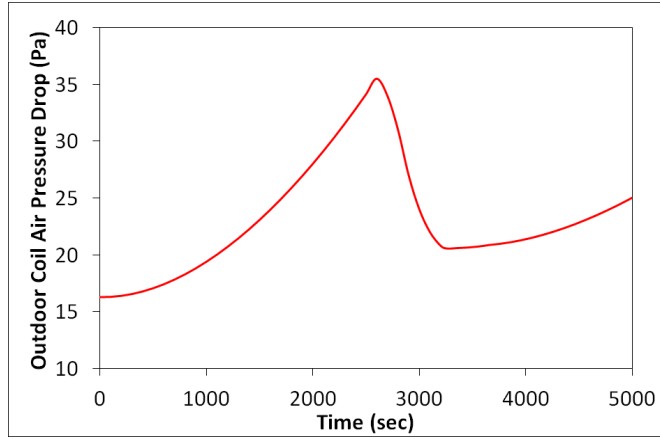
Figure 4.9 Outdoor coil air pressure drop
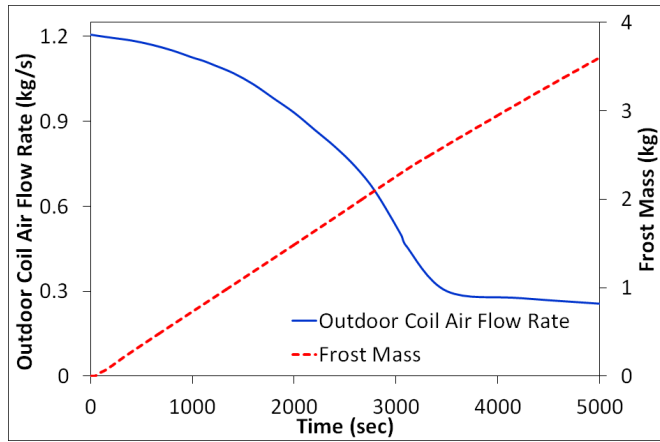
Figure 4.10 Frost mass accumulation and outdoor coil air mass flow rate
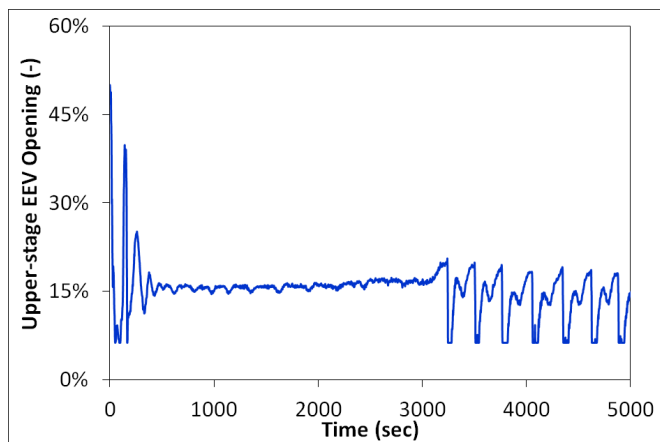
Figure 4.11 Upper-stage EEV opening fraction
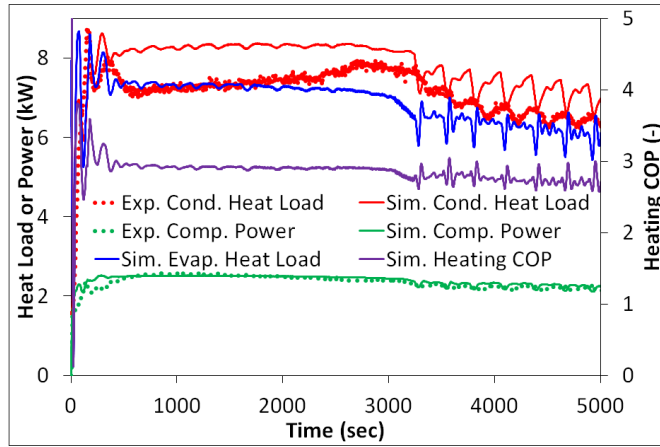
Figure 4.12 Transients of air side heat load and heating COP
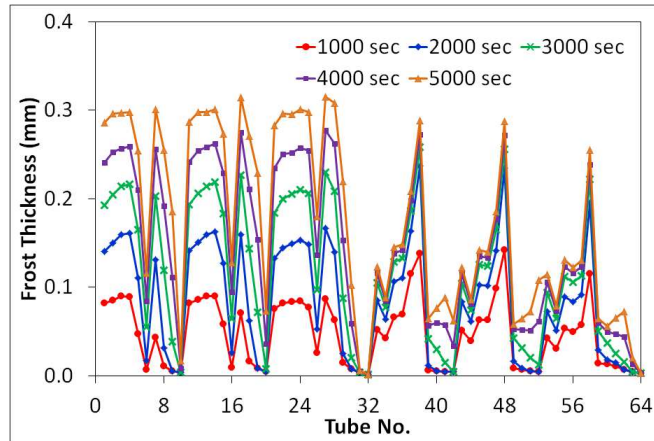
Figure 4.13 Frost thickness on each tube
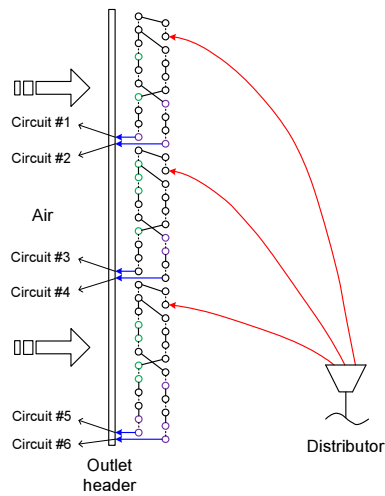
Figure 4.14 Tubes with the thickest frost accumulation (tubes in green) and tubes the thinnest frost accumulation (tubes in purple)
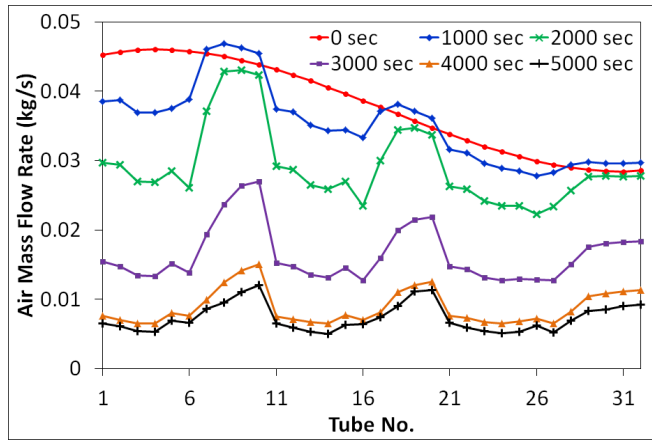
Figure 4.15 Dynamic air flow maldistribution over the evaporator
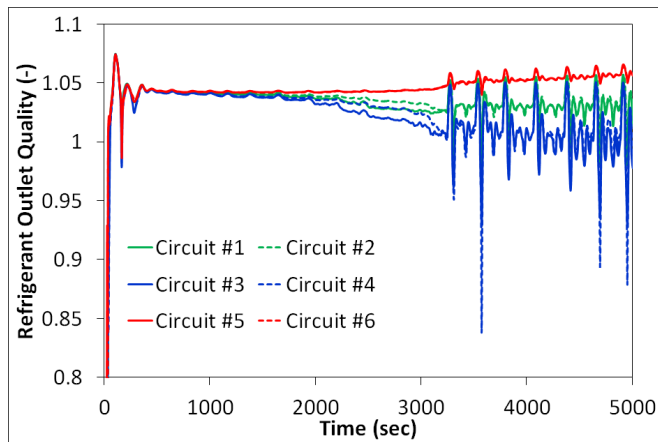
Figure 4.16 Refrigerant outlet quality of each circuit of the evaporator
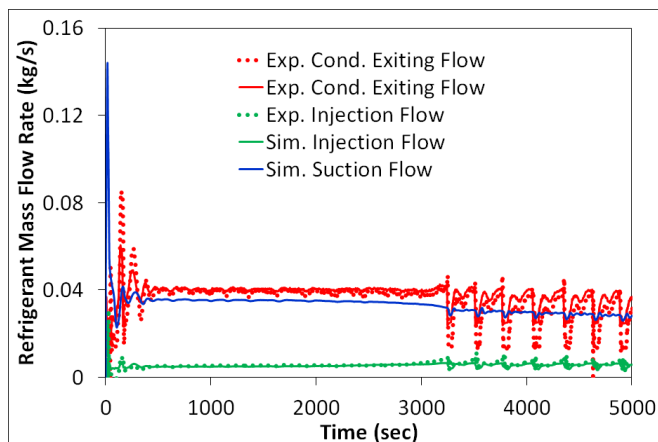
Figure 4.17 Transients of refrigerant mass flow rates

153
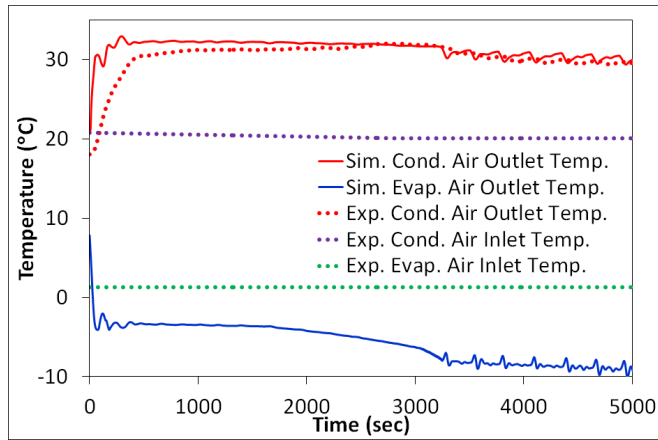
Figure 4.18 Air temperatures of the heat exchangers
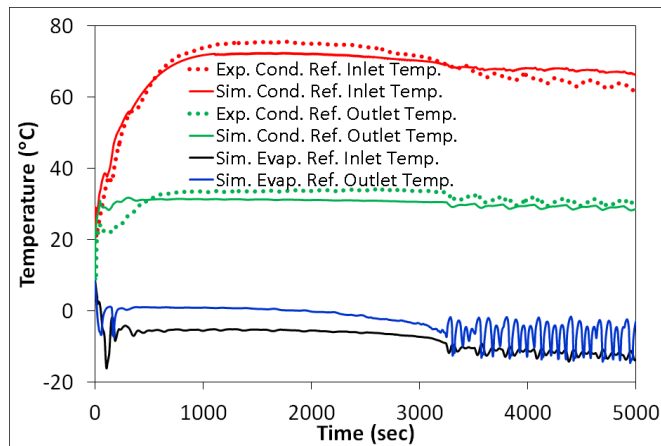
Figure 4.19 Refrigerant temperatures of the heat exchangers
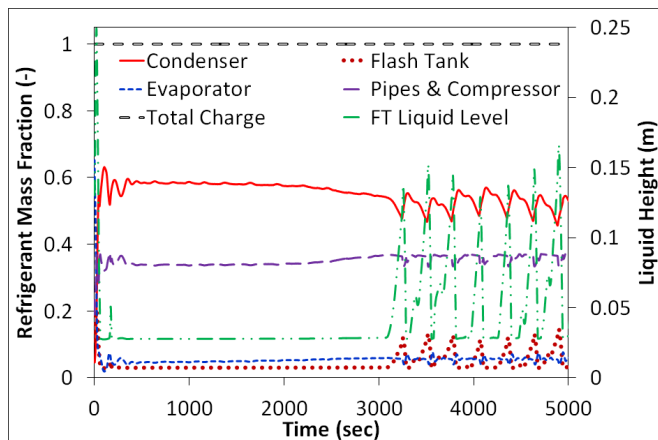
Figure 4.20 Predicted refrigerant mass distribution and flash tank liquid height

4.4.3 Pre-cyclic Hunting Stage

The pre-cyclic hunting stage ranges from 2600 sec to 3260 sec. During this stage, the frost continues to grow, and the air pressure drop through the outdoor coil rises to a maximum of 35 Pa and then abruptly drops to 20 Pa when the outdoor coil fan motor "stalls" under the high static pressure (Figure 4.9). With the fan motor unable to maintain torque under the high static pressure, the air flow drops rapidly to 30% of its initial flow rate. As a result, the suction pressure and the suction superheat decrease quickly. Since there is not much superheat leaving the outdoor coil, the TXV begins to close. In addition to lags and finite time constants in the sensing mechanism and valve pin motion, the newly released refrigerant must traverse the length of the evaporator. By the time the hotter refrigerant vapor reaches the outlet, the system may overshoot and "hunt" for a stable set point. This difficulty in arriving at a stable set point is therefore termed evaporator or TXV "hunting." This is exactly what the system has exhibited during this stage (Figure 4.8).

After this stage, the suction, discharge and intermediate pressures decrease to 465 kPa, 895 kPa and 2120 kPa, respectively. In the meantime, the liquid level in the flash tank keeps rising because of the decrease in the discharge pressure, and eventually the flash tank is almost filled with refrigerant liquid (Figure 4.20) (Please refer to Section 3.6.5 for details). However, excessively high liquid level can deteriorate the phase separation efficiency of the flash tank because liquid droplets can be entrained into the injection flow. As a result, the injection flow will lose the superheat and end up being two-phase.

4.4.4 Cyclic Hunting Stage

The cyclic hunting stage lasts from 3260 sec until the end of the frosting period. At the end of the previous stage, the injection superheat is zero because of the two-phase injection flow. As a result, the controller tries to reduce the upper-stage EEV opening in order to maintain the injection superheat at 4 K. With the diminished upper-stage valve opening, the refrigerant flow entering the flash tank from the condenser decreases. Consequently, the intermediate and suction pressures, and the flash tank liquid level will all drop because of insufficient refrigerant replenishment from the condenser. However, the pressure in the condenser rises because of the reduced outgoing flow. The lowered suction pressure results in a lower evaporating temperature and a larger heat transfer temperature difference between the refrigerant and the air, so the suction superheat will increase and the TXV tries to enlarge its opening. In the meantime, because the liquid level in flash tank decreases, there will be no droplet entrainment in the injection flow and the injection superheat starts to rise. In order to maintain the injection superheat, the controller then tries to enlarge the upper-stage EEV opening. As a consequence, the discharge pressure will decrease, but the intermediate and suction pressures, and the liquid level will all increase. The raised suction pressure results in a higher evaporating temperature and a smaller heat transfer temperature difference between the refrigerant and air flow. Therefore, the suction superheat will then fall. Because the TXV has enlarged its opening previously, it means more refrigerant flow will be fed into the evaporator at this time, which causes the refrigerant is not completely evaporated and leaves the evaporator as two-phase. Shortly, the TXV starts to sense this two-phase flow near the compressor suction, its opening will decrease. Meanwhile, since the liquid level in the flash tank

156

keeps increasing during this period, the injection superheat starts to drop. Then the above cycle will repeat itself again.

As analyzed above, the combination of the remarkable drop in the outdoor coil air flow and the injection superheat control results in the cyclic hunting of the system. However, the air flow maldistribution due to non-uniform frost growth exacerbates the cyclic hunting. As stated previously, the combination of asymmetric circuitry and air flow maldistribution leads to the refrigerant flow maldistribution, i.e., less refrigerant flow in Circuit #5 and #6 than in the other four circuits. As shown in Figure 4.16, the refrigerant outlet quality of Circuit #5 and #6 is always greater than unity, denoting that the refrigerant leaving these circuits is superheated. However, the refrigerant leaving the other four circuits can be intermittent two-phase flows during the period. As a result, the TXV cannot sense enough superheat at the outlet of the evaporator to regulate the refrigerant flow.

As shown in from Figure 4.7 to Figure 4.20, cyclic hunting leads to the unceasing fluctuations of the system parameters, including pressures, temperatures, mass flow rates and heat loads, etc. The mean values of these parameters decrease with the reduced air flow rate because the frost still keeps growing during this stage.

4.5 Discussions

As a consequence of simplifications and idealizations made in the calculations, the discrepancies between the simulation results and experimental data are observed and can be attributed to the following underlying causes:

(1) Valve hysteresis effects. The TXV and EEV adjust their openings drastically during the period, which inevitably increases modeling complexity.

(2) The predicted outdoor coil air flow rate deviates from the actual air flow rate in the experiment. Since the outdoor coil is not positioned in the wind tunnel, it is very difficult to obtain the actual variation in the air flow rate due to frost blockage.

(3) Different frost growth characteristics. In order to simplify the analysis, the model does not account for the local variation in the frost thickness within individual calculation domains, and assumes that the frost grows uniformly within each segment. However, as a matter of fact, the frost thickness does not only vary along the tubes, but also vary along the fins. Due to the difference in fin surface temperatures, the frost at the fin base tends to be thicker than that at the fin tip (Gao and Gong, 2011). Because the proposed model is unable to capture this phenomenon, the prediction for the air side pressure drop will be off, which in return causes the deviated prediction for the air flow variation.

(4) The proposed model is unable to capture the refrosting characteristics of the heat exchangers. However, due to the fin geometry, the corner formed by two adjacent fins tends to hold droplets during the defrosting period. The droplets freeze in subsequent refrosting cycles with significant effects on pressure drop and heat transfer (Xia *et al*., 2006).

4.6 Summary

A dynamic model that accounts for non-uniform frost growth on tube-fin heat exchangers is presented in this chapter. This model can be straightforwardly extended for analysis of microchannel heat exchangers. A novel scheme is proposed to solve the dynamic air flow redistribution by linearizing the system of non-linear air pressure drop equalization equations, which can significantly accelerate the

simulation. Table 4.1 compares the existing frosting heat exchanger models with the new model proposed in this chapter.

Table 4.1 Comparison between the existing frosting heat exchanger models and the new model

Citation	Methodology	Refrigerant Modeled	Geometry	Air Flow Redistribution	Fan Effect
Sanders (1974)			Tube fin HX		
Kondepudi & O'Neal (1993)			Tube fin HX		
Chen et al. (2003)			Tube fin HX		
Seker et al. (2004)			Tube fin HX		
Yao et al. (2004)	Segment-by-segment	1-ph & 2-ph	Tube fin HX		
Tso et al. (2006)	Segment-by-segment	1-ph	Tube fin HX		
Tso et al. (2006)	Segment-by-segment	1-ph & 2-ph	Tube fin HX		
Yang et al. (2006)	Segment-by-segment	1-ph & 2-ph	Tube fin HX		
Singh (2009)	Segment-by-segment	1-ph & 2-ph	Tube fin HX		
Silva et al. (2011)	Row-by-row	1-ph	Tube fin HX		Yes
Padhmanabhan et al. (2011)	Segment-by-segment	1-ph	Tube fin HX	Yes (complex)	
New model	**Segment-by-segment**	**1-ph & 2-ph**	**Tube fin HX**	**Yes (simple)**	**Yes**

Utilizing the developed model, the transient behavior of an FTVI heat pump under the frosting condition has been explored. Comparison between the simulation results and experimental data indicates that the proposed model can reasonably predict the time dependent performance of the system under the frosting condition.

Furthermore, the proposed model is useful for the evaluation of the influence of various variables such as fin spacing, fan characteristic and operating circumstances. However, further improvements for the model and more rigorous experimental validation are required to achieve a more accurate performance evaluation for heat pumps.

5 Modeling of Hot Gas Defrosting

5.1 Introduction

As stated in Chapter 4, one of major problems associated with air source heat pumps is that both heating capacity and energy efficiency decrease as the frost forms on the outdoor coil surfaces during winter operation. When the system performance degrades to a certain level, the frost has to be removed before the unit is able to restore the normal operation.

In general, there are various defrosting methods applied to heat pump applications, such as reverse-cycle, hot-gas bypass, spraying warm water and electrical resistance heating. The first two methods can be realized by the system itself without employing additional devices and therefore are widely used.

The reverse cycle defrost (RCD) is a procedure that switches the condenser and the evaporator from the heating mode, where the indoor coil acts as the condenser, and the outdoor coil acts as the evaporator, to the cooling mode, where the indoor coil acts as the evaporator, and the outdoor coil acts as the condenser. The hot gas discharged by the compressor, which was originally delivered into the indoor coil in the heating mode, is now pumped into the outdoor coil to melt the frost off the coil. Once the frost is completely melted off, the unit can switch back to the heating mode again. However, there are two major drawbacks associated with the RCD. One drawback is that the heat, which is used to melt the frost, is extracted from the indoor living environment. This will reduce the indoor temperature and greatly influence the indoor thermal comfort. The other drawback is the great noise during the rapid

refrigerant pressure equalization process resulting from the switch between heating and cooling mode (Huang *et al*., 2009).

Hot-gas bypass defrost (HGBD) is a procedure that introduces a portion of, not entire, high pressure and high temperature gas from the compressor discharge to the evaporator/suction side of the system, thus raising the temperatures and pressures of the outdoor coil and melting the frost. The HGBD does not require a reversal of the flow of refrigerant throughout the system. Although a much longer defrosting duration is anticipated compared to the RCD, one of the most significant advantages of the HGBD is that the unit does not have to halt the heating operation, as required by the RCD, to remove the frost. As a result, the undesirable temperature fluctuations of indoor air are much smaller compared to those during the RCD.

Recently, a series of improvements have been proposed to overcome the downsides of the above two defrosting methods, such as reverse cycle defrosting with refrigerant flow compensation (Ding *et al*., 2004b; Wang *et al*., 2008), sensible heat defrosting (Liang *et al*., 2010a), dual hot gas bypass defrosting (Choi *et al*., 2011a) and thermal energy storage based reverse-cycle defrosting (Hu *et al*., 2011).

There have been quite a few reported modeling studies on analyzing the defrosting process. Sanders (1976) was one of the pioneers who theoretically investigated the defrosting process for two different defrosting methods, i.e., hot-gas defrosting and electrical defrosting, and for two different extreme situations, i.e., (1) optimistic situation: the frost layer sticks to the tube wall during the melting period, and (2) pessimistic situation: air gaps occur between the melting frost layer and tube wall. Krakow *et al*. (1992a & 1992b) proposed an idealized hot-gas defrosting model,

which divided the defrosting process into four stages: preheating, melting, vaporizing and dry heating. In this model, certain heat and mass transfer parameters, including the maximum surface water, the free-convective air film conductance, the air/water film conductance, and the surface water vaporization coefficient, needed to be determined experimentally to solve for the defrosting characteristics. Sherif and Hertz (1998) presented a semi-empirical model for electrical defrosting of a cylindrical coil cooler. However, the model was incapable of determining the fraction of the energy loss to the refrigerant. Al-Mutawa and Sherif (1998a & b) developed a mathematical model for predicting the evaporation, sublimation, and melting heat rates on a frosted cylindrical cooler during hot-gas defrosting. It was concluded that the evaporation and sublimation heat rates were significantly larger than the melting heat rate. Hoffenbecker *et al*. (2005) developed a transient model to predict heat and mass transfer effects of a frosted industrial air-cooling evaporator during hot gas defrosting cycle. In order to simplify the analysis, the frost layer was assumed to only adhere to the finned surfaces, and the model did not account for the effects of phase change in the calculation domain resulting from frost melting. Aljuwayhel (2006) developed a hot gas defrost model, which divided the defrosting process into four stages: preheating, melting, dry-heating and bleeding stage. In the model, the frost presumably adhered to the coil surfaces during the melting period. More recently, Dopazo *et al*. (2010) developed a more rigorous model for hot-gas defrosting process, which was divided into six stages: preheating, tube frost melting start, fin frost melting start, air presence, tube-fin water film and dry-heating. A common problem with the above modeling studies is that they have only focused on the heat and mass

transfer phenomena on the air side during the defrosting process, and have neglected the complex dynamics on the refrigerant side. However, in order to conduct an unbiased analysis for frost melting process, it is necessary to investigate the transient characteristics of the overall system because the refrigerant dynamics of mass flow rates, pressures and temperatures have a great impact on the performance of the defrosting cycles and the subsequent frosting cycles. In light of this, Krakow *et al*. (1993a & 1993b) developed a simplified analytical model to predict the performance characteristics of the reverse-cycle defrosting process of a refrigeration system. However, the stage of a rapid pressure equalization resulting from energizing the reversing valve was omitted in the analysis. Later on, Liu *et al*. (2003 & 2008) performed a more comprehensive study including the pressure equalization stage after engaging the reversing valve. Tso *et al*. (2001) conducted a simulation study to compare the performance of the hot gas bypass control and the suction modulation control in refrigerated shipping containers. The suction modulation control strategy was shown to be more energy efficient than the hot gas bypass control.

Extensive experimental studies also have been undertaken to gain a more concrete understanding in physical processes of air-source heat pumps during the reverse cycle defrost (O'Neal *et al*., 1989; O'Neal and Peterson, 1990; O'Neal *et al*., 1991; Payne and O'Neal, 1995; Chen and Guo, 2009) and the hot gas bypass defrost (Hewitt and Huang, 2008; Byun *et al*. 2008; Lee and Byun, 2009; Liang *et al*., 2010a; Choi *et al*., 2011a). Niederer (1976) reported that the defrosting efficiency, defined as the ratio of the energy theoretically needed to remove the frost to the total energy actually supplied during the entire defrosting process (Machielsen and Kerschbaumer,

1989), was only 15-25%, and a similar conclusion was drawn by Cole (1989). Merrill (1981) claimed that the integrated COP of heat pump systems including defrosting cycles as a fraction of steady-state COP could be predicted with power law relationships involving capacity as a fraction of steady-state peak capacity. Stoecker *et al*. (1983) experimentally demonstrated that lower pressure hot gas could be used to achieve satisfactory defrost. Miller (1987) quantified the frosting and defrosting losses for an air-to-air residential heat pump and concluded that the demand frost control was more energy efficient compared to the time-temperature defrost control. Pre-starting the outdoor coil fan during the reverse cycle defrosting process has proven to be able to reduce compressor pressure spikes and the resulting mechanical shock (Anand *et al*., 1989; Huang *et al*., 2004). Xia *et al*. (2006) studied the thermal-hydraulic performance of folded-louvered-fin, microchannel heat exchangers under frosting, defrosting and refrosting conditions. It was concluded that the performance under refrosting conditions became periodic and repeatable after the third or fourth refrosting cycle. Huang *et al*. (2007) revealed that a critical point, after which the system parameters increased rapidly because the heat transfer mechanism outside the outdoor coil changed from the phase-change pattern of frost melting to the air natural convection, existed during the defrosting period. Hewitt and Huang (2008) experimentally investigated the reliability and effectiveness of hot gas bypass defrosting cycle of an air source heat pump with economizer and circular shape evaporator coil under high humidity conditions. Lawrence and Evans (2008) proposed an algorithm which was able to detect the need for defrosting based on the instability in the flow of refrigerant into the evaporator for the refrigerating systems

equipped with TXV. Byun *et al*. (2008) studied the feasibility of the hot gas bypass method to retard the formation and growth of frost on the outdoor coil. Chen and Guo (2009) studied the effects of the outdoor air parameters on the reverse cycle defrosting performance of an air-source heat pump unit. Lee and Byun (2009) investigated the effects of outdoor coil fan speed on the performance of the heat pump system by adopting the hot gas bypass. Shao *et al*. (2010) experimentally and numerically showed that the heating performance of a finned-tube heat pump system under frosting conditions was better than that of a microchannel heat pump system because the former could withstand a much longer frosting period. Wang *et al*. (2011) claimed that effective defrost control strategies based on the photoelectric technology (Byun *et al*., 2006) or the direct parameter, such as frost thickness, could mitigate the risks of the mal-defrost phenomena. Qu *et al*. (2012a & 2012b) reported that downward flowing of melted frost along coil surfaces thanks to gravity prolonged the entire defrosting process, and thus a lower defrosting efficiency should be expected. Xu *et al*. (2013a) experimentally showed that microchannel heat exchangers with vertical tube orientation possessed much better frosting and defrosting cycle performance because of more effective water drainage capability during the frost melting period compared to ones with horizontal tube orientation.

One of the key features of the hot gas defrost, such as the RCD and the HGBD, is that a transient process is involved. Although there are extensive studies on the performance of heat pump systems under hot gas defrost, very few modeling studies have focused on the system dynamics in this area (many studies have focused on the system dynamics during start-up and shut-down). Given the fact that both refrigerant

and air side undergo complex and drastic changes during the hot gas defrosting process, more detailed theoretical studies on the system level are required to facilitate the understanding of the resulting intricate phenomena. Moreover, the system-level simulation makes easier the performance evaluation for heat pump systems under the heating operation. Hence, this chapter aims to develop a hot gas defrosting model, which focuses on analyzing the simultaneous heat and mass transfer phenomena on the frost side. Along with the models presented in Chapter 2 and 3, users should be able to model the transients of heat pump systems under defrosting condition.

5.2 Model Development

It is impossible to develop a detailed, physics-based hot gas defrost model given the fact that hot gas defrost is an extremely complex phenomenon involving simultaneous heat and mass transfer mechanism: condensation of high pressure and high temperature refrigerant gas; heat conduction through tubes and fins; sensible heat transfer of the frost layer; melting and sublimation of frost layer; vaporization of retained melted water. In general, frost usually does not melt uniformly on coil surfaces, and the rate of frost melting depends on the rate of heat supply from the refrigerant into the frost layer. As pointed out by Aljuwayhel (2006), the frost might remain attached over some portions of the coil until it completely melts or sublimates, in other portions of the coil the frost might partially melt, and then detach from the coil and fall either onto a lower tube or into hot drain pan. This stochastic nature of the defrosting process inevitably increases modeling complexity. Therefore, the defrosting process must be idealized in order to obtain a practical model (Krakow *et al*., 1992a). In this study, the defrosting process is subdivided into five stages:

preheating, melting start, melting, vaporizing and dry heating. The temperature profile of each stage is shown in Figure 5.1 - Figure 5.5. The flow chart of the model algorithm is given in Figure 5.6.

5.2.1 Preheating Stage

In this stage, the high pressure and high temperature refrigerant gas will heat up the wall. This stage comes to an end once the temperature at the interface between the wall and the frost reaches to the melting point of ice, i.e., 273.15K. The heat flow is transported from the refrigerant to the internal surfaces of the wall by convection, then to the external surfaces of the wall and the frost layer by conduction, and finally dissipated to the ambient either by natural convection (fan is OFF) or by forced convection (fan is ON). Frost might sublimate during the defrost process. In this stage, there is no phase change, and the energy storage of the wall and the frost layer increases. In Figure 5.1 - Figure 5.5, the red dots represent the center of an element, whereas the blue dots represent the interface between adjacent elements. There is no energy storage at the interface, and all the energy is congregated at the center. The rate of temperature change with time at the center depends on the net rate of incoming heat flow from adjacent interfaces. The constituent equations of this stage are Eq. (5-1)- (5-7).

$$\alpha_i \left(T_r - T_{w,i} \right) = k_w \frac{T_{w,i} - T_w}{\delta_w / 2} \tag{5-1}$$

$$\rho_w c_{p,w} \delta_w \frac{dT_w}{dt} = k_w \frac{T_{w,i} + T_{w,o} - 2T_w}{\delta_w / 2} \tag{5-2}$$

$$k_w \frac{T_w - T_{w,o}}{\delta_w / 2} = k_f \frac{T_{w,o} - T_f}{\delta_f / 2} \tag{5-3}$$

$$\rho_f c_{p,f} \delta_f \frac{dT_f}{dt} = k_f \frac{T_{w,o} + T_{fs} - 2T_f}{\delta_f / 2} \tag{5-4}$$

$$\frac{d\delta_f}{dt} = 0 \tag{5-5}$$

In some special cases, the evaporator fan is ON during the defrosting process, and the heat transport between the frost surface and the ambient is determined by

$$k_f A_o \frac{T_f - T_{fs}}{\delta_f / 2} = \dot{m}_a c_{p,a} \left(T_{fs} - T_a\right) \left[1 - \exp\left(-\frac{\alpha_a A_{o,eff}}{\dot{m}_a c_{p,a}}\right)\right]$$
$$+ \dot{m}_a \left(\omega_{fs} - \omega_a\right) \Delta h_{ig} \left[1 - \exp\left(\frac{\alpha_a A_{o,eff}}{\dot{m}_a c_{p,a} Le^{2/3}}\right)\right] \tag{5-6}$$

In most cases, the evaporator is Off during the defrost process. The heat from the frost layer to the ambient is dissipated through natural convection.

$$k_f A_o \frac{T_f - T_{fs}}{\delta_f / 2} = A_{o,eff} \left[\alpha_a \left(T_{fs} - T_a\right) + \frac{\alpha_a}{c_{p,a} Le^{2/3}} \left(\omega_{fs} - \omega_a\right) \Delta h_{ig}\right] \tag{5-7}$$
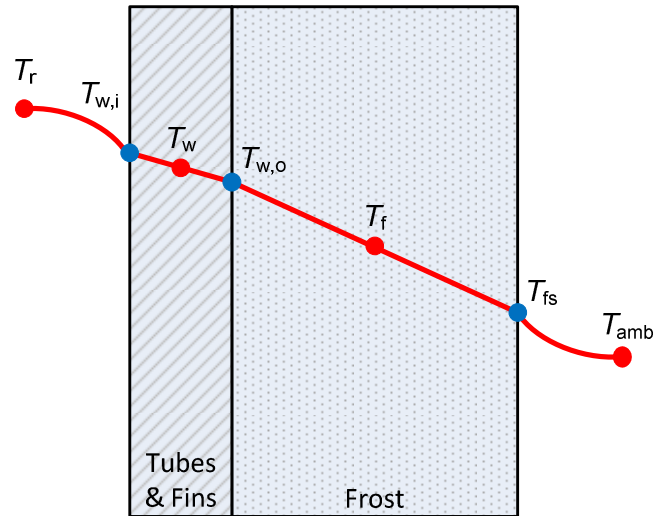
Figure 5.1 Preheating stage

169

5.2.2 Melting Start Stage

Once the temperature at the interface between the wall and the frost reaches to the melting point of ice, the frost adhering to the wall starts to thaw. As a result, a water film appears and sticks to the wall. As the frost continues to melt, the thickness of the water film increases until it reaches the maximum thickness. It is extremely difficult to analytically compute the maximum surface water on a coil after defrosting, which is determined by many factors including the gravity effect, water viscosity, coil geometry (tube pitch, row pitch, fin type, fin density and tube diameter, etc.), surface energy of the materials, and coil orientation (horizontal, vertical or tilted), etc. According to Krakow *et al.* (1992b), the maximum surface water per unit of surface area held on the coil is approximately 0.050 kg/m^2. During this stage, the temperature at the interface between the water film and the frost layer remains at 273.15 K. The constituent equations of this stage are Eq.(5-1), (5-2), (5-6) or (5-7), (5-8) - (5-12).

$$k_w \frac{T_w - T_{w,o}}{\delta_w / 2} = k_f \frac{T_{w,o} - T_{H_2O}}{\delta_{H_2O} / 2} \tag{5-8}$$

$$\rho_{H_2O} c_{p,H_2O} \delta_{H_2O} \frac{dT_{H_2O}}{dt} = k_{H_2O} \frac{T_{w,o} + 273.15 - 2T_{H_2O}}{\delta_{H_2O} / 2} \tag{5-9}$$

$$-\Delta h_{if} \rho_f \frac{d\delta_f}{dt} = k_{H_2O} \frac{T_{H_2O} - 273.15}{\delta_{H_2O} / 2} + k_f \frac{T_f - 273.15}{\delta_f / 2} \tag{5-10}$$

$$\rho_f c_{p,f} \delta_f \frac{dT_f}{dt} = k_f \frac{273.15 + T_{fs} - 2T_f}{\delta_f / 2} \tag{5-11}$$

$$\frac{d\delta_{H_2O}}{dt} = -\frac{d\delta_f}{dt} \tag{5-12}$$
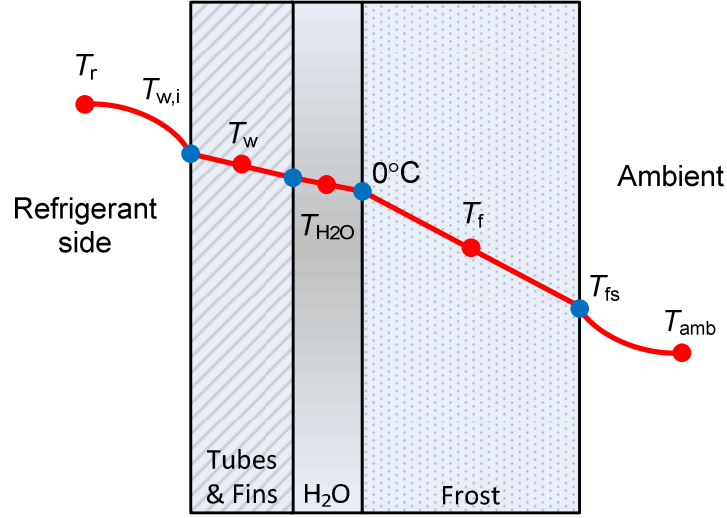
Figure 5.2 Melting start stage

5.2.3 Melting Stage

In this stage, the frost will continue to thaw and the melted frost will drain off from coil surfaces. As a consequence, a gap forms between the water film and the frost layer. The volume formerly occupied by the melted frost is replaced by the surrounding air. Through this air gap, heat is transferred by conduction. As the melting process proceeds, the air gap becomes larger and the heat supply will decrease. During this stage, the thickness of the water film remains constant, i.e., at its maximum thickness. The temperature at the interface between the air gap and the frost layer remains at 273.15 K. This stage ends when the frost layer is completely melted. The mathematical interpretation of complete melting is that the thickness of the frost layer is less than 10^{-3} mm. The constituent equations of this stage are Eq.(5-1), (5-2), (5-6) or (5-7), (5-8), (5-11), (5-13) - (5-17).
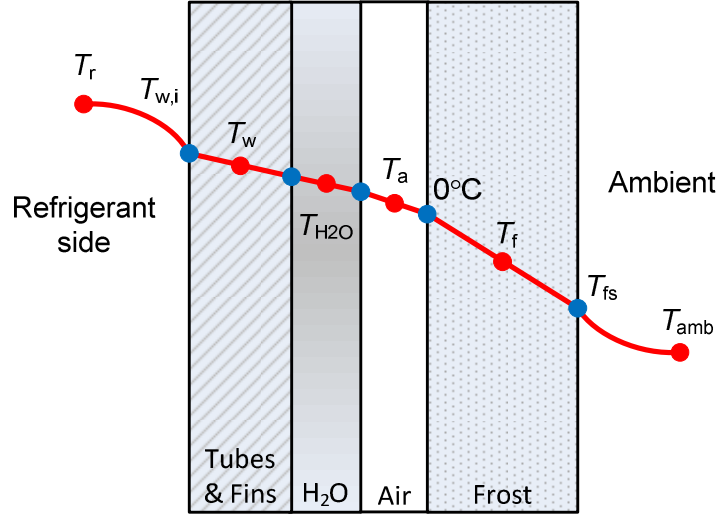
Figure 5.3 Melting stage

$$\rho_{H_2O} c_{p,H_2O} \delta_{H_2O} \frac{dT_{H_2O}}{dt} = k_{H_2O} \frac{T_{w,o} - T_{H_2O}}{\delta_{H_2O}/2} + \frac{T_a - T_{H_2O}}{\dfrac{\delta_a}{2k_a} + \dfrac{\delta_{H_2O}}{2k_{H_2O}}} \qquad (5\text{-}13)$$

$$\rho_a c_{p,a} \delta_a \frac{dT_a}{dt} = \frac{T_{H_2O} - T_a}{\dfrac{\delta_{H_2O}}{2k_{H_2O}} + \dfrac{\delta_a}{2k_a}} + k_a \frac{273.15 - T_a}{\delta_a/2} \qquad (5\text{-}14)$$

$$-\Delta h_{if} \rho_f \frac{d\delta_f}{dt} = k_a \frac{T_a - 273.15}{\delta_a/2} + k_f \frac{T_f - 273.15}{\delta_f/2} \qquad (5\text{-}15)$$

$$\frac{d\delta_a}{dt} = -\frac{d\delta_f}{dt} \qquad (5\text{-}16)$$

$$\frac{d\delta_{H_2O}}{dt} = 0 \qquad (5\text{-}17)$$

5.2.4 Vaporizing Stage

In this stage, only water retains on coil surfaces. This stage ends when the retained water completely vaporizes, i.e., the thickness of the water film is less than 10^{-3} mm. The constituent equations of this stage are Eq.(5-1), (5-2), (5-8), (5-18) - (5-20).

$$\rho_{H_2O} c_{p,H_2O} \delta_{H_2O} \frac{dT_{H_2O}}{dt} = k_{H_2O} \frac{T_{w,o} - T_{H_2O}}{\delta_{H_2O}/2} + k_{H_2O} \frac{T_{H_2O} - T_{H_2O,s}}{\delta_{H_2O}/2} \qquad (5\text{-}18)$$

The vaporization rate of surface water is assumed to be proportional to the difference between the saturation density of water vapor at $T_{\text{H2O,s}}$ and the density of water vapor in the ambient air. $T_{\text{H2O,s}}$ is the surface temperature of the retained water. The vaporization coefficient of surface water c_{sv} is estimated to be 0.0085 m/s (Krakow *et al.*, 1992b).

$$\rho_{H_2O} \frac{d\delta_{H_2O}}{dt} = c_{sv} \left(\rho_{H_2O,amb} - \rho_{H_2O,s} \right) \qquad (5\text{-}19)$$

$$k_{H_2O} \frac{T_{H_2O} - T_{H_2O,s}}{\delta_{H_2O}/2} = \alpha_a \left(T_{H_2O,s} - T_{amb} \right) + c_{sv} \left(\rho_{H_2O,s} - \rho_{H_2O,amb} \right) \Delta h_{fg} \qquad (5\text{-}20)$$
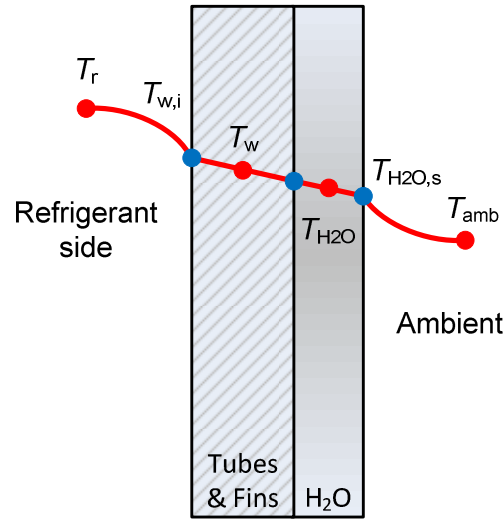
Figure 5.4 Vaporizing stage

5.2.5 Dry Heating Stage

In this stage, there is only sensible heat transfer between the wall and the ambient since there is no water retention on coil surfaces. Once reaching this stage, it means that the defrosting process is completed. The constituent equations of this

stage are Eq.(5-1), (5-2) and (5-21). The heat transport between the wall and the ambient is determined based on whether the evaporator fan is On or Off.

$$k_w A_o \frac{T_w - T_{w,o}}{\delta_w / 2} = \begin{cases} \dot{m}_a c_{p,a} (T_{w,o} - T_a) \left[1 - \exp\left(-\frac{\alpha_a A_{o,eff}}{\dot{m}_a c_{p,a}} \right) \right] & Fan\ On \\ \alpha_a A_{o,eff} (T_{w,o} - T_a) & Fan\ Off \end{cases} \tag{5-21}$$
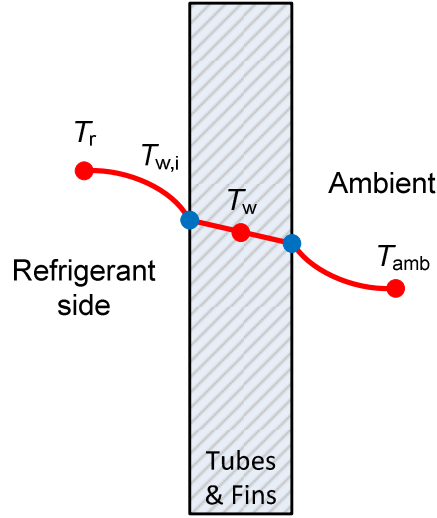
Figure 5.5 Dry heating stage
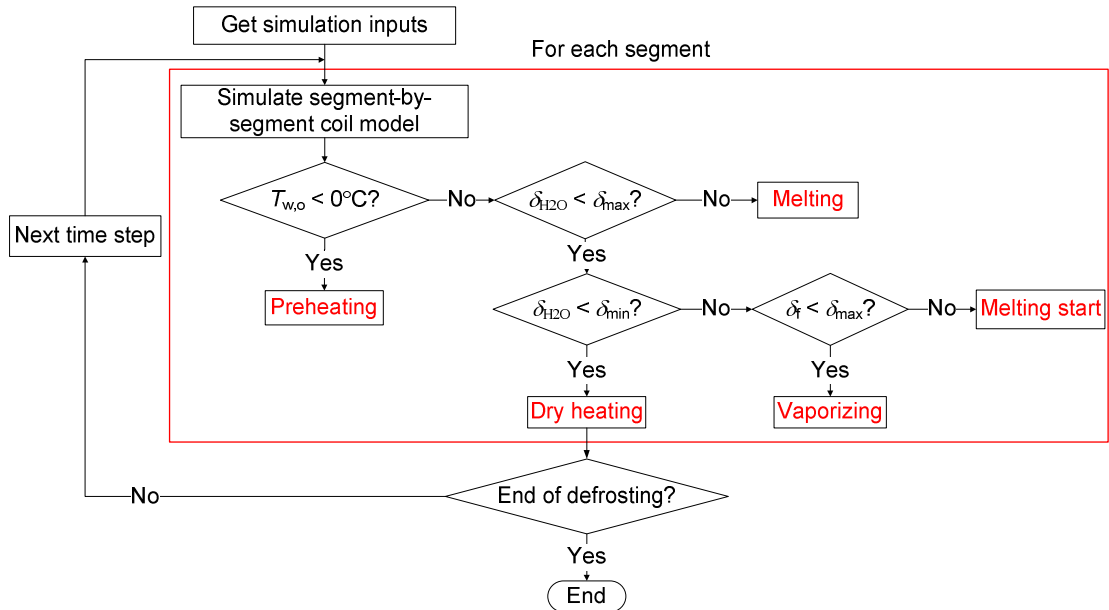
Figure 5.6 Algorithm for defrosting model

174

5.3 Simulation Results

Utilizing the developed model, the transients of the FTVI heat pump system during the reverse-cycle defrosting are explored. Unfortunately, there are no good experimental data to validate the proposed defrosting model. Hence, only simulation results are presented here.

The simulation case is set up as follows: After it has been running the heating mode for 3000 sec, the unit is shut down for 25 sec. Then the reverse-cycle defrosting is initiated by turning on the unit again with the reversing valve being energized. In the meantime, two three-way valves before the flash tank are energized to ensure that the inlet and outlet are not switched in the reversed mode. During the defrosting period, the fans for the both coils are turned off; the upper-stage EEV is fully opened and the vapor injection is disabled by closing the solenoid valve prior to the injection port of the compressor (Figure 5.7). The defrosting process is terminated at 3700 sec by shutting off the system. The system is turned on and restored to the heating mode again at 3725 sec.
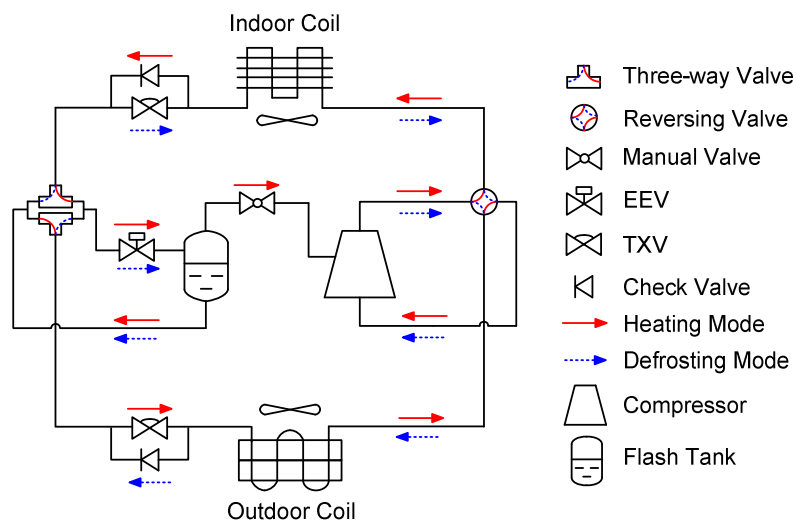
Figure 5.7 Heating and defrosting mode of the FTVI system

The following provides a detailed description of the system dynamics during the frosting/defrosting cycle. Simulation results are plotted and discussed.

5.3.1 Frosting Dynamics

The case in Chapter 4 tells us that TXV hunting is about to kick in after the system has been running the heating mode for 50 minutes. In order to avoid the resulting operating instabilities, the frosting cycle is terminated after 50 min of operation. The system dynamics during the frosting cycle have been presented in Chapter 4 in great detail and will not be repeated. The case in this chapter differs from the case in Chapter 4 only in that the upper-stage EEV opening is fixed at 16% in the heating mode to avoid any complications caused by the controllers.

5.3.2 Shut-down Period

The shut-down period ranges from 3000 sec to 3025 sec. The frost cycle is terminated at 3000 sec by shutting down the system. At the same time, both coil fans are de-energized. During this short period, the refrigerant migrates to the low-pressure side from the high-pressure side. As a result, the discharge and intermediate pressures tend to decrease, whereas the suction pressure tends to rise. Readers are referred to Section 3.6.4 for more details about the shut-down transients.

5.3.3 Defrost Initiation

The defrost initiation period ranges from 3025 sec to 3060 sec. At 3025 sec, the system is turned on again, and the reversing valve is engaged and switched to the defrosting mode. At the same time, two three-way valves before the flash tank are engaged as well to ensure that the inlet and outlet are not switched in the reversed mode, and the vapor injection is disabled by closing the solenoid valve prior to the injection port of the compressor. Meanwhile, the upper-stage EEV opening increases

176

from 16% to 100%. Please note that both coil fans are still de-energized during the defrosting cycle, which means the air flow rate is zero.

When the system is switched, the refrigerant inlet of the coils during the frosting cycle is turned into the outlet during the defrosting cycle, while the refrigerant outlet of the coils during the frosting cycle is turned into the inlet during the defrosting cycle. However, in the graphs presented in this section, please note that the inlet and outlet of the coils in the defrosting cycle still follow the definitions in the frosting cycle.

Shortly after the engagement of the reversing valve, the discharge, flash tank and suction pressures equalize together at 3026 sec (Figure 5.8). Within this very short period, the discharge pressure decreases from 1800 kPa to 1270 kPa, whereas the suction and the flash tank pressures surge to 1270 kPa from 734 kPa and 1010 kPa, respectively. This abrupt drop in the discharge pressure can be explained as the result of the sudden exposure of the compressor discharge to the lower pressure in the outdoor coil, whereas the abrupt rise of the suction pressure is attributed as the sudden exposure of the compressor suction to the higher pressure in the indoor coil. The rapid increase in the flash tank pressure is because of the sudden exposure of the liquid outlet of the flash tank to the high pressure in the indoor coil.

After the pressure equalization, the suction pressure will further rise slightly to 1320 kPa at 3034 sec. This is because the sudden decrease in the pressure in the indoor coil causes the liquid refrigerant to vaporize and flush to the compressor suction. After 3034 sec, the suction pressure starts to decrease since the compressor continuously draws the refrigerant from the indoor coil on the one hand; on the other

hand, the refrigerant replenishment through the TXV of the indoor coil is insufficient due to small pressure differential between the flash tank and the indoor coil (remember the refrigerant liquid from the flash tank will enter the indoor coil during the defrosting cycle).

However, the discharge pressure will decrease further to 992 kPa at 3032 sec after the pressure equalization. This is because the sudden rise in the pressure in the outdoor coil during the pressure equalization results in the massive condensation of refrigerant (the outdoor coil is fully covered by the frost and tube wall temperatures are very low) and thus lowering the refrigerant pressure. After that, the pressure in the outdoor coil rises to 1280 kPa at 3050 sec because the compressor continuously pumps the refrigerant to the outdoor coil. Moreover, the refrigerant in the flash tank flows back to the outdoor coil during this period as well because the flash tank pressure is still higher than the pressure in the outdoor coil. After 3050 sec, the refrigerant flow is reversed because the pressure in the outdoor coil becomes higher than that in the flash tank, resulting in a drop in the outdoor coil pressure.

After the pressure equalization, the outgoing flow from the indoor coil to the flash tank does not halt until 3046 sec. With the further fall in pressure in the indoor coil, the refrigerant starts to flush back from the flash tank. However, this replenishment is still insufficient to compensate the refrigerant flow drawn by the compressor at this point. As a result, the pressure in the indoor coil continues to decrease and reaches to its minimum of 461 kPa at 3060 sec.

During the period from 3026 sec to 3052 sec, the refrigerant in the flash tank continues flowing back to the outdoor coil via the inlet even after the engagement of

the three-way valves because of pressure difference. Because the incoming flow from the indoor coil does not suffice to compensate the outgoing flow during the same period, the flash tank pressure continues to fall. After 3052 sec, the reversed pressure difference is established between the indoor coil and flash tank, the refrigerant flow is reversed from the flash tank to the indoor coil. Since the upper-stage EEV is fully opened, there is little flow restriction between the outdoor coil and the flash tank, and the pressure in the flash tank will synchronize with that in the outdoor coil.

After the defrosting cycle is initiated, the heating capacity (indoor coil heat load) decreases rapidly from 8.1 kW to -1.8 kW within 60 sec. The sudden decrease in the heating capacity is the result of massive evaporation of the refrigerant in the indoor coil, which is corroborated by the fact that the refrigerant quality in the indoor coil increases shortly after the pressure equalization (Figure 5.10). During the same period, the cooling capacity (outdoor coil heat load) increases from -6.4 kW to 6.0 kW, which is the result of massive condensation of the refrigerant in the outdoor coil due to the sudden increase in the pressure in the outdoor coil.

The refrigerant superheat at the outlet of the indoor coil (referred as the inlet of the indoor coil in Figure 5.11) drops to zero for 20 sec after the pressure equalization, indicating that two-phase refrigerant leaves the indoor coil. Then the superheat increases rapidly, denoting all the refrigerant in the indoor coil completely vaporizes and no liquid floods into the suction line. At 3052 sec, the refrigerant liquid starts to leave the outdoor coil since noticeable subcooling at the outlet of the outdoor coil (referred as the inlet of the outdoor coil in Figure 5.11) occurs.

179

The refrigerant mass distribution in various components is shown in Figure 5.12. After the defrosting cycle is initiated, the refrigerant in the indoor coil depletes because of two reasons: (1) the refrigerant drains to the flash tank due to the pressure difference; (2) the compressor draws the refrigerant from the indoor coil. During the same the period, the rapid increase in the refrigerant mass in the outdoor coil is caused by two reasons as well: (1) the refrigerant replenishment from the flash tank due to the pressure difference; (2) the refrigerant from the indoor coil has been transferred to the outdoor coil by the compressor. At 3050 sec, the refrigerant mass in the outdoor coil reaches to the maximum, representing approximately 70% of the total charge. With the buildup of the pressure in the outdoor coil, the excessively stored refrigerant in the outdoor coil will be redistributed to other components.

The liquid level in the flash tank increases rapidly after the system is shut down, because a large amount of the refrigerant flushes to the flash tank from the indoor coil. As shown in Figure 5.8, a reversed pressure difference between the outdoor coil and flash tank is not established until 3060 sec, resulting in no replenishment of refrigerant to the flash tank at all during the period. Therefore, the liquid level in the flash tank falls shortly after the pressure equalization.

The variation in the refrigerant inventory in various components can also be justified by the variation in the refrigerant mass flow rates in Figure 5.13a. The positive mass flow denotes the incoming flow, whereas the negative flow denotes the outgoing flow. Because of the engagement of the reversing valve and two three-way valves at 3025 sec, reverse flows occur at the inlet of the indoor coil, outlet of the outdoor coil, inlet and outlet of the flash tank. When the reversed pressure differences

among the indoor coil, flash tank and outdoor coil are established around at 3050 sec, reverse flows occur again at the inlet and outlet of the flash tank, outlet of the indoor coil, and inlet of the outdoor coil.

The variation in the frost thickness on each tube is given in Figure 5.14. It can be seen that the frost already starts to melt during this period.

5.3.4 Melting Frost

The melting frost period ranges from 3060 sec to 3522 sec. With continuous evaporation of refrigerant in the indoor coil and augmented incoming flow from the flash tank, the pressure in the indoor coil starts to increase after it reaches to its minimum at 3060 sec, and finally plateaus at 694 kPa. The increase in the pressure in the indoor coil causes the heat transfer temperature difference between the refrigerant and tube walls to diminish, resulting in that two-phase flow leaves the indoor coil from 3230 sec to 3342 sec (Figure 5.10). Eventually the superheat leaving the indoor coil stabilizes at approximately 8 K.

From 3050 sec the pressure in the outdoor coil starts to decrease as a result of the rising outgoing flow to the flash tank. At 3136 sec, it reaches to its local minimum of 1040 kPa and increases thereafter along with the pressure in the indoor coil. At 3366 sec, the pressure in the outdoor coil maintains 1150 kPa.

There is more total frost accumulation for Circuit #5 and #6 in the outdoor coil because these two circuits have more tubes than the other four circuits. Meanwhile, more tubes means that the refrigerant has to travel longer distance, resulting in less refrigerant flow entering these two circuits. Consequently, it takes longer time to completely melt the frost deposited on the 24 tubes at the bottom of the outdoor coil. In terms of the defrosting duration, Tube #1 is the longest among the 20 tubes on the

top of the coil, Tube #11 is the longest among the 20 tubes in the middle, while Tube #21 is the longest among the 24 tubes at the bottom. An interesting fact among these three tubes is that they are all in the first row and they are all close to the refrigerant outlet during the defrosting cycle. That they are all in the first row ensures that they have relatively more frost accumulation. That they are all close to the refrigerant outlet during the defrosting cycle means that the high temperature refrigerant has to melt the frost on the preceding tubes first before reaching to them. Among these three tubes, the defrosting duration of Tube #21 is the longest thanks to the colder refrigerant flowing through it (Figure 5.15).

(a)

(b)

182
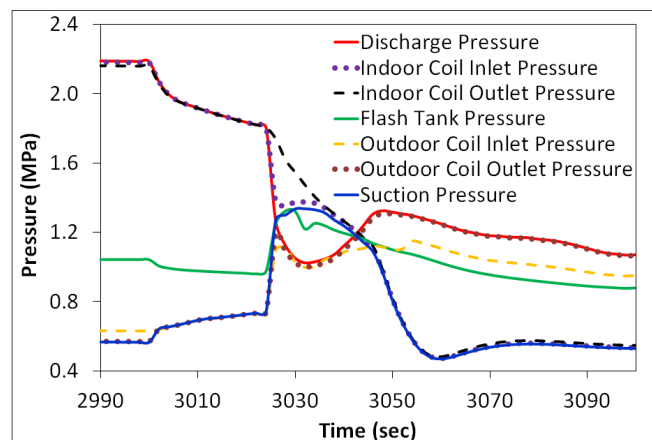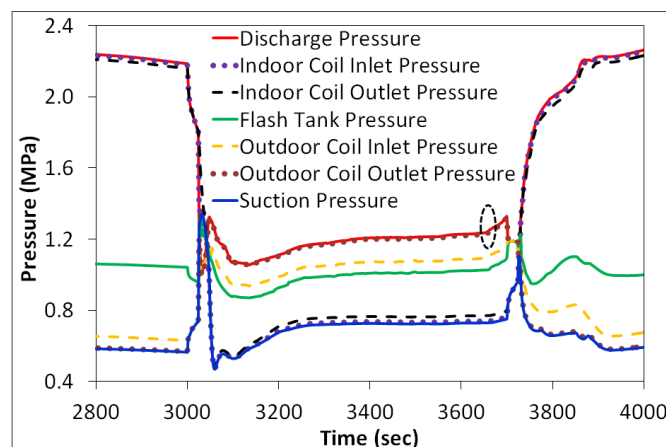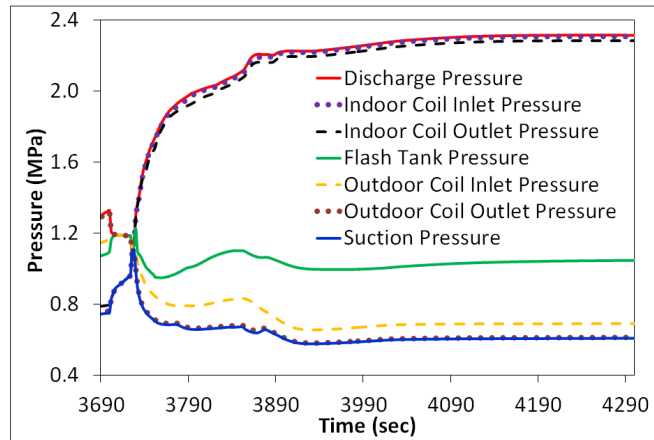
Figure 5.8 Pressure transients: (a) - During defrosting initiation; (b) - During the complete defrosting cycle; (c) - At the defrosting termination
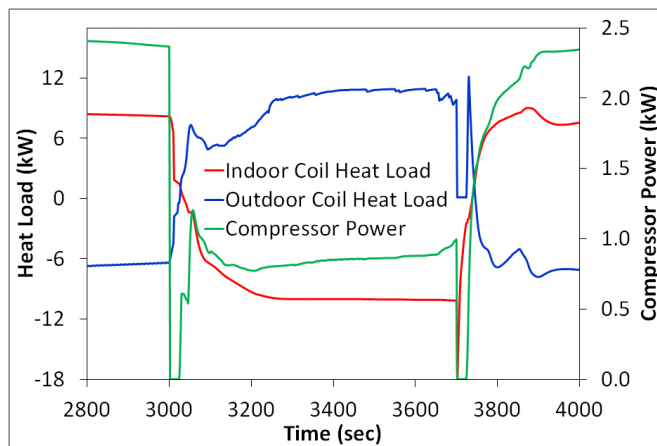
Figure 5.9 Air side heat loads and compressor power
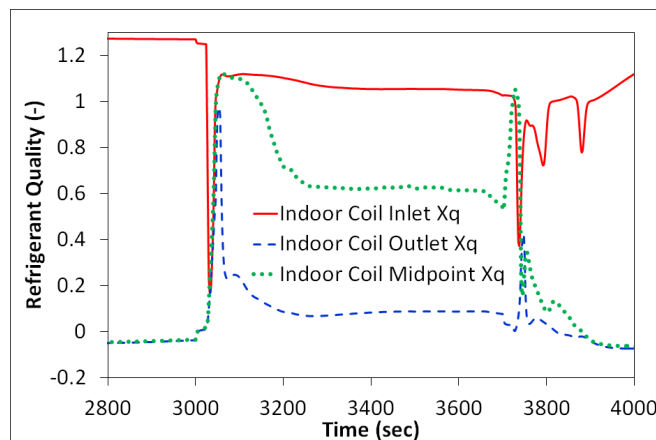
Figure 5.10 Refrigerant quality of the indoor coil

183
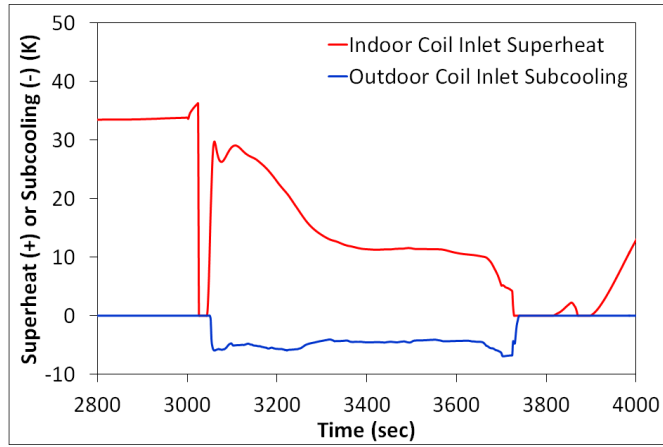
Figure 5.11 Refrigerant superheat/subcooling
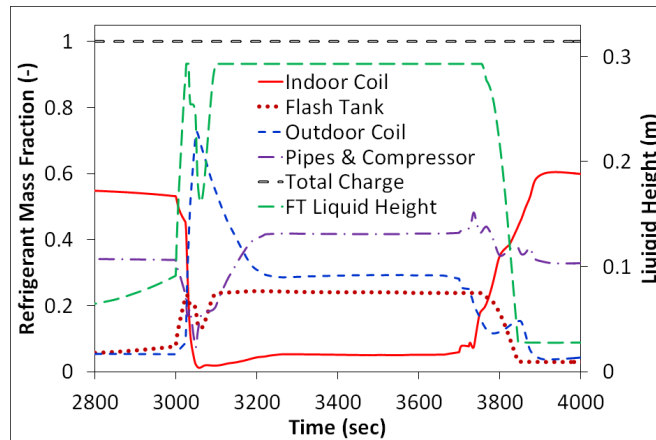
Figure 5.12 Predicted refrigerant mass distribution and flash tank liquid height
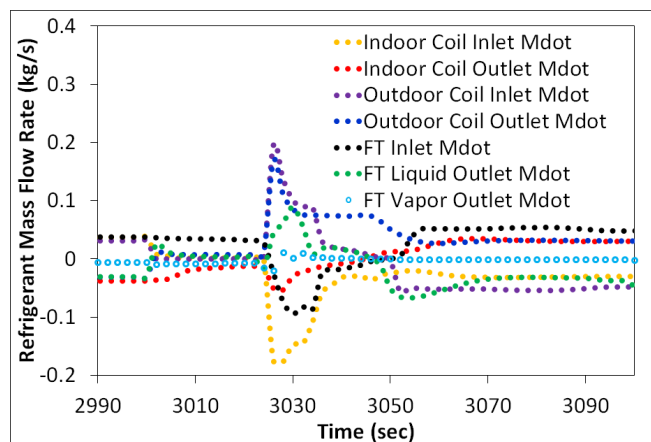
(a)
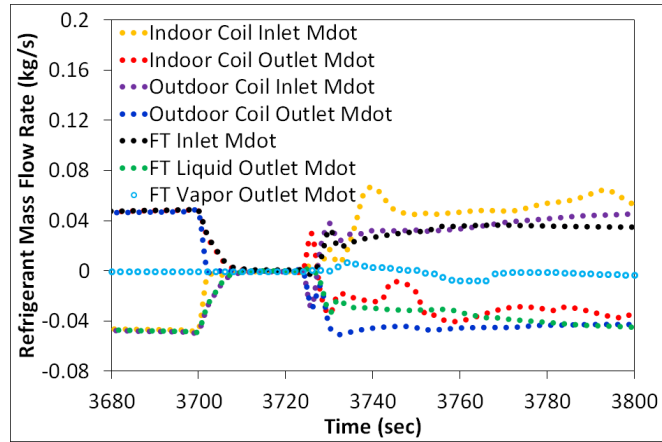
(b)

Figure 5.13 Refrigerant mass flow rates: (a) - Defrosting initiation; (b) - Frosting restoration
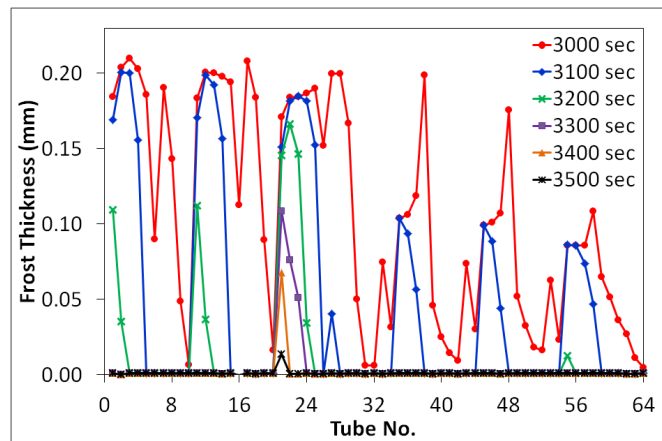
Figure 5.14 Variation in the frost thickness on each tube
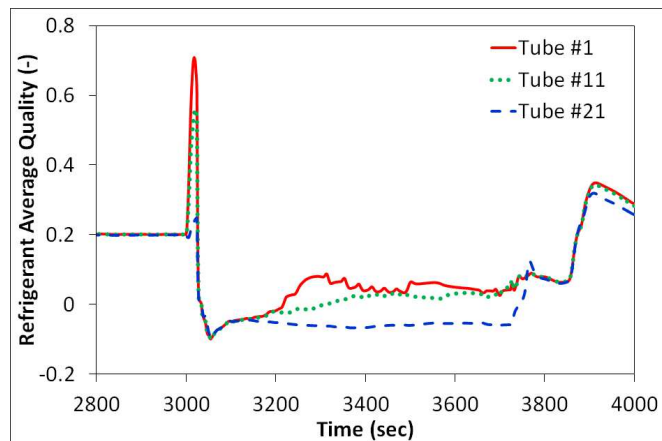
Figure 5.15 Refrigerant quality in Tube #1, #11 and #21 of the outdoor coil

185
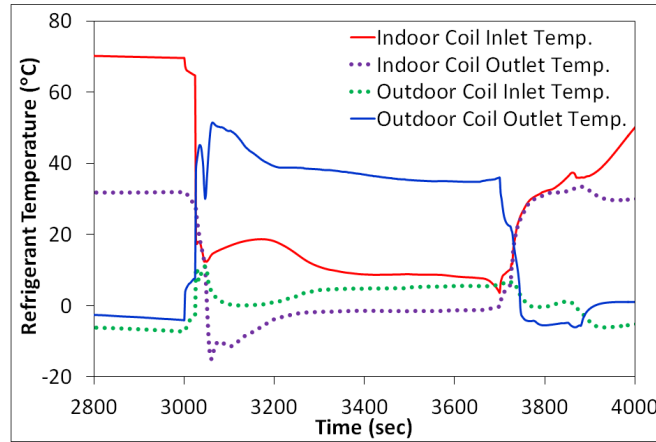
Figure 5.16 Refrigerant temperatures of the heat exchangers

5.3.5 Draining Melted Frost

The draining stage ranges from 3522 sec to 3700 sec. By 3522 sec all of the frost has already melted from the outdoor coil, and the temperature of the refrigerant exiting the outdoor coil has stabilized at 5.4 °C (Figure 5.16).

By 3656 sec, some of the melted surface water on the outdoor coil has evaporated, and a portion of the outdoor coil surfaces has been exposed to the ambient air, resulting in a reduction of heat transfer. The latent heat on the air side has dropped from 7955 W to 6695 W between 3656 sec and 3700 sec, and the refrigerant pressure in the outdoor coil has increased by 90 kPa during the same period (Figure 5.8b). It can be concluded that 3656 sec is the critical point where the system parameters change rapidly and at which the defrosting process can be terminated. A similar finding was reported by Huang *et al*. (2007).

5.3.6 Defrost Termination and Recovery

At 3700 sec, the defrosting process is terminated and the system is restored to the heating mode at 3725 sec after it has been shut down for 25 sec. Shortly after the system is shut down, the pressure in the outdoor coil and the flash tank pressure

equalize and decrease. Meanwhile, the suction pressure and the pressure in the indoor coil equalize and increase together.

At 3725 sec, the system is turned on. At the same time, the reversing valve and three-way valves are switched. At 3730 sec, the opening of the upper-stage EEV is adjusted back to 16% from 100%, and the solenoid valve prior to the injection port of the compressor is opened. Large pressure swings occur after the switch of the reversing valve. Since the compressor draws the refrigerant from the outdoor coil to the indoor coil, the pressure in the indoor coil rises, while the pressure in the outdoor coil decreases (Figure 5.8c). The pressure in the flash tank reaches to the maximum at 3730 sec and falls down thereafter. This is because of (1) the reduced refrigerant supply from the indoor coil due to the decreased opening of the upper-stage EEV and (2) the onset of the injection flow.

Unlike the beginning of the defrosting process where the pressures exhibit more drastic changes, the pressure transients at the beginning of the restoration process are much more benign. This can be explained as the inactive refrigerant stored in the flash tank during the defrosting process is released out to supply the outdoor coil during the restoration process (Figure 5.13b). As a result, the compressor is not starved for refrigerant.

5.3.7 Defrosting Efficiency

During the defrosting process, the total energy supplied by the refrigerant predicted by the model is 5191.9 kJ. The energy that is used to melt the frost is 849.8 kJ, which accounts for 16.4% of the total energy supplied by the refrigerant. This percentage is consistent with the study by Niederer (1976), who claimed that the

efficiency for a typical defrosting process was only 15-25%. The breakdown of the energy flow during the defrosting cycle is shown in Table 5.1.

Table 5.1 Energy breakdown during the defrosting period

Parameter	Model Prediction (kJ)	Percentage
Q_r	5191.9	100%
Q_a	3931.4	75.7%
Q_{sen}	611.1	11.8%
Q_{lat}	3320.3	63.9%
Q_{st}	410.8	7.9%
Q_{melt}	849.8	16.4%

Q_r: the total energy supplied by the refrigerant

Q_a: the total energy transferred to the surroundings

Q_{sen}: the convective heat transfer to the surroundings

Q_{lat}: the latent energy transferred to the surroundings due to the mass transport between the frost and the air

Q_{st}: the energy stored by tubes and fins

Q_{melt}: the energy used to warm and melt the frost

5.4 Summary

Utilizing the developed models, the dynamic behavior of the FTVI heat pump during the reverse-cycle defrosting is explored. The unified heat exchanger model with the frosting and defrosting modeling capabilities allows more accurate performance assessment for heat pump systems.

Although the concept of the reverse-cycle defrosting is quite simple, the resulting transient processes in the system are very complex. A detailed understanding of this process requires a comprehensive analysis of various

parameters throughout the system. Although no experimental validation is provided, the presented simulation study facilitates the characterization of the transient behavior of heat pumps undergoing the reverse-cycle defrost, and can also be used to design the defrost control strategy to improve the overall performance of heat pumps.

6 Moving Boundary Heat Exchanger Models

6.1 Introduction

In the transient simulations of thermo-fluid systems, two modeling techniques are usually applied for heat exchangers: namely phase-independent Finite Volume Method (FVM) and phase-dependent Moving Boundary Method (MBM). The FVM based models are often referred to as the discretized or distributed parameter models, as described in Chapter 2. This chapter will focus on the MBM based models, often referred to as the moving boundary models.

Compared to moving boundary models, distributed parameter models ensure high fidelity predictions in heat transfer and fluid flow phenomena. However, these models are not well suited for control design where moving boundary models are more favorable. By casting the resulting equations into a linearized state-space form, moving boundary models were initially used to predict the transients under minor variations around a steady-state operating point and investigate the multivariable feedback control of HVAC systems. Recently, there is an emerging interest in applying moving boundary modeling framework to predict the cycling transients of vapor compression systems. The underlying challenge of this aspect of research is to develop robust switching schemes to handle transitions between different model representations to accommodate the changing number of fluid phases under large disturbances.

Table 6.1 Comparison of moving boundary models

Moving boundary model	Evaporator	Condenser	Switching	Δp	$\dfrac{d\bar{\gamma}}{dt}$	$\dfrac{dh_{out}}{dt}$
Grald & MacArthur (1992)	TP-V					
He (1996)	TP-V	V-TP-L				Yes
Willatzen et al. (1998)		V-TP-L				Yes
Pettit et al. (1998)	L-TP-V; TP-V; TP; L-TP		Yes			Yes
Jensen & Tummescheit (2002)	L-TP-V					Yes
Leducq et al. (2003)	TP-V	V-TP-L				
Tian & Li (2005)	TP; TP-V	V-TP-L		Yes		
Yebra et al. (2005)		V-TP-L		Yes		Yes
Rasmussen (2006)	TP-V					Yes
Zhang & Zhang (2006)	TP; TP-V		Yes			Yes
Diaz (2007)	TP-V					Yes
Kumar et al. (2008)	TP-V	V-TP-L				
McKinley & Alleyne (2008)		V-TP-L; V-TP	Yes		Yes	
Bendapudi et al. (2008)	TP-V; TP	V, V-TP; V-TP-SC	Yes			Yes
Eldredge et al. (2008)	TP-V	V-TP-L			Yes	
Liang et al. (2010b)	TP-L; TP	V-TP-L	Yes			Yes
Li & Alleyne (2010)	TP-V; TP	V-TP-L; V-TP; TP-L; TP; V	Yes		Yes	
Cecchinato & Mancini (2012)	TP-V; TP		Yes			
Proposed Model	**All possible modes**	**All possible modes**	**Yes**	**Yes**	**Yes**	**Yes**

The following conclusions can be drawn from a thorough review of the moving boundary models reported in the literature (Table 6.1):

(1) A majority of these models are not capable of predicting cycling transients of vapor compression systems except the recent model presented by Li and Alleyne (2010). However, Li & Alleyne's work is far from flawless and there is still a plenty of room for further improvement, especially for the calculation on the air side heat transfer.

(2) Most models do not take into account refrigerant pressure drop. In fact, it is important to include the fluid momentum conservation in some applications, such as electronics cooling, where micro channels are commonly used and significant

pressure drop can be observed in micro-scale heat exchangers (Kandlikar *et al.*, 2006), and large-scale heat exchangers in solar thermal plants (tube length can be as long as over one thousand meters), where pressure drop must be considered. A couple of exceptions are found in Tian and Li (2005) and Yebra *et al.* (2005). In Tian's work, static pressure loss is assumed to concentrate at the end of each phase regime. However, this approach only works fine when there is no creation or destruction of fluid phases, otherwise, a mathematical discontinuity in pressure calculation will be encountered. Following the finite volume method with the staggered-grid discretization scheme, Yebra *et al.* (2005) presented a general moving boundary model containing the momentum conservation. But the inclusion of the transient form of the momentum conservation in their model makes the computation very complicated.

(3) These models can be classified into two categories: (a) the category including mean two-phase void fraction in the state vector, and (b) the category including refrigerant outlet enthalpy in the state vector. Both approaches have upsides and downsides. The inclusion of mean two-phase void fraction in the state vector ensures that mean void fraction is continuous during the switch. Therefore, refrigerant mass can be conserved. However, an implicit transcendental equation needs to be solved for the refrigerant outlet enthalpy. That is the reason why Thermosys (McKinley & Alleyne, 2008; Li & Alleyne, 2010) uses huge look-up tables correlating mean void fraction, the refrigerant pressure, and the outlet vapor quality before conducting the simulation in order to improve the computational efficiency. However, generating such huge look-up tables is very tedious and

time-consuming since these tables are generally refrigerant dependent and application specific.

When refrigerant outlet enthalpy is a state variable instead, there is no need to solve an implicit transcendental equation. However, refrigerant mass is not conserved because mean void fraction is not continuous during the switch.

Clearly, there is a need to develop an improved moving boundary model to address the above research gaps. This chapter aims at developing an advanced moving boundary model to fulfill the following objectives:

(1) Be capable of handling transitions between different model representations to accommodate the changing number of fluid phases;

(2) Be capable of accounting for refrigerant pressure drop in a simple fashion;

(3) Eliminate the need of solving the implicit transcendental equation to calculate the refrigerant outlet enthalpy, but in the meantime the refrigerant mass can be conserved;

(4) A more accurate evaluation for the air side heat transfer.

6.2 Modeling Assumptions

Two different approaches (Figure 6.1) are proposed to account for refrigerant pressure drop in the proposed moving boundary models.

Approach #1: It is assumed that refrigerant pressure is uniform within the heat exchanger and the pressure drop is concentrated at the outlet of the heat exchanger.

Approach #2: It is assumed that refrigerant pressure varies linearly within the entire heat exchanger.

The conventional moving boundary models without refrigerant pressure drop use the inlet mass flow rate, inlet enthalpy and outlet mass flow rate as the boundary conditions. However, the outlet pressure is used in place of the outlet mass flow rate in the proposed models.
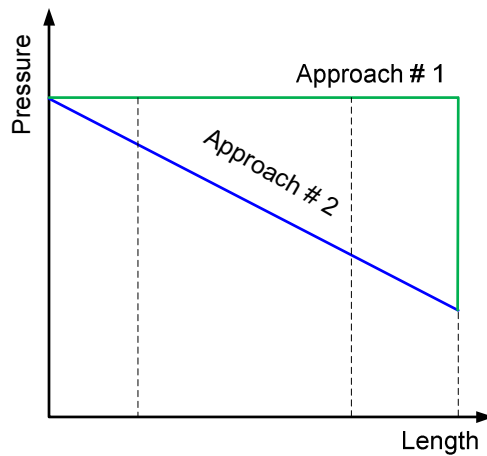
Figure 6.1 Two different approaches to calculate pressure drop

The following key assumptions are made:

(1)   one-dimensional unsteady refrigerant flow;

(2)   quasi-steady air flow;

(3)   negligible viscous dissipation;

(4)   negligible axial conduction in fluid and pipe;

(5)   negligible kinetic energy and gravitational potential energy;

(6)   linear refrigerant enthalpy profile in each region;

(7)   dynamic pressure waves are of minor importance for a heat transfer analysis and thus are neglected;

(8)   average properties in each region;

(9)   thermodynamic equilibrium for the vapor and liquid in two-phase flows;

(10)   constant cross sectional area in the pipe.

6.3 Condenser Model

For brevity, only the detailed derivations for the governing equations of the V-TP-L mode of the condenser model are given. The equations for the other modes can be derived similarly.

6.3.1 V-TP-L Mode
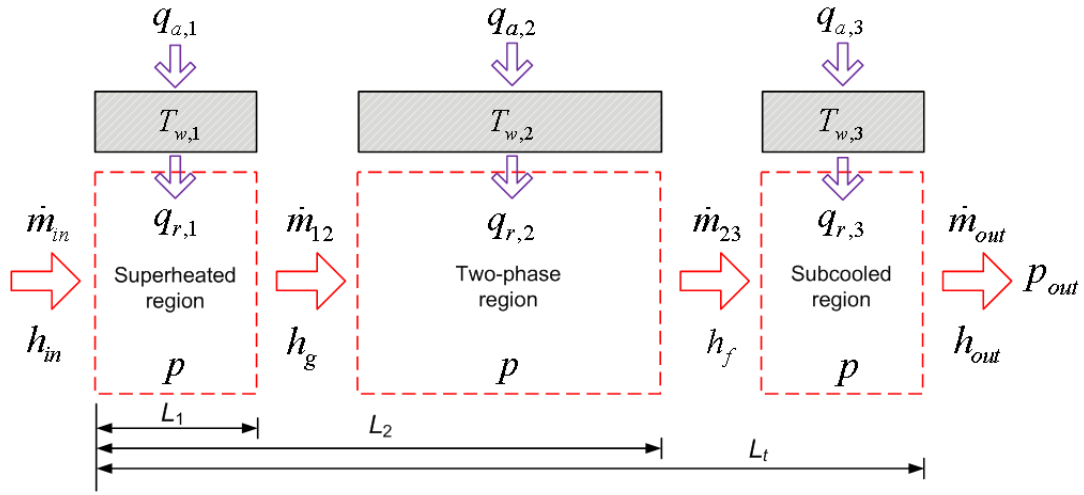
Figure 6.2 V-TP-L mode with approach #1

The condenser can have as many as three regions, i.e., superheated, two-phase and subcooled region. In moving boundary models, each region is analyzed using the lumped-parameter approach. The three-zone condenser model with pressure drop concentrated at the outlet of the heat exchanger (Figure 6.2) yields 22 parameters. Subscript "1" denotes the superheated region, "2" denotes the two-phase region and "3" denotes the subcooled region.

q_a = heat transfer rate from the ambient to the tube wall;

T_w = average wall temperature;

q_r = heat transfer rate from the tube wall to the refrigerant flow;

L_1 = zone length of region 1;

L_2 = combined zone length of region 1 & 2;

L_t = overall length of the condenser;

p = refrigerant pressure in region 1, 2 & 3;

p_{out} = refrigerant pressure at the outlet of the heat exchanger;

$\dot{m}_{in}$ = refrigerant mass flow rate entering the heat exchanger;

$\dot{m}_{12}$ = refrigerant mass flow rate at the boundary between region 1 and region 2 (a positive value denotes that the refrigerant flows from region 1 to region 2; a negative value denotes that the refrigerant flows from region 2 to region 1)

$\dot{m}_{23}$ = refrigerant mass flow rate at the boundary between region 2 and region 3;

$\dot{m}_{out}$ = refrigerant mass flow rate leaving the heat exchanger;

h_{in} = enthalpy of the refrigerant entering the heat exchanger;

h_g = enthalpy of the refrigerant at the boundary between the superheated region and two-phase region;

h_f = enthalpy of the refrigerant liquid at the boundary between the two-phase region and subcooled region;

h_{out} = enthalpy of refrigerant leaving the heat exchanger.

6.3.1.1 Governing Equations: Refrigerant Flow

Mass balance of one-dimensional flow

$$\frac{\partial(\rho A)}{\partial t} + \frac{\partial \dot{m}}{\partial z} = 0 \tag{6-1}$$

Energy balance of one-dimensional flow

$$\frac{\partial \left[A(\rho h - p) \right]}{\partial t} + \frac{\partial (\dot{m}h)}{\partial z} = \alpha_r \pi d_i \left(T_w - T_r \right)$$
(6-2)

6.3.1.1.1 V Region

6.3.1.1.1.1 Mass Balance

Integrating Eq. (6-1) for the superheated region from $z = 0$ to $z = L_1$ yields

$$\int_0^{L_1} \frac{\partial (\rho A)}{\partial t} dz + \int_0^{L_1} \frac{\partial \dot{m}}{\partial z} dz = 0$$
(6-3)

Applying Leibniz's rule for the first term of Eq. (6-3)

$$\frac{d}{dt} \int_{a(t)}^{b(t)} f(x,t) dx = f(b(t),t) b'(t) - f(a(t),t) a'(t) + \int_{a(t)}^{b(t)} \frac{\partial f(x,t)}{\partial t} dx$$
(6-4)

By recognizing that refrigerant density at $z = L_1$ is actually the density of saturated refrigerant vapor ρ_g, one can get

$$A \frac{d}{dt} \int_0^{L_1} \rho dz - A \rho_g \frac{dL_1}{dt} = \dot{m}_{in} - \dot{m}_{12}$$
(6-5)

The first term of Eq. (6-5) can be greatly simplified by introducing the mean refrigerant density of the superheated region, $\bar{\rho}_1 = \frac{1}{L_1} \int_0^{L_1} \rho dz$

$$\frac{d}{dt} \int_0^{L_1} \rho dz = \frac{d}{dt} \left(\bar{\rho}_1 L_1 \right) = L_1 \frac{d\bar{\rho}_1}{dt} + \bar{\rho}_1 \frac{dL_1}{dt}$$
(6-6)

Substituting Eq. (6-6) into Eq. (6-5) yields

$$A L_1 \frac{d\bar{\rho}_1}{dt} + A \left(\bar{\rho}_1 - \rho_g \right) \frac{dL_1}{dt} = \dot{m}_{in} - \dot{m}_{12}$$
(6-7)

The mean refrigerant properties in the superheat region can be determined based on the pressure p and the mean enthalpy $\bar{h}_1 = \frac{1}{2} \left(h_{in} + h_g \right)$. Therefore,

197

$$\bar{\rho}_1 \approx \rho\left(p, \bar{h}_1\right) \tag{6-8}$$

The derivative of the density with respect to the time can be expanded as follows by applying the chain rule

$$
\begin{aligned}
\frac{d\bar{\rho}_1}{dt} &= \left.\frac{\partial\bar{\rho}_1}{\partial p}\right|_h \frac{dp}{dt} + \left.\frac{\partial\bar{\rho}_1}{\partial \bar{h}_1}\right|_p \frac{d\bar{h}_1}{dt} \\
&= \left.\frac{\partial\bar{\rho}_1}{\partial p}\right|_h \frac{dp}{dt} + \frac{1}{2}\left.\frac{\partial\bar{\rho}_1}{\partial \bar{h}_1}\right|_p \left(\frac{dh_{in}}{dt} + \frac{dh_g}{dt}\right) \\
&= \left.\frac{\partial\bar{\rho}_1}{\partial p}\right|_h \frac{dp}{dt} + \frac{1}{2}\left.\frac{\partial\bar{\rho}_1}{\partial \bar{h}_1}\right|_p \left(\frac{dh_{in}}{dt} + \frac{dh_g}{dp}\frac{dp}{dt}\right) \\
&= \left(\left.\frac{\partial\bar{\rho}_1}{\partial p}\right|_h + \frac{1}{2}\left.\frac{\partial\bar{\rho}_1}{\partial \bar{h}_1}\right|_p \frac{dh_g}{dp}\right)\frac{dp}{dt} + \frac{1}{2}\left.\frac{\partial\bar{\rho}_1}{\partial \bar{h}_1}\right|_p \frac{dh_{in}}{dt}
\end{aligned} \tag{6-9}
$$

Substituting Eq. (6-9) into Eq. (6-7) finally yields

$$A\left[L_1\left(\left.\frac{\partial\bar{\rho}_1}{\partial p}\right|_h + \frac{1}{2}\left.\frac{\partial\bar{\rho}_1}{\partial \bar{h}_1}\right|_p \frac{dh_g}{dp}\right)\frac{dp}{dt} + \frac{1}{2}L_1\left.\frac{\partial\bar{\rho}_1}{\partial \bar{h}_1}\right|_p \frac{dh_{in}}{dt} + \left(\bar{\rho}_1 - \rho_g\right)\frac{dL_1}{dt}\right] = \dot{m}_{in} - \dot{m}_{12} \tag{6-10}$$

6.3.1.1.1.2 *Energy Balance*

Integrating the energy balance equation Eq. (6-2) for the superheated region from $z = 0$ to $z = L_1$ yields

$$\int_0^{L_1}\frac{\partial\left[A\left(\rho h - p\right)\right]}{\partial t}dz + \int_0^{L_1}\frac{\partial\left(\dot{m}h\right)}{\partial z}dz = \int_0^{L_1}\alpha_r \pi d_i\left(T_w - T_r\right)dz \tag{6-11}$$

Applying Leibniz's rule to the first term of Eq. (6-11) and integrating the remaining terms by assuming a constant heat transfer coefficient gives

$$A\left(\frac{d}{dt}\int_0^{L_1}\rho h\,dz - \rho_g h_g\frac{dL_1}{dt} - L_1\frac{dp}{dt}\right) = \dot{m}_{in}h_{in} - \dot{m}_{12}h_g + \alpha_{r,1}\pi d_i\int_0^{L_1}\left(T_w - T_r\right)dz \tag{6-12}$$

Let

$$\overline{\rho h} = \frac{1}{L_1} \int_0^{L_1} \rho h \, dz \approx \overline{\rho_1} \overline{h_1} \tag{6-13}$$

and

$$\overline{T}_{r,1} = \frac{1}{L_1} \int_0^{L_1} T_r \, dz \approx T\left(p, \overline{h_1}\right) \tag{6-14}$$

Substituting Eq. (6-13) & (6-14) into Eq. (6-12) becomes

$$A\frac{d}{dt}\left(\overline{\rho_1}\overline{h_1}L_1\right) - A\rho_g h_g \frac{dL_1}{dt} - AL_1 \frac{dp}{dt} = \dot{m}_{in} h_{in} - \dot{m}_{12} h_g + \pi d_i L_1 \alpha_{r,1}\left(T_{w,1} - \overline{T}_{r,1}\right) \tag{6-15}$$

The first term of Eq. (6-15) can be expanded as

$$A\frac{d}{dt}\left(\overline{\rho_1}\overline{h_1}L_1\right) = A\overline{\rho_1}\overline{h_1}\frac{dL_1}{dt} + A\overline{\rho_1}L_1\frac{d\overline{h_1}}{dt} + A\overline{h_1}L_1\frac{d\overline{\rho_1}}{dt} \tag{6-16}$$

Solving for $AL_1 \dfrac{d\overline{\rho_1}}{dt}$ from Eq. (6-7) and substituting it into Eq. (6-16) gives

$$\begin{aligned} A\frac{d}{dt}\left(\overline{\rho_1}\overline{h_1}L_1\right) &= A\overline{\rho_1}\overline{h_1}\frac{dL_1}{dt} + A\overline{\rho_1}L_1\frac{d\overline{h_1}}{dt} + \left(\dot{m}_{in} - \dot{m}_{12}\right)\overline{h_1} - A\left(\overline{\rho_1} - \rho_g\right)\overline{h_1}\frac{dL_1}{dt} \\ &= A\rho_g\overline{h_1}\frac{dL_1}{dt} + A\overline{\rho_1}L_1\frac{d\overline{h_1}}{dt} + \left(\dot{m}_{in} - \dot{m}_{12}\right)\overline{h_1} \end{aligned} \tag{6-17}$$

Substituting Eq. (6-17) into Eq. (6-15) yields

$$\begin{aligned} AL_1 &\left[\frac{1}{2}\overline{\rho_1}\frac{dh_{in}}{dt} + \left(\frac{1}{2}\overline{\rho_1}\frac{dh_g}{dp} - 1\right)\frac{dp}{dt}\right] + A\rho_g\left(\overline{h_1} - h_g\right)\frac{dL_1}{dt} \\ &= \dot{m}_{in}\left(h_{in} - \overline{h_1}\right) - \dot{m}_{r,12}\left(h_g - \overline{h_1}\right) + \pi d_i L_1 \alpha_{r,1}\left(T_{w,1} - \overline{T}_{r,1}\right) \end{aligned} \tag{6-18}$$

6.3.1.1.2 TP Region

6.3.1.1.2.1 *Mass Balance*

Integrating Eq. (6-1) for the two-phase region from $z = L_1$ to $z = L_2$ yields

$$\int_{L_1}^{L_2} \frac{\partial(\rho A)}{\partial t} \, dz + \int_{L_1}^{L_2} \frac{\partial \dot{m}}{\partial z} \, dz = 0 \tag{6-19}$$

199

Applying Leibniz's rule and recognizing that refrigerant density at $z = L_2$ is actually the density of saturated refrigerant liquid ρ_f gives

$$A\left(\frac{d}{dt}\int_{L_1}^{L_2}\rho dz + \rho_g\frac{dL_1}{dt} - \rho_f\frac{dL_2}{dt}\right) = \dot{m}_{12} - \dot{m}_{23} \tag{6-20}$$

The density of two-phase flow is determined based on the local void fraction

$$\rho = \rho_f + \left(\rho_g - \rho_f\right)\gamma \tag{6-21}$$

Substituting Eq. (6-21) into Eq. (6-20) becomes

$$A\frac{d}{dt}\left[\rho_f\left(L_2 - L_1\right)\right] + A\frac{d}{dt}\left[\left(\rho_g - \rho_f\right)\int_{L_1}^{L_2}\gamma dz\right] + A\rho_g\frac{dL_1}{dt} - A\rho_f\frac{dL_2}{dt} = \dot{m}_{12} - \dot{m}_{23} \tag{6-22}$$

Let

$$\overline{\gamma} = \frac{1}{L_2 - L_1}\int_{L_1}^{L_2}\gamma dz \tag{6-23}$$

The second term of Eq. (6-22) can be simplified as

$$A\frac{d}{dt}\left[\left(\rho_g - \rho_f\right)\int_{L_1}^{L_2}\gamma dz\right] = A\frac{d}{dt}\left[\left(\rho_g - \rho_f\right)\overline{\gamma}\left(L_2 - L_1\right)\right] \tag{6-24}$$

Substituting Eq. (6-24) into Eq. (6-22) and rearranging yields

$$\begin{aligned}
&A\left(L_2 - L_1\right)\left[\left(1 - \overline{\gamma}\right)\frac{d\rho_f}{dp} + \overline{\gamma}\frac{d\rho_g}{dp}\right]\frac{dp}{dt} + A\left(\rho_g - \rho_f\right)\overline{\gamma}\frac{dL_2}{dt} \\
&-A\left(\rho_g - \rho_f\right)\left(\overline{\gamma} - 1\right)\frac{dL_1}{dt} + A\left(\rho_g - \rho_f\right)\left(L_2 - L_1\right)\frac{d\overline{\gamma}}{dt} = \dot{m}_{12} - \dot{m}_{23}
\end{aligned} \tag{6-25}$$

6.3.1.1.2.2 Energy Balance

Integrating the energy balance equation Eq. (6-2) for the two-phase region from z = L_1 to z = L_2 yields

$$\int_{L_1}^{L_2}\frac{\partial\left[A\left(\rho h - p\right)\right]}{\partial t}dz + \int_{L_1}^{L_2}\frac{\partial\left(\dot{m}h\right)}{\partial z}dz = \int_{L_1}^{L_2}\alpha_r\pi d_i\left(T_w - T_r\right)dz \tag{6-26}$$

200

Applying Leibniz's rule to the first term of Eq. (6-26) and integrating the remaining terms by assuming a constant heat transfer coefficient gives

$$A\frac{d}{dt}\int_{L_1}^{L_2}\rho h dz + A\rho_g h_g \frac{dL_1}{dt} - A\rho_f h_f \frac{dL_2}{dt} - A(L_2 - L_1)\frac{dp}{dt}$$
$$= \dot{m}_{12}h_g - \dot{m}_{23}h_f + \alpha_{r,2}\pi d_i \int_{L_1}^{L_2}(T_w - T_r)dz$$

(6-27)

The first term of Eq. (6-27) can be expanded as

$$A\frac{d}{dt}\int_{L_1}^{L_2}\rho h dz = A\frac{d}{dt}\int_{L_1}^{L_2}\left[(1-\gamma)\rho_f h_f + \gamma\rho_g h_g\right]dz$$
$$= A\frac{d}{dt}\left[\rho_f h_f \int_{L_1}^{L_2}(1-\gamma)dz\right] + A\frac{d}{dt}\left[\rho_g h_g \int_{L_1}^{L_2}\gamma dz\right]$$
$$= A\frac{d}{dt}\left\{\left[\rho_f h_f(1-\bar{\gamma}) + \rho_g h_g \bar{\gamma}\right](L_2 - L_1)\right\}$$

(6-28)

$$= A\left[\rho_f h_f(1-\bar{\gamma}) + \rho_g h_g \bar{\gamma}\right]\left(\frac{dL_2}{dt} - \frac{dL_1}{dt}\right) +$$
$$A(L_2 - L_1)\left[(1-\bar{\gamma})\frac{d(\rho_f h_f)}{dt} + \bar{\gamma}\frac{d(\rho_g h_g)}{dt} + (\rho_g h_g - \rho_f h_f)\frac{d\bar{\gamma}}{dt}\right]$$

Let

$$\bar{T}_{r,2} = \frac{1}{L_2 - L_1}\int_{L_1}^{L_2}T_r dz \approx \frac{1}{2}(T_{dew} + T_{bub})$$

(6-29)

Substituting Eq. (6-28) & (6-29) into Eq. (6-27) and rearranging yields the final form of the energy equation of the two-phase region.

$$A(L_2 - L_1)\left[(1-\bar{\gamma})\frac{d(\rho_f h_f)}{dp} + \bar{\gamma}\frac{d(\rho_g h_g)}{dp} - 1\right]\frac{dp}{dt} + A(\rho_g h_g - \rho_f h_f)\bar{\gamma}\frac{dL_2}{dt}$$
$$-A(\rho_g h_g - \rho_f h_f)(\bar{\gamma}-1)\frac{dL_1}{dt} + A(L_2 - L_1)(\rho_g h_g - \rho_f h_f)\frac{d\bar{\gamma}}{dt}$$

(6-30)

$$= \dot{m}_{12}h_g - \dot{m}_{23}h_f + \pi d_i(L_2 - L_1)\alpha_{r,2}(T_{w,2} - \bar{T}_{r,2})$$

where $\dfrac{d(\rho_f h_f)}{dp} = \rho_f\dfrac{dh_f}{dp} + h_f\dfrac{d\rho_f}{dp}$, $\dfrac{d(\rho_g h_g)}{dp} = \rho_g\dfrac{dh_g}{dp} + h_g\dfrac{d\rho_g}{dp}$.

6.3.1.1.2.3 *Time Varying Effect of Mean Void Fraction*

Assuming a linear refrigerant enthalpy profile in the two-phase region, mean void fraction can be determined as follows

$$
\begin{aligned}
\bar{\gamma} &= \frac{1}{L_2 - L_1} \int_{L_1}^{L_2} \gamma \, dz \\
&= \frac{1}{x_{tp,out} - x_{tp,in}} \int_{x_{tp,in}}^{x_{tp,out}} \gamma \, dx
\end{aligned}
\tag{6-31}
$$

In order to avoid computational complexity, the Zivi void fraction model (1964) is used. Hence, Eq. (6-31) becomes

$$
\bar{\gamma} = \frac{c}{\left(x_{tp,out} - x_{tp,in} \right)(c-1)^2} \ln \left[\frac{x_{tp,in}(c-1) - c}{x_{tp,out}(c-1) - c} \right] + \frac{1}{c-1}
\tag{6-32}
$$

where

$$
c = \left(\frac{\rho_g}{\rho_f} \right)^{2/3}
$$

The time derivative of mean void fraction $\bar{\gamma}$ is included in the mass balance equation (6-25) and energy balance equation (6-30) of the two-phase region. Early models (He, 1996; Willatzen *et al.*, 1998; Jensen & Tummescheit, 2002) generally neglected the time-varying effect of mean void fraction $\bar{\gamma}$ and hence the term including $\frac{d\bar{\gamma}}{dt}$ in Eq. (6-25) & (6-30) was cancelled out. Later on, McKinley & Alleyne (2008) and Li & Alleyne (2010) found that it was advantageous to include $\frac{d\bar{\gamma}}{dt}$ for switching purposes by establishing a first-order filter on the difference between $\bar{\gamma}$ and $\bar{\gamma}_{tot}$ (the equilibrium value for complete condensation or evaporation). One of the drawbacks of this approach was that $\bar{\gamma}$ was never exactly equal to $\bar{\gamma}_{tot}$ and

there was an inevitable delay for $\bar{\gamma}$ to catch up with $\bar{\gamma}_{tot}$. Moreover, the transcendental equation (6-32) needed to be solved for refrigerant quality leaving the heat exchanger $x_{tp,out}$ if the outlet state is two-phase.

In light of this, the proposed model tries to adopt a different approach to account for the time-varying effect of mean void fraction. The time derivative of mean void fraction, $\dfrac{d\bar{\gamma}}{dt}$, can be determined by differentiating Eq. (6-32)

$$\frac{d\bar{\gamma}}{dt} = \left(\left. \frac{\partial\bar{\gamma}}{\partial c} \right|_{x_{tp,in},x_{tp,out}} \frac{dc}{dp} + \left. \frac{\partial\bar{\gamma}}{\partial x_{tp,in}} \right|_{c,x_{tp,out}} \left. \frac{\partial x_{tp,in}}{\partial p} \right|_{h_{tp,in}} + \left. \frac{\partial\bar{\gamma}}{\partial x_{tp,out}} \right|_{c,x_{tp,in}} \left. \frac{\partial x_{tp,out}}{\partial p} \right|_{h_{tp,out}} \right) \frac{dp}{dt}$$
$$+ \left. \frac{\partial\bar{\gamma}}{\partial x_{tp,in}} \right|_{c,x_{tp,out}} \left. \frac{\partial x_{tp,in}}{\partial h_{tp,in}} \right|_{p} \frac{dh_{tp,in}}{dt} + \left. \frac{\partial\bar{\gamma}}{\partial x_{tp,out}} \right|_{c,x_{tp,in}} \left. \frac{\partial x_{tp,out}}{\partial h_{tp,out}} \right|_{p} \frac{dh_{tp,out}}{dt} \tag{6-33}$$

where

$$\frac{dc}{dp} = \frac{2}{3}\left(\frac{\rho_g}{\rho_f}\right)^{-1/3} \left(\frac{1}{\rho_f}\frac{d\rho_g}{dp} - \frac{\rho_g}{\rho_f^2}\frac{d\rho_f}{dp} \right) \tag{6-34}$$

$$\left. \frac{\partial x_{tp,in}}{\partial p} \right|_{h_{tp,in}} = -\frac{1}{h_g - h_f}\left[\left(1-x_{tp,in}\right)\frac{dh_f}{dp} + x_{tp,in}\frac{dh_g}{dp} \right] \tag{6-35}$$

$$\left. \frac{\partial x_{tp,out}}{\partial p} \right|_{h_{tp,out}} = -\frac{1}{h_g - h_f}\left[\left(1-x_{tp,out}\right)\frac{dh_f}{dp} + x_{tp,out}\frac{dh_g}{dp} \right] \tag{6-36}$$

$$\left. \frac{\partial x_{tp,in}}{\partial h_{tp,in}} \right|_{p} = \left. \frac{\partial x_{tp,out}}{\partial h_{tp,out}} \right|_{p} = \frac{1}{h_g - h_f} \tag{6-37}$$

If $x_{tp,in} \neq x_{tp,out}$

$$\frac{\partial \bar{\gamma}}{\partial c}\bigg|_{x_{tp,in},x_{tp,out}} = \frac{1}{(1-c)^2} + \frac{1}{x_{tp,out} - x_{tp,in}}\left[\frac{1}{(c-1)^2} - \frac{2c}{(c-1)^3}\right]\ln\left[\frac{c + x_{tp,in}(1-c)}{c + x_{tp,out}(1-c)}\right] +$$

$$\frac{1}{x_{tp,out} - x_{tp,in}}\frac{c}{(c-1)^2}\left[\frac{1-x_{tp,in}}{c + x_{tp,in}(1-c)} - \frac{1-x_{tp,out}}{c + x_{tp,out}(1-c)}\right]$$

(6-38)

$$\frac{\partial \bar{\gamma}}{\partial x_{tp,in}}\bigg|_{c,x_{tp,out}} = \frac{c}{(c-1)^2}\frac{1}{(x_{tp,out} - x_{tp,in})^2}\ln\left[\frac{c + x_{tp,in}(1-c)}{c + x_{tp,out}(1-c)}\right] + \frac{c}{(c-1)^2}\frac{1}{x_{tp,out} - x_{tp,in}}\frac{1-c}{c + x_{tp,in}(1-c)}$$

(6-39)

$$\frac{\partial \bar{\gamma}}{\partial x_{tp,out}}\bigg|_{c,x_{tp,in}} = -\frac{c}{(c-1)^2}\frac{1}{(x_{tp,out} - x_{tp,in})^2}\ln\left[\frac{c + x_{tp,in}(1-c)}{c + x_{tp,out}(1-c)}\right] - \frac{c}{(c-1)^2}\frac{1}{x_{tp,out} - x_{tp,in}}\frac{1-c}{c + x_{tp,out}(1-c)}$$

(6-40)

If $x_{tp,in} = x_{tp,out}$

$$\frac{\partial \bar{\gamma}}{\partial c}\bigg|_{x_{tp,in},x_{tp,out}} = -\frac{x_{tp,in}(1-x_{tp,in})}{\left[x_{tp,in} + (1-x_{tp,in})c\right]^2}$$

(6-41)

$$\frac{\partial \bar{\gamma}}{\partial x_{tp,in}}\bigg|_{c,x_{tp,out}} = \frac{\partial \bar{\gamma}}{\partial x_{tp,out}}\bigg|_{c,x_{tp,in}} = \frac{1}{x_{tp,in} + (1-x_{tp,in})c} - \frac{x_{tp,in}(1-c)}{\left[x_{tp,in} + (1-x_{tp,in})c\right]^2}$$

(6-42)

Please be noted that in the three zone mode (V-TP-L), there is a complete

condensation. Therefore, $\dfrac{\partial x_{tp,in}}{\partial p}\bigg|_{h_{tp,in}}$, $\dfrac{\partial x_{tp,out}}{\partial p}\bigg|_{h_{tp,out}}$, $\dfrac{\partial x_{tp,in}}{\partial h_{tp,in}}\bigg|_{p}$ and $\dfrac{\partial x_{tp,out}}{\partial h_{tp,out}}\bigg|_{p}$ are all equal to

zero since $x_{tp,in}$ and $x_{tp,out}$ are constants. Thus Eq. (6-33) becomes

$$\frac{d\bar{\gamma}}{dt} = \frac{\partial \bar{\gamma}}{\partial c}\bigg|_{x_{tp,in},x_{tp,out}}\frac{dc}{dp}\frac{dp}{dt}$$

(6-43)

Since the time derivative of mean void fraction can be readily determined, $\bar{\gamma}$ in Eq.

(6-25) & (6-30) will be a state variable and integrated through Eq. (6-33), and $\dfrac{d\bar{\gamma}}{dt}$ is

calculated by Eq. (6-43). Hence, there is no need to use Eq. (6-32) to calculate $\bar{\gamma}$ any

more. Eq. (6-32) is only used to calculate the partial derivatives in Eq. (6-33). One of the advantages of applying Eq. (6-33) is that there is no delay in calculating $\bar{\gamma}$. Moreover, the refrigerant mass is conserved since $\bar{\gamma}$ is continuous while switching between different models, as will be seen later.

6.3.1.1.3 L Region

6.3.1.1.3.1 Mass Balance

Integrating Eq. (6-1) for the subcooled region from $z = L_2$ to $z = L_t$ yields

$$\int_{L_2}^{L_t} \frac{\partial(\rho A)}{\partial t} dz + \int_{L_2}^{L_t} \frac{\partial \dot{m}}{\partial z} dz = 0 \tag{6-44}$$

Applying Leibniz's rule gives

$$A \frac{d}{dt} \int_{L_2}^{L_t} \rho dz + A \rho_f \frac{dL_2}{dt} = \dot{m}_{23} - \dot{m}_{out} \tag{6-45}$$

The first term of Eq. (6-45) can be greatly simplified by introducing the mean refrigerant density of the subcooled region, $\bar{\rho}_3 = \frac{1}{L_t - L_2} \int_{L_2}^{L_t} \rho dz$

$$\frac{d}{dt} \int_{L_2}^{L_t} \rho dz = \frac{d}{dt} \left[\bar{\rho}_3 (L_t - L_2) \right] = (L_t - L_2) \frac{d\bar{\rho}_3}{dt} - \bar{\rho}_3 \frac{dL_2}{dt} \tag{6-46}$$

Substituting Eq. (6-46) into Eq. (6-45) yields

$$A(L_t - L_2) \frac{d\bar{\rho}_3}{dt} + A(\rho_f - \bar{\rho}_3) \frac{dL_2}{dt} = \dot{m}_{23} - \dot{m}_{out} \tag{6-47}$$

The mean refrigerant properties in the subcooled region can be determined based on the pressure p and the mean enthalpy $\bar{h}_3 = \frac{1}{2}(h_f + h_{out})$. Therefore,

$$\bar{\rho}_3 \approx \rho(p, \bar{h}_3) \tag{6-48}$$

The derivative of the density with respect to the time can be expanded as follows by applying the chain rule

$$
\begin{aligned}
\frac{d\bar{\rho}_3}{dt} &= \frac{\partial \bar{\rho}_3}{\partial p}\bigg|_h \frac{dp}{dt} + \frac{\partial \bar{\rho}_3}{\partial \bar{h}_3}\bigg|_p \frac{d\bar{h}_3}{dt} \\
&= \frac{\partial \bar{\rho}_3}{\partial p}\bigg|_h \frac{dp}{dt} + \frac{1}{2}\frac{\partial \bar{\rho}_3}{\partial \bar{h}_3}\bigg|_p \left(\frac{dh_f}{dt} + \frac{dh_{out}}{dt}\right) \\
&= \frac{\partial \bar{\rho}_3}{\partial p}\bigg|_h \frac{dp}{dt} + \frac{1}{2}\frac{\partial \bar{\rho}_3}{\partial \bar{h}_3}\bigg|_p \left(\frac{dh_f}{dp}\frac{dp}{dt} + \frac{dh_{out}}{dt}\right) \\
&= \left(\frac{\partial \bar{\rho}_3}{\partial p}\bigg|_h + \frac{1}{2}\frac{\partial \bar{\rho}_3}{\partial \bar{h}_3}\bigg|_p \frac{dh_f}{dp}\right)\frac{dp}{dt} + \frac{1}{2}\frac{\partial \bar{\rho}_3}{\partial \bar{h}_3}\bigg|_p \frac{dh_{out}}{dt}
\end{aligned}
$$

(6-49)

Substituting Eq. (6-49) into Eq. (6-47) finally yields

$$
A(L_t - L_2)\left[\left(\frac{\partial \bar{\rho}_3}{\partial p}\bigg|_h + \frac{1}{2}\frac{\partial \bar{\rho}_3}{\partial \bar{h}_3}\bigg|_p \frac{dh_f}{dp}\right)\frac{dp}{dt} + \frac{1}{2}\frac{\partial \bar{\rho}_3}{\partial \bar{h}_3}\bigg|_p \frac{dh_{out}}{dt}\right] - A(\bar{\rho}_3 - \rho_f)\frac{dL_2}{dt} = \dot{m}_{23} - \dot{m}_{out}
$$

(6-50)

6.3.1.1.3.2 *Energy Balance*

Integrating the energy balance equation Eq. (6-2) for the subcooled region from $z = L_2$ to $z = L_t$ yields

$$
\int_{L_2}^{L_t} \frac{\partial[A(\rho h - p)]}{\partial t}dz + \int_{L_2}^{L_t}\frac{\partial(\dot{m}h)}{\partial z}dz = \int_{L_2}^{L_t}\alpha_r \pi d_i (T_w - T_r)dz
$$

(6-51)

Applying Leibniz's rule and integrating gives

$$
A\left[\frac{d}{dt}\int_{L_2}^{L_t}\rho h dz + \rho_f h_f \frac{dL_2}{dt} - (L_t - L_2)\frac{dp}{dt}\right] = \dot{m}_{23}h_f - \dot{m}_{out}h_{out} + \int_{L_2}^{L_t}\alpha_r \pi d_i (T_w - T_r)dz
$$

(6-52)

Let

$$\overline{\rho h} = \frac{1}{L_t - L_2} \int_{L_2}^{L_t} \rho h \, dz \approx \overline{\rho}_3 \overline{h}_3 \qquad (6\text{-}53)$$

Substituting Eq.(6-53) into Eq. (6-52) becomes

$$A \frac{d}{dt} \left[\overline{\rho}_3 \overline{h}_3 \left(L_t - L_2 \right) \right] + A \rho_f h_f \frac{dL_2}{dt} - A \left(L_t - L_2 \right) \frac{dp}{dt} = \dot{m}_{23} h_f - \dot{m}_{out} h_{out} + \int_{L_2}^{L_t} \alpha_r \pi d_i \left(T_w - T_r \right) dz$$
$$(6\text{-}54)$$

The first term of Eq. (6-54) can be expanded as

$$A \frac{d}{dt} \left[\overline{\rho}_3 \overline{h}_3 \left(L_t - L_2 \right) \right] = -A \overline{\rho}_3 \overline{h}_3 \frac{dL_2}{dt} + A \overline{\rho}_3 \left(L_t - L_2 \right) \frac{d\overline{h}_3}{dt} + A \overline{h}_3 \left(L_t - L_2 \right) \frac{d\overline{\rho}_3}{dt} \qquad (6\text{-}55)$$

Solving for $A \left(L_t - L_2 \right) \dfrac{d\overline{\rho}_3}{dt}$ from Eq. (6-47) and substituting it into Eq. (6-55) gives

$$A \frac{d}{dt} \left[\overline{\rho}_3 \overline{h}_3 \left(L_t - L_2 \right) \right] = -A \rho_f \overline{h}_3 \frac{dL_2}{dt} + A \overline{\rho}_3 \left(L_t - L_2 \right) \frac{d\overline{h}_3}{dt} + \left(\dot{m}_{23} - \dot{m}_{out} \right) \overline{h}_3 \qquad (6\text{-}56)$$

Substituting Eq. (6-56) into Eq. (6-54)yields

$$A \left(L_t - L_2 \right) \left(\overline{\rho}_3 \frac{d\overline{h}_3}{dt} - \frac{dp}{dt} \right) - A \rho_f \left(\overline{h}_3 - h_f \right) \frac{dL_2}{dt}$$
$$= \dot{m}_{23} \left(h_f - \overline{h}_3 \right) - \dot{m}_{out} \left(h_{out} - \overline{h}_3 \right) + \int_{L_2}^{L_t} \alpha_r \pi d_i \left(T_w - T_r \right) dz \qquad (6\text{-}57)$$

6.3.1.1.3.3 *Wall-to-Refrigerant Heat Transfer*

The existing moving boundary models calculate the heat transfer between the refrigerant and the tube wall in the subcooled region via

$$\int_{L_2}^{L_t} \alpha_r \pi d_i \left(T_w - T_r \right) dz = \pi \alpha_{r,3} d_i \left(L_t - L_2 \right) \left(\overline{T}_{w,3} - \overline{T}_{r,3} \right) \qquad (6\text{-}58)$$

where

$$\overline{T}_{w,3} \approx T \left(p, \overline{h}_3 \right)$$

Eq. (6-58) can be well justified if the approach is used to calculate the heat transfer between the refrigerant and the tube wall in the superheated region. However, this approach might cause temperature crossing at the outlet of the heat exchanger for the subcooled region. This can be analyzed as follows.

Under the steady-state condition, on can have

$$\pi \alpha_{r,3} d_i \left(L_t - L_2 \right) \left(T_{w,3} - \overline{T}_{r,3} \right) = \dot{m}_{23} \left(h_f - h_{out} \right)$$ (6-59)

where $\overline{T}_{r,3}$ can be related to the arithmetic mean of T_f and T_{out}, i.e.

$$\overline{T}_{r,3} = \frac{1}{2} \left(T_f + T_{out} \right) + \varepsilon$$ (6-60)

where generally ε is a very small positive value.

Eq. (6-59) can be rewritten as

$$\pi \alpha_{r,3} d_i \left(L_t - L_2 \right) \left[\left(T_{w,3} - \varepsilon \right) - \frac{1}{2} \left(T_f + T_{out} \right) \right] = \dot{m}_{23} \overline{c}_{p,3} \left(T_f - T_{out} \right)$$ (6-61)

Solving for the temperature of refrigerant leaving the heat exchanger T_{out} from Eq. (6-61)

$$T_{out} = \frac{\dfrac{\pi \alpha_{r,3} d_i \left(L_t - L_2 \right)}{\dot{m}_{23} \overline{c}_{p,3}} \left(T_{w,3} - \varepsilon \right) - \left[\dfrac{\pi \alpha_{r,3} d_i \left(L_t - L_2 \right)}{2 \dot{m}_{23} \overline{c}_{p,3}} + 1 \right] T_f}{\dfrac{\pi \alpha_{r,3} d_i \left(L_t - L_2 \right)}{2 \dot{m}_{23} \overline{c}_{p,3}} - 1}$$ (6-62)

Under the steady-state operation, T_{out} must be higher than $T_{w,3}$. Otherwise, temperature crossing occurs and the second law of thermodynamics is violated

$$\frac{\dfrac{\pi \alpha_{r,3} d_i \left(L_t - L_2 \right)}{\dot{m}_{23} \overline{c}_{p,3}} \left(T_{w,3} - \varepsilon \right) - \left[\dfrac{\pi \alpha_{r,3} d_i \left(L_t - L_2 \right)}{2 \dot{m}_{23} \overline{c}_{p,3}} + 1 \right] T_f}{\dfrac{\pi \alpha_{r,3} d_i \left(L_t - L_2 \right)}{2 \dot{m}_{23} \overline{c}_{p,3}} - 1} > T_{w,3}$$ (6-63)

In order for Eq. (6-63) to hold, the following expression must be satisfied

$$T_{w,3} > T_f + \frac{2A}{A+1}\varepsilon \tag{6-64}$$

which means the average wall temperature in the subcooled region must be higher than the temperature of saturated refrigerant liquid, otherwise, temperature crossing at the outlet of the heat exchanger occurs. However, Eq. (6-64) is impossible to hold under the steady-state conditions. Under this circumstance, a different approach must be adopted to avoid the violation of the second law of thermodynamics in the subcooled region.

We can prove that Eq. (6-64) does not hold under steady-state conditions from another perspective. Eq. (6-61) can be rewritten using LMTD (Log-Mean Temperature Difference) instead of arithmetic mean temperature difference

$$\pi\alpha_{r,3}d_i\left(L_t - L_2\right)\frac{T_f - T_{out}}{\ln\dfrac{T_f - T_{w,3}}{T_{out} - T_{w,3}}} = \dot{m}_{23}\overline{c}_{p,3}\left(T_f - T_{out}\right) \tag{6-65}$$

Rearranging Eq. (6-65) yields

$$T_{out} - T_{w,3} = \frac{T_f - T_{w,3}}{\exp\left[\dfrac{\pi\alpha_{r,3}d_i}{\dot{m}_{23}\overline{c}_{p,3}}\left(L_t - L_2\right)\right]} \tag{6-66}$$

It is easy to observe that in order to avoid temperature crossing at the outlet of the heat exchanger, the following expression must hold

$$T_f > T_{w,3} \tag{6-67}$$

Obviously, Eq. (6-67) contradicts with Eq. (6-64). Since Eq. (6-67) always holds under steady-state conditions, LMTD could be used to avoid temperature crossing. However, one of the disadvantages of applying LMTD is that the

209

calculation of the logarithm will fail when T_{out} might be lower than $T_{w,3}$ under transient conditions. A remedy to this problem is to construct a smooth and differentiable function that can extrapolate the LMTD calculation when temperature difference on one side is negative. The details of developing an improved LMTD method that accounts for temperature crossing are presented below.

6.3.1.1.3.3.1 Improved LMTD Method Accounting for Temperature Crossing

Figure 6.3 shows seven possible temperature profiles of the refrigerant flow and the walls in the subcooled region that might occur under transient conditions. Each of these seven cases will be analyzed below.
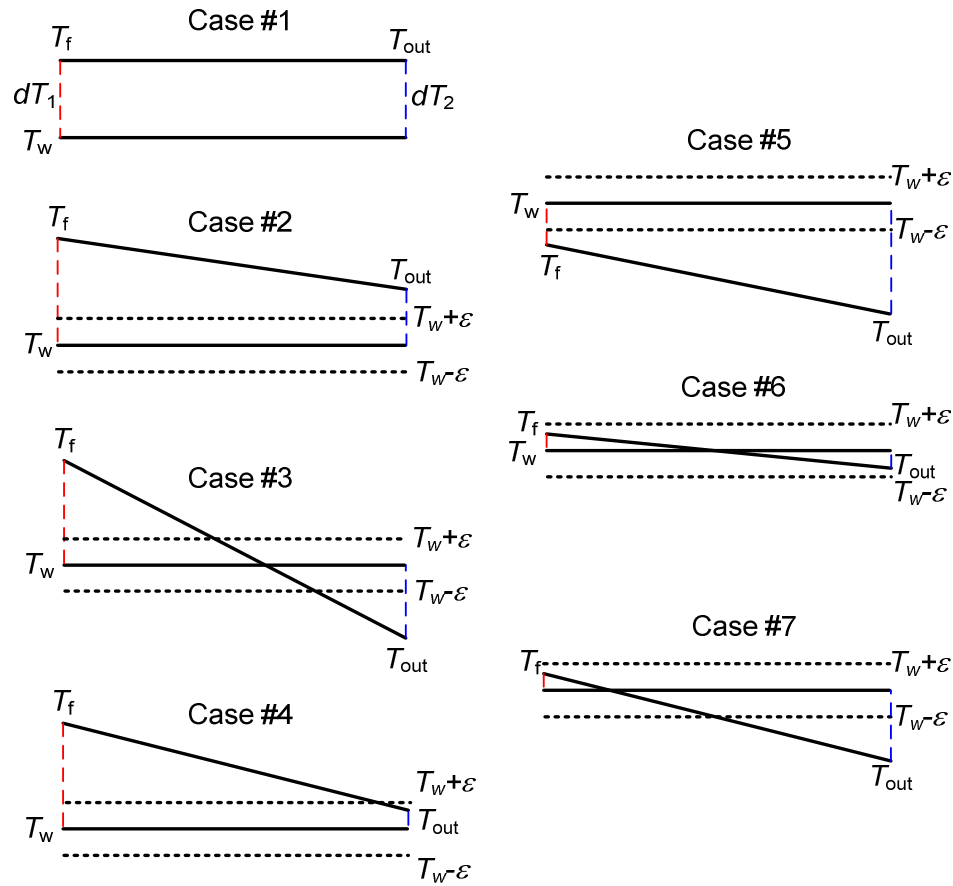
Figure 6.3 Seven possible temperature profiles

First of all, let's define

$$dT_1 = T_f - T_w$$
$$dT_2 = T_{out} - T_w$$

(6-68)

Since T_{out} is always lower than T_f, one can have $dT_1 \geq dT_2$.

<u>Case #1</u>: $\left| dT_1 - dT_2 \right| < dT_{min}$ where dT_{min} is a very small value, e.g. 1e-6 K.

One must be aware that LMTD cannot handle this case because of the resulting division by zero error. Therefore, the temperature difference should be calculated via

$$\Delta T_{LMTD} = \frac{dT_1 + dT_2}{2}$$

(6-69)

<u>Case #2</u>: $dT_1 > \varepsilon$ & $dT_2 > \varepsilon$ and <u>Case #5</u>: $dT_1 < -\varepsilon$ & $dT_2 < -\varepsilon$ (ε is a very small value)

The temperature difference can be calculated using the original LMTD equation.

$$\Delta T_{LMTD}\left(dT_1, dT_2 \right) = \frac{dT_1 - dT_2}{\ln \dfrac{dT_1}{dT_2}}$$

(6-70)

<u>Case #3</u>: $dT_1 > \varepsilon$ & $dT_2 < -\varepsilon$

If dT_1 and dT_2 have different signs, the overall LMTD consists of two parts, i.e., the first part is the temperature difference between dT_1 and $-\varepsilon$, and the second part is the temperature difference between $-\varepsilon$ and dT_2. For the first part, the original LMTD equation cannot be used because of the negative temperature difference. Instead, one needs to first calculate the LMTD between dT_1 and ε, and then linearly extrapolate the calculation to obtain the LMTD between dT_1 and $-\varepsilon$. The second part can be directly calculated using the original LMTD equation. The overall LMTD is the weighted sum of the two parts

211

$$\Delta T_{LMTD}(dT_1, dT_2) = \frac{|dT_1 + \varepsilon|}{|dT_1| + |dT_2|} \left[\Delta T_{LMTD}(dT_1, \varepsilon) - 2\varepsilon \frac{\partial(\Delta T_{LMTD})}{\partial(dT_2)}\bigg|_{dT_2 = \varepsilon} \right] +$$

$$\left(1 - \frac{|dT_1 + \varepsilon|}{|dT_1| + |dT_2|}\right) \Delta T_{LMTD}(-\varepsilon, dT_2) \tag{6-71}$$

where

$$\Delta T_{LMTD}(dT_1, \varepsilon) = \frac{dT_1 - \varepsilon}{\ln \dfrac{dT_1}{\varepsilon}} \tag{6-72}$$

$$\Delta T_{LMTD}(-\varepsilon, dT_2) = \frac{-\varepsilon - dT_2}{\ln \dfrac{-\varepsilon}{dT_2}} \tag{6-73}$$

$$\frac{\partial(\Delta T_{LMTD})}{\partial(dT_2)} = \frac{1}{\ln \dfrac{dT_2}{dT_1}} - \frac{1 - \dfrac{dT_1}{dT_2}}{\left(\ln \dfrac{dT_2}{dT_1}\right)^2} \Rightarrow \frac{\partial(\Delta T_{LMTD})}{\partial(dT_2)}\bigg|_{dT_2 = \varepsilon} = \frac{1}{\ln \dfrac{\varepsilon}{dT_1}} - \frac{1 - \dfrac{dT_1}{\varepsilon}}{\left(\ln \dfrac{\varepsilon}{dT_1}\right)^2} \tag{6-74}$$

Case #4: $dT_1 > \varepsilon$ & $-\varepsilon < dT_2 < \varepsilon$

The overall LMTD can be calculated by extrapolation

$$\Delta T_{LMTD}(dT_1, dT_2) = \Delta T_{LMTD}(dT_1, \varepsilon) + (dT_2 - \varepsilon) \frac{\partial(\Delta T_{LMTD})}{\partial(dT_2)}\bigg|_{dT_2 = \varepsilon} \tag{6-75}$$

where $\Delta T_{LMTD}(dT_1, \varepsilon)$ is calculated using Eq. (6-70).

Case #6: $-\varepsilon \leq dT_1 \leq \varepsilon$ & $-\varepsilon \leq dT_2 \leq \varepsilon$

The overall LMTD can be calculated

$$\Delta T_{LMTD}(dT_1, dT_2) = \frac{dT_1 + dT_2}{2} \tag{6-76}$$

Case #7: $-\varepsilon < dT_1 < \varepsilon$ & $dT_2 \leq -\varepsilon$

This case is similar to the case #4. The overall LMTD can be calculated by interpolation

$$\Delta T_{LMTD}\left(dT_1,dT_2\right)=\Delta T_{LMTD}\left(-\varepsilon,dT_2\right)+\left(dT_1+\varepsilon\right)\frac{\partial\left(\Delta T_{LMTD}\right)}{\partial\left(dT_1\right)}\Bigg|_{dT_1=-\varepsilon} \tag{6-77}$$

$$\frac{\partial\left(\Delta T_{LMTD}\right)}{\partial\left(dT_1\right)}=\frac{1}{\ln\dfrac{dT_1}{dT_2}}-\frac{1-\dfrac{dT_2}{dT_1}}{\left(\ln\dfrac{dT_1}{dT_2}\right)^2}\Rightarrow\frac{\partial\left(\Delta T_{LMTD}\right)}{\partial\left(dT_1\right)}\Bigg|_{dT_1=-\varepsilon}=\frac{1}{\ln\dfrac{-\varepsilon}{dT_2}}-\frac{1+\dfrac{dT_2}{\varepsilon}}{\left(\ln\dfrac{-\varepsilon}{dT_2}\right)^2} \tag{6-78}$$

where $\Delta T_{LMTD}\left(-\varepsilon,dT_2\right)$ is obtained via Eq. (6-70).

6.3.1.1.3.3.2 Effectiveness-NTU Method

Although the proposed improved LMTD approach is adequate to account for the temperature crossing under transient operating conditions, the Effective-NTU method is much easier to be applied.

It is not difficult to derive the following equation to calculate the heat transfer rate in the subcooled region using the Effective-NTU method

$$\int_{L_2}^{L_t}\alpha_r\pi d_i\left(T_w-T_r\right)dz\approx\left|\dot{m}_{23}\right|c_{p,f}\left(T_{w,3}-T_f\right)\left\{1-\exp\left[-\frac{\alpha_{r,3}\pi d_i\left(L_t-L_2\right)}{\left|\dot{m}_{23}\right|c_{p,f}}\right]\right\} \tag{6-79}$$

It can be noted that temperature crossing does not occur under the steady-state conditions when the Effective-NTU method is used. Since the heat transfer rate in the subcooled region only accounts for a small fraction of the overall heat transfer, it is reasonable to apply Eq. (6-79) even under transient operating conditions, although it is derived based on the assumption of the steady-state flow.

Finally, the energy equation for the subcooled region becomes

213

$$A\left(L_t - L_2\right)\left(\bar{\rho}_3 \frac{d\bar{h}_3}{dt} - \frac{dp}{dt}\right) - A\rho_f\left(\bar{h}_3 - h_f\right)\frac{dL_2}{dt}$$

$$= \dot{m}_{23}\left(h_f - \bar{h}_3\right) - \dot{m}_{out}\left(h_{out} - \bar{h}_3\right) + \left|\dot{m}_{23}\right|c_{p,f}\left(T_{w,3} - T_f\right)\left\{1 - \exp\left[-\frac{\alpha_{r,3}\pi d_i\left(L_t - L_2\right)}{\left|\dot{m}_{23}\right|c_{p,f}}\right]\right\}$$

(6-80)

6.3.1.1.4 Global Momentum Balance

6.3.1.1.4.1 *Approach # 1*

It is assumed that that refrigerant pressure is uniform within the heat exchanger, and the pressure drop is concentrated at the outlet of the heat exchanger. In this case, an equation accounting for the global momentum balance is required to calculate the mass flow rate leaving the heat exchanger. Recall that the outlet refrigerant pressure instead of the outlet refrigerant mass flow is the boundary condition in the new moving boundary models.

As suggested by Brasz and Koenig (1983), dynamic pressure waves are of minor importance for a heat transfer analysis, and they can be neglected while still preserving the prevailing physics. As a result, the following global momentum balance equation accounting for refrigerant pressure drop solely due to the frictional loss can be solved for the refrigerant outlet mass flow rate.

$$\left(p - p_{out}\right) = \sum_{j=1}^{3} \Delta p_j$$

(6-81)

where Δp_j is the pressure drop for region $j = 1, 2$ & 3.

The pressure drop in the single-phase regions ($j = 1$ & 3) can be expressed as

214

$$\Delta p_j = f_j \frac{\Delta z_j}{d_i} \frac{G_j^2}{2\bar{\rho}_j} \tag{6-82}$$

where f_j is the frictional loss factor for region j and can be calculated using empirical correlations, Δz_j is the length for region j, and G_j is the mass flux calculated based on the average of inlet and outlet mass flow rates of region j.

The pressure drop in the two-phase region can be expressed as (Carey, 2008)

$$\Delta p_2 = \frac{2 f_{lo} G^2 \Delta z_2}{d_i \rho_f} \frac{1}{x_{tp,out} - x_{tp,in}} \int_{x_{tp,in}}^{x_{tp,out}} \varphi_{lo}^2 dx \tag{6-83}$$

where the subscript "lo" denotes the frictional pressure gradient that would result if liquid only flowed through the heat exchanger at the same total mass flow rate (GA), f_{lo} is the friction factor, and φ_{lo} is two-phase pressure drop multiplier.

Now the governing equations for the refrigerant flow can be summarized, i.e., Eq. (6-10), (6-18), (6-25), (6-30), (6-43), (6-50), (6-80) & (6-81). There are eight variables including five state variables and three algebraic variables need to be determined. The five state variables are $\left[p \ \bar{\gamma} \ h_{out} \ L_1 \ L_2 \right]$, and the three algebraic variables are $\dot{m}_{12}$, $\dot{m}_{23}$ & $\dot{m}_{out}$. Along with the average wall temperature for each region, the conditions within the heat exchanger at each instant of time can be represented by the state vector $\left[p \ \bar{\gamma} \ h_{out} \ L_1 \ L_2 \ T_{w,1} \ T_{w,2} \ T_{w,3} \right]$. Compared to the existing models available in the literature, the state vector of the new model includes both $\bar{\gamma}$ and h_{out}. The underlying advantages are that not only the need of solving the implicit transcendental equation to calculate the refrigerant outlet enthalpy can be eliminated, but also the refrigerant mass can be conserved in the meantime.

6.3.1.1.4.2 Approach #2
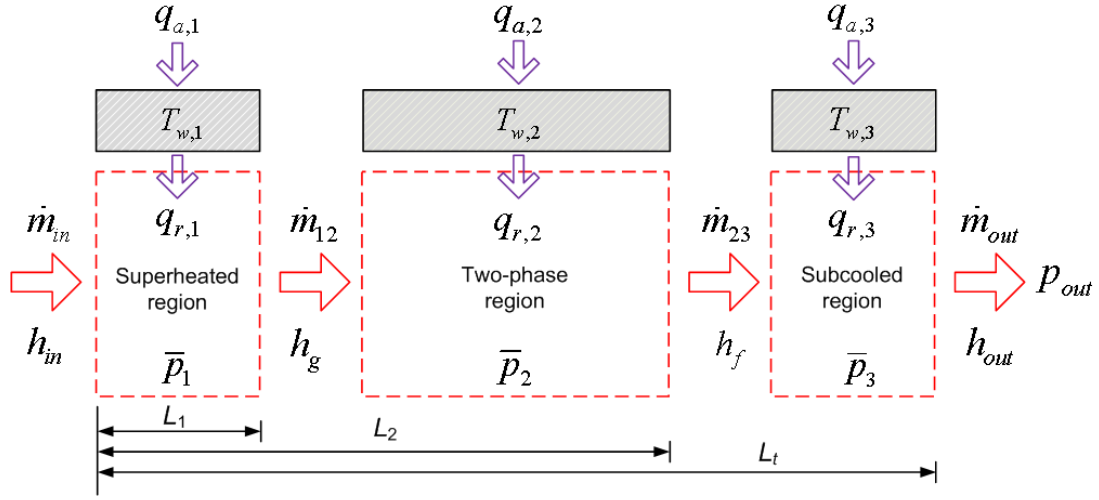
Figure 6.4 V-TP-L condenser model with linear pressure profile

It is assumed that the refrigerant pressure varies linearly within the entire heat exchanger (Figure 6.4). Similarly, only one equation is required to account for the global momentum balance. In this case, the state vector is defined as $\left[p_{in} \; \bar{\gamma} \; h_{out} \; L_1 \; L_2 \; T_{w,1} \; T_{w,2} \; T_{w,3} \right]$.

The mean refrigerant pressure for each region is defined as the pressure at the midpoint of the region, i.e.,

$$\bar{p}_1 = p_{in} - \frac{p_{in} - p_{out}}{L_t} \frac{L_1}{2}$$

$$\bar{p}_2 = p_{in} - \frac{p_{in} - p_{out}}{L_t} \frac{L_1 + L_2}{2}$$

$$\bar{p}_3 = p_{in} - \frac{p_{in} - p_{out}}{L_t} \frac{L_2 + L_t}{2}$$

$$\frac{d\bar{p}_1}{dt} = \frac{dp_{in}}{dt} - \frac{L_1}{2L_t}\left(\frac{dp_{in}}{dt} - \frac{dp_{out}}{dt}\right) - \frac{p_{in} - p_{out}}{2L_t}\frac{dL_1}{dt}$$

$$\frac{d\bar{p}_2}{dt} = \frac{dp_{in}}{dt} - \frac{L_1 + L_2}{2L_t}\left(\frac{dp_{in}}{dt} - \frac{dp_{out}}{dt}\right) - \frac{p_{in} - p_{out}}{2L_t}\left(\frac{dL_1}{dt} + \frac{dL_2}{dt}\right)$$

$$\frac{d\bar{p}_3}{dt} = \frac{dp_{in}}{dt} - \frac{L_2 + L_t}{2L_t}\left(\frac{dp_{in}}{dt} - \frac{dp_{out}}{dt}\right) - \frac{p_{in} - p_{out}}{2L_t}\frac{dL_2}{dt}$$

(6-84)

The mean pressure in individual regions is used to calculate the refrigerant properties, including the mean refrigerant temperature $\bar{T}$, mean refrigerant density $\bar{\rho}$ and mean refrigerant enthalpy $\bar{h}$. Pressures at boundaries are calculated as

$$p(L_1) = p_{in} - \frac{p_{in} - p_{out}}{L_t}L_1$$

$$p(L_2) = p_{in} - \frac{p_{in} - p_{out}}{L_t}L_2$$

$$\frac{dp(L_1)}{dt} = \frac{dp_{in}}{dt} - \frac{L_1}{L_t}\left(\frac{dp_{in}}{dt} - \frac{dp_{out}}{dt}\right) - \frac{p_{in} - p_{out}}{L_t}\frac{dL_1}{dt}$$

$$\frac{dp(L_2)}{dt} = \frac{dp_{in}}{dt} - \frac{L_2}{L_t}\left(\frac{dp_{in}}{dt} - \frac{dp_{out}}{dt}\right) - \frac{p_{in} - p_{out}}{L_t}\frac{dL_2}{dt}$$

(6-85)

Thus, the mass balance for the superheated region becomes

$$AL_1\left[\left.\frac{\partial\bar{\rho}_1}{\partial\bar{p}_1}\right|_{\bar{h}_1}\frac{d\bar{p}_1}{dt} + \frac{1}{2}\left.\frac{\partial\bar{\rho}_1}{\partial\bar{h}_1}\right|_{\bar{p}_1}\frac{dh_{in}}{dt} + \frac{1}{2}\left.\frac{\partial\bar{\rho}_1}{\partial\bar{h}_1}\right|_{\bar{p}_1}\frac{dh(L_1)}{dp}\frac{dp(L_1)}{dt}\right] + A\left[\bar{\rho}_1 - \rho(L_1)\right]\frac{dL_1}{dt} = \dot{m}_{in} - \dot{m}_{12}$$

(6-86)

where $\dfrac{d\bar{p}_1}{dt}$ and $\dfrac{dp(L_1)}{dt}$ can be evaluated based on Eq. (6-84) & (6-85).

Assuming that time derivatives of pressures are spatially invariant (Lemke, 2005), i.e.,

$$\frac{dp_{in}}{dt} \approx \frac{d\overline{p}_1}{dt} \approx \frac{d\overline{p}_2}{dt} \approx \frac{d\overline{p}_3}{dt} \approx \frac{dp(L_1)}{dt} \approx \frac{dp(L_2)}{dt}$$, Eq. (6-86) can be simplified as

$$AL_1\left[\left.\frac{\partial\overline{\rho}_1}{\partial\overline{p}_1}\right|_{\overline{h}_1}\frac{dp_{in}}{dt} + \frac{1}{2}\left.\frac{\partial\overline{\rho}_1}{\partial\overline{h}_1}\right|_{\overline{p}_1}\frac{dh_{in}}{dt} + \frac{1}{2}\left.\frac{\partial\overline{\rho}_1}{\partial\overline{h}_1}\right|_{\overline{p}_1}\frac{dh(L_1)}{dp}\frac{dp_{in}}{dt}\right] + A\left[\overline{\rho}_1 - \rho(L_1)\right]\frac{dL_1}{dt} = \dot{m}_{in} - \dot{m}_{12}$$

$$(6\text{-}87)$$

By applying this assumption, the equations governing the refrigerant flow are almost the same for these two approaches, and are not repeated for brevity. The only difference lies in that $\dfrac{dp}{dt}$ in the first approach should be replaced by $\dfrac{dp_{in}}{dt}$ in the second approach, and the all the refrigerant properties at the phase boundaries should be evaluated based on the pressures defined in Eq. (6-85). It is not difficult to conclude that the second approach is more accurate than the first one since the variations in the refrigerant properties due to pressure drop, especially the variation in refrigerant temperatures, have been taken into account in the analysis.

6.3.1.2 Energy Balance*:* Air Side

The existing moving boundary models have unanimously adopted an audacious assumption when calculating air side heat transfer, i.e., each circuit is regarded as a long horizontal single-pass tube that has the uniform inlet air temperature (McKinley and Alleyne, 2008; Li *et al*., 2012a). However, this assumption is only valid for single-row coils (Figure 6.5a). For multi-row coils (Figure 6.5b), this assumption significantly yields a significant over prediction for the air side heat transfer.

Therefore, it is necessary to revise this prevailing assumption in order to obtain a more accurate prediction for the air side performance. Hence, the following rules are proposed for simplifying multi-row coils:

o Rule 1: The coil is simplified to be a single-circuit coil with both refrigerant mass flow rate and air flow rate reduced by a factor of $1/N_{cir}$, where N_{cir} is the number of coil circuits (in Figure 6.5b, N_{cir} is equal to 3).

o Rule 2: The simplified coil is an N_{row} pass coil with N_{row} horizontal tubes, where N_{row} is the number of rows in the original coil (in Figure 6.5b, N_{row} is equal to 3).

o Rule 3: The new tube length in the simplified coil is $\dfrac{N_t}{N_{cir}N_{row}}L_t$, where L_t and N_t are the tube length and the total number of tubes in the original coil, respectively (in Figure 6.5b, N_t is equal to 78).

o Rule 4: The simplified coil needs to retain the same flow configuration as the original coil, i.e., parallel or counter flow (parallel flow for the coil in Figure 6.5b).

a) a single tube bank coil   b) a multi-tube bank coil
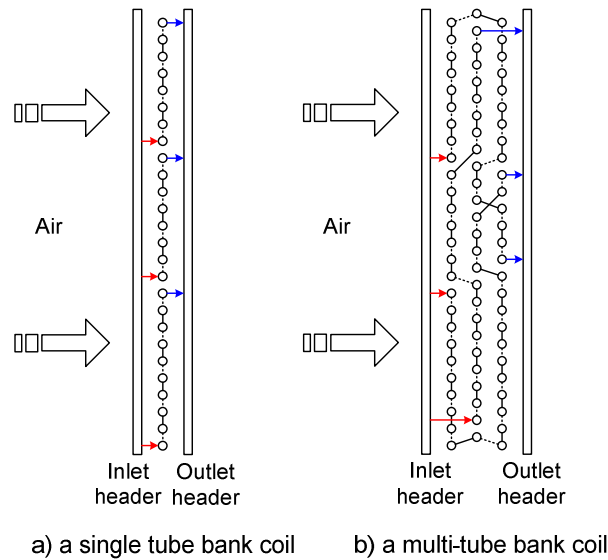
Figure 6.5 a) Schematic of a single-row coil; b) Schematic of a multi-row coil

219

Following the above rules, the coil in Figure 6.5b can be simplified as a single-circuit, three-pass coil with parallel flow configuration (Figure 6.6). The tube length increases to 78/9 times its original tube length. Both refrigerant mass flow rate and air flow rate are reduced to one third of their original values.
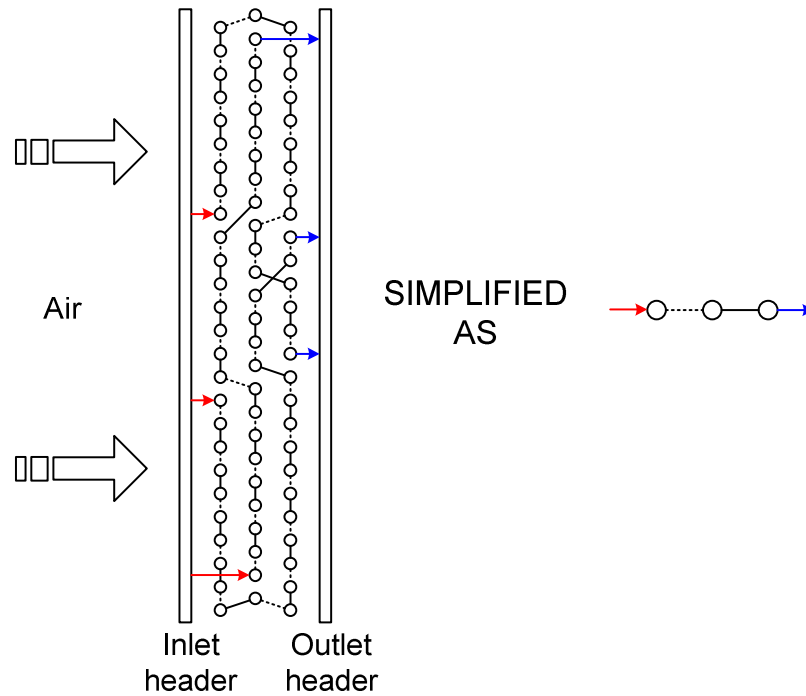
Figure 6.6 Simplification of the multi-row coil in Figure 6.5

With the simplification dictated by the above rules, the air flow propagation must be taken into account in the analysis. As a result, a tube-by-tube analysis is conducted in the new model. In order to separately calculate the heat transfer between air flow and each tube in the simplified coil, the percentage of each tube contributing to each region needs to be computed first.

Tubes in the simplified coil are numbered starting from the refrigerant inlet, i.e., the refrigerant inlet is the first tube and the refrigerant outlet is the last tube. For the parallel flow configuration coil, the first tube sees the fresh air; whereas for the counter flow coil, the last tube sees the fresh air.

The fraction of the ith tube covered by region 1 (the superheated region for the condenser) is

$$\beta_1^i = \min\left[1, \max\left(0, \zeta_1 N_{row} - i + 1\right)\right] \tag{6-88}$$

where ζ_1 is the fraction of the total heat exchanger length covered by the region 1. The superscript "i" here denotes the ith tube.

The percentage of the ith tube covered by region 2 (the two-phase region for the condenser) is

$$\beta_2^i = \min\left[1, \max\left(0, \zeta_1 N_{row} + \zeta_2 N_{row} - i + 1\right)\right] - \beta_1^i \tag{6-89}$$

where ζ_2 is the fraction of the total heat exchanger length covered by the region 2.

The percentage of the ith tube covered by region 3 (the subcooled region for the condenser) is

$$\beta_3^i = 1 - \beta_2^i - \beta_1^i \tag{6-90}$$

The sensible heat transfer between the air stream and the portion of the ith tube covered by region j ($j=1$, 2 and 3) is

$$q_{dry,j}^i = \dot{m}_a c_{p,a} \beta_j^i \left(T_a^i - T_{w,j}\right) \left[1 - \exp\left(-\frac{\alpha_a A_{o,eff}}{\dot{m}_a c_{p,a} N_{row}}\right)\right] \tag{6-91}$$

where $\dot{m}_a$ is the mass flow rate of dry air in the simplified coil, and T_a^i is the air temperature entering the ith tube.

The latent heat transfer between the air stream and the portion of the ith tube covered by region j ($j=1$, 2 and 3) is

$$q_{wet,j}^i = \dot{m}_a c_{p,a} \beta_j^i \max\left(0, \omega_a^i - \omega_{a,sat,j}\right) \Delta h_{fg,j} \left[1 - \exp\left(-\frac{\alpha_a A_{o,eff}}{\dot{m}_a c_{p,a} Le^{2/3} N_{row}}\right)\right] \tag{6-92}$$

where ω_a^i is the air inlet humidity ratio of the ith tube, $\omega_{a,sat,j}$ is the humidity ratio of saturated moist air evaluated at $T_{w,j}$, and $\Delta h_{fg,j}$ is the latent heat of water vapor at $T_{w,j}$. The water condensate flow rate that occurs on the portion of ith tube covered by region j ($j = 1$, 2 and 3) is

$$\dot{m}_{water,j}^i = \dot{m}_a c_{p,a} \beta_j^i \max\left(0, \omega_a^i - \omega_{a,sat,j}\right)\left[1 - \exp\left(-\frac{\alpha_a A_{o,eff}}{\dot{m}_a c_{p,a} Le^{2/3} N_{row}}\right)\right]$$
(6-93)

Therefore, air-to-wall heat transfer for region j ($j = 1$, 2 & 3) is

$$q_{a,j} = \sum_{i=1}^{N_{row}}\left(q_{dry,j}^i + q_{wet,j}^i\right)$$
(6-94)

The air-to-wall heat transfer for the ith tube

$$q_a^i = \sum_{j=1}^{3}\left(q_{dry,j}^i + q_{wet,j}^i\right)$$
(6-95)

Energy balance for the air stream across each tube needs to be considered to solve the air state at the intermediate tubes. For the parallel flow configuration, h_a^1 & ω_a^1 are known as the air inlet conditions, and $h_a^{N_{row}+1}$ & $\omega_a^{N_{row}+1}$ are solved as the air outlet conditions. For the counter flow configuration, $h_a^{N_{row}}$ & $\omega_a^{N_{row}}$ are known as the air inlet conditions, and h_a^0 & ω_a^0 are solved as the air outlet conditions.

Parallel flow configuration

$$\dot{m}_a(h_a^i - h_a^{i+1}) = q_a^i + \sum_{j=1}^{3}\left(\dot{m}_{water,j}^i h_{water,j}\right)$$
(6-96)

$$\dot{m}_a(\omega_a^i - \omega_a^{i+1}) = \sum_{j=1}^{3}\dot{m}_{water,j}^i$$
(6-97)

Counter flow configuration

$$\dot{m}_a (h_a^i - h_a^{i-1}) = q_a^i + \sum_{j=1}^{3} \left(\dot{m}_{water,j}^i h_{water,j} \right) \tag{6-98}$$

$$\dot{m}_a (\omega_a^i - \omega_a^{i-1}) = \sum_{j=1}^{3} \dot{m}_{water,j}^i \tag{6-99}$$

6.3.1.3 Energy Balance: Walls

The differential energy balance equation for the tubes and fins is

$$C_w \frac{\partial T_w}{\partial t} = q_a' - q_r' \tag{6-100}$$

where C_w is the heat capacity of the walls per unit length, q_a' is the air-to-wall heat flow rate per unit length, and q_r' is the refrigerant-to-wall heat flow rate per unit length.

C_w should be the total heat capacity of the tube and the fins per unit length

$$C_w = \frac{\pi}{4} (d_o^2 - d_i^2) \rho_t c_{p,t} + \frac{FPI}{0.0254} \left(P_t P_r - \frac{\pi}{4} d_o^2 \right) \delta_{fin} \rho_{fin} c_{p,fin} \tag{6-101}$$

where FPI is the number of fins per inch.

Integrating Eq. (6-100) from $z = 0$ to $z = L_1$ (superheated region for the condenser) gives

$$C_w \int_0^{L_1} \frac{\partial T_w}{\partial t} dz = \int_0^{L_1} q_a' dz - \int_0^{L_1} q_r' dz = q_{a,1} - q_{r,1} \tag{6-102}$$

Applying Leibniz's rule to Eq. (6-102) yields

$$C_w \frac{d}{dt} \left(\int_0^{L_1} T_w dz \right) - C_w T_w (L_1) \frac{dL_1}{dt} = q_{a,1} - q_{r,1} \tag{6-103}$$

Let $T_{w,1}$ be the average tube wall temperature for region 1, i.e.

$$T_{w,1} = \frac{1}{L_1} \int_0^{L_1} T_w dz \tag{6-104}$$

223

Eq. (6-103) can be rewritten as

$$\frac{dT_{w,1}}{dt} = \frac{q_{a,1} - q_{r,1}}{C_w L_1} - \frac{T_{w,1} - T_w(L_1)}{L_1} \frac{dL_1}{dt}$$

(6-105)

where $T_w(L_1)$ is the tube wall temperature at $z = L_1$, i.e., the tube wall temperature at the boundary between region 1 and 2. According to Zhang and Zhang (2006), a weighted mean temperature is used

$$T_w(L_1) = \left(1 - \frac{L_1}{L_2}\right) T_{w,1} + \frac{L_1}{L_2} T_{w,2}$$

(6-106)

Finally, the energy balance equation for the tube walls in region 1 becomes

$$\frac{dT_{w,1}}{dt} = \frac{q_{a,1} - q_{r,1}}{C_w L_1} + \frac{(T_{w,2} - T_{w,1})}{L_2} \frac{dL_1}{dt}$$

(6-107)

Similarly, the energy balance equation for the tube walls in region 2 is

$$\frac{dT_{w,2}}{dt} = \frac{q_{a,2} - q_{r,2}}{C_w(L_2 - L_1)} + \frac{T_{w,2} - T_{w,1}}{L_2} \frac{dL_1}{dt} + \frac{T_{w,3} - T_{w,2}}{L_t - L_1} \frac{dL_2}{dt}$$

(6-108)

The energy balance equation for the tube walls in region 3 is

$$\frac{dT_{w,3}}{dt} = \frac{q_{a,3} - q_{r,3}}{C_w(L_t - L_2)} + \frac{T_{w,3} - T_{w,2}}{L_t - L_1} \frac{dL_2}{dt}$$

(6-109)

6.3.2 V-TP Mode

In V-TP mode, the liquid region is not present in the heat exchanger, but the superheated region is unaffected. Therefore, Eq. (6-10) & (6-18) still apply.

The equations for mass and energy balance for the two-phase region are

$$A(L_2 - L_1)\left[(1 - \overline{\gamma})\frac{d\rho_f}{dp} + \overline{\gamma}\frac{d\rho_g}{dp}\right]\frac{dp}{dt} - A(\rho_g - \rho_f)(\overline{\gamma} - 1)\frac{dL_1}{dt}$$

$$+ A(\rho_g - \rho_f)(L_2 - L_1)\frac{d\overline{\gamma}}{dt} = \dot{m}_{12} - \dot{m}_{23}$$

(6-110)

$$A(L_2 - L_1)\left[(1-\bar{\gamma})\frac{d(\rho_f h_f)}{dp} + \bar{\gamma}\frac{d(\rho_g h_g)}{dp} - 1\right]\frac{dp}{dt}$$

$$-A(\rho_g h_g - \rho_f h_f)(\bar{\gamma}-1)\frac{dL_1}{dt} + A(L_2 - L_1)(\rho_g h_g - \rho_f h_f)\frac{d\bar{\gamma}}{dt} \quad\quad (6\text{-}111)$$

$$= \dot{m}_{12}h_f - \dot{m}_{23}h_{out} + q_{r,2}$$

The time derivative of mean void fraction becomes

$$\frac{d\bar{\gamma}}{dt} = \left(\left.\frac{\partial\bar{\gamma}}{\partial c}\right|_{x_{tp,in},x_{out}}\frac{dc}{dp} + \left.\frac{\partial\bar{\gamma}}{\partial x_{out}}\right|_{c,x_{tp,in}}\left.\frac{\partial x_{out}}{\partial p}\right|_{h_{out}}\right)\frac{dp}{dt} + \left.\frac{\partial\bar{\gamma}}{\partial x_{out}}\right|_{c,x_{tp,in}}\left.\frac{\partial x_{out}}{\partial h_{out}}\right|_p\frac{dh_{out}}{dt} \quad\quad (6\text{-}112)$$

where h_{out} is not only the refrigerant enthalpy leaving the two-phase region, but also

the refrigerant enthalpy leaving the heat exchanger.

As indicated in Eq. (6-112), the time derivative of both $\bar{\gamma}$ and h_{out} shows up. Since

h_{out} is already a state variable, there is no need to calculate it from Eq. (6-32).

Meanwhile, $\bar{\gamma}$ is continuous since it is a state variable as well, which ensures the

mass conservation during the switch between different model representations.

Since the liquid region is inactive, one can easily obtain

$$\dot{m}_{23} = \dot{m}_{out} \quad\quad (6\text{-}113)$$

$$\frac{dL_2}{dt} = 0 \qu\quad\quad (6\text{-}114)$$

The redundant wall temperature $T_{w,3}$ is calculated with the following pseudo state

equation

$$\frac{dT_{w,3}}{dt} = -K_w\left(T_{w,3} - T_{w,2}\right) \qu\quad\quad (6\text{-}115)$$

where K_w is a constant for $T_{w,3}$ tracking $T_{w,2}$.

The equations for the air side calculation given in Section 6.3.1.2 and the equation of global momentum balance Eq. (6-81) apply for this and other remaining modes as well.

6.3.3 TP-L Mode

In TP-L mode, the vapor region is not present in the heat exchanger, but the subcooled region is unaffected. Therefore, Eq. (6-50) & (6-80) still apply.

The equations for mass and energy balance for the two-phase region are

$$
AL_2 \left[(1-\bar{\gamma}) \frac{d\rho_f}{dp} + \bar{\gamma} \frac{d\rho_g}{dp} \right] \frac{dp}{dt} + A\left(\rho_g - \rho_f\right)\bar{\gamma} \frac{dL_2}{dt}
$$
$$
+ A\left(\rho_g - \rho_f\right) L_2 \frac{d\bar{\gamma}}{dt} = \dot{m}_{in} - \dot{m}_{23}
\tag{6-116}
$$

$$
AL_2 \left[(1-\bar{\gamma}) \frac{d\left(\rho_f h_f\right)}{dp} + \bar{\gamma} \frac{d\left(\rho_g h_g\right)}{dp} - 1 \right] \frac{dp}{dt} + A\left(\rho_g h_g - \rho_f h_f\right)\bar{\gamma} \frac{dL_2}{dt}
$$
$$
+ AL_2 \left(\rho_g h_g - \rho_f h_f\right) \frac{d\bar{\gamma}}{dt} = \dot{m}_{in} h_{in} - \dot{m}_{23} h_f + q_{r,2}
\tag{6-117}
$$

The time derivative of mean void fraction becomes

$$
\frac{d\bar{\gamma}}{dt} = \left(\left.\frac{\partial\bar{\gamma}}{\partial c}\right|_{x_{in},x_{tp,out}} \frac{dc}{dp} + \left.\frac{\partial\bar{\gamma}}{\partial x_{in}}\right|_{c,x_{tp,out}} \left.\frac{\partial x_{in}}{\partial p}\right|_{h_{in}} \right) \frac{dp}{dt} + \left.\frac{\partial\bar{\gamma}}{\partial x_{in}}\right|_{c,x_{tp,out}} \left.\frac{\partial x_{in}}{\partial h_{in}}\right|_{p} \frac{dh_{in}}{dt}
\tag{6-118}
$$

where h_{in} is not only the refrigerant enthalpy entering the two-phase region, but also the refrigerant enthalpy entering the heat exchanger.

The redundant parameters are calculated as

$$
\dot{m}_{12} = \dot{m}_{in}
\tag{6-119}
$$

$$
\frac{dL_1}{dt} = -K_L \left(L_1 - \varepsilon \right)
\tag{6-120}
$$

$$
\frac{dT_{w,1}}{dt} = -K_w \left(T_{w,1} - T_{w,2} \right)
\tag{6-121}
$$

6.3.4 TP Mode

The equations for mass and energy balance for the two-phase region are

$$AL_t\left[(1-\bar{\gamma})\frac{d\rho_f}{dp}+\bar{\gamma}\frac{d\rho_g}{dp}\right]\frac{dp}{dt}+A\left(\rho_g-\rho_f\right)L_t\frac{d\bar{\gamma}}{dt}=\dot{m}_{in}-\dot{m}_{out} \tag{6-122}$$

$$AL_t\left[(1-\bar{\gamma})\frac{d\left(\rho_f h_f\right)}{dp}+\bar{\gamma}\frac{d\left(\rho_g h_g\right)}{dp}-1\right]\frac{dp}{dt}+AL_t\left(\rho_g h_g-\rho_f h_f\right)\frac{d\bar{\gamma}}{dt} \tag{6-123}$$

$$=\dot{m}_{in}h_{in}-\dot{m}_{out}h_{out}+q_{r,2}$$

The time derivative of mean void fraction is calculated by Eq. (6-33) with h_{in} and h_{out}

in place of $h_{tp,in}$ and $h_{tp,out}$, respectively.

The equations for the redundant variables are Eq. (6-113), (6-114), (6-115), (6-119),

(6-120) & (6-121).

6.3.5 V Mode (Linear Enthalpy Profile)

The equations for mass and energy balance for the superheated region are

$$AL_1\left(\left.\frac{\partial\bar{\rho}_1}{\partial p}\right|_h\frac{dp}{dt}+\frac{1}{2}\left.\frac{\partial\bar{\rho}_1}{\partial\bar{h}_1}\right|_p\frac{dh_{in}}{dt}+\frac{1}{2}\left.\frac{\partial\bar{\rho}_1}{\partial\bar{h}_1}\right|_p\frac{dh_{out}}{dt}\right)=\dot{m}_{in}-\dot{m}_{out} \tag{6-124}$$

$$AL_1\left[\frac{1}{2}\left.\frac{\partial\bar{\rho}_1}{\partial\bar{h}_1}\right|_p\left(\frac{dh_{in}}{dt}+\frac{dh_{out}}{dt}\right)-\frac{dp}{dt}\right]=\dot{m}_{in}\left(h_{in}-\bar{h}_1\right)-\dot{m}_{out}\left(h_{out}-\bar{h}_1\right)+q_{r,1} \tag{6-125}$$

where $\bar{h}_1=\frac{1}{2}\left(h_{in}+h_{out}\right)$.

The equation for $T_{w,2}$ tracking $T_{w,1}$ is

$$\frac{dT_{w,2}}{dt}=-K_w\left(T_{w,2}-T_{w,1}\right) \tag{6-126}$$

The equation for $T_{w,3}$ tracking $T_{w,2}$ is Eq. (6-115).

The equations for L_1 and L_2 are

$$\frac{dL_1}{dt} = 0 \tag{6-127}$$

$$\frac{dL_2}{dt} = -K_L \left(L_2 - L_1 - \varepsilon \right) \tag{6-128}$$

The remaining constituent equations are Eq. (6-113) & (6-119).

6.3.6 V Mode (Uniform Enthalpy Profile)

The governing equations for this mode are the same as the V mode with linear enthalpy profile except $\overline{h}_1 = h_{out}$. It denotes that the mean refrigerant enthalpy inside the condenser will be represented by h_{out} in this mode. In general, the condenser model switches to this mode from the TP mode after the system is shut down, and the initial condition for $\overline{h}_1$ upon initiating this mode is the enthalpy of the saturated refrigerant vapor.

After the system is turned on, there is a possibility for the condenser model to switch back to the V mode with linear enthalpy profile from this mode. The switching criterion is $h_{in} > h_{out}$.

6.3.7 L Mode

The equations for mass and energy balance for the liquid region are

$$AL_t \left(\left. \frac{\partial \overline{\rho}_3}{\partial p} \right|_h \frac{dp}{dt} + \frac{1}{2} \left. \frac{\partial \overline{\rho}_3}{\partial \overline{h}_3} \right|_p \frac{dh_{in}}{dt} + \frac{1}{2} \left. \frac{\partial \overline{\rho}_3}{\partial \overline{h}_3} \right|_p \frac{dh_{out}}{dt} \right) = \dot{m}_{in} - \dot{m}_{out} \tag{6-129}$$

$$AL_t \left[\frac{1}{2} \left. \frac{\partial \overline{\rho}_3}{\partial \overline{h}_3} \right|_p \left(\frac{dh_{in}}{dt} + \frac{dh_{out}}{dt} \right) - \frac{dp}{dt} \right] = \dot{m}_{in} \left(h_{in} - \overline{h}_3 \right) - \dot{m}_{out} \left(h_{out} - \overline{h}_3 \right) + q_{r,3} \tag{6-130}$$

where $\overline{h}_3 = \frac{1}{2} \left(h_{in} + h_{out} \right)$.

The equation for $T_{w,2}$ tracking $T_{w,3}$ is

$$\frac{dT_{w,2}}{dt} = -K_w \left(T_{w,2} - T_{w,3} \right) \tag{6-131}$$

The equation for $T_{w,1}$ tracking $T_{w,2}$ is Eq. (6-121).

The equations for L_1 and L_2 are Eq. (6-114) & (6-127) . The remaining constituent equations are Eq. (6-119) & (6-132).

$$\dot{m}_{23} = \dot{m}_{in} \tag{6-132}$$

6.4 Evaporator Model

In the evaporator model, there are six modes, i.e., L-TP-V, L-TP, TP-V, TP (linearized enthalpy profile), TP (uniform enthalpy profile), V and L mode. The governing equations of each mode can be easily formulated by following the derivations presented in Section 6.3 and hence are not repeated for brevity. The equations are given in Appendix II.

6.5 Switching Criteria

The number of available fluid phases in the heat exchanger may vary under large disturbances and fluid phases can form or disappear. For instance, the condenser may experience phase change during the start-up operation. When the system starts up, the condenser may be filled with superheated vapor. As time goes by, the condensation takes place and the two-phase region forms. Eventually, the condenser will end up having three regions, i.e., vapor, two-phase and liquid region. In this scenario, the condenser will experience phase transition at least twice, i.e., V → V-TP → V-TP-L. In order to handle smooth transitions between different model modes, it is necessary to develop generalized and robust switching schemes.

6.5.1 When a Zone Disappears

In the work presented by Li and Alleyne (2010), the switching conditions for a zone to disappear are that the normalized zone length is nearly zero and continuing to decrease, i.e., $\zeta < \varepsilon_{min}$ and $\dfrac{d\zeta}{dt} < 0$. However, if looking into these switching conditions more carefully, one can conclude that $\dfrac{d\zeta}{dt} < 0$ is redundant and is always satisfied when a zone disappears. Take the transition from V-TP-L mode to V-TP mode as an example. When the liquid zone disappears, its length decreases from a value slightly larger than ε_{min} to a value slightly smaller than ε_{min}, and the time derivative of the normalized zone length is automatically ensured to be negative. Once the model is switched to V-TP mode, the length of the inactive liquid region does not change based on Eq. (6-114) and maintains its value right at the instant when the switch occurs. Since the length of the inactive liquid region does not change in V-TP mode, it will be still smaller than ε_{min} and its time derivative is zero, which does not violate the switching criteria for a zone to disappear. In other words, the model will not switch back to V-TP-L mode. Therefore, it is safe to eliminate the requirement of $\dfrac{d\zeta}{dt} < 0$ in the switching criteria for a zone to disappear.

It is found that using the actual zone length instead of the normalized zone length is more accurate for switching purposes because using the latter may cause large discrepancies in the case of long tube length. In all, the switching condition for a zone to disappear is summarized as: once the actual length of a zone is smaller than the threshold, which is regarded as the minimum length for a zone, it is believed that that zone disappears.

$$L_{zone} < \varepsilon_{\min} \qquad \text{(6-133)}$$

6.5.2 When a New Zone Forms

In the framework presented by Li and Alleyne (2010), the switching conditions for a new zone to form are on a case-by-case basis. For instance, the switching conditions from two-zone mode to three-zone mode are quite different from those from one zone mode to two-zone mode. This means that the customized switching schemes need to be devised for each switching scenario. This increases modeling complexity and is unnecessary. Hence, a generalized switching scheme needs to be devised in order to handle the cases in which the number of fluid phases increases.

The analysis is started by taking the switching from V-TP mode to V-TP-L mode as an example. Assume that a very small portion of liquid region already exists in the condenser, but at this point the condenser model is still in V-TP mode. The refrigerant mass stored in the two-phase zone can be calculated as

$$M = AL_{tp}\overline{\rho}_{tp} \qquad \text{(6-134)}$$

where $\overline{\rho}_{tp}$ is the mean refrigerant density of the two-phase zone whose length is L_{tp}, and can be readily calculated based on current mean void fraction $\overline{\gamma}$. Please be noted that L_{tp} already contains the small portion of refrigerant liquid. Assume the length of this liquid zone is $L_{sc,pseudo}$, based on the mass conservation, the refrigerant mass M can be also calculated as

$$M = AL_{sc,pseudo}\rho_f + A\left(L_{tp} - L_{sc,pseudo}\right)\overline{\rho}_{tp,tot} \qquad \text{(6-135)}$$

where $\bar{\rho}_{tp,tot}$ is the mean refrigerant density for the complete two-phase zone from saturated vapor to saturated liquid, can be calculated based on mean void fraction calculated by Eq. (6-32) with $x_{tp,in} = 1$ and $x_{tp,out} = 0$.

Combining Eq. (6-134) & (6-135) and solving for $L_{sc,pseudo}$

$$L_{sc,pseudo} = \frac{\bar{\rho}_{tp} - \bar{\rho}_{tp,tot}}{\rho_f - \bar{\rho}_{tp,tot}} L_{tp} \tag{6-136}$$

If the length of the liquid zone $L_{sc,pseudo}$ is greater than the threshold, which is regarded as the minimum length for a zone, it is believed that a noticeable amount of liquid is already in the condenser and thus a new zone forms.

The same derivation can be extended to other cases and it is not difficult to obtain the following generalized formulation of calculating the pseudo length of a new zone

$$L_{new\ zone,pseudo} = \frac{\bar{\rho}_{parent\ zone} - \bar{\rho}_{total\ parent\ zone}}{\rho_{new\ zone} - \bar{\rho}_{total\ parent\ zone}} L_{parent\ zone} \tag{6-137}$$

where

$L_{new\ zone,pseudo}$ - pseudo length of the new zone

$\rho_{new\ zone}$ - refrigerant density of the new zone

$L_{parent\ zone}$ - length of the parent zone in which the new zone forms, e.g., from V to V-TP, V is the parent zone; from TP-L to V-TP-L, TP is the parent zone;

$\bar{\rho}_{parent\ zone}$ - mean refrigerant density of the parent zone in which the new zone is included

$\bar{\rho}_{total\ parent\ zone}$ - mean refrigerant density of the complete parent zone in which the new zone is excluded

232

The switching condition for a new zone to form is that the pseudo length of this new zone needs to be greater than the threshold, i.e.,

$$L_{new\ zone, pseudo} > \varepsilon_{min} \tag{6-138}$$

The minimum threshold ε_{min} can be adjusted based on the application.

6.6 Model Validation

Utilizing the same supporting component models presented in Chapter 3 and the proposed moving boundary models presented in this chapter, the cycling transients of the FTVI system can be explored. Approach #2 is chosen to calculate the refrigerant pressure drop. The simulation results are compared against those obtained by the disretized model and experimental data.

Figure 6.7 shows the mode transition of both condenser and evaporator during the start-up operation. Let's take a look at the variation in the fluid phases in the condenser first. When the system starts up, the condenser is full of superheated refrigerant vapor (Mode 1). With the condenser pressure building up, the refrigerant condenses and the two-phase zone forms (Mode 2). Shortly, the vapor zone disappears (Mode 3) because the refrigerant in the evaporator has not fully vaporized yet at this point, resulting in the liquid-flooded compression, i.e., two-phase refrigerant leaves the compressor and enters the condenser. With the further refrigerant condensation, the liquid zone appears (Mode 4). Eventually, the vapor zone appears (Mode 5) after the liquid-flooded compression comes to an end because of complete vaporiziation in the evaporator.

The variation in the evaporator mode is much simpler than that of the condenser mode. While the system is in off-period, the refrigerant tends to migrate to the

evaporator and sedate itself there as the two-phase mixture. Since the refrigerant is static or nearly static, and the rate of heat transfer between the refrigerant and tube walls is quite small, it is reasonable to treat the evaporator as a pool and assume that the refrigerant enthalpy is spatially invariant. Shortly after the system starts up, the refrigerant vapor from the high pressure side, whose enthalpy is much higher, enters the evaporator through the expansion device. Shortly, with the appearance of the liquid zone in the condenser, the enthalpy of the incoming refrigerant flow will become smaller than the enthalpy of the refrigerant in the evaporator. During this very short period the state of the incoming flow changes rapidly, i.e., from vapor to two-phase. In order to simplify the analysis and avoid unnecessary mode switching, the refrigerant enthalpy is presumably uniform within the evaporator as long as the enthalpy of the incoming flow is greater than mean refrigerant enthalpy of the evaporator (Mode 1). Once the enthalpy of the incoming flow becomes greater than mean refrigerant enthalpy of the evaporator, it is switched to the TP mode with a linearly varying enthalpy profile (Mode 2). With full vaporization of the liquid refrigerant, the evaporator will eventually have two zones with the two-phase zone followed by the vapor zone. A clear view of how the length of each zone varies during the start-up operation for both heat exchangers is presented in Figure 6.8 and Figure 6.9.
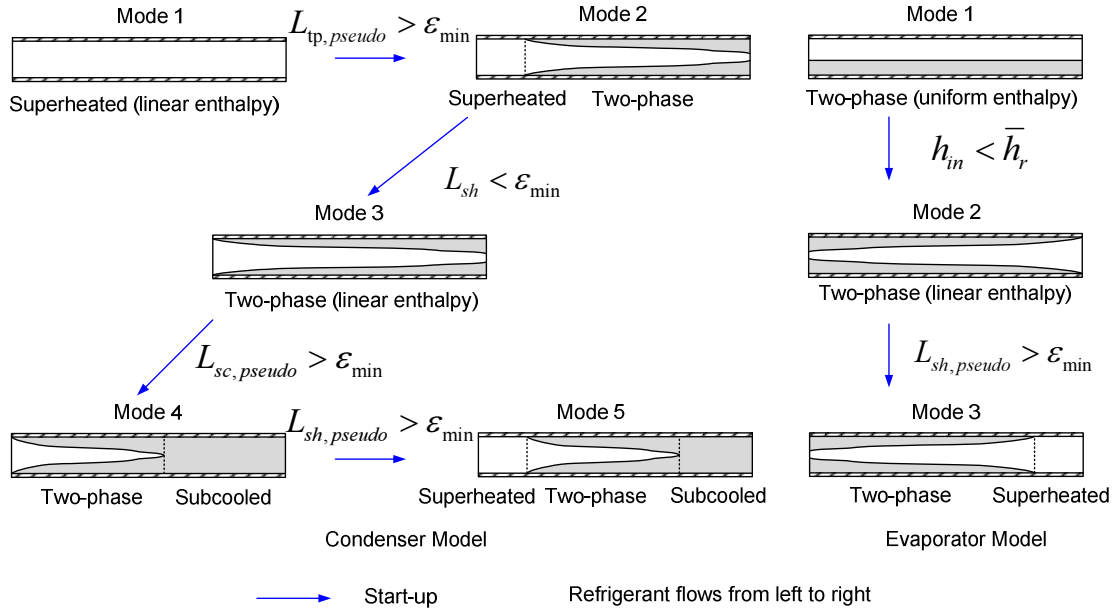
234

Figure 6.7 Mode switch of both heat exchangers during start-up

System start-up transients are shown in Figure 6.10 to Figure 6.17. The system transient responses subjected to a step change in upper-stage EEV opening are shown in Figure 6.18 to Figure 6.26. System shut-down transients are given in Figure 6.27 and Figure 6.28.

Overall, the simulation results obtained by the moving boundary models agree very well with those obtained by the validated discretized model. However, the former's computation speed is three times faster due to much lower number of resulting equations. The refrigerant mass integration errors of both heat exchangers are given in Figure 6.29. The maximum mass conservation error is less than 0.015%, demonstrating good performance of the new model.

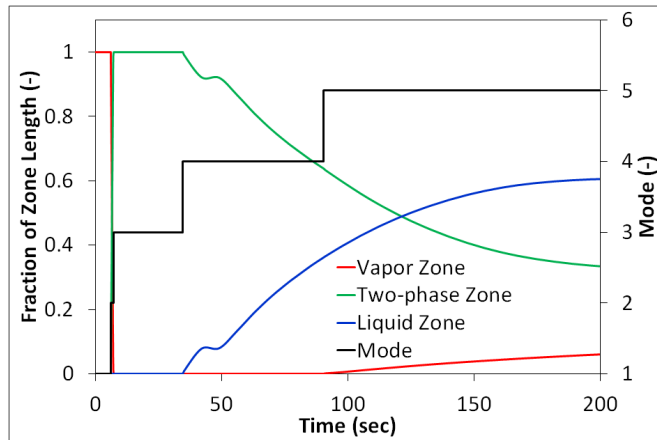**Figure 6.8 Fraction of zone length and the mode for condenser during start-up**
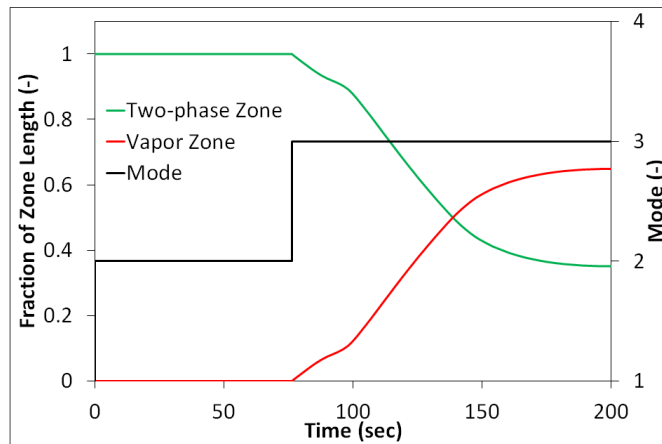
Figure 6.9 Fraction of zone length and the mode for evaporator during start-up
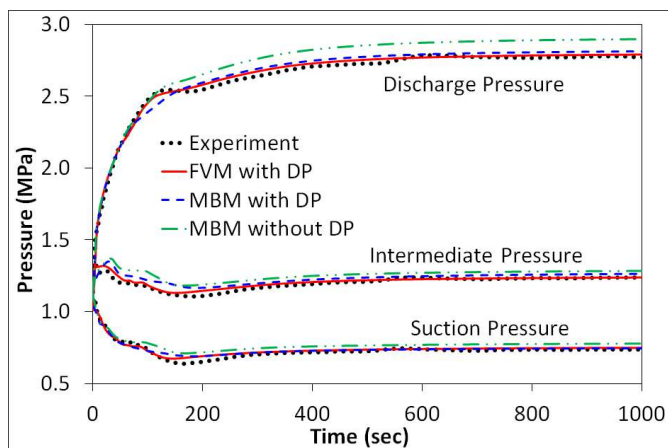
Figure 6.10 Pressure transients during start-up
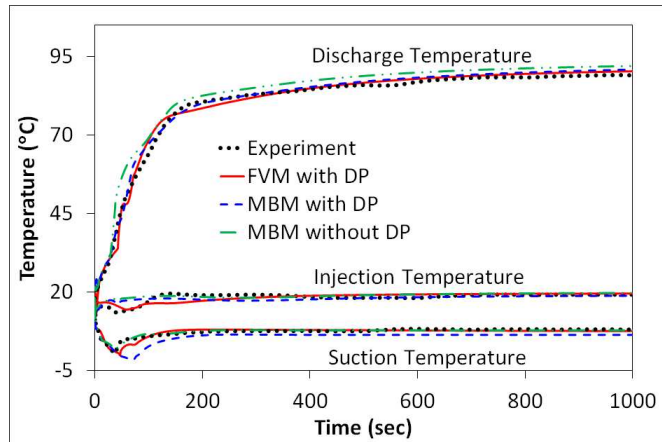
Figure 6.11 Temperature transients during start-up
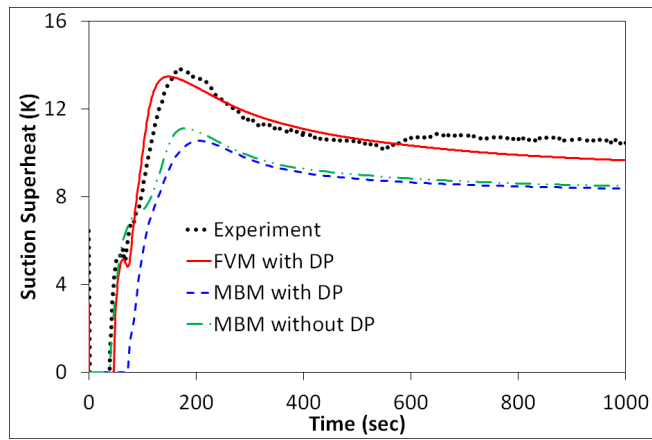
Figure 6.12 Suction superheat transients during start-up
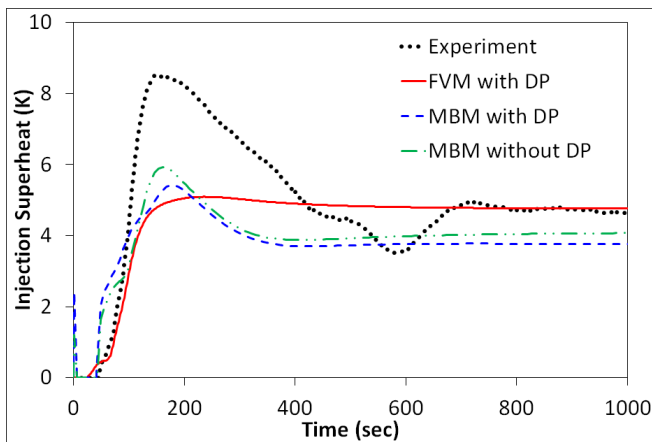
Figure 6.13 Injection superheat transients during start-up

237
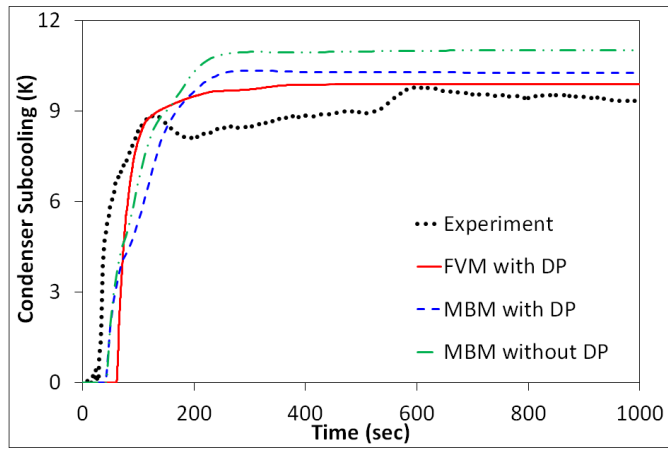
Figure 6.14 Condenser subcooling transients during start-up
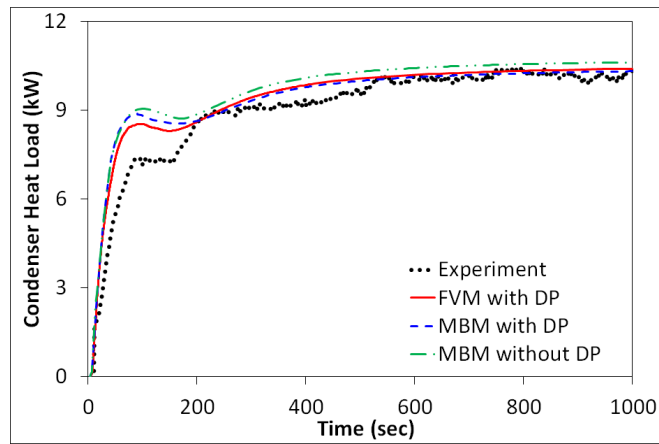
Figure 6.15 Condenser air side heat load transients during start-up
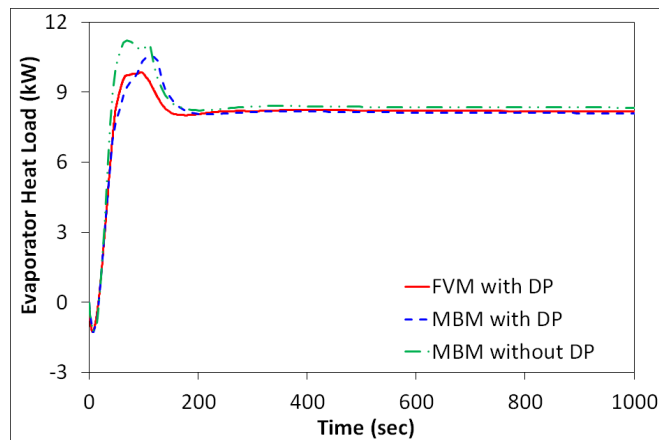
Figure 6.16 Evaporator air side heat load transients during start-up
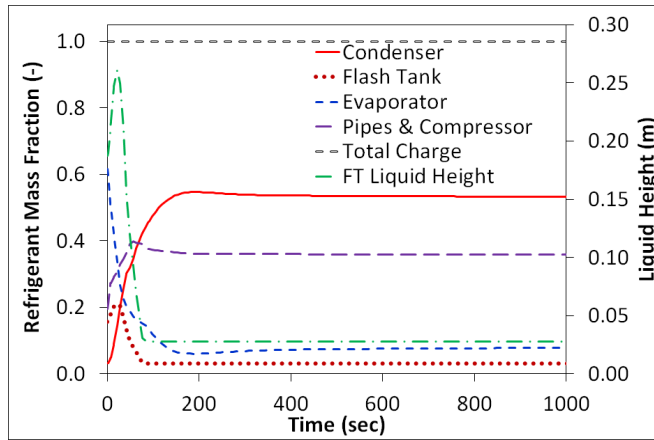
Figure 6.17 Predicted refrigerant mass distribution and flash tank liquid height during start-up
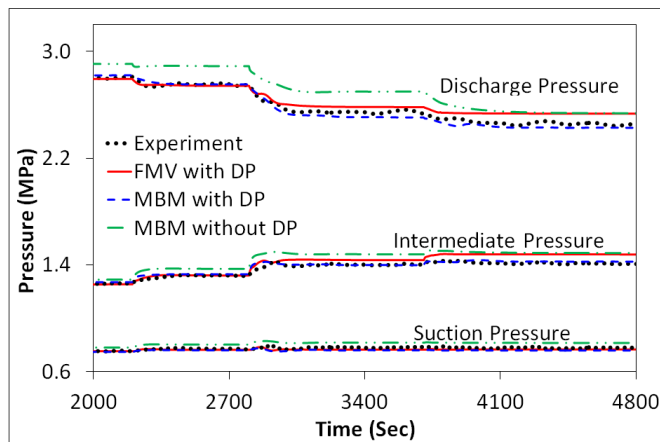
Figure 6.18 Pressure transients during the step change in EEV opening
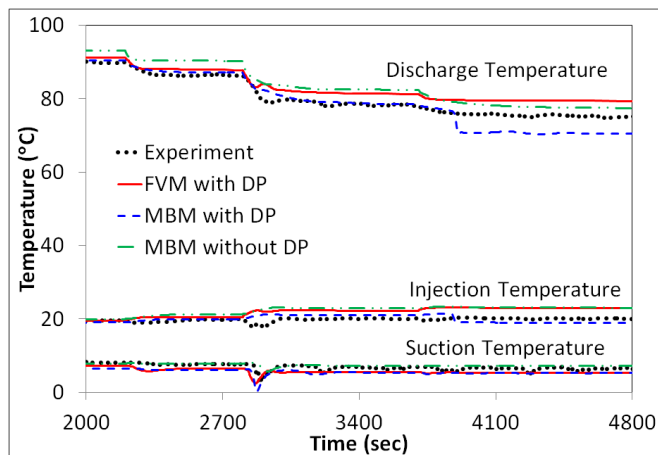
Figure 6.19 Temperature transients during the step change in EEV opening
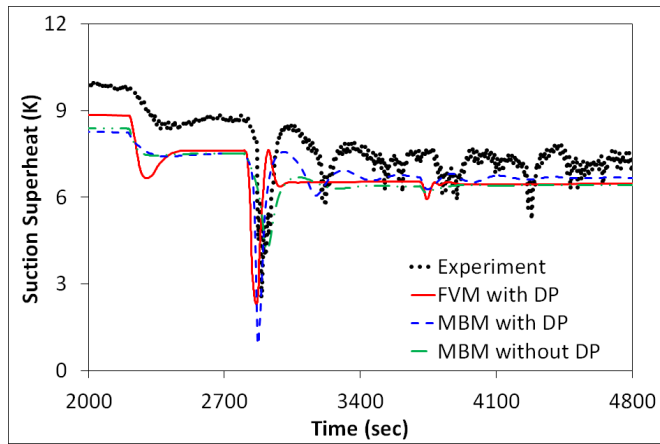
Figure 6.20 Suction superheat transients during the step change in EEV opening
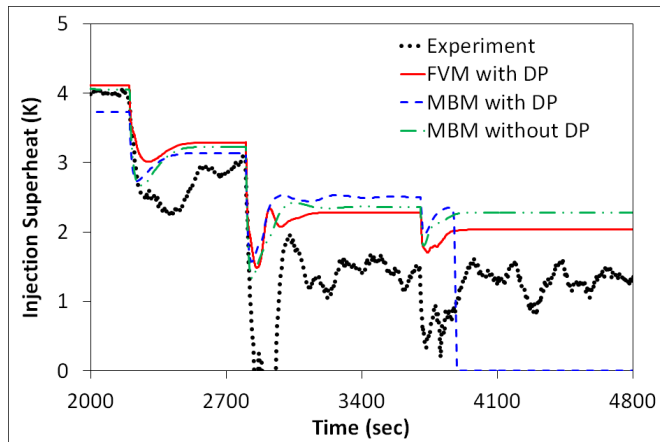
Figure 6.21 Injection superheat transients during the step change in EEV opening
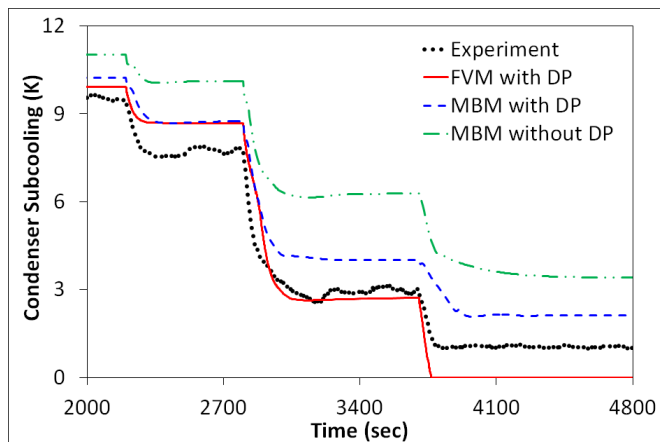
Figure 6.22 Condenser subcooling transients during the step change in EEV opening

240
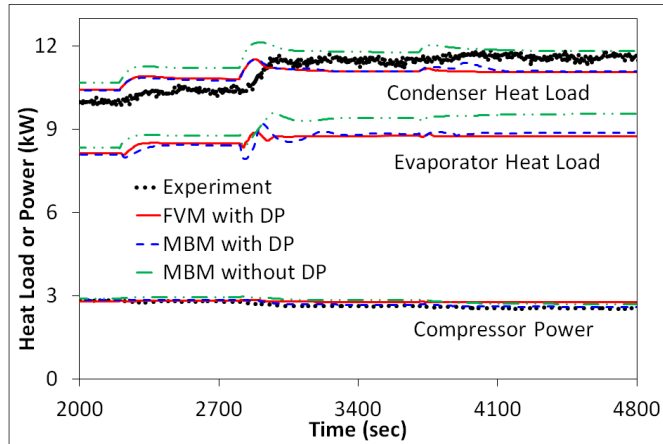
Figure 6.23 Transients of air side heat load and compressor power during the step change in EEV opening
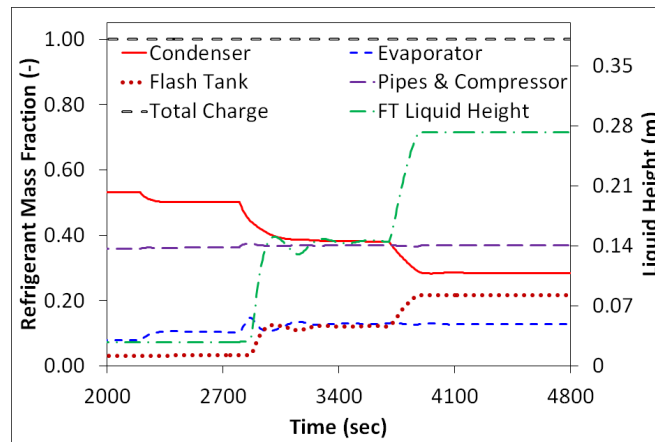
Figure 6.24 Predicted refrigerant distribution and flash tank liquid height during the step change in EEV opening
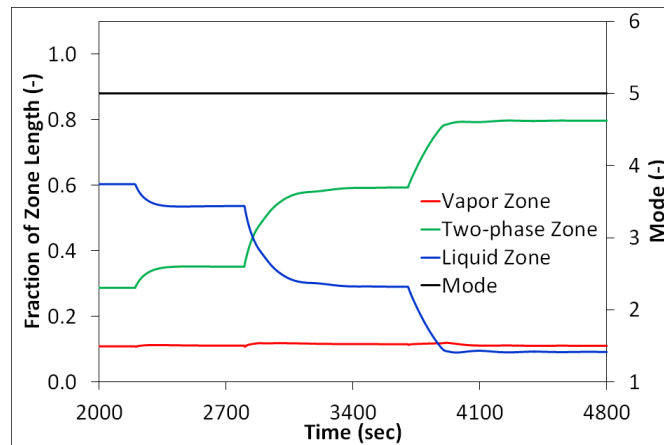
Figure 6.25 Fraction of condenser zone length during the step change in EEV opening

241
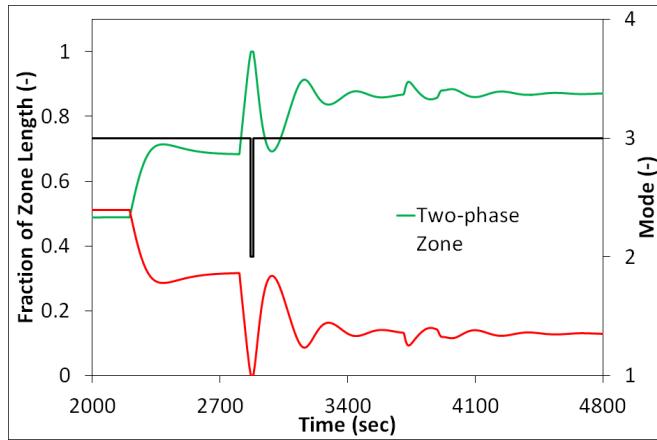
Figure 6.26 Fraction of evaporator zone length during the step change in EEV opening
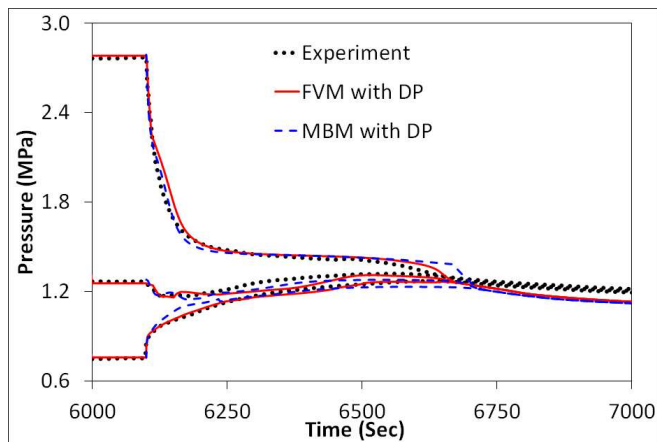
Figure 6.27 Pressure transients during shut-down
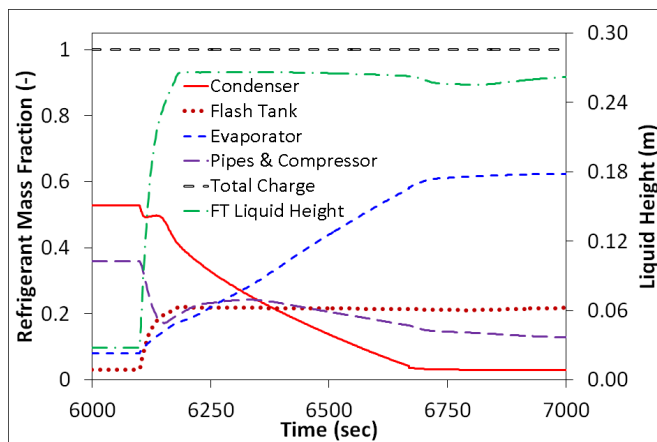
Figure 6.28 Predicted refrigerant mass distribution and flash tank liquid height during shut-down
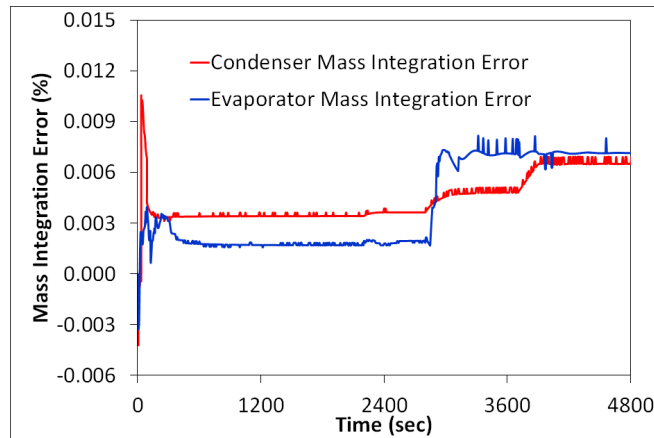
Figure 6.29 Refrigerant mass integration error

6.7 Discussions

Although being extensively used in the dynamic modeling of thermo-fluid systems and good prediction accuracy can be achieved with it, moving boundary method is not a panacea. Instead, there are some limitations associated with this paradigm, which prevent it from being applied in broader applications. However, these limitations have never been scrutinized in open literature. Thus, the author believes that it is conducive to discuss the difficulties that are encountered and the lessons that have been leaned during this study in order to stimulate insights for future research.

(1) Moving boundary models cannot manage reverse flows. In these models, it is strictly assumed that refrigerant flow enters the heat exchanger from one end, and leaves from the other. Reverse flows are not allowed to occur during the calculation; otherwise the problem is mathematically either over-determined or under-determined. Specifically, if the refrigerant flow is discharged on both ends of the heat exchanger, the problem is underdetermined. In this case, the number of governing equations remains the same, but the refrigerant enthalpy leaving both

243

ends needs to be solved. Consequently, the number of equations is one less than the number of unknowns, and the problem is considered under-determined. On the contrary, if the refrigerant flow enters the heat exchanger from both ends, the problem is over-determined. In this case, the number of equations is one more than the number of unknowns because the refrigerant enthalpy at neither ends needs to be solved.

(2) Moving boundary models can only manage non-zero flows. One of the boundary conditions for these models is refrigerant inlet enthalpy. If the incoming flow becomes zero, the models will fail because refrigerant inlet enthalpy cannot be determined.

(3) Close attention must be paid when modeling the shut-down transients. It is found that the refrigerant flow at the inlet of the condenser fluctuates around zero (it could be an incoming or outgoing flow) after the system has been shut down for a while. As stated above, moving boundary models cannot manage reverse flows. In order to avoid numerical failures, the simulation needs to switch to use the finite volume method before reverse flows are about to occur. The original zones before switch will be regarded as conventional non-deforming control volumes in the ensuing calculation, and the boundaries between these control volumes will be stationary as well.

On the other hand, as described in Section 3.6.4, shortly after the system is shut down, the refrigerant in the flash tank will enter the evaporator from both ends. According to the above reasoning, moving boundary models cannot handle this situation and the finite volume method should be used instead. This is the reason

why Figure 6.7 does not show the mode transition of the evaporator for the shut-down case because the simulation is switched to the finite volume modeling paradigm after the system is turned off.

(4) Mode switching is on a case-by-case basis. One should be aware that the mode switching sequence depicted in Figure 6.7 is not universally valid. Likewise, the switching sequence presented by Li and Alleyne's (2010) only works for their cases. Each case is different and modelers should be able to envision all the possible modes that the heat exchangers could encounter in their applications. For some special occasions, the heat exchanger might switch to unusual modes. For instance, in the work presented by Li *et al*. (2012), the evaporator can not only be in TP-V or TP mode, but also can be in V-TP mode, which is rarely encountered in most of the applications. However, once modelers have grasped the methodology, it should be fairly easy to extend the proposed framework to handle unusual modes even if they are not covered here.

(5) In moving boundary models, the variation in refrigerant outlet enthalpy does not always synchronize with the variation in the zone length when a zone tends to disappear, particularly under large disturbances. This issue was encountered in the shut-down case. In order to clearly elucidate this phenomenon, the variation in the length of the liquid zone is plotted along with that in the refrigerant outlet quality for the beginning of the shut-down operation of this FTVI system (Figure 6.30). The system is shut down at 6100 sec. The quality of the refrigerant flow leaving the condenser approaches to zero at 6104 sec. At this point, however, the fraction of the liquid zone is still greater than 0.5, which means that a significant portion

of the condenser is occupied by the saturated liquid. The original subcooled region turns into a region full of saturated liquid (Figure 6.31), and the condenser has transitioned from the V-TP-L mode to the V-TP-SAT_L mode. If the simulation proceeds without any special treatment, the condenser will not maintain the V-TP-SAT_L mode and will switch to the V-TP-TP mode because the calculated refrigerant outlet enthalpy will become greater than the enthalpy of the saturated liquid. However, this switch is physically incorrect. When the vapor zone disappears, the condenser model switches to TP-SAT_L mode. With the saturated liquid zone being depleted, the condenser model switches to TP mode. Sooner or later, all of refrigerant liquid vaporizes and the condenser will switch to the V mode.

Although there are three distinct zones in the V-TP-SAT_L mode (vapor, two-phase and saturated liquid), the mass and energy balances of these three zones cannot be evaluated separately. Otherwise, the problem will be over-determined. Instead, the two-phase zone and saturated liquid zone must be combined and evaluated together. Separate analysis of these two zones results in eight equations on the refrigerant side, i.e., two equations for each zone (the mass balance and energy balance), one equation for global momentum balance and one equation for the time-varying effect of mean void fraction. However, there are only 7 variables, i.e., $p, L_1, L_2, \bar{\gamma}, \dot{m}_{12}, \dot{m}_{23}$ and $\dot{m}_{out}$, because h_{out} will not be a variable anymore since it is always equal to the enthalpy of the saturated refrigerant liquid in this mode.

A remedy to this dilemma is to combine the two-phase zone and the saturated liquid zone together and apply the mass and energy balances to this combined zone. It will result in 6 equations (two for each zone, one for the global momentum balance and one for the time-varying effect of mean void fraction) and 6 variables (p, L_1, L_2, $\bar{\gamma}$, $\dot{m}_{12}$ and $\dot{m}_{out}$). L_2 is the position of the boundary between the two-phase zone and the saturated liquid zone. The complete set of the governing equations for the refrigerant flow is given below.

Since the superheated region is unaffected, Eq. (6-10) & (6-18) still apply. The mass balance and energy balance for the combined zone are given by Eq. (6-139) & (6-140), respectively

$$
A\left(L_2 - L_1\right)\left[\left(1-\bar{\gamma}\right)\frac{d\rho_f}{dp} + \bar{\gamma}\frac{d\rho_g}{dp}\right]\frac{dp}{dt} + A\left(L_t - L_2\right)\frac{d\rho_f}{dp}\frac{dp}{dt} + A\left(\rho_g - \rho_f\right)\bar{\gamma}\frac{dL_2}{dt}
$$
$$
-A\left(\rho_g - \rho_f\right)\left(\bar{\gamma}-1\right)\frac{dL_1}{dt} + A\left(\rho_g - \rho_f\right)\left(L_2 - L_1\right)\frac{d\bar{\gamma}}{dt} = \dot{m}_{12} - \dot{m}_{out}
$$
(6-139)

$$
A\left(L_2 - L_1\right)\left[\left(1-\bar{\gamma}\right)\frac{d\left(\rho_f h_f\right)}{dp} + \bar{\gamma}\frac{d\left(\rho_g h_g\right)}{dp} - 1\right]\frac{dp}{dt} + A\left(L_t - L_2\right)\left[\frac{d\left(\rho_f h_f\right)}{dt} - 1\right]\frac{dp}{dt}
$$
$$
+A\left(\rho_g h_g - \rho_f h_f\right)\bar{\gamma}\frac{dL_2}{dt} - A\left(\rho_g h_g - \rho_f h_f\right)\left(\bar{\gamma}-1\right)\frac{dL_1}{dt} + A\left(L_2 - L_1\right)\left(\rho_g h_g - \rho_f h_f\right)\frac{d\bar{\gamma}}{dt} \quad (6\text{-}140)
$$
$$
= \dot{m}_{12} h_g - \dot{m}_{out} h_f + \pi d_i\left(L_2 - L_1\right)\alpha_{r,2}\left(T_{w,2} - \bar{T}_{r,2}\right) + \pi d_i\left(L_t - L_2\right)\alpha_{r,3}\left(T_{w,3} - T_f\right)
$$

Eq. (6-43) still applies to calculate the time derivative of mean void fraction because a complete condensation still exists.

The remaining constituent equations for two redundant variables, i.e., $\dot{m}_{23}$ and h_{out}, are Eq. (6-113) & (6-141).

$$
\frac{dh_{out}}{dt} = \frac{dh_f}{dp}\frac{dp}{dt}
\tag{6-141}
$$

Of course, the global momentum equation Eq. (6-81) always applies. Therefore, one will have 8 equations and 8 variables and the problem should be able to solve. Although the refrigerant side is analyzed by combining the two-phase zone and the saturated liquid zone together, the air side and the walls should be calculated as if there were still three separate zones because mean wall temperature of the saturate liquid zone is still required in the heat transfer calculation.
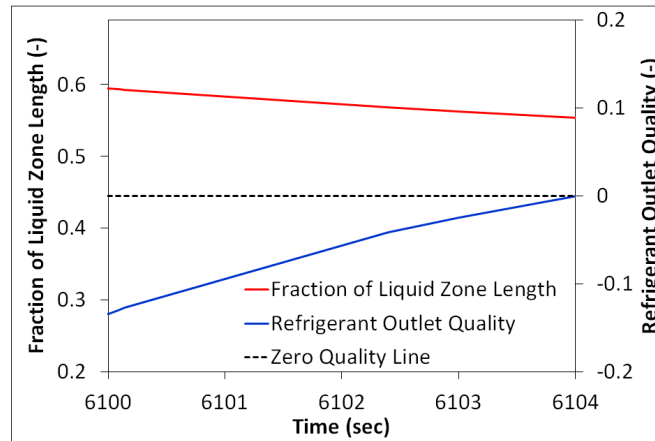
Figure 6.30 Subcooled length vs. refrigerant outlet quality
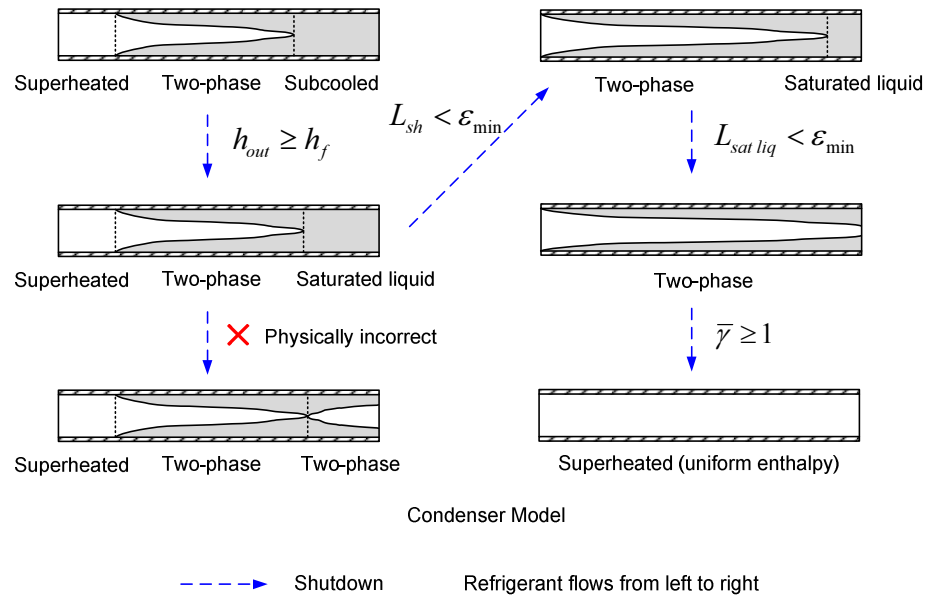
Figure 6.31 Mode switch of condenser during the shut-down operation

248

(6) Continuous model transition needs to be ensured to avoid chattering. Since the proposed model can be used to model the cycling transients of vapor compression systems, it is anticipated that the switch between different modes occurs frequently. Therefore, one must ensure that all the mode transitions must be at least continuous, if not smooth. Otherwise, chattering could occur during the switch, which will slow down the computation significantly.

(7) Model reduction. Although the proposed model is more computationally efficient than the FVM, it is still a little bit over complicated for the control purposes. Therefore, model reduction is necessary in order to have an even more efficient model for control design. Common practices include neglecting the dynamics in the single-phase region and lumping the wall and fluid temperature to set them equal to each other. By doing this, the order of the model can be further reduced. However, more investigations are still necessary even though the thesis is not obligated to focus on this area.

6.8 Summary

An advanced moving boundary heat exchanger model has been developed with switched model representations to accommodate the changing numbers of fluid zones under large disturbances. Novel switching schemes have been introduced to ensure smooth transition between different model representations. In the model, two novel approaches have been developed to account for refrigerant pressure drop. The first approach concentrates the pressure drop at the outlet of the heat exchanger, whereas the second approach assumes a linearly varying pressure profile within the heat exchanger. An improved LMTD method, which is able to handle temperature

crossing, has been developed to replace the mean temperature difference method that is massively used by the existing models in the literature. Given the fact that the existing moving boundary models greatly over predict air side heat transfer, a series of rules have been proposed to simplify multi-row coils in order to obtain a more accurate prediction for the heat exchanger performance. The model includes both mean void fraction and refrigerant outlet enthalpy into the state vector, which can not only ensure the refrigerant mass conservation during model switch, but also eliminate the need to solve for the refrigerant outlet enthalpy from the implicit transcendental equation.

7 Transient Modeling of a Multi-Split Air-Conditioning System and Control Method Investigation

7.1 Introduction

Multi-split VRF systems are increasingly some gaining in popularity over traditional air conditioning systems due to higher energy saving potential and better indoor thermal comfort as well as the ability of controlling individual zones. A typical VRF air conditioning system has a single outdoor unit and multiple indoor units, as shown in Figure 7.1. The outdoor unit incorporates a variable speed compressor, an accumulator and a condenser-fan coil, whereas each indoor unit encompasses an EEV (note: in some cases, EEVs are located in the condensing unit close to the compressor), an evaporator coil and an air circulating blower. Such a system exhibits much more complicated dynamics compared to the conventional systems with single evaporator because the operation in one zone may influence the units in other zones since all the evaporators are simultaneously served by one outdoor unit (Choi and Kim, 2003; Shah *et al*., 2003).

Over the past decade, both experimental and numerical studies have been extensively reported to explore the operating characteristics and control strategies of VRF systems. Park *et al*. (2001) analyzed the performance of a multi-type air conditioner with dual evaporators and pointed out the major control parameter of the system is the EEV opening. Choi and Kim (2003) conducted a series of experimental studies to scrutinize the capacity modulating characteristics of a VRF system with two indoor units by varying indoor load, EEV opening and compressor speed. It was concluded that VRF systems exhibit strong coupling effects between different indoor

units and thus simultaneous control of compressor speed and EEV opening is required. Shah *et al.* (2004) presented a generalized dynamic modeling approach for multi-evaporator air-conditioning cycles. A strong cross coupling effect between different evaporators was observed in the simulation studies. Chen *et al.* (2005) developed a simplified lumped-parameter transient thermodynamic model for a triple-evaporator air conditioning system and proposed a novel control strategy that was embodied with a self-tuning fuzzy control algorithm. Chiou *et al.* (2009) experimentally revealed that the fuzzy control method can be effectively applied in VRF systems to improve energy efficiency and achieve a steady temperature regulation for the conditioned zones. Zhang and Zhang (2011b) presented a validated dynamic model of a multi-indoor unit air conditioning system with a rapid cycling scroll compressor. Shao *et al.* (2012) developed a dynamic simulation model with the framework of two-phase fluid network to investigate the transient characteristics of multi-unit air conditioners. The state-space forms are used to model the system and components, and the component models are embedded in the fluid network model, which makes it possible to update the system model and components models independently. Xu *et al.* (2013c) proposed a novel capacity control algorithm for VRF systems which imitated the on/off control of a single evaporator air conditioning system. Zhu *et al.* (2013) developed generic simulation models based on TRNSYS to analyze the performance of VRF systems. With the aid of the developed models, system responses subject to the variations in the indoor and outdoor air temperatures, and EEV opening were inspected. No control strategy was reported. Elliott and Rasmussen (2013) introduced decentralized control architecture for multiple evaporator cooling systems in which the compressor speed is

used to regulate the suction pressure while the EEV opening and indoor coil fan speed are used to control the evaporator superheat and cooling rate set point.

It can be concluded from the above literature review that although there are extensive studies on the performance evaluation and control methods of VRF systems, not many investigations have been focused on the transient modeling of such systems. The aim of this paper is to explore the dynamic behavior of a VRF heat pump system with six indoor units in the cooling mode from a numerical simulation perspective. First-principles models are developed for each component and all the models are linked together in a systematic manner to analyze the transient operating characteristics of the system. A control strategy whose intention is to maintain the desired indoor air temperatures is proposed. Case studies are carried out to demonstrate the capability of the developed models and the feasibility of the proposed control strategy.
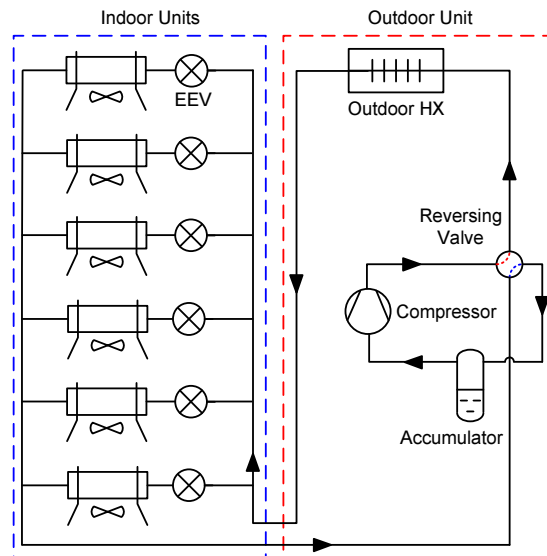
Figure 7.1 Schematic of a VRF system

7.2 Model Development

7.2.1 Variable-Speed Compressor Model

In the studied system, a variable-speed high-side scroll compressor is used, which means that the motor is cooled by the compressed high-pressure discharge refrigerant (Figure 7.2). The performance map, provided by the compressor manufacturer, is usually tabulated over a specific range of saturated discharge and suction temperatures and does not have a good accuracy when extrapolated beyond those temperature ranges. In light of this, it is wise to convert the performance map into curve-fitted equations to avoid numerical pitfalls during the simulations.
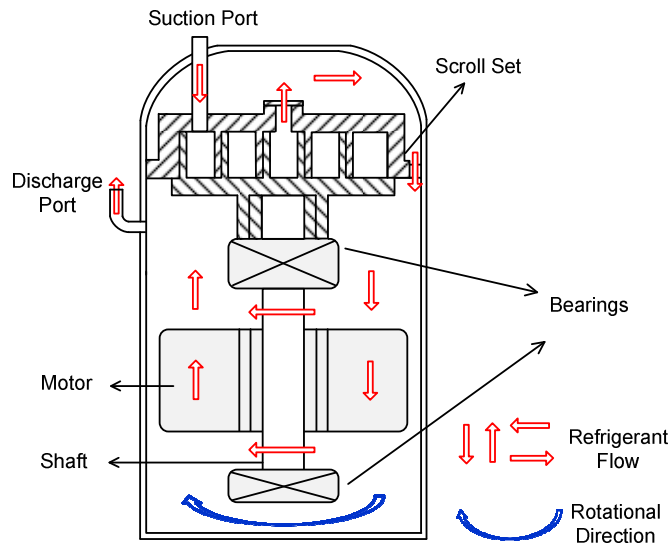
Figure 7.2 A high-side scroll compressor

The volumetric efficiency is a function of the suction pressure, discharge pressure and compressor frequency, and can be calculated by

$$\eta_v = c_0 + c_1\phi + c_2\phi^2 + c_3\phi^3 + c_4(p_{dis} - p_{suc})(1 + c_5 p_{suc}) \tag{7-1}$$

where

$$\phi = \frac{p_{dis}}{p_{suc}}$$

$$c_0 = a_1 + a_2\varpi + a_3\varpi^2$$

$$c_1 = a_4 + a_5\varpi + a_6\varpi^2$$

$$c_2 = a_7 + a_8\varpi + a_9\varpi^2$$

$$c_3 = a_{10} + a_{11}\varpi + a_{12}\varpi^2 \qquad (7\text{-}2)$$

$$c_4 = a_{13} + a_{14}\varpi + a_{15}\varpi^2$$

$$c_5 = a_{16} + a_{17}\varpi + a_{18}\varpi^2$$

$$\varpi = \frac{f}{f_{nom}}$$

The power consumed by the compressor is determined by

$$\dot{W}_{tot} = z_1 p_{suc} \dot{V}_{suc} \left(\phi^{z_2} - z_3 \right) + z_4 \qquad (7\text{-}3)$$

where

$$z_1 = b_1 + b_2\varpi + b_3\varpi^2$$

$$z_1 = b_4 + b_5\varpi + b_6\varpi^2$$

$$z_3 = b_7 + b_8\varpi + b_9\varpi^2 \qquad (7\text{-}4)$$

$$z_4 = b_{10} + b_{11}\varpi + b_{12}\varpi^2$$

The mass flow rate delivered by the compressor is determined by

$$\dot{m} = \eta_v f \rho_{suc} V_{disp} \qquad (7\text{-}5)$$

The enthalpy of the discharged refrigerant is calculated by

$$h_{dis} = \frac{(1-\chi)\dot{W}}{\dot{m}} + h_{suc} \qquad (7\text{-}6)$$

where χ is the fraction of the compressor power dissipated to the ambient.

7.2.2 Electronic Expansion Valve Model

The EEV model is given in Section 3.3.2.1.

7.2.3 Accumulator Model

The accumulator is modeled as a lumped control volume with an inlet and an outlet (Figure 7.3) by adopting the same assumption as those in the flash tank model (Section 3.3.4).

The governing equations for the accumulator can be described as follows

$$V_{acc} \frac{d\bar{\rho}_{acc}}{dt} = \dot{m}_{in} - \dot{m}_{out} \tag{7-7}$$

$$V_{acc} \left(\bar{\rho}_{acc} \frac{d\bar{h}_{acc}}{dt} - \frac{dp_{acc}}{dt} \right) = \dot{m}_{in} \left(h_{in} - \bar{h}_{acc} \right) - \dot{m}_{out} \left(h_{out} - \bar{h}_{acc} \right) \tag{7-8}$$

The leaving enthalpy is dependent upon the state of the refrigerant in the accumulator. There are two cases which need to be taken into account: 1) the refrigerant state is two-phase ($h_f < \bar{h}_{acc} < h_g$) and 2) the refrigerant state is single-phase ($\bar{h}_{acc} <= h_f$ or $\bar{h}_{acc} >= h_g$).

Case 1: the enthalpy of the outlet stream is determined as

$$h_{out} = \begin{cases} h_f & \text{if } H_{liq} > H_{out} + d_{out} \\ h_g - \left(\dfrac{H_{liq} - H_{out}}{d_{out}} \right) \left(h_g - h_f \right) & \text{if } H_{out} + d_{out} \geq H_{liq} \geq H_{out} \\ h_g & \text{if } H_{liq} < H_{out} \end{cases} \tag{7-9}$$

where the liquid height is determined as

$$H_{liq} = \frac{\bar{\rho}_{acc} - \rho_g}{\rho_f - \rho_g} H_{acc} \tag{7-10}$$

Case 2: the enthalpy of the outlet stream should be equal to the mean enthalpy of the refrigerant in the accumulator

$$h_{out} = \bar{h}_{acc} \tag{7-11}$$

256

The outlet mass flow rate can be calculated by

$$\dot{m}_{out} = \frac{\sqrt{(p_{acc} - p_{out})}}{f_{acc}} \tag{7-12}$$
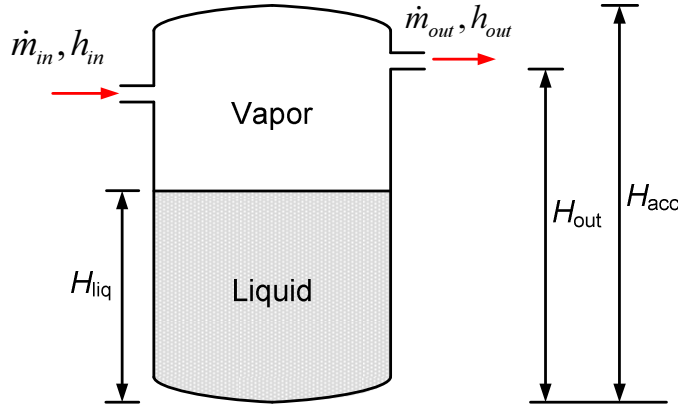
Figure 7.3 Schematic of an accumulator
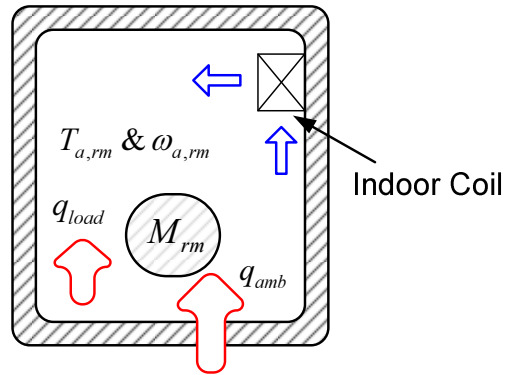
Figure 7.4 Lumped-parameter room model

7.2.4 Room Model

The conditioned rooms are emulated as lumped-parameter control volumes, as shown in Figure 7.4. Assuming that the objects inside the room are in thermal equilibrium with the indoor air, the governing equations that calculate the time-derivative of air temperature and humidity ratio can be easily formulated as

$$\left(M_{rm}c_{p,rm} + V_{rm}\rho_{a,rm}c_{p,a}\right)\frac{dT_{a,rm}}{dt} = \dot{m}_a\left(h_{a,in} - h_{a,rm}\right) + q_{amb} + q_{load} \tag{7-13}$$

$$\rho_{a,rm} V_{rm} \frac{d\omega_{a,rm}}{dt} = \dot{m}_a \left(\omega_{a,in} - \omega_{a,rm} \right) \tag{7-14}$$

Please note that $h_{a,in}$ and $\omega_{a,in}$ should be the state of air leaving the indoor coil, $h_{a,rm}$ and $\omega_{a,rm}$ are the enthalpy and humidity ratio of the room air, respectively.

7.2.5 Heat Exchanger Models

The moving boundary heat exchanger models presented in Chapter 6 are used in this study.

7.3 Control Strategy Development

VRF systems exhibit unique operating characteristics compared to the conventional air-conditioners. Their control strategies are also much more complicated than those of the conventional systems. Since the control strategies of VRF systems are often regarded as confidential, they are not commonly discussed in open literature. This paper tries to put forward a feasible control strategy for the studied system to maintain the indoor air temperatures during the operation in summer. This strategy can be summarized as follows:

(1) If $T_{a,rm} > T_{a,set} + \Delta T$, EEV is open to control the evaporator superheat and indoor coil fan is turned on.

(2) If $T_{a,rm} < T_{a,set} - \Delta T$, EEV is closed and indoor coil fan is turned off.

(3) If $T_{a,set} - \Delta T < T_{a,rm} < T_{a,set} + \Delta T$, the status of EEV and indoor coil fan keeps unchanged.

(4) The compressor frequency is used to regulate the saturated suction temperature.

(5) The compressor is turned off when all the indoor units are switched off.

(6) EEV openings and compressor frequency are controlled by PI controller.

7.4 Simulation Study

The studied system in the paper has six indoor units with different capacities. In order to verify the validity of the developed models and the proposed control strategy, a pull-down transient simulation is carried out. Before the simulation, all the indoor air temperatures are at 35°C, the same as the ambient temperature. When the system starts, the indoor air temperatures will start to drop and will be maintained within the desired range. The system operates for 10,000 seconds. The operating conditions of the studied system are listed in Table 7.1. The simulation results are shown in Figure 7.5 and Figure 7.6.
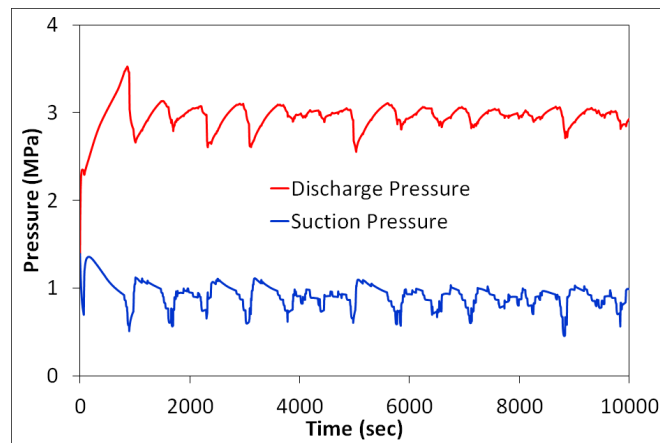
(a)
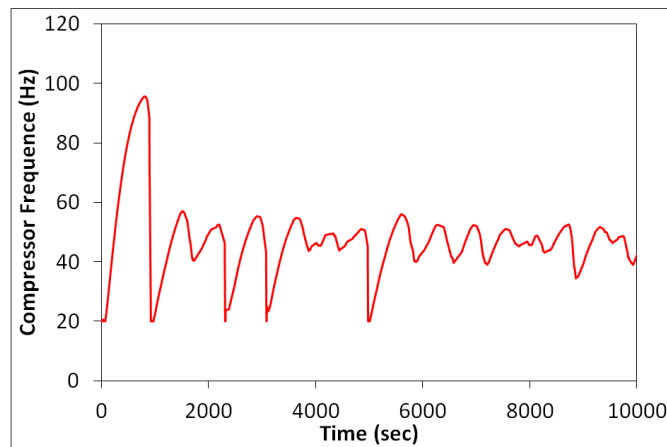
(b)
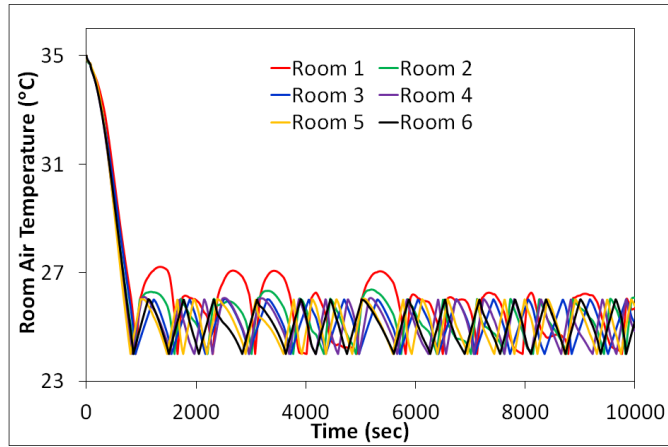
(c)
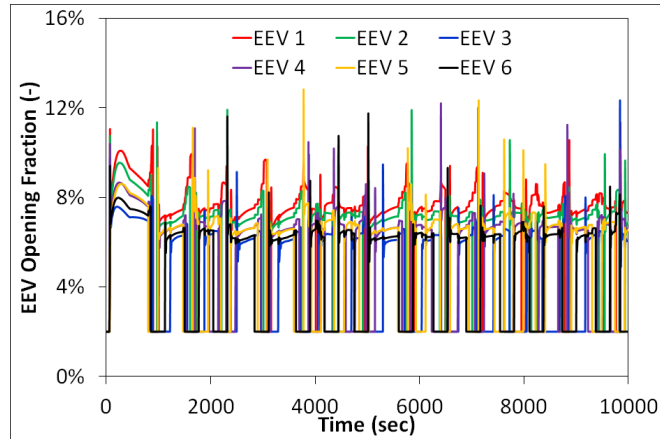
(d)

Figure 7.5 (a) Pressure vs. time; (b) Compressor frequency vs. time; (c) Room air temperature vs. time; (d) EEV opening fraction vs. time

Figure 7.5a shows the variations in suction pressure and discharge pressure. It can be observed that the suction pressure exhibits obvious fluctuations, which is caused by the variations in EEV openings. At the very beginning of the pull-down process, the suction pressure shows a sudden decrease for two reasons, i.e., 1) the compressor starts to draw a significant amount of refrigerant out of the accumulator and 2) EEVs are initially closed when the system starts up. After a short period, the suction pressure starts to rise because EEV openings increase. After 200 seconds, the

suction pressure starts to drop again because the indoor air is cooling down. Compared to the suction pressure, the discharge pressure undergoes much more benign variations except that it increases continuously during the pull-down period. The abrupt change in the discharge pressure thereafter is due to the sudden variations in the compressor frequency seen in Figure 7.5b. Figure 7.5c illustrates the variations in indoor air temperature for each room. Figure 7.5d represents the variations in EEV openings. All the EEVs can quickly respond to the required cooling capacity.

Figure 7.6a shows the capacity variations in each indoor unit. These six indoor units deliver different capacities that increase with the rise in the compressor frequency. Figure 7.6b demonstrates the variations in the suction temperature and discharge temperature as well as the compressor power. The suction temperature oscillates around 15°C, while the discharge temperature oscillates around 90°C. The compressor power is proportional to the variations of the compressor frequency. Figure 7.6c shows the variations in refrigerant mass flow through all the indoor units. Figure 7.6d illustrates the refrigerant mass distribution within the various components during the operation. Over 80% of refrigerant mass is located in the outdoor coil that serves as the condenser. The remainder is distributed within the accumulator and indoor coils.
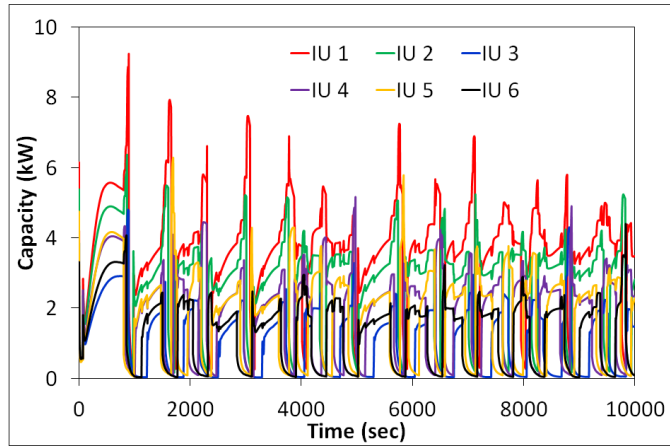
(a)
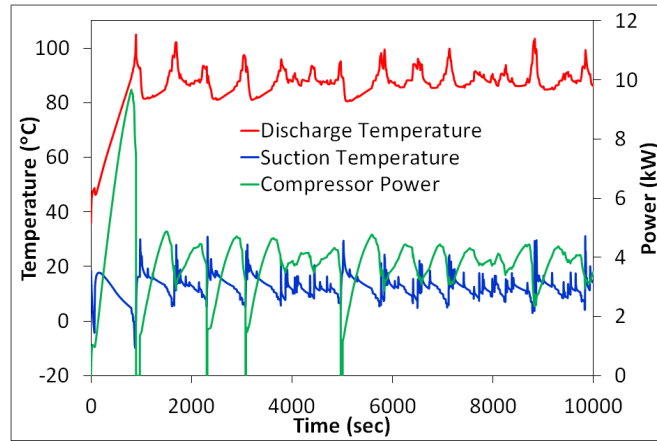
(b)
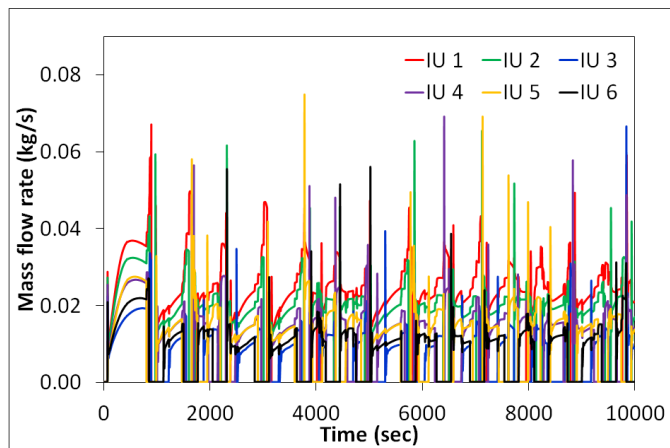
(c)
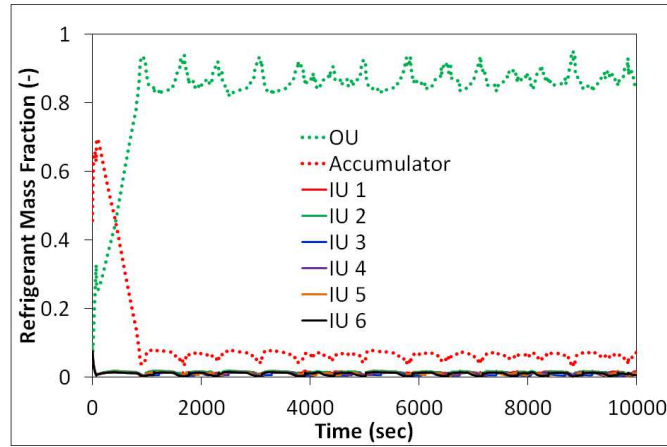
(d)

Figure 7.6 **(a) Indoor unit air-side capacity vs. time; (b) Suction temperature, discharge temperature & compressor power vs. time; (c) Refrigerant mass flow rate vs. time; (d) Refrigerant mass distribution vs. time**

Table 7.1 Operating conditions of the VRF system

Parameter	Value
Outdoor ambient temperature	35°C
Thermal load of each room	
Room 1	3.6 kW
Room 2	2.7 kW
Room 3	0.9 kW
Room 4	1.7 kW
Room 5	1.6 kW
Room 6	1.1 kW
Room air temperature setting	25±1°C
Compressor frequency	0 ~ 120 Hz

7.5 Summary

VRF systems exhibit more complicated dynamics compared to conventional single-evaporator systems. In this paper, a transient model for a VRF system with six indoor units is developed. Heat exchangers are modeled with the moving boundary method that is equipped with a comprehensive and robust switching scheme. Other components are analyzed using a lumped-parameter method. Considering unique operating characteristics of VRF systems, a control strategy that maintains the indoor

263

air temperatures at set values is proposed. The compressor frequency is used to regulate the saturated suction temperature. EEV openings are used to control the superheat degree of the evaporator coils. Room temperatures are regulated by hysteresis on-off control. The simulation test for controllability showed that the proposed control strategy is feasible to achieve individual zone control.

8 Summary and Conclusions

This thesis concerns itself with transient modeling of vapor compression systems focusing on two aspects in particular. The first part focuses on developing a comprehensive Modelica based framework for simulating the transient performance of vapor compression systems, which includes first-principles based heat exchanger models and a wide range of supporting component models. The second part concentrates on using the developed framework to explore the transient characteristics of advanced vapor compression systems, specifically, flash tank vapor injection heat pump system and multi-split variable refrigerant flow system. These two objectives have been completed and the conclusions are summarized as follows.

8.1 Transient Modeling Framework

8.1.1 Discretized Heat Exchanger Model

o A new discretized heat exchanger model has been developed based on a decoupled approach to modeling the heat transfer and pressure drop performance of the heat exchanger. The model is capable of accounting for the complex tube circuitry of the heat exchanger and handling dry and dehumidifying conditions. To reduce the computational complexity, the equation for the momentum balance has been simplified by neglecting the inertia term and the acceleration term. However, this simplification can still preserve the prevailing physics of fluid flow characteristics.

o The separated flow model without interfacial exchange is utilized for analysis of two-phase flows to incorporate the non-homogeneous effects so that a more accurate prediction for the transient characteristics of two-phase flows can be

achieved. The method of "enthalpy correction" has been developed to account for the slip effect in two-phase flows.

8.1.2 Moving Boundary Heat Exchanger Models

o An advanced moving boundary heat exchanger model has been developed with switched model representations to accommodate the changing numbers of fluid zones under large disturbances. Novel switching schemes have been introduced to ensure smooth transition between different model representations.

o In the model, two novel approaches have been developed to account for refrigerant pressure drop. The first approach concentrates the pressure drop at the outlet of the heat exchanger, whereas the second approach assumes a linearly varying pressure profile within the heat exchanger.

o An improved LMTD method, which is able to handle temperature crossing, has been developed to replace the mean temperature difference method that is massively used by the existing models in the literature.

o Given the fact that the existing moving boundary models greatly over predict air side heat transfer, a series of rules have been proposed to simplify multi-row coils in order to obtain a more accurate prediction for the heat exchanger performance.

o The model includes both mean void fraction and refrigerant outlet enthalpy into the state vector, which can not only ensure the refrigerant mass conservation during model switch, but also eliminate the need to solve for the refrigerant outlet enthalpy from the implicit transcendental equation.

8.1.3 Frosting Model

o A model that predicts non-uniform frost growth on the tube-fin heat exchangers and accounts for the resulting dynamic air flow maldistribution has been

266

developed. A novel scheme is presented to directly solve for the dynamic air flow redistribution as a result of non-uniform frost growth by linearizing the system of non-linear air pressure drop equalization equations. The proposed scheme has proven to be able to preserve accuracy and significantly expedite the simulation.

8.1.4 Hot Gas Defrost Model

o A five-stage hot gas defrost model has been developed. This model divides the defrosting period into five stages: preheating, melting start, melting, vaporizing and dry heating. Along with the frosting model, this model has been integrated into the discretized heat exchanger model. This enhanced heat exchanger model allows more accurate performance assessment for heat pumps.

8.1.5 Supporting Component Models

In addition to the above models, models for other supporting components are also developed to perform the transient simulations of vapor compression systems. The models that are pertinent to the research in this thesis are summarized below. Please refer to Appendix III for a complete list of model development for this modeling framework.

o A new transient model has been developed to predict the performance of vapor injection scroll compressor. This model is divided into two parts: the steady-state part for the mass flow rate calculation and the transient part for the compressor shell temperature and the refrigerant storage inside the compressor shell. The internal heat transfer between the refrigerant and metallic parts has been taken into account. The backflow phenomenon through the injection port is managed carefully. The prevailing physics of the refrigerant during compressor "on" and "off" period are represented in the model.

o A flash tank model has been developed. In the model, ideal phase separation is assumed and all the possible scenarios of refrigerant state inside the tank have been considered (excluding the supercritical condition).

o Various expansion device models have been developed. The throttling portion of the electronic expansion valve and the thermostatic expansion valve is modeled using an empirical correlation, whereas the sensor bulb portion of the latter is modeled based on the energy balance.

o A reversing valve model has been developed. This model enables that the same system model can be utilized to simulate both cooling and heating mode of heat pump systems. This is particularly convenient when characterizing the transients of heat pumps undergoing reverse-cycle defrosting.

o In order to study the transient performance of variable refrigerant flow systems, a curve-fitted variable speed compressor model, an accumulator model and a lumped-parameter zone have been developed.

8.1.6 Component Standard

o One of the salient features of this modeling framework is its modular nature that allows flexibility in the system configuration. The component models can be seamlessly linked together in an arbitrary manner. In order to fulfill this objective, a component standard has been developed. Each component model is comprised of an alternative sequence of control volumes and throttles, and always begins with a control volume and ends with a throttle. Mass and energy conservation is evaluated within the control volume, whereas the momentum conservation is solved using the throttle. With such a standard, the unified boundary conditions

for the component can be defined, i.e., the upstream connected mass flow rate and enthalpy flow rate, and the downstream connected pressure and enthalpy.

8.2 Transient System Simulation

8.2.1 Flash Tank Vapor Injection Heat Pump System

o   The transient simulations were carried out to explore the transient behavior of the system under cycling conditions. The comparisons between the simulation and experimental data showed that the model can capture the major heat transfer and fluid flow phenomena of the system.

o   The dynamic system response when subjected to step changes in the opening of the upper-stage EEV was studied. The results demonstrated that EEV opening has a crucial impact on the system performance and the liquid level in the flash tank. It was also found that a moderate adjustment of the upper-stage EEV has little impact on the suction pressure.

o   The characteristics of the system under the frosting condition have been adequately characterized. A detailed description of the physical processes was provided, and the causes that led to cyclic TXV hunting were identified and analyzed.

o   The characteristics of the system undergoing the reverse-cycle defrosting have been explored through the simulation. This simulation study can greatly facilitate the understanding of the complicated dynamic processes associated with the reverse-cycle defrosting.

8.2.2 Multi-split Variable Refrigerant Flow Air-conditioning System

o A pull down simulation for a multi-split VRF system with six indoor units has been conducted. Control strategy that aims to maintain the indoor air temperatures at set values was proposed. The simulation test for controllability showed that the proposed control strategy is feasible to achieve individual zone control.

9 List of Major Contributions and Future Work

9.1 Major Contributions

The modeling framework presented in this thesis can greatly assist the air-conditioning and refrigeration research and development community in the design of advanced vapor compression systems. The major contributions of this thesis include:

- o A comprehensive transient modeling framework supporting arbitrary vapor compression system configurations

- o A fully-fledged discretized heat exchanger model that accounts for

  - Non-homogeneous effects in two-phase flows

  - Air flow maldistribution

  - Dry, dehumidifying, frosting and defrosting conditions

- o Advanced switched moving boundary heat exchanger modeling paradigm with refrigerant pressure drop

- o Advanced system modeling and validation

  - The transient characteristics of an FTVI heat pump system undergoing cycling, frosting and reverse-cycle defrosting operations have been thoroughly explored. To the author's best knowledge, it is the first time to present such a comprehensive transient analysis for this system in open literature.

  - The pull-down transients of a multi-split VRF system have been investigated. The proposed control strategy is capable of achieving temperature control for individual zone.

- o Comprehensive experimental validation

- Favorable agreement between the simulations and experiments demonstrates the fidelity of the models.

o This Modelica model library provides the HVAC&R industry a tool for design, optimization and control of vapor compression systems. So far, this library has already been successfully used in a variety of applications, including two-stage FTVI and internal heat exchanger (IHX) systems, single-stage heat pump system, secondary-loop air-conditioning system and multi-split VRF system. The following papers have been published:

Journal papers:

- [233] "Transient modeling of a flash tank vapor injection heat pump system - Part I: Model development"

- [235] "Transient modeling of a flash tank vapor injection heat pump system - Part II: Simulation results and experimental validation"

Conference papers:

- [229] "Transient modeling of a multi-evaporator air conditioning system and control method investigation"

- [230] "A new dynamic heat exchanger model with frosting and defrosting"

- [231] "An improved moving boundary heat exchanger model with pressure drop"

- [232] "Comparison of equation-based and non-equation-based approaches for transient modeling of a vapor compression cycle"

- [234] "Modelica-based transient modeling for a flash tank vapor injection

272

system and experimental validation"

Co-author conference papers:

- [172] "Modelica-based heat pump model for transient and steady-state simulation using low-GWP refrigerants"

- [173] "Transient modeling and validation of an automotive secondary loop air-conditioning system"

The following journal papers are currently under development:

- Qiao, H., Aute, V., and Radermacher, R. "An improved heat exchanger model adopting the moving boundary method with pressure drop". Journal: Applied Thermal Engineering.

- Qiao, H., Aute, V., and Radermacher, R. "Modeling of non-uniform frost growth on tube-fin heat exchangers with dynamic air flow redistribution". Journal: International Journal of Heat and Mass Transfer.

- Qiao, H., Aute, V., and Radermacher, R. "Transient simulation of a flash tank vapor injection heat pump system under the reverse-cycle defrosting operation". Journal: HVAC&R Research.

- Qiao, H., Aute, V., and Radermacher, R. "Transient modeling of a multi-split variable refrigerant flow air-conditioning system and control strategy investigation". Journal: HVAC&R Research.

9.2 Future Work

Even though this thesis continues to advance the transient modeling capabilities of vapor compression system, the following would further enhance the research in

this field and quite possibly make the developed modeling framework more useful to the industry.

o Need to account for the effects of oil presence (Youbi-Idrissi and Bonjour, 2008). There are very few studies on this topic possibly because of unavailable thermophysical properties of the refrigerant-oil mixture. However, the oil presence can have a significant impact on the cycling transients of vapor compression systems. Specifically, during the flooded startup of the compressor, the refrigerant explodes out of the oil, possibly carrying oil with it out of the crankcase. This phenomenon greatly affects the transients of the suction pressure. Moreover, the oil affects the refrigerant migration in off-cycles as well. While the compressor is off, the refrigerant vapor migrates to the compressor crankcase, where it condenses into a liquid and is absorbed by the oil. Without considering the presence of the lubricant oil, the equalizing refrigerant pressure during the cycling transients cannot be predicted accurately.

o More rigorous experimental validation needs to be conducted, especially for the frosting and defrosting studies. In this thesis, the experimental measurements of the FTVI heat pump system did not include the frost thickness and the outdoor coil air flow rate. This inevitably increases the modeling complexity and causes more uncertainties in the prediction. Although the concept of the reverse-cycle defrosting is very simple, the resulting dynamic processes in the system are quite involved. More experiments can further enhance the understanding of these processes and in return compensate the theoretical studies.

o Model the transient behavior of heat pump systems undergoing hot gas bypass defrosting. There are quite a few experimental studies on the hot gas bypass defrosting of heat pumps. However, no modeling studies have been performed. Comparison between the reverse-cycle defrosting and hot gas bypass defrosting from a simulation perspective should be very attractive.

o With the aid of the numerical simulation, develop more efficient defrosting strategies for heat pumps. More efficient defrosting strategies can significantly improve the performance of heat pumps.

o Need to develop a more accurate valve model that handles the hysteresis effect. The hysteresis effect greatly increases the difficulty in the prediction of the mass flow rate through the valve. Without taking this effect into account, it is impossible to accurately capture the fluid flow phenomena of the system, especially when the influences of the control are present.

o A more thorough investigation of the performance of multi-split VRF systems. This thesis only provides a preliminary study on the transient behavior of such systems. However, these systems are gaining in popularity and their functionalities are becoming more and more sophisticated. In this context, modeling studies become necessary and more research needs to be carried out in this area, especially developing more sophisticated control strategies to achieve the comfort (temperature and humidity) control of individual zones.

o This Modelica model library is developed based on an old version of Modelica Language Specification (MLS) and cannot manage zero flow. Upgrading the

275

current library by using stream connector in the most recent version of MLS can resolve this issue.

o Speed up the simulation of off-cycles. Depending on the level of modeling complexity, on-cycles can be simulated in real time. However, for off-cycles, the simulation becomes much slower, especially when refrigerant mass flow rate approaches zero. Under this circumstance, relatively large time steps might allow for quicker computation if an adaptive but stable time-step approach can be used. However, this is challenging when using commercially available simulation platforms since the built-in solvers determine the time-steps based on the local truncation error. Therefore, model reduction can be a potential direction to pursue.

o Systematic research on refrigerant migration during off periods. It is found that the initial refrigerant distribution has a pronounced impact on start-up transients. However, to accurately determine the initial conditions for the transient simulation is very challenging. Therefore, it necessitates a more thorough and systematic study for the refrigerant migration during off-cycles in order to provide appropriate initial conditions for subsequent on-cycles.

o Numerical study on the cycling losses of vapor compression systems. Oil solubility, refrigerant migration and redistribution are three factors affecting the transient and cycling performance of all refrigeration and air conditioning equipment. How to quantitatively identify the effects of these factors on the energy losses is worthy of investigation.

o In the two-phase flow models, it is often assumed that vapor and liquid are in thermodynamic equilibrium. However, it is well known that this is a

simplification. How to identify the resulting influences of this assumption needs to develop a two-fluid model for two-phase flow, which accounts for the interphase interactions.

o Develop a CoilDesigner input file translator that essentially reads all the inputs from the CoilDesigner file and automatically generates the tube circuitries for the Modelica heat exchanger model.

o Evaluate different forms of the momentum balance, i.e., fully transient, steady-state, no pressure drop, the spatially invariant derivative of the pressure, and the linearized pressure profile. Modeling of the refrigerant side can be significantly simplified if choosing an appropriate approach of calculating the momentum balance. But this needs to a comprehensive evaluation for the effects of different forms of the momentum balance on the prediction accuracy and computation speed.

o More control-oriented dynamic modeling of vapor compression systems. Transient simulations of vapor compression systems serve two purposes in general: (1) to explore the low level detailed dynamics; (2) to design and evaluate control strategies. Since this thesis has primarily focused on the first aspect, more reduced order models suitable for controller design need to be developed to fulfill the second goal. Moreover, these models need to be used in various applications for controller design and verified with experimental implementation.

Appendix I - Partial Derivatives of Fluid Properties

Note – This appendix provides detailed derivations of the partial derivatives of fluid properties commonly used in the dynamic simulation of vapor compression systems. The original formulations are given in Richter (2008) without the derivations.

In dynamic simulations, the equations for energy, mass and momentum for a control volume are rewritten in terms of derivatives with respect to time. The mass and energy balances contain the derivative of density with respect to time. If the properties of pressure and specific enthalpy (and their evolution over time) are known, the derivative of density can be rewritten as

$$\frac{d\rho}{dt} = \left(\frac{\partial\rho}{\partial p}\right)_h \frac{dp}{dt} + \left(\frac{\partial\rho}{\partial h}\right)_p \frac{dh}{dt} \tag{I-1}$$

In order to compute the two partial derivatives, two different cases are required: single-phase and two-phase. Sometimes, the equations become simpler to derive for the specific volume instead of the density. The resulting partial derivatives of specific volume can be transformed into partial derivatives of density using the following simple relation

$$\frac{\partial v}{\partial \rho} = -\frac{1}{\rho^2} \tag{I-2}$$

I.1 Single-phase State

The partial derivatives for the single-phase fluid can be calculated as a function of β, k and c_p

$$\left(\frac{\partial\rho}{\partial h}\right)_p = \frac{\left(\frac{\partial\rho}{\partial T}\right)_p}{\left(\frac{\partial h}{\partial T}\right)_p} = -\frac{\beta\rho}{c_p} \tag{I-3}$$

$$\left(\frac{\partial\rho}{\partial p}\right)_h = \frac{-T\beta^2 + \beta + k\rho c_p}{c_p} \tag{I-4}$$

where β is the isobaric coefficient of expansion, k is the isothermal compressibility, and c_p is the specific heat capacity at constant pressure which can be determined from the fluid properties

$$\beta = -\frac{1}{\rho}\left(\frac{\partial\rho}{\partial T}\right)_p \tag{I-5}$$

$$k = \frac{1}{\rho}\left(\frac{\partial\rho}{\partial p}\right)_T \tag{I-6}$$

$$c_p = \left(\frac{\partial h}{\partial T}\right)_p \tag{I-7}$$

The derivation of Eq. (I-4) is given below.

From any thermodynamics textbook, one can obtain

$$c_p - c_v = T\left(\frac{\partial v}{\partial T}\right)_p\left(\frac{\partial p}{\partial T}\right)_v \tag{I-8}$$

It is easy to obtain (please refer to Eq. (I-34))

$$\left(\frac{\partial h}{\partial p}\right)_T = -T\left(\frac{\partial v}{\partial T}\right)_p + v \tag{I-9}$$

Because

$$\left(\frac{\partial h}{\partial p}\right)_T = \frac{\left(\frac{\partial h}{\partial v}\right)_T}{\left(\frac{\partial p}{\partial v}\right)_T} \tag{I-10}$$

So Eq. (I-9) can be rearranged as

$$\left(\frac{\partial v}{\partial p}\right)_T = \left(\frac{\partial v}{\partial h}\right)_T \left[-T\left(\frac{\partial v}{\partial T}\right)_p + v\right] \tag{I-11}$$

Also

$$\left(\frac{\partial v}{\partial p}\right)_T \left(\frac{\partial p}{\partial T}\right)_v \left(\frac{\partial T}{\partial v}\right)_p = -1$$

$$\Rightarrow \left(\frac{\partial v}{\partial T}\right)_p = -\left(\frac{\partial v}{\partial p}\right)_T \left(\frac{\partial p}{\partial T}\right)_v \tag{I-12}$$

Substituting Eq. (I-11) into Eq. (I-12) yields

$$\left(\frac{\partial v}{\partial T}\right)_p = -\left(\frac{\partial v}{\partial h}\right)_T \left(\frac{\partial p}{\partial T}\right)_v \left[-T\left(\frac{\partial v}{\partial T}\right)_p + v\right]$$

$$= \left(\frac{\partial v}{\partial h}\right)_T \left[T\left(\frac{\partial v}{\partial T}\right)_p \left(\frac{\partial p}{\partial T}\right)_v - v\left(\frac{\partial p}{\partial T}\right)_v\right] \tag{I-13}$$

Substituting Eq. (I-8) into Eq. (I-13)

$$\left(\frac{\partial v}{\partial T}\right)_p = -\left(\frac{\partial v}{\partial h}\right)_T \left(\frac{\partial p}{\partial T}\right)_v \left[-T\left(\frac{\partial v}{\partial T}\right)_p + v\right]$$

$$= \left(\frac{\partial v}{\partial h}\right)_T \left[c_p - c_v - v\left(\frac{\partial p}{\partial T}\right)_v\right] \tag{I-14}$$

Because

$$h = u + pv$$

$$\Rightarrow \left(\frac{\partial h}{\partial T}\right)_v = \left(\frac{\partial u}{\partial T}\right)_v + v\left(\frac{\partial p}{\partial T}\right)_v + p\left(\frac{\partial v}{\partial T}\right)_v = c_v + v\left(\frac{\partial p}{\partial T}\right)_v \tag{I-15}$$

Therefore, Eq. (I-14)

$$\left(\frac{\partial v}{\partial T}\right)_p = \left(\frac{\partial v}{\partial h}\right)_T \left[c_p - \left(\frac{\partial h}{\partial T}\right)_v\right] \tag{I-16}$$

Since

$$\left(\frac{\partial v}{\partial h}\right)_T \left(\frac{\partial h}{\partial T}\right)_v \left(\frac{\partial T}{\partial v}\right)_h = -1$$

$$\Rightarrow \left(\frac{\partial v}{\partial T}\right)_h = -\left(\frac{\partial v}{\partial h}\right)_T \left(\frac{\partial h}{\partial T}\right)_v \tag{I-17}$$

Substituting Eq. (I-17) into Eq. (I-16) yields

$$\left(\frac{\partial v}{\partial T}\right)_p = c_p \left(\frac{\partial v}{\partial h}\right)_T + \left(\frac{\partial v}{\partial T}\right)_h$$

$$\Rightarrow \left(\frac{\partial \rho}{\partial T}\right)_p = c_p \left(\frac{\partial \rho}{\partial h}\right)_T + \left(\frac{\partial \rho}{\partial T}\right)_h \tag{I-18}$$

$$\Rightarrow \left(\frac{\partial \rho}{\partial T}\right)_h = \left(\frac{\partial \rho}{\partial T}\right)_p - c_p \left(\frac{\partial \rho}{\partial h}\right)_T$$

Since

$$\left(\frac{\partial h}{\partial T}\right)_p \left(\frac{\partial T}{\partial p}\right)_h \left(\frac{\partial p}{\partial h}\right)_T = -1$$

$$\Rightarrow c_p = -\left(\frac{\partial p}{\partial T}\right)_h \left(\frac{\partial h}{\partial p}\right)_T \tag{I-19}$$

Substituting Eq. (I-19) into Eq. (I-18) yields

$$\left(\frac{\partial \rho}{\partial T}\right)_h = \left(\frac{\partial \rho}{\partial T}\right)_p + \left(\frac{\partial p}{\partial T}\right)_h \left(\frac{\partial h}{\partial p}\right)_T \left(\frac{\partial \rho}{\partial h}\right)_T$$

$$= \left(\frac{\partial \rho}{\partial T}\right)_p + \left(\frac{\partial p}{\partial T}\right)_h \left(\frac{\partial \rho}{\partial p}\right)_T$$

$$= -\beta\rho - k\rho\left(\frac{\partial h}{\partial T}\right)_p \left(\frac{\partial p}{\partial h}\right)_T$$

$$= -\beta\rho - k\rho c_p \left(\frac{\partial p}{\partial h}\right)_T$$

$$= -\beta\rho - \frac{k\rho c_p}{-T\left(\frac{\partial v}{\partial T}\right)_p + v}$$

$$= -\beta\rho - \frac{k\rho c_p}{-T\dfrac{dv}{d\rho}\left(\frac{\partial \rho}{\partial T}\right)_p + v}$$

$$= -\beta\rho + \frac{k\rho c_p}{\beta T v - v}$$

$$= \frac{-T\beta^2 + \beta + k\rho c_p}{\beta T v - v} \qquad \text{(I-20)}$$

From Eq. (I-19), one can obtain

$$\left(\frac{\partial T}{\partial p}\right)_h = -\frac{1}{c_p}\left(\frac{\partial p}{\partial h}\right)_T \qquad \text{(I-21)}$$

Eventually,

$$\left(\frac{\partial \rho}{\partial p}\right)_h = \frac{\left(\dfrac{\partial \rho}{\partial T}\right)_h}{\left(\dfrac{\partial p}{\partial T}\right)_h} = \left(\frac{\partial \rho}{\partial T}\right)_h \left(\frac{\partial T}{\partial p}\right)_h = -\frac{1}{c_p}\left(\frac{\partial \rho}{\partial T}\right)_h \left(\frac{\partial p}{\partial h}\right)_T$$

$$= -\frac{1}{c_p}\frac{-T\beta^2 + \beta + k\rho c_p}{\beta T v - v}\left(v - \beta T v\right) \qquad \text{(I-22)}$$

$$= \frac{-T\beta^2 + \beta + k\rho c_p}{c_p}$$

282

I.2 Two-phase State

The equations for the partial derivatives for the two-phase state can be derived using a homogeneous model to describe the fluid flow

$$v = v_f + \frac{h - h_f}{h_g - h_f}\left(v_g - v_f\right) \tag{I-23}$$

where the quotient at the right-hand side describes the static quality $\hat{x}$ of the two-phase fluid

$$\hat{x} = \frac{h - h_f}{h_g - h_f} \tag{I-24}$$

This yields the following differentiation

$$\left(\frac{\partial v}{\partial h}\right)_p = \frac{v_g - v_f}{h_g - h_f} \tag{I-25}$$

The partial derivative of specific volume with respect to the pressure can be written as

$$\left(\frac{\partial v}{\partial p}\right)_h = \frac{dv_f}{dp} + \frac{d\hat{x}}{dp}\left(v_g - v_f\right) + \hat{x}\left(\frac{dv_g}{dp} - \frac{dv_f}{dp}\right) \tag{I-26}$$

where

$$\frac{d\hat{x}}{dp} = \frac{\hat{x}\dfrac{dh_g}{dp} + \left(1 - \hat{x}\right)\dfrac{dh_f}{dp}}{\left(h_g - h_f\right)} \tag{I-27}$$

With

$$\frac{dh_f}{dp} = v_f\left(1 - \beta_f T\right) + c_{p,f}\frac{dT}{dp} \tag{I-28}$$

$$\frac{dh_g}{dp} = v_g\left(1 - \beta_g T\right) + c_{p,g}\frac{dT}{dp} \tag{I-29}$$

Eq. (I-28) & (I-29) can be derived as

283

$$dh = \left(\frac{\partial h}{\partial p}\right)_T dp + \left(\frac{\partial h}{\partial T}\right)_p dT$$

$$\Rightarrow \frac{dh}{dp} = \left(\frac{\partial h}{\partial p}\right)_T + \left(\frac{\partial h}{\partial T}\right)_p \frac{dT}{dp} \qquad \text{(I-30)}$$

$$= \left(\frac{\partial h}{\partial p}\right)_T + c_{p,f} \frac{dT}{dp}$$

While

$$dh = Tds + vdp \qquad \text{(I-31)}$$

One can have

$$\left(\frac{\partial h}{\partial p}\right)_T = T\left(\frac{\partial s}{\partial p}\right)_T + v\left(\frac{\partial p}{\partial p}\right)_T \qquad \text{(I-32)}$$

From Maxwell's relations, one can have

$$\left(\frac{\partial s}{\partial p}\right)_T = -\left(\frac{\partial v}{\partial T}\right)_p \qquad \text{(I-33)}$$

Therefore, one can have

$$\left(\frac{\partial h}{\partial p}\right)_T = -T\left(\frac{\partial v}{\partial T}\right)_p + v$$

$$= -T\left(\frac{\partial \rho}{\partial T}\right)_p \frac{dv}{d\rho} + v \qquad \text{(I-34)}$$

$$= v\left(1 - \beta T\right)$$

The derivatives of density at the phase boundaries can be expressed as

$$\frac{dv_f}{dp} = \beta_f v_f \frac{dT}{dp} - k_f v_f \qquad \text{(I-35)}$$

$$\frac{dv_g}{dp} = \beta_g v_g \frac{dT}{dp} - k_g v_g \qquad \text{(I-36)}$$

Eq. (I-35) & (I-36) can be derived as

$$dv = \left(\frac{\partial v}{\partial p}\right)_T dp + \left(\frac{\partial v}{\partial T}\right)_p dT$$

$$\Rightarrow \frac{dv}{dp} = \left(\frac{\partial v}{\partial T}\right)_p \frac{dT}{dp} + \left(\frac{\partial v}{\partial p}\right)_T \tag{I-37}$$

$$\Rightarrow \frac{dv}{dp} = \beta v \frac{dT}{dp} - kv$$

The derivative of temperature in Eq. (I-37) can be derived from Clausius-Clapeyron relation

$$\frac{dT}{dp} = T \frac{v_g - v_f}{h_g - h_f} \tag{I-38}$$

I.3 Further Partial Derivatives

<u>Temperature</u>

For the single-phase region

$$\left(\frac{\partial T}{\partial h}\right)_p = \frac{1}{c_p} \tag{I-39}$$

$$\left(\frac{\partial T}{\partial p}\right)_h = -\frac{\left(\frac{\partial h}{\partial p}\right)_T}{\left(\frac{\partial h}{\partial T}\right)_p} = \frac{-v + \beta T v}{c_p} \tag{I-40}$$

For the two-phase region

$$\left(\frac{\partial T}{\partial h}\right)_p = 0 \tag{I-41}$$

$$\left(\frac{\partial T}{\partial p}\right)_h = \frac{dT}{dp} \tag{I-42}$$

<u>Specific Entropy</u>

For the single-phase region

285

$$\left(\frac{\partial s}{\partial h}\right)_p = \frac{1}{T} \tag{I-43}$$

$$\left(\frac{\partial s}{\partial p}\right)_h = -\frac{v}{T} \tag{I-44}$$

Eq. (I-43) & (I-44) can be derived as follows.

$$dh = Tds + vdp$$

$$\Rightarrow ds = \frac{1}{T}dh - \frac{v}{T}dp \tag{I-45}$$

$$\Rightarrow \left(\frac{\partial s}{\partial h}\right)_p = \frac{1}{T} \ \& \ \left(\frac{\partial s}{\partial p}\right)_h = -\frac{v}{T}$$

For the two-phase region

$$\left(\frac{\partial s}{\partial h}\right)_p = \frac{s_g - s_f}{h_g - h_f} \tag{I-46}$$

$$\left(\frac{\partial s}{\partial p}\right)_h = \frac{ds_f}{dp} + \frac{d\hat{x}}{dp}\left(s_g - s_f\right) + \hat{x}\left(\frac{ds_g}{dp} - \frac{ds_f}{dp}\right) \tag{I-47}$$

where

$$\frac{ds_f}{dp} = \frac{c_{p,f}}{T}\frac{dT}{dp} - \beta_f v_f \tag{I-48}$$

$$\frac{ds_g}{dp} = \frac{c_{p,g}}{T}\frac{dT}{dp} - \beta_g v_g \tag{I-49}$$

Eq. (I-48) & (I-49) can be derived as

$$ds = \left(\frac{\partial s}{\partial T}\right)_p dT + \left(\frac{\partial s}{\partial p}\right)_T dp \tag{I-50}$$

Since

$$\left(\frac{\partial s}{\partial T}\right)_p = \frac{\left(\frac{\partial s}{\partial h}\right)_p}{\left(\frac{\partial T}{\partial h}\right)_p} = c_p \left(\frac{\partial s}{\partial h}\right)_p \qquad \text{(I-51)}$$

While

$$dh = Tds + vdp$$
$$\Rightarrow Tds = dh - vdp$$
$$\Rightarrow ds = \frac{1}{T}dh - \frac{v}{T}dp \qquad \text{(I-52)}$$
$$\Rightarrow \left(\frac{\partial s}{\partial h}\right)_p = \frac{1}{T}$$

Therefore, Eq. (I-51) becomes

$$\left(\frac{\partial s}{\partial T}\right)_p = \frac{\left(\frac{\partial s}{\partial h}\right)_p}{\left(\frac{\partial T}{\partial h}\right)_p} = \frac{c_p}{T} \qquad \text{(I-53)}$$

Applying one of the Maxwell's relations Eq. (I-33), Eq. (I-50) becomes

$$ds = \frac{c_p}{T}dT - \left(\frac{\partial v}{\partial T}\right)_p dp \qquad \text{(I-54)}$$

Therefore,

$$\frac{ds}{dp} = \frac{c_p}{T}\frac{dT}{dp} - \left(\frac{\partial v}{\partial T}\right)_p$$
$$= \frac{c_p}{T}\frac{dT}{dp} - \left(\frac{\partial \rho}{\partial T}\right)_p \frac{dv}{d\rho} \qquad \text{(I-55)}$$
$$= \frac{c_p}{T}\frac{dT}{dp} - \beta v$$

Appendix II - Moving Boundary Evaporator Model
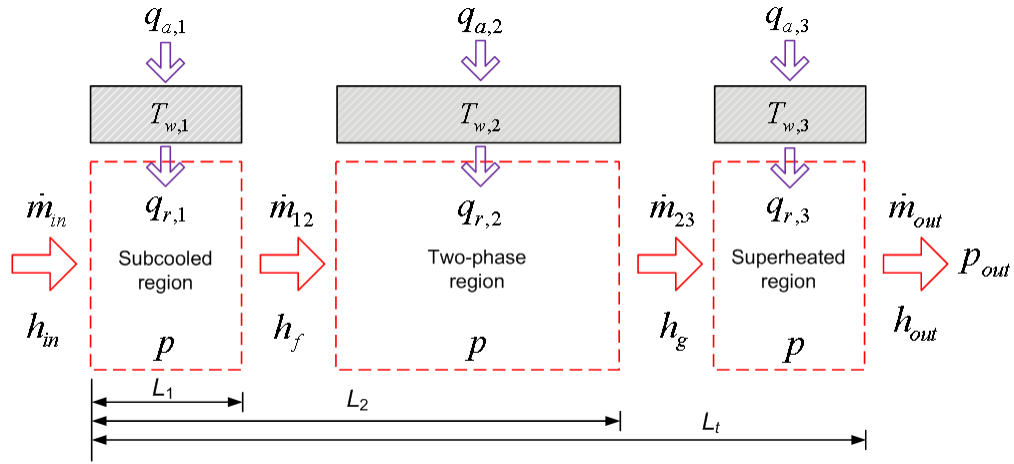
Figure II.1 Moving boundary evaporator model

The three-zone evaporator model is shown in Figure II.1. Subscript "1" denotes the subcooled region, "2" denotes the two-phase region and "3" denotes the superheated region.

q_a = heat transfer rate from the ambient to the tube wall;

T_w = average wall temperature;

q_r = heat transfer rate from the tube wall to the refrigerant flow;

L_1 = zone length of region 1;

L_2 = combined zone length of region 1 & 2;

L_t = overall length of the condenser;

p = refrigerant pressure in region 1, 2 & 3;

p_{out} = refrigerant pressure at the outlet of the heat exchanger;

$\dot{m}_{in}$ = refrigerant mass flow rate entering the heat exchanger;

$\dot{m}_{12}$ = refrigerant mass flow rate at the interface between region 1 and region 2 (a positive value denotes that the refrigerant flows from region 1 to region 2; a negative value denotes that the refrigerant flows from region 2 to region 1)

$\dot{m}_{23}$ = refrigerant mass flow rate at the interface between region 2 and region 3;

$\dot{m}_{out}$ = refrigerant mass flow rate leaving the heat exchanger;

h_{in} = enthalpy of the refrigerant entering the heat exchanger;

h_g = enthalpy of the refrigerant at the boundary between region 2 and 3;

h_f = enthalpy of the refrigerant at the boundary between region 1 and 2;

h_{out} = enthalpy of refrigerant leaving the heat exchanger.

This appendix only provides the governing equations for the refrigerant flow, the equations for the walls, the air side and the global momentum balance are the same as those in Chapter 6 and therefore not repeated for brevity.

II.1 L-TP-V Mode

II.1.1 L Region

II.1.1.1 Mass Balance

$$A\left[L_1\left(\left.\frac{\partial \bar{\rho}_1}{\partial p}\right|_h + \frac{1}{2}\left.\frac{\partial \bar{\rho}_1}{\partial \bar{h}_1}\right|_p \frac{dh_f}{dp}\right)\frac{dp}{dt} + \frac{1}{2}L_1\left.\frac{\partial \bar{\rho}_1}{\partial \bar{h}_1}\right|_p \frac{dh_{in}}{dt} + \left(\bar{\rho}_1 - \rho_f\right)\frac{dL_1}{dt}\right] = \dot{m}_{in} - \dot{m}_{12} \quad \text{(II-1)}$$

II.1.1.2 Energy Balance

$$AL_1\left[\frac{1}{2}\bar{\rho}_1\frac{dh_{in}}{dt} + \left(\frac{1}{2}\bar{\rho}_1\frac{dh_f}{dp} - 1\right)\frac{dp}{dt}\right] + A\rho_f\left(\bar{h}_1 - h_f\right)\frac{dL_1}{dt}$$
$$= \dot{m}_{in}\left(h_{in} - \bar{h}_1\right) - \dot{m}_{12}\left(h_f - \bar{h}_1\right) + q_{r,1} \quad \text{(II-2)}$$

II.1.2 TP Region

II.1.2.1 Mass Balance

$$A(L_2 - L_1)\left[(1-\bar{\gamma})\frac{d\rho_f}{dp} + \bar{\gamma}\frac{d\rho_g}{dp}\right]\frac{dp}{dt} - A(\rho_g - \rho_f)\bar{\gamma}\frac{dL_1}{dt}$$

$$+A(\rho_g - \rho_f)(\bar{\gamma}-1)\frac{dL_2}{dt} + A(\rho_g - \rho_f)(L_2 - L_1)\frac{d\bar{\gamma}}{dt} = \dot{m}_{12} - \dot{m}_{23} \tag{II-3}$$

II.1.2.2 Energy Balance

$$A(L_2 - L_1)\left[(1-\bar{\gamma})\frac{d(\rho_f h_f)}{dp} + \bar{\gamma}\frac{d(\rho_g h_g)}{dp} - 1\right]\frac{dp}{dt} - A(\rho_g h_g - \rho_f h_f)\bar{\gamma}\frac{dL_1}{dt}$$

$$+A(\rho_g h_g - \rho_f h_f)(\bar{\gamma}-1)\frac{dL_2}{dt} + A(L_2 - L_1)(\rho_g h_g - \rho_f h_f)\frac{d\bar{\gamma}}{dt} \tag{II-4}$$

$$= \dot{m}_{12}h_f - \dot{m}_{23}h_g + q_{r,2}$$

The time derivative of mean void fraction is calculated by Eq. (6-43)

II.1.3 V Region

II.1.3.1 Mass Balance

$$A(L_t - L_2)\left[\left(\left.\frac{\partial\bar{\rho}_3}{\partial p}\right|_h + \frac{1}{2}\left.\frac{\partial\bar{\rho}_3}{\partial\bar{h}_3}\right|_p\frac{dh_g}{dp}\right)\frac{dp}{dt} + \frac{1}{2}\left.\frac{\partial\bar{\rho}_3}{\partial\bar{h}_3}\right|_p\frac{dh_{out}}{dt}\right] - A(\bar{\rho}_3 - \rho_g)\frac{dL_2}{dt} \tag{II-5}$$

$$= \dot{m}_{23} - \dot{m}_{out}$$

II.1.3.2 Energy Balance

$$A(L_t - L_2)\left(\bar{\rho}_3\frac{d\bar{h}_3}{dt} - \frac{dp}{dt}\right) - A\rho_g\left(\bar{h}_3 - h_g\right)\frac{dL_2}{dt} \tag{II-6}$$

$$= \dot{m}_{23}\left(h_g - \bar{h}_3\right) - \dot{m}_{out}\left(h_{out} - \bar{h}_3\right) + q_{r,3}$$

II.2 L-TP Mode

Eq. (II-1) & (II-2) still apply for the liquid region. The governing equations for the two-phase region are

$$A(L_2 - L_1)\left[(1-\bar{\gamma})\frac{d\rho_f}{dp} + \bar{\gamma}\frac{d\rho_g}{dp}\right]\frac{dp}{dt} - A(\rho_g - \rho_f)\bar{\gamma}\frac{dL_1}{dt}$$

$$+A(\rho_g - \rho_f)(L_2 - L_1)\frac{d\bar{\gamma}}{dt} = \dot{m}_{12} - \dot{m}_{23} \tag{II-7}$$

$$A(L_2 - L_1)\left[(1-\bar{\gamma})\frac{d(\rho_f h_f)}{dp} + \bar{\gamma}\frac{d(\rho_g h_g)}{dp} - 1\right]\frac{dp}{dt} - A(\rho_g h_g - \rho_f h_f)\bar{\gamma}\frac{dL_1}{dt}$$

$$+A(L_2 - L_1)(\rho_g h_g - \rho_f h_f)\frac{d\bar{\gamma}}{dt} = \dot{m}_{12}h_f - \dot{m}_{23}h_{out} + q_{r,2} \tag{II-8}$$

Other constituent equations are the same as those in the V-TP mode of the condenser model (Section 6.3.2).

II.3 TP-V Mode

In TP-V mode, the liquid region is not present in the heat exchanger, but the vapor region is unaffected. Therefore, Eq. (II-5) & (II-6) still apply.

The equations for mass and energy balance for the two-phase region are

$$AL_2\left[(1-\bar{\gamma})\frac{d\rho_f}{dp} + \bar{\gamma}\frac{d\rho_g}{dp}\right]\frac{dp}{dt} + A(\rho_g - \rho_f)(\bar{\gamma} - 1)\frac{dL_2}{dt}$$

$$+A(\rho_g - \rho_f)L_2\frac{d\bar{\gamma}}{dt} = \dot{m}_{in} - \dot{m}_{23} \tag{II-9}$$

$$AL_2\left[(1-\bar{\gamma})\frac{d(\rho_f h_f)}{dp} + \bar{\gamma}\frac{d(\rho_g h_g)}{dp} - 1\right]\frac{dp}{dt} + A(\rho_g h_g - \rho_f h_f)(\bar{\gamma} - 1)\frac{dL_2}{dt}$$

$$+AL_2(\rho_g h_g - \rho_f h_f)\frac{d\bar{\gamma}}{dt} = \dot{m}_{in}h_{in} - \dot{m}_{23}h_g + q_{r,2} \tag{II-10}$$

Other constituent equations are the same as those in the TP-L mode of the condenser model (Section 6.3.3).

II.4 TP Mode (Linear Enthalpy Profile)

The equations for this mode are the same as those for the TP mode of the condenser model (Section 6.3.4).

II.5 TP Mode (Uniform Enthalpy Profile)

The equations for this model are the same as those for the TP mode (Linear Enthalpy Profile) except the calculation for the time derivative of mean void fraction.

$$\frac{d\bar{\gamma}}{dt} = \left(\frac{\partial \bar{\gamma}}{\partial c}\bigg|_{x_{tp,out}} \frac{dc}{dp} + \frac{\partial \bar{\gamma}}{\partial x_{tp,out}}\bigg|_{c} \frac{\partial x_{tp,out}}{\partial p}\bigg|_{h_{tp,out}} \right) \frac{dp}{dt} + \frac{\partial \bar{\gamma}}{\partial x_{tp,out}}\bigg|_{c} \frac{\partial x_{tp,out}}{\partial h_{tp,out}}\bigg|_{p} \frac{dh_{tp,out}}{dt} \tag{II-11}$$

where the partial derivatives of mean void fraction should be calculated based on the following equation

$$\bar{\gamma} = \frac{x_{tp,out}}{x_{tp,out} + \left(1 - x_{tp,out}\right)c} \tag{II-12}$$

where

$$c = \left(\frac{\rho_g}{\rho_l} \right)^{2/3} \tag{II-13}$$

II.6 V Mode & L Mode

The governing equations for the V mode of the evaporator model (the last zone is the vapor zone) are the same as those for the L mode of the condenser model (the last zone is the liquid zone), while the governing equations for the L mode of the evaporator model are the same as those for the V mode of the condenser model.

Appendix III - Model List of the Modeling Framework

This appendix lists the models developed in this Modelica-based modeling framework for the transient simulation of vapor compression systems:

o Air, brine and refrigerant flow network, including a variety of flow source and sink models, and the standards for the fluid ports (air flow port, refrigerant flow port and brine flow port)

o Map-based fixed-speed compressor model

o Map-based variable-speed compressor model

o Map-based vapor injection compressor model

o Generic orifice model

o Adiabatic capillary tube model

o Check valve model

o Reversing valve model

o TXV model

o EEV model

o Accumulator model

o Receiver model

o Flash tank model

o Discretized tube fin heat exchanger model

o Discretized microchannel heat exchanger model

o Discretized brine-to-refrigerant plate heat exchanger model

o Moving boundary heat exchanger models

o Refrigerant-to-refrigerant heat exchanger model

- Pipe model

- Frosting model

- Hot gas defrosting model

- Fan model

- Room model

References

[1]   AB Dassault Systemes. *Dymola.* 2014.

[2]   Agrawal, N., and S. Bhattacharyya. "Non-adiabatic capillary tube flow of carbon dioxide in a transcritical heat pump cycle." *Energy Conversion and Management* 48 (2007): 2491–2501.

[3]   Agrawal, N., and S. Bhattacharyya. "Optimized transcritical CO2 heat pumps: performance comparison of capillary tubes against expansion valves." *International Journal of Refrigeration* 31 (2008): 388-395.

[4]   Aljuwayhel, N.F. *Numerical and experimental study of the influence of frost formation and defrosting on the performance of industrial evaporator coils.* Ph.D. Thesis, University of Wisconsin-Madison, USA, 2006.

[5]   Al-Mutawa, N.K., and S.A. Sherif. "An analytical model for hot-gas defrosting of a cylindrical coil cooler: Part I – Model development." *ASHRAE Transaction* 104 (Part I) (1998a): 1722-1730.

[6]   Al-Mutawa, N.K., and S.A. Sherif. "An analytical model for hot-gas defrosting of a cylindrical coil cooler: Part II – Model results and conclusions." *ASHRAE Transaction* 104 (Part I) (1998b): 1731-1737.

[7]   Anand, N.K., J.S. Schliesing, D.L. O'Neal, and K.T. Peterson. "Effects of outdoor coil fan pre-start on pressure transients during the reverse cycle defrost of a heat pump." *ASHRAE Transaction* 95 (Part II) (1989): 699-704.

[8]   ANS/AHRI Standard 540. *Performance rating of positive displacement refrigerant compressors and compressor units.* Arlington, VA: Air-conditioning, Heating and Refrigeraiton Institute, 2004.

[9]   Aprea, C., and C. Renno. "A numerical approach to a very fast thermal transient in an air cooling evaporator." *Applied Thermal Engineering* 22 (2002): 219-228.

[10]   Aprea, C., and C. Renno. "An air cooled tube-fin evaporator model for an expansion valve control law." *Mathematical and Computer Modeling* 30 (1999): 135-146.

[11]   Aprea, C., and C. Renno. "Experimental analysis of a transfer function for an air cooled evaporator." *Applied Thermal Engineering* 21 (2001): 481-493.

[12]   ASHRAE. *ASHRAE Handbook: Refrigeration.* American Society of Heating, Refrigerating, and Air-Conditioning Engineers, 2002.

[13]   ASHRAE Standard 116. *Methods of testing for rating seasonal efficiency of unitary air conditioners and heat pumps.* Atlanta, GA, USA: ASHRAE, 2010.

[14]   ASHRAE Standard 37. *Methods of testing for rating electrically driven unitary air-conditioning and heat pump equipment.* Atlanta, GA, USA: ASHRAE, 2009.

[15]   Baek, C., E. Lee, H. Kang, and Kim Y. "Experimental study on the heating performance of a CO2 heat pump with gas injection." West Lafayette, IN, USA: 12th International Refrigeration and Air Conditioning Conference at Purdue, 2008.

[16]   Bansal, P.K., and A. S. Rupasinghe. "An homogeneous model for adiabatic capillary tubes." *Applied Thermal Engineering* 18, no. 3-4 (1998): 207—219.

[17]   Baroczy, C.J. "Correlation of liquid fraction in two-phase flow with applications to liquid metals." *Chemical Engineering Progress Symposium Series* 61 (1965): 179-191.

[18]   Bassiounay, R., and D. L. O'Neal. "Analysis of refrigerant flow and deformation for a flexible short-tube using a finite element model." *International Journal of Refrigeration* 27 (2004): 176-183.

[19]   Bauer, O. *Modeling of two-phase flows with Modelica.* Master Thesis, Department of Automatic Control, Lund Institute of Technology, Sweden, 1999.

[20]   Beck, B.T., and G.L. Wedekind. "A generalization of the system mean void fraction model for transient two-phase evaporating flows." *Journal of Heat Transfer* 103 (1981): 81-85.

[21]   Beghi, A., and L. Cecchinato. "A simulation environment of dry-expansion evaporators with application to the design of auto tuning control algorithms for electronic expansion valves." *International Journal of Refrigeration* 32, no. 7 (2009): 1765-1775.

[22]   Bendapudi, S. A., J. E. Braun, and E. A. Groll. "Dynamic model of a centrifugal chiller system - model development, numerical study, and validation." *ASHRAE Transactions* 111 (Part 1) (2005): 132-148.

[23]   Bendapudi, S.A. *Development and evaluation of modeling approaches for transients in centrifugal chillers.* Ph.D. Thesis, Purdue University, 2004.

[24]   Bendapudi, S.A., and J.E. Braun. "A review of literature on dynamic models of vapor compression equipment." ASHRAE Research Project 1043-RP, 2002.

[25]   Bendapudi, S.A., J. E. Braun, and E. A. Groll. "A comparison of moving-boundary and finite-volume formulation for transients in centrifugal chillers." *International Journal of Refrigeration* 31 (2008): 1437-1452.

[26]   Björk, E., and B. Palm. "Refrigerant mass charge distribution in a domestic refrigerator. Part I: transient conditions." *Applied Thermal Engineering* 26, no. 8-9 (2006a): 829-837.

[27]   Björk, E., and B. Palm. "Refrigerant mass charge distribution in a domestic refrigerator. Part II: steady state conditions." *Applied Thermal Engineering* 26, no. 8-9 (2006b): 866-871.

[28]   Bonilla, J., L.J. Yebra, and S. Dormido. "A heuristic method to minimize the chattering problem in dynamic mathematical two-phase flow models." *Mathematical and Computer Modeling* 54, no. 5-6 (2011): 1549-1560.

[29]   Bonilla, J., L.J. Yebra, and S. Dormido. "Chattering in dynamic mathematical two-phase flow models." *Applied Mathematical Modeling* 36, no. 5 (2012): 2067-2081.

[30]   Brasz, J.J., and K Koenig. "Numerical methods for the transient behavior of two-phase flow heat transfer in evaporators and condensers." Edited by T.M. Shih. *Numerical Properties and Methodologies in Heat Transfer* (Springer Verlag), 1983: 461-476.

[31]   Brian, P.L.T., R.C. Reid, and Y.T. Shah. "Frost deposition on cold surfaces." *Industrial & Engineering Chemistry Fundamentals* 9, no. 3 (1970): 375-380.

[32]   Broersen, P.M.T, and M.F.G. van der Jagt. "Hunting of evaporators controlled by a thermostatic expansion valve." *ASME Journal of Dynamic Systems Measurement & Control* 102, no. 2 (1980): 130-145.

[33]   Browne, M.W., and P.K. Bansal. "Transient simulation of vapor-compression packaged liquid chillers." *International Journal of Refrigeration* 25, no. 5 (2002): 597-610.

[34]   Butterworth, D. "A comparison of some void-fraction relationships for cocurrent gas-liquid flow." *International Journal of Multiphase Flow* 1, no. 6 (1975): 845-850.

[35]   Byun, J.S., C.D. Jeon, J.H. Jung, and J. Lee. "The application of photo-coupler for frost detecting in an air-source heat pump." *International Journal of Refrigeration* 29, no. 2 (2006): 191-198.

[36]   Byun, J.S., J. Lee, and C.D. Jeon. "Frost retardation of an air-source heat pump by the hot gas bypass method." *International Journal of Refrigeration* 31, no. 2 (2008): 328-334.

[37]   Carey, V.P. *Liquid-vapor phase change phenomena (2nd edition).* New York: Taylor & Francis Group, 2008.

[38]   Casella, F., and F. Schiavo. "Modelling and simulation of heat exchangers in Modelica with finite element methods." *3rd International Modelica Conference.* Linkoping, Sweden, 2003.

[39]   Casella, F., M. Otter, K. Proelss, C.C. Richter, and H. Tummescheit. "The Modelica fluid and media library for modeling of incompressible and compressible thermo-fluid pipe networks." *Modelica Conference.* Vienna, Austria, 2006.

[40]   Cecchinato, L., and F. Mancini. "An intrinsically mass conservative switched evaporator model adopting the moving-boundary method." *International Journal of Refrigeration* 35 (2012): 349-364.

[41]   Chamoun, M., R. Rulliere, P. Haberschill, and J.F. Berail. "Dynamic model of an industrial heat pump using water as refrigerant." *International Journal of Refrigeration* 35, no. 4 (2012): 1080-1091.

[42]   Cheikh, A.E., and A. Jacobi. "A mathematical model for frost growth and densification on flat surfaces." *International Journal of Heat and Mass Transfer* 77 (2014): 604-611.

[43]   Chen, H., L. Thomas, and R.W. Besant. "Fan supplied heat exchanger fin performance under frosting conditions." *International Journal of Refrigeration* 26 (2003): 140-149.

[44]   Chen, W., X. Zhou, and S. Deng. "Development of control method and dynamic model for multi-evaporator air conditions (MEAC)." *Energy Conversion and Management* 46 (2005): 451-465.

[45]   Chen, Y., and J. Gu. "Non-adiabatic capillary tube flow of carbon dioxide in a novel refrigeration cycle." *Applied thermal Engineering* 25 (2005): 1670-1683.

[46]   Chen, Y., Braun J., and E. Groll. "Modeling of hermetic scroll compressors: Model development." *HVAC&R RESEARCH* 10, no. 2 (2004): 129-152.

[47]   Chen, Y., N. Halm, E. Groll, and J. Braun. "Mathematical modeling of scroll compressors: Part I – Compression process modeling." *International Journal of Refrigeration* 25, no. 6 (2002): 731-750.

[48]   Chen, Y.G., and X.M. Guo. "Dynamic defrosting characteristics of air source heat pump and effects of outdoor air parameters on defrost cycle performance." *Applied Thermal Engineering* 29 (2009): 2701-2707.

[49]   Chen, Z.J., and W.H. Lin. "Dynamic simulation and optimal matching of a small-scale refrigeration system." *International Journal of Refrigeration* 14 (1991): 329-335.

[50]   Cheng, C., and Y. Cheng. "Predictions of frost growth on a cold plate in atmospheric air." *International Communications in Heat and Mass Transfer* 28, no. 7 (2001): 953-962.

[51]   Chi, J., and D. Didion. "A Simulation Model of the Transient Performance of a Heat Pump." *International Journal of Refrigeration* 53 (1982): 176-184.

[52]   Chiou, C.B., C.H. Chiou, C.M. Chu, and S.L. Lin. "The application of fuzzy control on energy saving for multi-unit room air-conditioners." *Applied Thermal Engineering* 29 (2009): 310-316.

[53]   Cho, H., C. Baek, C. Park, and Y. Kim. "Performance evaluation of a two-stage CO2 cycle with gas injection in the cooling mode operation." *International Journal of Refrigeration* 32 (2009): 40-46.

[54]   Cho, J., Kim Y., and H. Kim. "A generalized correlation for refrigerant mass flow rate through adiabatic capillary tubes." *International Journal of Refrigeration* 26 (2003): 881-888.

[55]   Choi, H.J., B.S. Kim, D. Kang, and K.C. Kim. "Defrosting method adopting dual hot gas bypass for an air-to-air heat pump." *Applied Energy* 88 (2011a): 4544-4555.

[56]   Choi, J.M., and Y.C. Kim. "Capacity modulation of an inverter-driven multi-air conditioner using electronic expansion valves." *Energy* 28 (2003): 141-155.

[57]   Choi, J.W., G. Lee, and M.S. Kim. "Numerical study on the steady state and transient performance of a multi-type heat pump system." *International Journal of Refrigeration* 34, no. 2 (2011b): 429-443.

[58]   Churchill, S.W., and H.H.S. Chu. "Correlating equations for laminar and turbulent free convection from a vertical plate." *International Journal of Heat and Mass Transfer* 18, no. 11 (1975): 1323-1329.

[59]   Cole, R.A. "Refrigeration loads in a freezer due to hot gas defrost and their associated costs." *ASHRAE Transaction* 95 (Part II) (1989): 1149-1154.

[60]   Colorado, D., J.A. Hernández, O. García-Valladares, A. Huicochea, and J. Siqueiros. "Numerical simulation and experimental validation of a helical double-pipe vertical condenser." *Applied Energy* 88, no. 6 (2011): 2136-2145.

[61]   Cooper, M.G. "Saturation nucleate pool boiling: a simple correlation." *1st U.K. National Conference on Heat Transfer* 2 (1984): 785-793.

[62]   Cui, J., W.Z. Li, Y. Liu, and Y.S. Zhao. "A new model for predicting performance of fin-and-tube heat exchanger under frost condition." *International Journal of Heat and Fluid Flow* 32, no. 1 (2011): 249-260.

[63]   Dhar, M.T. *Transient analysis of refrigeration system.* West Lafayette, IN: Ph.D. Thesis, Department of Mechanical Engineering, Purdue University, 1978.

[64]   Diaz, G. "Controllability of cross-flow two-phase heat exchangers." *International Journal of Heat and Mass Transfer* 50 (2007): 4559-4567.

[65]   Ding, G.L. "Recent developments in simulation techniques for vapor-compression refrigeration systems." *International Journal of Refrigeration* 30, no. 7 (2007): 1119-1133.

[66]   Ding, G.L., C.L. Zhang, and Z.L. Lu. "Dynamic simulation of natural convection bypass two-circuit cycle refrigerator-freezer and its application. Part I: Component models." *Applied Thermal Engineering* 24, no. 10 (2004a): 1513-1524.

[67]   Ding, Y., G. Ma, Q. Chai, and Y. Jiang. "Experimental investigation of reverse cycle defrosting methods on air source heat pump with TXV as the throttle regulator." *International Journal of Refrigeration* 27 (2004b): 671-678.

[68]   Dittus, F.W., and L.M.K. Boelter. "Heat transfer in automobile radiators of the tubular type." *International Communications in Heat and Mass Transfer* 12, no. 1 (1985): 3-22.

[69]   Dopazo, J.A., J. Fernandez-Seara, F.J. Uhía, and R. Diz. "Modelling and experimental validation of the hot-gas defrost process of an air-cooled evaporator." *International Journal of Refrigeration* 33 (2010): 829-839.

[70]   Eborn, J. *On Modelica library for thermo-hydraulic applications.* Lund, Sweden: Ph.D. Thesis, Department of Automatic Control, Lund Institute of Technology, 2001.

[71]   Eckert, E.R.G., and R.M.JR. Drake. *Analysis of heat and mass transfer.* New York: McGraw-Hill, 1987.

[72]   Eldredge, B.D., B.P. Rasmussen, and A.G. Alleyne. "Moving-boundary heat exchanger models with variable outlet phase." *Journal of Dynamic Systems, Measurement, and Control* 130, no. 6 (2008): 061003 (12 pages).

[73]   Elliot, M.S., and B.P. Rasmussen. "Decentralized model predictive control of a multiple evaporator air conditioning system." *Control Engineering Practice* 21 (2013): 1665-1677.

[74]   Elmahdy, A.H., and R.C. Biggs. "Efficiency of extended surfaces with simultaneous heat and mass transfer." *ASHRAE Transactions* 89 (Part I) (1983): 135-143.

[75]   Elmqvist, H., H. Tummescheit, and M. Otter. "Object-Oriented modeling of thermo-fluid systems." *3rd International Modelica Conference.* Linkoping, Sweden, 2003. 269-286.

[76]   Fu, L., G.L. Ding, and C.L. Zhang. "Dynamic simulation of air-to-water dual-mode heat pump with screw compressor." *Applied Thermal Engineering* 23, no. 13 (2003): 1629-1645.

[77]   Fukata, S., and K. Inoue. "Internal mass flux through frost." *AIChE Journal* 45, no. 2 (1999): 2646-2652.

[78]   Gao, T., and J. Gong. "Modeling the airside dynamic behavior of a heat exchanger under frosting conditions." *Journal of Mechanical Science and Technology* 25, no. 10 (2011): 2719-2728.

[79]   García-Valladares, O. "Numerical simulation of triple concentric-tube heat exchangers." *International Journal of Thermal Sciences* 43, no. 10 (2004): 979-991.

[80]   García-Valladares, O., C.D. Perez-Segarra, and A. Oliva. "Numerical simulation of capillary tube expansion devices behavior with pure and mixed refrigerants considering metastable region. Part I: Mathematical formulation and numerical model." *Applied Thermal Engineering* 22 (2002): 173-182.

[81]   García-Valladares, O., C.D. Pérez-Segarra, and J. Rigola. "Numerical simulation of double-pipe condensers and evaporators." *International Journal of Refrigeration* 27, no. 6 (2004): 656-670.

[82]   Getu, H.M., and P.K. Bansal. "New frost property correlations for a flat-finned-tube heat exchanger." *International Journal of Thermal Sciences* 50 (2011): 544-557.

[83]   Gnielinski, V. "New equations for heat and mass transfer in turbulent pipe and channel flow." *International Journal of Chemical Engineering* 16, no. 2 (1976): 359-368.

[84]   Gong, J., T. Gao, X. Yuan, and D. Huang. "Effects of air flow maldistribution on refrigeration system dynamics of an air source heat pump chiller under frosting conditions." *Energy Conversion and Management* 49 (2008): 1645-1651.

[85]   Gordon, B.W., S. Liu, and H.H. Asada. "Dynamic modeling of multiple-zone vapor compression cycle using variable order representations." *Proceedings of the American Control Conference.* San Diego, CA, 1999.

[86]   Grald, E.W., and J.W. MacArthur. "A moving-boundary formulation for modeling time-dependent two-phase flows." *International Journal of Heat and Fluid Flow* 13 (1992): 266-272.

[87]   Grönnerud, R. "Investigation of liquid hold-up, flow-resistance and heat transfer in circulation type evaporators, part IV: two-phase flow resistance in boiling refrigerants." Paris: Annexe 1972-1, Bull. de l'Inst. du Froid, International Inst. of Refrigeration, 1979.

[88]   Gruhle, W.D., and R. Isermann. "Modeling and control of a refrigerant evaporator." *Journal of Dynamic Systems, Measurement, and Control* 107 (1985): 235-240.

[89]   Gungor, K.E., and R.H.S. Winterton. "Simplified general correlation for saturated flow boiling and comparisons of correlations with data." *Chemical Engineering Research and Design* 65 (1987): 148-156.

[90]   Guo, X.M., Y.G. Chen, W.H. Wang, and C.Z. Chen. "Experimental study on frost growth and dynamic performance of air source heat pump system." *Applied Thermal Engineering* 28, no. 17-18 (2008): 2267-2278.

[91]   Haberschill, P., L. Gay, P. Auboin, and M. Lallemand. "Dynamic model of a vapour compression refrigerating machine using R-407C." *HVAC&R Research* 9, no. 4 (2003): 451-466.

[92]   Hayashi, Y., A. Aoki, S. Adachi, and K. Hori. "Study of frost properties correlating with frost formation types." *Journal of Heat Transfer* 99 (1977): 239-245.

[93]   He, X. *Dynamic modeling and multivariable control of vapor compression cycles in air-conditioning systems.* Cambridge, MA: Ph.D. Thesis, Deptartment of Mechanical Engineering, MIT, 1996.

[94]   He, X., S. Liu, and H. Asada. "A moving-interface model of two-phase flow heat exchanger dynamics for control of vapor compression cycle." *Heat Pump and Refrigeration System Design, Analysis, and Applications (ASME AES 32)*, 1994: 69-75.

[95]   He, X., S. Liu, and H.H. Asada. "Modeling of vapor compression cycles for multivariable feedback control of HVAC systems." *Journal of Dynamic Systems, Measurement and Control* 119, no. 2 (1997): 183-191.

[96]   He, X., S. Liu, H.H. Asada, and H. Itoh. "Multivariable control of vapor compression systems." *HVAC&R Research* 4, no. 3 (1998): 205-230.

[97]   Hermes, C.J. L., R.O. Piucco, J.R. Barbosa Jr., and C. Melo. "A study of frost growth and densification on flat surfaces." *Experimental Thermal and Fluid Science* 33, no. 2 (2009): 371-379.

[98]   Hermes, C.J.L. "An analytical solution to the problem of frost growth and densification on flat surfaces." *International Journal of Heat and Mass Transfer* 55 (2012): 7346-7351.

[99]   Hermes, C.J.L., and C. Melo. "A first-principles simulation model for the start-up and cycling transients of household refrigerators." *International Journal of Refrigeration* 31 (2008): 1341-1357.

[100]   Hermes, C.J.L., C. Melo, and J.M. Goncalves. "Modeling of non-adiabatic capillary tube flows: A simplified approach and comprehensive experimental validation." *International Journal of Refrigeration* 31, no. 8 (2008): 1358-1367.

[101]   Hewitt, N., and M.J. Huang. "Defrost cycle performance for a circular shape evaporator air source heat pump." *International Journal of Refrigeration* 31 (2008): 444-452.

[102]   Hoffenbecker, N., S.A. Klein, and D.T. Reindl. "Hot gas defrost model development and validation." *International Journal of Refrigeration* 28 (2005): 605-615.

[103]   Hong, K.T., and R.L. Webb. "Calculation of fin efficiency for wet and dry fins." *HVAC&R Research* 2, no. 1 (1996): 27-41.

[104]   Hu, W., Y. Jiang, M. Qu, L. Ni, Y. Yao, and S. Deng. "An experimental study on the operating performance of a novel reverse-cycle hot gas defrosting method for air source heat pumps." *Applied Thermal Engineering* 31 (2011): 363-369.

[105]   Huang, D., Q. Li, and X. Yuan. "Comparison between hot-gas bypass defrosting and reverse-cycle defrosting methods on an air-to-water heat pump." *Applied Energy* 86, no. 9 (2009): 1697–1703.

[106]   Huang, D., X. Yuan, and X. Zhang. "Effects of fan-starting methods on the reverse-cycle defrost performance of an air to water heat pump." *International Journal of Refrigeration* 27, no. 8 (2004): 869-875.

[107]   Huang, D., Z.L. He, and X.L. Yan. "Dynamic characteristics of an air-to-water heat pump under frosting/defrosting conditions." *Applied Thermal Engineering* 27, no. 11-12 (2007): 1996-2002.

[108]   Hwang, J., and K. Cho. "Numerical prediction of frost properties and performance of fin-tube heat exchanger with plain fin under frosting."

International Journal of Refrigeration, doi: 10.1016/j.ijrefrig.2014.04.026, 2014.

[109]   Ibrahim, G.A. "Effect of sudden changes in evaporator external parameters on a refrigeration system with an evaporator controlled by a thermostatic expansion valve." *International Journal of Refrigeration* 24, no. 6 (2001): 566-576.

[110]   Incropera, F.P., and D.P. DeWitt. *Introduction to Heat Transfer.* 3rd Edition. New York: John Wiley & Sons, 1996.

[111]   Iragorry, J., Y.X. Tao, and S. Jia. "A critical review of properties and models for frost formation analysis." *HVAC&R Research* 10, no. 4 (2004): 393-420.

[112]   Ismail, K.A.R., and C.S. Salinas. "Modeling of frost formation over parallel cold plates." *International Journal of Refrigeration* 22 (1999): 425-441.

[113]   Jabardo, J., W. Mamani, and M. Lanella. "Modeling and experimental vvaluation of an automotive air conditioning system with a variable capacity compressor." *International Journal of Refrigeration* 25 (2002): 1157-1172.

[114]   Jakobsen, A., J. Antonius, and H.J. Hagaard-Knudsen. "Experimental evaluation of the use of homogeneous and slip flow two-phase dynamic models in evaporator modeling." Sydney: Proceedings of the 20th International Congress of Refrigeration (Page No. 135), 1999.

[115]   Janssen, M.J.P., J.A de Wit, and L.J.M. Kuijpers. "Cycling losses in domestic appliances: an experimental and theoretical analysis." *International Journal of Refrigeration* 15, no. 3 (1992): 152-158.

[116]   Janssen, M.J.P., L.J.M. Kuijipers, and J.A. de Wit. "Theoretical and experimental investigation of a dynamic model for small refrigeration systems." Wet Lafayette, IN: Proc IIR Meeting at Purdue, 1988.

[117]   Jensen, J.M. *Dynamic modeling of thermo-fluid systems with focus on evaporators for refrigeration.* Ph.D. Thesis, Technical University of Denmark, Department of Mechanical Engineering, 2003.

[118]   Jensen, J.M., and H. Tummescheit. "Moving boundary models for dynamic simulations of two-phase flows." Oberpfaffenhofen, Germany: 2nd International Modelica Conference, 2002. 235-244.

[119]   Jia, X., C.P. Tso, P.G Jolly, and Y.W. Wong. "Distributed steady and dynamic modeling of dry-expansion evaporators." *International Journal of Refrigeration* 22 (1999): 126-136.

[120]   Jia, X., C.P. Tso, P.G. Jolly, and Y.W. Wong. "Distributed study of air temperature inside a dry-expansion evaporator." *Applied Thermal Engineering* 16, no. 4 (1996): 305-311.

[121]   Jia, X., C.P. Tso, P.K. Chia, and P. Jolly. "A distributed model for prediction of the transient response of an evaporator." *International Journal of Refrigeration* 18, no. 5 (1995): 336–342.

[122]   Jiang, H., and R. Radermacher. "A distributed model of a space heat pump under transient conditions." *International Journal of Energy Research* 27 (2003): 145-160.

[123]   Jiang, H., V. Aute, and R. Radermacher. "CoilDesigner: a general-purpose simulation and design tool for air to refrigerant heat exchangers." *International Journal of Refrigeration* 29 (2006): 601-610.

[124]   Jones, B.W., and J.D. Parker. "Frost formation with varying environmental parameters." *Journal of Heat Transfer* 97 (1975): 255-259.

[125]   Judge, J., and R. Radermacher. "A heat exchanger model for mixtures and pure refrigerant cycle simulations." *International Journal of Refrigeration* 20, no. 4 (1997): 244-255.

[126]   Kærn, M.R, W. Brix, B. Elmegaard, and L.F.S. Larsen. "Performance of residential air-conditioning systems with flow maldistribution in fin-and-tube evaporators." *International Journal of Refrigeration* 34, no. 3 (2011a): 696-706.

[127]   Kærn, M.R., B. Elmegaard, and L.F.S. Larsen. "Experimental comparison of the dynamic evaporator response using homogeneous and slip flow modeling." Dresden, Germany: Proceedings 8th Modelica Conference, 2011b.

[128]   Kærn, R.M. *Analysis of flow maldistribution in fin-and-tube evaporators for residential air-conditioning systems.* Ph.D. Thesis, Technical University of Denmark, Department of Mechanical Engineering, 2011.

[129]   Kandlikar, S.G. "A general correlation for saturated two-phase flow boiling heat transfer inside horizontal and vertical tubes." *ASME Journal of Heat Transfer* 112 (1990): 219-228.

[130]   Kandlikar, S.G., S. Garimell, D. Li, S. Colin, and M.R. King. *Heat transfer and fluid flow in minichannels and microchannels.* 1st Edition. Elsevier, 2006.

[131]   Kandula, M. "Frost growth and densification in laminar flow over flat surfaces." *International Journal of Heat and Mass Transfer* 54, no. 15-16 (2011): 3719-3731.

[132]   Kapadia, R.G., S. Jain, and R.S. Agarwal. "Transient characteristics of split air-conditioning systems using R-22 and R-410A as refrigerants." *HVAC&R Research* 15, no. 3 (2009): 617-649.

[133]   Kays, W.M., and A.L. London. *Compact heat exchangers .* 3rd Edition. New York: Mcgraw-Hill, 1984.

[134]   Kim, J.S., K.S. Lee, and S.J. Yook. "Frost behavior on a fin considering the heat conduction of heat exchanger fins." *International Journal of Heat and Mass Transfer* 52, no. 11-12 (2009): 2581-2588.

[135]   Kim, Y., and D. L. O'Neal. "A comparison of critical flow models for estimating two-phase flow HCFC22 and HFC134a through short-tube orifices." *International Journal of Refrigeration* 18 (1995): 447-455.

[136] Kim, Y., and D. L. O'Neal. "Two-phase flow of R-22 through short-tube orifices." *ASHRAE Transactions* 100 (Part I) (1994): 323-334.

[137] Kim, Y., D. L. O'Neal, and X. Yuan. "Two-phase flow of HFC-R134a and CFC-12 through short-tube orifices." *ASHRAE Transactions*, 1994: 582-591.

[138] Kondepudi, S.N., and D.L. O'Neal. "Performance of finned-tube heat exchangers under frosting conditions: I. Simulation model." *International Journal of Refrigeration* 16, no. 3 (1993): 175-180.

[139] Koury, R.N.N., L. Machado, and K.A.R. Ismail. "Numerical simulation of a variable speed refrigeration system." *International Journal of Refrigeration* 24, no. 2 (2001): 192-200.

[140] Koury, R.N.N., R.N. Faria, R.O. Nunes, K.A.R. Ismail, and L. Machado. "Dynamic model and experimental study of an air-water heat pump for residential use." *International Journal of Refrigeration* 36, no. 3 (2013): 674-688.

[141] Krakow, K.I., L. Van, and S. Lin. "A model of hot gas defrosting of evaporators – Part 1: Heat and mass transfer theory." *ASHRAE Transaction* 98 (Part I) (1992a): 451-461.

[142] Krakow, K.I., L. Van, and S. Lin. "A model of hot gas defrosting of evaporators – Part 2: Experimental analysis." *ASHRAE Transaction* 98 (Part I) (1992b): 462-474.

[143] Krakow, K.I., S. Lin, and L. Yan. "An idealized model of reversed-cycle hot gas defrosting – Part 1: Theory." *ASHRAE Transaction* 99 (Part II) (1993a): 317-327.

[144] Krakow, K.I., S. Lin, and L. Yan. "An idealized model of reversed-cycle hot gas defrosting – Part 2: Experimental analysis and validation." *ASHRAE Transaction* 99 (Part II) (1993b): 329-337.

[145] Kuehn, T.H., J.W. Ramsey, and J.L. Threlkeld. *Thermal Environmental Engineering.* 3rd Edition. Prentice Hall, 1998.

[146] Kumar, M., I. Kar, and A. Ray. "State space based modeling and performance evaluation of an air conditioning system." *HVAC&R Research* 14, no. 5 (2008): 797-816.

[147] Lawrence, J.M.W., and J.A. Evans. "Refrigerant flow instability as a means to predict the need for defrosting the evaporator in a retail display freezer cabinet." *International Journal of Refrigeration* 31 (2008): 107-112.

[148] Le Gall, R., J.M. Grillot, and C. Jallut. "Modelling of frost growth and densification." *International Journal of Heat and Mass Transfer* 40, no. 13 (1997): 3177-3187.

[149] Leducq, D., J. Guilpart, and G. Trystram. "Low order dynamic model of a vapor compression cycle for process control design." *Journal of Food Process Engineering* 26, no. 1 (2003): 67-91.

[150]   Lee, J., and J.S. Byun. "Experiment on the performance improvement of air-to-air heat pump adopting the hot gas bypass method by outdoor fan speed variation." *Journal of Mechanical Science and Technology* 23 (2009): 3407-3415.

[151]   Lee, K.S., S. Jhee, and D.K. Yang. "Prediction of the frost formation on a cold flat surface." *International Journal of Heat and Mass Transfer* 46, no. 20 (2003): 3789-3796.

[152]   Lee, K.S., W.S. Kim, and T.H. Lee. "A one-dimensional model for frost formation on a cold flat surface." *International Journal of Heat and Mass Transfer* 40, no. 18 (1997): 4359-4365.

[153]   Lee, Y.B., and S.T. Ro. "Analysis of the frost growth on a flat plate by simple models of saturation and supersaturation." *Experimental Thermal and Fluid Science* 29 (2005): 685-696.

[154]   Lei, Z., and M. Zaheeruddin. "Dynamic simulation and analysis of a water chiller refrigeration system." *Applied Thermal Engineering* 25 (2005): 2258-2271.

[155]   Lemke, N. C. "Untersuchung zweistufiger Flüssigkeitskühler mit dem Kältemittel CO2." Forschungsberichte des Deutschen Kälte- und Klimatechnischen Vereins Nr. 73, DKV, Stuttgart, 42-43, 2005.

[156]   Lemmon, E.W., M.L. Huber, and M.O. McLinden. *NIST reference fluid thermodynamic and transport properties - REFPROP version 9.0.* National Institute of Standard and Technology, 2010.

[157]   Lenic, K., A. Trp, and B. Frankovic. "Prediction of an effective cooling output of the fin-and-tube heat exchanger under frosting conditions." *Applied Thermal Engineering* 29 (2009a): 2534-2543.

[158]   Lenic, K., A. Trp, and B. Frankovic. "Transient two-dimensional model of frost formation on a fin-and-tube heat exchanger." *International Journal of Heat Mass Transfer* 52 (2009b): 22-32.

[159]   Levy, S. *Two-phase flow in complex systems.* New York: John Wiley & Sons, 1999.

[160]   Li, B., and A. Alleyne. "A dynamic model of a vapor compression cycle with shut-down and start-up operations." *International Journal of Refrigeration* (33) 33 (2010): 538-552.

[161]   Li, B., et al. "Dynamic modeling of refrigerated transport systems with cooling/heating mode switch operations." *HVAC&R Research* 18, no. 5 (2012a): 974-996.

[162]   Li, B., R. Otten, V. Chandan, W.F. Mohs, J. Berge, and A. Alleyne. "Optimal on–off control of refrigerated transport systems." *Control Engineering Practice* 18, no. 12 (2010a): 1406-1417.

[163]   Li, B., S. Peuker, Hrnjak P., and A. Alleyne. "Evaluation of transient refrigerant migration modeling approach on automotive air conditioning

systems." *SAE International Journal of Materials and Manufacturing* 4 (2011a): 864-874.

[164]   Li, B., S. Peuker, Hrnjak P., and A. Alleyne. "Refrigerant Mass Migration Modeling and Simulation for Air Conditioning Systems." *Applied Thermal Engineering* 31, no. 10 (2011b): 1770-1779.

[165]   Li, H., J. Braun, and B. Shen. "Modeling adjustable throat-area expansion valves." West Lafayette, IN, USA: International Refrigeration and Air Conditioning Conference at Purdue, Paper No. 2130, 2004.

[166]   Li, P., J.E. Seem, and Y. Li. "Experimental validation for dp/dt assumption of heat exchangers in vapor compression refrigeration cycles." *ASME Journal of Heat Transfer* 134, no. 11 (2012b): 114502 (6 pages).

[167]   Li, P., Y. Li, and J. E. Seem. "Consistent initialization of system of differential-algebraic equations for dynamic simulation of centrifugal chillers." *Journal of Building Performance Simulation* 5, no. 2 (2012c): 115-139.

[168]   Li, P., Y. Li, and J. E. Seem. "Modelica-based dynamic modeling of a chilled-water cooling coil." *HVAC&R Research* 16, no. 1 (2010b): 35-58.

[169]   Liang, C.H., X.S. Zhang, X.W. Li, and Z.Q. Chen. "Control strategy and experimental study on a novel defrosting method for air-source heat pump." *Applied Thermal Engineering* 30, no. 8-9 (2010a): 892–899.

[170]   Liang, N., S. Shao, C. Tian, and Y. Yan. "Dynamic simulation of variable capacity refrigeration systems under abnormal conditions." *Applied Thermal Engineering* 30, no. 10 (2010b): 1205-1214.

[171]   Liao, N.S., and C.C. Wang. "Transient response characteristics of two-phase condensing flows." *International Journal of Multiphase Flow* 16, no. 1 (1990): 139-151.

[172]   Ling, J., A. Alabdulkarem, H. Qiao, V. Aute, and R. Radermacher. "Modelica-based heat pump model for transient and steady-state simulation using low-GWP refrigerants." West Lafayette, IN: 15th International Refrigeration and Air-conditioning Conference at Purdue, 2014a.

[173]   Ling, J., M. Eisele, H. Qiao, and V. Aute. "Transient modeling and validation of an automotive secondary loop air-conditioning system." SAE Technical Paper 2014-01-0647, 2014b.

[174]   Liu, Z., G. Tang, and F. Zhao. "Dynamic simulation of air-source heat pump during hot-gas defrost." *Applied Thermal Engineering* 23, no. 6 (2003): 675-685.

[175]   Liu, Z., X. Li, H. Wang, and W. Peng. "Performance comparison of air source heat pump with R407C and R22 under frosting and defrosting." *Energy Conversion and Management* 49, no. 2 (2008): 232-239.

[176]   Ljubijankic, M., C. Nytsch-Geusen, and S. Unger. "Modelling of complex thermal energy supply systems based on the Modelica-Library FluidFlow." Como, Italy: Proceedings of the 7th Modelica Conference, 2009.

[177]   Llopis, R., R. Cabello, and E. Torrella. "A dynamic model of a shell-and-tube condenser operating in a vapor compression refrigeration plant." *International Journal of Thermal Sciences* 47 (2008): 926-934.

[178]   Lockhart, R.W., and R.C. Martinelli. "Proposed correlation of data for isothermal two-phase, two-component flow in pipes." *Chemical Engineering Progress* 45, no. 1 (1949): 39-48.

[179]   Lu, Z.L., G.L. Ding, and C.L. Zhang. "Dynamic simulation of natural convection bypass two-circuit cycle refrigerator-freezer and its application Part II: system simulation and application." *Applied Thermal Engineering* 24 (2004): 1525-1533 .

[180]   Ma, G.Y., and H.X. Zhao. "Experimental study of a heat pump system with flash tank coupled with scroll compressors." *Energy and Buildings* 50 (2008): 697-701.

[181]   MacArthur, J. W. "Analytical representation of the transient energy interactions in vapor compression heat pumps." *ASHRAE Transactions* 91 (Part 1B) (1984a): 982-996.

[182]   MacArthur, J. W., and E. W. Grald. "Prediction of cyclic heat pump performance with a fully distributed model and a comparison with experimental data." *ASHRAE Transactions* 93 (Part 2) (1987): 1159-1178.

[183]   MacArthur, J. W., and E. W. Grald. "Unsteady two-phase compressible flow model for predicting cyclic heat pump performance and a comparison with experimental data." *International Journal of Refrigeration* 12 (1989): 29-41.

[184]   MacArthur, J.W. "Transient heat pump behavior: a theoretical investigation." *International Journal of Refrigeration* 7, no. 2 (1984b): 123-132.

[185]   Machielsen, C.H.M., and H.G. Kerschbaumer. "Influence of frost formation and defrosting on the performance of air coolers: standards and dimensionless coefficients for the system designer." *International Journal of Refrigeration* 12, no. 3 (1989): 283-290.

[186]   Madsen, K., C. Poulsen, and Wiesenfarth M. "Study of capillary tubes in a transcritical CO2 refrigeration system." *International Journal of Refrigeration* 28 (2005): 1212-1218.

[187]   Mao, Y, Besant, R.W., and H. Chen. "Frost characteristics and heat transfer on a flat plate under freezer operating conditions - Part I: Experimental and correlations." *ASHRAE Transactions* 105 (Part II) (1999): 231-251.

[188]   Mao, Y., R.W. Besant, and K.S. Rezkallah. "Measurement and correlations of frost properties with airflow over a flat plate." *ASHRAE Transactions* 98 (Part II) (1992): 65-77.

[189]   Martínez-Frías, J., and S.M. Aceves. "Effects of evaporator frosting on the performance of an air-to-air heat pump." *Journal of Energy Resources Technology* 121 (1999): 60-65.

[190]   Mathison, M., J. Braun, and E. Groll. "Modeling of a two-stage rotary compressor." *HVAC&R RESEARCH* 14, no. 5 (2008): 719-748.

[191]   MathWorks. *Simscape 3.12.* 2014a. http://www.mathworks.com/products/simscape/.

[192]   MathWorks. *Simulink 8.4.* 2014b. http://www.mathworks.com/products/simulink/.

[193]   McKinley, T., and A. Alleyne. "An advanced nonlinear switched heat exchanged model for vapor compression cycles using the moving boundary method." *International Journal of Refrigeration* 31, no. 7 (2008): 1253-1264.

[194]   Merrill, P. "Heat pumps on-off capacity control and defrost performance tests using demand and time-temperature defrost controls." *ASHRAE Transaction* 95 (Part II) (1981): 689-698.

[195]   Miller, W.A. "Laboratory examination and seasonal analysis of frosting and defrosting for an air-to-air heat pump." *ASHRAE Transaction* 93 (Part I) (1987): 1474-1489.

[196]   Mithraratne, P., and N.E. Wijeysundera. "An experimental and numerical study of hunting in thermostatic-expansion-valve-controlled evaporators." *International Journal of Refrigeration* 25 (2002): 992-998.

[197]   Mithraratne, P., and N.E. Wijeysundera. "An experimental and numerical study of the dynamic behavior of a counter-flow evaporator." *International Journal of Refrigeration* 24 (2001): 554-565.

[198]   Mithraratne, P., N.E. Wijeysundera, and T.Y. Bong. "Dynamic simulation of a thermostatically controlled counter-flow evaporator." *International Journal of Refrigeration* 23, no. 3 (2000): 174 –189.

[199]   Modelica Association. "Modelica specification, version 3.3." 2014. www.modelica.org.

[200]   Modelon. "Air Conditioning Library User Guide v1.8.4." 2014. http://www.modelon.com.

[201]   Morales-Ruiz, S., J. Rigola, C.D. Pérez-Segarra, and O. García-Valladares. "Numerical analysis of two-phase flow in condensers and evaporators with special emphasis on single-phase/two-phase transition zones." *Applied Thermal Engineering* 29, no. 5-6 (2009): 1032-1042.

[202]   Mortada, S., A. Zoughaib, D. Clodic, and C. Arzano-Daurelle. "Dynamic modeling of an integrated air-to-air heat pump using Modelica." *International Journal of Refrigeration* 35, no. 5 (2012): 1335-1348.

[203]   Murphy, W. E., and V. W. Goldschmidt. "Cyclic characteristics of a typical residential air conditioner - modeling of start-up transients." *ASHRAE Transactions* 91(Part 2A) (1985): 427-444.

[204]   Murphy, W. E., and V. W. Goldschmidt. "Cycling characteristics of a residential air conditioner - modeling of shutdown characteristics." *ASHRAE Transactions* 92 (Part 1A) (1986): 186-202.

[205]   Murphy, W.E., and V.W. Goldschmidt. "Transient response of air conditioners – a qualitative interpretation through a sample case." *ASHRAE Transactions* 90 (Part 1B) (1984): 997-1008.

[206]   Na, B. *Analysis of frost formation in an evaporator.* Ph.D. Thesis, The Pennsylvania State University, 2003.

[207]   Na, B., and R.L. Webb. "A fundamental understanding of factors affecting frost nucleation." *International Journal of Heat and Mass Transfer* 46 (2003): 3797-3808.

[208]   Na, B., and R.L. Webb. "Mass transfer on and within a frost layer." *International Journal of Heat and Mass Transfer* 47 (2004a): 899-911.

[209]   Na, B., and R.L. Webb. "New model for frost growth rate." *International Journal of Heat and Mass Transfer* 47 (2004b): 925-936.

[210]   Ndiaye, D., and M. Bernier. "Transient model of a geothermal heat pump in cycling conditions – Part A: the model." *Interntional Journal of Refrigeration* 35, no. 8 (2012a): 2110-2123.

[211]   Ndiaye, D., and M. Bernier. "Transient model of a geothermal heat pump in cycling conditions – Part B: experimental validation and results." *International Journal of Refrigeration* 35, no. 8 (2012b): 2124-2137.

[212]   Ndiaye, D., and M. Bernier. "Transient modeling of refrigerant-to-air fin-and-tube heat exchangers." *HVAC&R Research* 16 (2010b): 355-381.

[213]   Niederer, D.H. "Frosting and defrosting effects on coil heat transfer." *ASHRAE Transaction* 82 (Part I) (1976): 467-473.

[214]   Nyers, J., and G. Stoyan. "A dynamical model adequate for controlling the evaporator of a heat pump." *International Journal of Refrigeration* 17, no. 2 (1994): 101–108.

[215]   O'Neal, D. L., and Tree D. R. "A review of frost formation in simple geometries." *ASHRAE Transactions* 98 (Part 2) (1992): 65-78.

[216]   O'Neal, D.L., and K.T. Peterson. "A comparison of orifice and TXV control characteristics during the reverse-cycle defrost." *ASHRAE Transaction* 96 (Part I) (1990): 337-343.

[217]   O'Neal, D.L., K.T. Peterson, and N.K. Anand. "Effect of shot-tube orifice size on the performance of an air source heat pump during the reverse-cycle defrost." *International Journal of Refrigeration* 14 (1991): 52-57.

[218]   O'Neal, D.L., K.T. Peterson, N.K. Anand, and J.S. Schliesing. "Refrigeration system dynamics during the reverse cycle defrost." *ASHRAE Transaction* 95 (Part II) (1989): 689-698.

[219]   Padhmanabhan, S.K., D.E. Fisher, L. Cremaschi, and E. Moallem. "Modeling non-uniform frost growth on a fin-and-tube heat exchanger." *International Journal of Refrigeration* 34 (2011): 2018-2030.

[220]   Park, C., H. Cho, Y. Lee, and Y. Kim. "Mass flow characteristics and empirical ,odeling of R22 and R410A flowing through electronic expansion valves." *International Journal of Refrigeration* 30, no. 8 (2007): 1401-1407.

[221]   Park, Y.C., Y.C. Kim, and M.K. Min. " Performance analysis on a multi-type inverter air conditioner." *Energy Conversion and Management* 42, no. 13 (2001): 1607-1621.

[222]   Patankar, S.V. *Numerical heat transfer and fluid flow.* New York: Hemisphere Publishing Corporation, Taylor & Francis Group, 1980.

[223]   Payne, V., and D.L. O'Neal. "Defrost cycle performance for an air-source heat pump with a scroll and a reciprocating compressor." *International Journal of Refrigeration* 18, no. 2 (1995): 107-112.

[224]   Pettit, N.B.O.L., M. Willatzen, and L. Ploug-Sørensen. "A general dynamic simulation model for evaporators and condensers in refrigeration. Part II: simulation and control of an evaporator." *International Journal of Refrigeration* 21, no. 5 (1998): 404–414.

[225]   Pfafferott, T., and G. Schmitz. "Modeling and simulation of refrigeration systems with natural refrigerant CO2." Oberpfaffenhofen, Germany, Modelica Association: Proceedings of the 2th Modelica conference, 2002.

[226]   Pfafferott, T., and G. Schmitz. "Modeling and transient simulation of CO2-refrigeration systems with Modelica." *International Journal of Refrigeration* 27 (2004): 42-52.

[227]   Ploug-Sørensen, L., J.P. Fredsted, and M. Willatzen. "Improvements in modeling and simulation of refrigerant systems: aerospace tools applied to a domestic refrigerator." *HVAC&R Research* 34, no. 4 (1997): 387-403.

[228]   Prölss, K., and G. Schmitz. "Modeling of frost growth on heat exchanger surfaces." Proceedings of Modelica, 2006.

[229]   Qiao, H., L. Kwon, V. Aute, and R. Radermacher. "Transient modeling of a multi-evaporator air conditioning system and control method investigation." Montréal, Canada: 11th IEA Heat Pump Conference, 2014a.

[230]   Qiao, H., V. Aute, and R. Radermacher. "A new dynamic heat exchanger model with frosting and defrosting." West Lafayette, IN: 15th Int. Ref. and A-C Conf. at Purdue, 2014b.

[231]   Qiao, H., V. Aute, and R. Radermacher. "An improved moving boundary heat exchanger model with pressure drop." West Lafayette, IN: 15th Int. Ref. and A-C Conf. at Purdue, 2014c.

311

[232]   Qiao, H., V. Aute, and R. Radermacher. "Comparison of equation-based and non-equation-based approaches for transient modeling of a vapor compression cycle." West Lafayette, IN: 14th Int. Ref. and A-C Conf. at Purdue, 2012a.

[233]   Qiao, H., V. Aute, and R. Radermacher. "Transient modeling of a flash tank vapor injection heat pump system - Part I: Model development." *International Journal of Refrigeration*, 2014d.

[234]   Qiao, H., X. Xu, V. Aute, and R. Radermacher. "Modelica-based transient modeling for a flash tank vapor injection system and experimental validation." West Lafayette, IN: 14th Int. Ref. and A-C Conf. at Purdue, 2012b.

[235]   Qiao, H., X. Xu, V. Aute, and R. Radermacher. "Transient modeling of a flash tank vapor injection heat pump system - Part II: Simulation results and experimental validation." *International Journal of Refrigeration*, 2014e.

[236]   Qu, M., L. Xia, S. Deng, and Y. Jiang. "A study of the reverse cycle defrosting performance on a multi-circuit outdoor coil unit in an air source heat pump – Part I: Experiments ." *Applied Energy* 91, no. 1 (2012a): 122-129.

[237]   Qu, M., L. Xia, S. Deng, and Y. Jiang. "A study of the reverse cycle defrosting performance on a multi-circuit outdoor coil unit in an air source heat pump – Part II: Modeling analysis." *Applied Energy* 91, no. 1 (2012b): 274-280.

[238]   Rasmussen, B. *Dynamic modeling and advanced control of air conditioning and refrigeration systems.* Ph.D. Thesis, ACRC, University of Illinois At Urbana- Champaign, 2006.

[239]   Rasmussen, B. "Dynamic modeling for vapor compression systems-Part I: Literature review." *HVAC&R Research* 18, no. 5 (2012): 934-955.

[240]   Rasmussen, B., and A. Alleyne. "Control-oriented modeling of transcritical vapor compression systems." *ASME Journal of Dynamic Systems, Measurement, and Control* 126, no. 1 (2004): 54-64.

[241]   Rice, C.K. "The effect of void fraction correlation and heat flux assumption on refrigerant charge inventory predictions." *ASHRAE Transactions* 93 (Part I) (1987): 341-367.

[242]   Richter, C.C. *Proposal of new object-oriented equation-based model libraries for thermodynamic systems.* Ph.D. Thesis, Technische Universität Braunschweig, Institut für Thermodynamik., 2008.

[243]   Rigola, J., C.D. Pérez-Segarra, and A. Oliva. "Parametric studies on hermetic reciprocating compressors." *International Journal of Refrigeration* 28 (2005): 253-266.

[244]   Rossi, T.M., and J.E. Braun. "A real-time transient model for air conditioners." Proceedings of the 20th International Congress of Refrigeration, paper #743, 1999.

[245] Rubas, P.J., and C.W. Bullard. "Factors contributing to refrigerator cycling losses." *International Journal of Refrigeration* 18, no. 3 (1995): 168-176.

[246] Şahin, A.Z. "Effective thermal conductivity of frost during the crystal growth period." *International Jouranl of Heat and Mass Transfer* 43, no. 4 (2000): 539-553.

[247] Sami, S.M., and A. Dahmani. "Numerical prediction of dynamic performance of vapor compression heat pump using HFC alternatives to HCFC-22." *Applied Thermal Engineering* 16 (1996): 691-705.

[248] Sami, S.M., and Comeau M.A. "Development of a simulation model for predicting dynamic behaviour of heat pumps with non-azeotropic refrigerant mixtures." *International Journal of Energy Research* 16, no. 5 (1992): 431-444.

[249] Sami, S.M., and T.N. Duong. "Dynamic performance of heat pumps using refrigerant R-134a." *ASHRAE Transaction* 97 (Part 2) (1991): 41-47.

[250] Sami, S.M., and T.N. Duong. "Mass and heat transfer during frost growth." *ASHRAE Transactions* 95 (Part I) (1989): 158-165.

[251] Sami, S.M., and Y. Zhou. "Numerical prediction of heat pump dynamic behaviour using ternary non-azeotropic refrigerant mixtures." *International Journal of Energy Research* 19, no. 1 (1995): 19-35.

[252] Sami, S.M., T.N. Duong, Y. Mercadier, and N. Galanis. "Prediction of the transient response of heat pumps." *ASHRAE Transactions* 93 (Part 2) (1987): 471-490.

[253] Sanders, C.T. *The influence of frost formation and defrosting on the performance of air coolers.* Netherlands: Ph.D. Thesis, Delft Technical University, 1974.

[254] Scarcella, J., and Y.H. Chen. Liquid vapor separation in transcritical refrigerant cycle. USA Patent WO2010039682A2. 2010.

[255] Schalbart, P., and P. Haberschill. "Simulation of the behavior of a centrifugal chiller during quick start-up." *International Journal of Refrigeration* 36, no. 1 (2013): 222-236.

[256] Schmidt, T.E. "Heat transfer calculations for extended surfaces." *Refrigerating Engineering* 4 (1949): 281-289.

[257] Schurt, L.C., C.J.L. Hermes, and A.T. Neto. "A model-driven multivariable controller for vapor compression refrigeration systems." *International Journal of Refrigeration* 32, no. 7 (2009): 1672-1682.

[258] Seker, D., H. Karatas, and N. Egrican. "Frost formation on fin-and-tube heat exchangers. Part I – Modeling of frost formation on fin-and-tube heat exchangers." *International Journal of Refrigeration* 27 (2004): 367-374.

[259]   Shah, M.M. "A general correlation for heat transfer during film condensation inside pipes." *International Journal of Heat and Mass Transfer* 22 (1979): 547-556.

[260]   Shah, R., A. G. Alleyne, and C. W. Bullard. "Dynamic modeling and control of multi-evaporator air conditioning systems." *ASHRAE Transactions* 110 (Part 1) (2004): 109-119.

[261]   Shao, L.L., L. Yang, and C.L. Zhang. "Comparison of heat pump performance using fin-and-tube and microchannel heat exchangers under frost conditions." *Applied Energy* 87, no. 4 (2010): 1187-1197.

[262]   Shao, S., W. Shi, X. Li, and H. Chen. "Performance representation of variable-speed compressor for inverter air conditioners based on experimental data." *International Journal of Refrigeration* 27 (2004): 805-815.

[263]   Shao, S.Q., H.B. Xu, and C.Q. Tian. "Dynamic simulation of multi-unit air conditioners based on two-phase fluid network model." *Applied Thermal Engineering* 40 (2012): 378-388.

[264]   Sherif, S.A., and M.G. Hertz. "A semi-empirical model for electrical defrosting of a cylindrical coil cooler." *International Journal of Energy Research* 22 (1998): 85-92.

[265]   Sherif, S.A., S.P. Raju, M.M. Padki, and A.B. Chan. "A semi-empirical transient method for modeling frost formation on a flat plate." *International Journal of Refrigeration* 16, no. 5 (1993): 321-329.

[266]   Silva, D.L.da, C.J.L. Hermes, and C. Melo. "First-principles modeling of frost accumulation on fan-supplied tube-fin evaporators." *Applied Thermal Engineering* 31, no. 14-15 (2011): 2616-2621.

[267]   Smith, S.L. "Void fraction in two-phase flow: a correlation based upon an equal velocity head model." *Proceedings of the Institution of Mechanical Engineers* 184, no. 36 (1969): 647-664.

[268]   Stoecker, W.F. *Refrigeration and air conditioning.* 2nd edition. McGraw-Hill, 1983.

[269]   Stoecker, W.F., J.J. Lux Jr, and R.J. Kooy. "Energy considerations in hot-gas defrosting of industrial refrigeration coils." *ASHRAE Transaction* 89 (Part II) (1983): 549-573.

[270]   Tahavvor, A.R., and M. Yaghoubi. "Experimental and numerical study of frost formation by natural convection over a cold horizontal circular cylinder." *International Journal of Refrigeration* 33, no. 7 (2010): 1444-1458.

[271]   Tao, Y.X., R.W. Besant, and K.S. Rezkallah. "A mathematical model for predicting the densification and growth of frost on a flat plate." *International Journal of Heat and Mass Transfer* 36, no. 2 (1993): 353-363.

[272]   Thome, J.R.S. "Prediction of pressure drop during forced circulation boiling of water." *International Journal of Heat and Mass Transfer* 7 (1964): 709-724.

[273]   Tian, C., and X. Li. "Transient behavior evaluation of an automotive air conditioning system with a variable displacement compressor." *Applied Thermal Engineering* 25, no. 13 (2005): 1922–1948.

[274]   Tian, C., C. Dou, X. Yang, and X. Li. "Instability of automotive air conditioning system with a variable displacement compressor. Part 2. Numerical simulation." *International Journal of Refrigeration* 28, no. 7 (2005): 1111–1123.

[275]   Tokura, I., H. Saito, and K. Kishinami. "Study on properties and growth rate of frost layers on cold surfaces." *Journal of Heat Transfer* 105 (1983): 895-901.

[276]   Tso, C.P., Y.C. Cheng, and A.C.K. Lai. "An improved model for predicting performance of finned tube heat exchanger under frosting condition, with frost thickness variation along fin." *Applied Thermal Engineering* 26, no. 1 (2006a): 111-120.

[277]   Tso, C.P., Y.C. Cheng, and A.C.K. Lai. "Dynamic behavior of a direct expansion evaporator under frosting condition. Part I. Distributed model." *International Journal of Refrigeration* 29, no. 4 (2006b): 611–623.

[278]   Tso, C.P., Y.W. Wong, P.G. Jolly, and S.M. Ng. "A comparison of hot-gas by-pass and suction modulation method for partial load control in refrigerated shipping containers." *International Journal of Refrigeration* 24 (2001): 544-553.

[279]   Tummescheit, H. *Design and implementation of object-oriented model libraries using Modelica.* Lund, Sweden: Ph.D. Thesis, Department of Automatic Control, Lund Institute of Technology, 2002.

[280]   Turner, J.M. *Annular two-phase flow.* Hanover, NH.: Ph.D. Thesis, Dartmouth College, 1966.

[281]   Uhlmann, M., and S.S. Bertsch. "Theoretical and experimental investigation of startup and shutdown behavior of residential heat pumps." *International Journal of Refrigeration* 35, no. 8 (2012): 2138-2149.

[282]   Umezu, K., and S. Suma. "Heat pump room air-conditioner using variable capacity compressor." *ASHRAE Transaction* 90 (1984): 335-349.

[283]   Vargas, J.V.C., and J.A.R. Parise. "Simulation in transient regime of a heat pump with closed-loop and on-off control." *International Journal of Refrigeration* 18, no. 4 (1995): 235-243.

[284]   Videla, J. I., and B. Lie. "A new energy building simulation library." Proceedings of Modelica 2006, 2006.

[285]   Wallis, G.B. *One-dimensional two-phase flow.* New York: MacGraw-Hill, 1969.

[286]   Wang, C.C., C.J. Lee, C.T. Chang, and S.P. Lin. "Heat transfer and friction correlation for compact louvered fin-and-tube heat exchangers." *International Journal of Heat and Mass Transfer* 42 (1999): 1945-1956.

[287]   Wang, C.C., Y.T. Lin, and C.J. Lee. "Heat and momentum transfer for compact louvered fin-and-tube heat exchangers in wet conditions." *International Journal of Heat and Mass Transfer* 43 (2000): 3443-3452.

[288]   Wang, F.Q., G.G. Maidment, J.F. Missenden, and R.M. Tozer. "A novel special distributed method for dynamic refrigeration system simulation." *International Journal of Refrigeration* 30, no. 5 (2007): 887-903.

[289]   Wang, H., and S. Touber. "Distributed and non-steady-state modelling of an air cooler." *International Journal of Refrigeration* 14 (1991): 98-111.

[290]   Wang, J., and Y. Wu. "Start-up and shut-down operation in a reciprocating compressor refrigeration system with capillary tubes." *International Journal of Refrigeration* 13, no. 3 (1990): 187-190.

[291]   Wang, W., J. Xiao, Q.C. Guo, W.P. Lu, and Y.C. Feng. "Field test investigation of the characteristics for the air source heat pump under two typical mal-defrost phenomena." *Applied Energy* 88 (2011): 4470-4480.

[292]   Wang, W., Q.C. Guo, W.P. Lu, Y.C. Feng, and W. Na. "A generalized simple model for predicting frost growth on cold flat plate." *International Journal of Refrigeration* 35 (2012): 475-486.

[293]   Wang, Z.Y., X.M. Wang, and Z.M. Dong. "Defrost improvement by heat pump refrigerant charge compensating." *Applied Energy* 85, no. 11 (2008): 1050-1059.

[294]   Wedekind, G.L., and W.F. Stoecker. "Theoretical model for predicting the transient response of the mixture-vapor transition point in horizontal evaporating flow." *Journal of Heat Transfer* 90, no. 1 (1968): 165-174.

[295]   Wedekind, G.L., B.L. Bhatt, and B.T. Beck. "A system mean void fraction model for predicting various transient phenomena associated with two phase evaporating and condensing flows." *International Journal of Multiphase Flow* 4 (1978): 97–114.

[296]   Wei, D.H., X.S. Lu, Z. Lu, and J.M. Gu. "Dynamic modeling and simulation of an Organic Rankine Cycle (ORC) system for water heat recovery." *Applied Thermal Engineering* 28 (2008): 1216-1224.

[297]   Willatzen, M., N.B.O.L. Pettit, and L. Ploug-Sørensen. "A general dynamic simulation model for evaporators and condenser in refrigeration. Part I: moving boundary formulation of two phase flows with heat exchange." *International Journal of Refrigeration* 21, no. 5 (1998): 398–403.

[298]   Winandy, E.L., and J. Lebrun. "Scroll compressors using gas and liquid injection: experimental analysis and modeling." *International Journal of Refrigeration* 25 (2002): 1143-1156.

[299]   Winkler, J. *Development of a component based simulation tool for the steady state and transient analysis of vapor compression systems.* Ph.D. Thesis, University of Maryland College Park, 2009.

[300] Wong, T.N., and K.T. Ooi. "Adiabatic capillary tube expansion device: a comparison of the homogenous flow and the separation flow models." *Applied Thermal Engineering* 16, no. 7 (1996): 625-634.

[301] Xia, Y., Y. Zhong, P.S. Hrnjak, and A.M. Jacobi. "Frost, defrost, and refrost and its impact on the air-side thermal-hydraulic performance of louvered-fin, flat-tube heat exchangers." *International Journal of Refrigeration* 29 (2006): 1066-1079.

[302] Xu, B., et al. "Experimental investigation of frost and defrost performance of microchannel heat exchangers for heat pump systems." *Applied Energy* 103 (2013a): 180-188.

[303] Xu, S., G. Ma, Q. Liu, and Z. Liu. "Experiment study of an enhanced vapor injection refrigeration/heat pump system using R32." *International Journal of Thermal Sciences* 68 (2013b): 103-109.

[304] Xu, X., P. Yan, S. Deng, L. Xia, and M. Chan. "Experimental study of a novel capacity control algorithm for a multi-evaporator air conditioning system." *Applied Thermal Engineering* 50 (2013c): 975-984.

[305] Xu, X., Y. Hwang, and R. Radermacher. "Performance comparison of R410A and R32 in vapor injection cycles." *International Journal of Refrigeration* 36, no. 3 (2013d): 892-903.

[306] Xu, X., Y. Hwang, and R. Radermacher. "Refrigerant injection for heat pumping/air conditioning systems: Literature review and challenges discussions." *International Journal of Refrigeration* 34 (2011a): 402-415.

[307] Xu, X., Y. Hwang, and R. Radermacher. "Transient and steady-state experimental investigation of flash tank vapor injection heat pump cycle control strategy." *International Journal of Refrigeration* 34 (2011b): 1922-1933.

[308] Xuan, S. *Generic dynamic model for a range of thermal system components.* Ph.D. Thesis, University of Maryland College Park, 2010.

[309] Yang, D.K., K.S. Lee, and D.J. Cha. "Frost formation on a cold surface under turbulent flow." *International Journal of Refrigeration* 29, no. 2 (2006a): 164-169.

[310] Yang, D.K., K.S. Lee, and S. Song. "Fin spacing optimization of a fin-tube heat exchanger under frosting conditions." *International Journal of Heat and Mass Transfer* 48 (2006b): 2619-2625.

[311] Yang, D.K., K.S. Lee, and S. Song. "Modeling of prediction frosting behavior of a fin-tube heat exchanger." *International Journal of Heat and Mass Transfer* 49 (2006c): 1472-1479.

[312] Yang, L., and C.L. Zhang. "Two-fluid model of refrigeration two-phase flow through short tube orifice." *International Journal of Refrigeration* 28, no. 3 (2005): 419-427.

[313]   Yao, Y., Y. Jiang, S. Deng, and Z. Ma. "A study on the performance of the airside heat exchanger under frosting in an air source heat pump water heater/chiller unit." *International Journal of Heat and Mass Transfer* 47, no. 17-18 (2004): 3745-3756.

[314]   Yasuda, H., S. Touber, and C.H.M. Machielsen. "Simulation model of a vapor compression refrigeration system." *ASHARE Transactions* 89 (Part 2A) (1983): 408-425.

[315]   Yasuda, H., T. Senshu, S. Kuroda, A. Atsumi, and K. Oguni. "Heat pump performance under frosting conditions: Part II – Simulation of heat pump cycle characteristics under frosting conditions." *ASHRAE Transaction* 96 (Part I) (1990): 330-336.

[316]   Yebra, L.J., M. Berenguel, and S. Dormido. "Extended moving boundary model for two-phase flows." 16th IFAC World Congress, 2005.

[317]   Youbi-Idrissi, M., and J. Bonjour. "The effect of oil in refrigeration: current research issues and critical review of thermodynamic aspects." *International Journal of Refrigeration* 31, no. 2 (2008): 165-179.

[318]   Yun, R., Y. Kim, and M.K. Min. "Modeling of frost growth and frost properties with airflow over a flat plate." *International Journal of Refrigeration* 25 (2002): 362-371.

[319]   Zhang, C.L., and G.L. Ding. "Modified general equation for the design of capillary tubes." *Journal of Fluids Engineering* 123, no. 4 (2001): 914-919.

[320]   Zhang, C.L., and L. Yang. "Modeling of supercritical CO2 flow through short tube orifices." *Transactions of ASME* 127 (2005): 1194-1198.

[321]   Zhang, T., J.T. Wen, J. Catano, and R. Zhou. "Stability analysis of heat exchanger dynamics." St. Louise, MO, USA: American Control Conference, 2009a.

[322]   Zhang, W.J., and C.L. Zhang. "A correlation-free on-line optimal control method of heat rejection pressures in CO2 transcirical systems." *International Journal of Refrigeration* 34, no. 4 (2011a): 844-850.

[323]   Zhang, W.J., and C.L. Zhang. "A generalized moving-boundary model for transient simulation of dry-expansion evaporators under larger disturbances." *International Journal of Refrigeration* 29 (2006): 1119-1127.

[324]   Zhang, W.J., and C.L. Zhang. "Transient modeling of an air conditioner with a rapid cycling compressor and multi-indoor units." *Energy Conversion and Management* 52, no. 1 (2011b): 1-7.

[325]   Zhang, W.J., C.L. Zhang, and G.L. Ding. "On three forms of momentum equation in transient modeling of residential refrigeration systems." *International Journal of Refrigeration* 32 (2009b): 938-944.

[326]   Zhang, W.J., C.L. Zhang, and G.L. Ding. "Transient modeling of an air-cooled chiller with economized compressor. Part I: Model development and validation." *Applied Thermal Engineering* 29 (2009c): 2396-2402.

[327]   Zhang, W.J., S.F Ding, and Zhang, C.L. "Transient modeling of an air-cooled chiller with economized compressor Part II: Application to control design." *Applied Thermal Engineering* 29 (2009d): 2403-2407.

[328]   Zhao, L.X., C.L. Zhang, and B. Gu. "Neural-network-based polynomial correlation of single- and variable-speed compressor performance." *HVAC&R Research* 15, no. 2 (2009): 255-268.

[329]   Zhou, X., and J.E. Braun. "A simplified dynamic model for chilled-water cooling and dehumidifying coils – Part I: Development (RP-1194)." *HVAC&R Research* 13 (2007a): 785-804.

[330]   Zhou, X., and J.E. Braun. "A simplified dynamic model for chilled-water cooling and dehumidifying coils – Part II: Experimental validation (RP-1194)." *HVAC&R Research* 13 (2007b): 805-817.

[331]   Zhu, Y., X. Jin, Z. Du, B. Fan, and S. Su. "Generic simulation model of multi-evaporator variable refrigerant flow air conditioning system for control analysis." *International Journal of Refrigeration* 36 (2013): 1602-1615.

[332]   Zivi, S.M. "Estimation of steady-state steam void-fraction by means of the principle of minimum entropy production." *ASME Journal of Heat Transfer* 86 (1964): 247-252.